

Searching for quasicrystals in block copolymer phase separation



Merin Joseph

Department of Applied Mathematics

University of Leeds

Submitted in accordance with the requirements

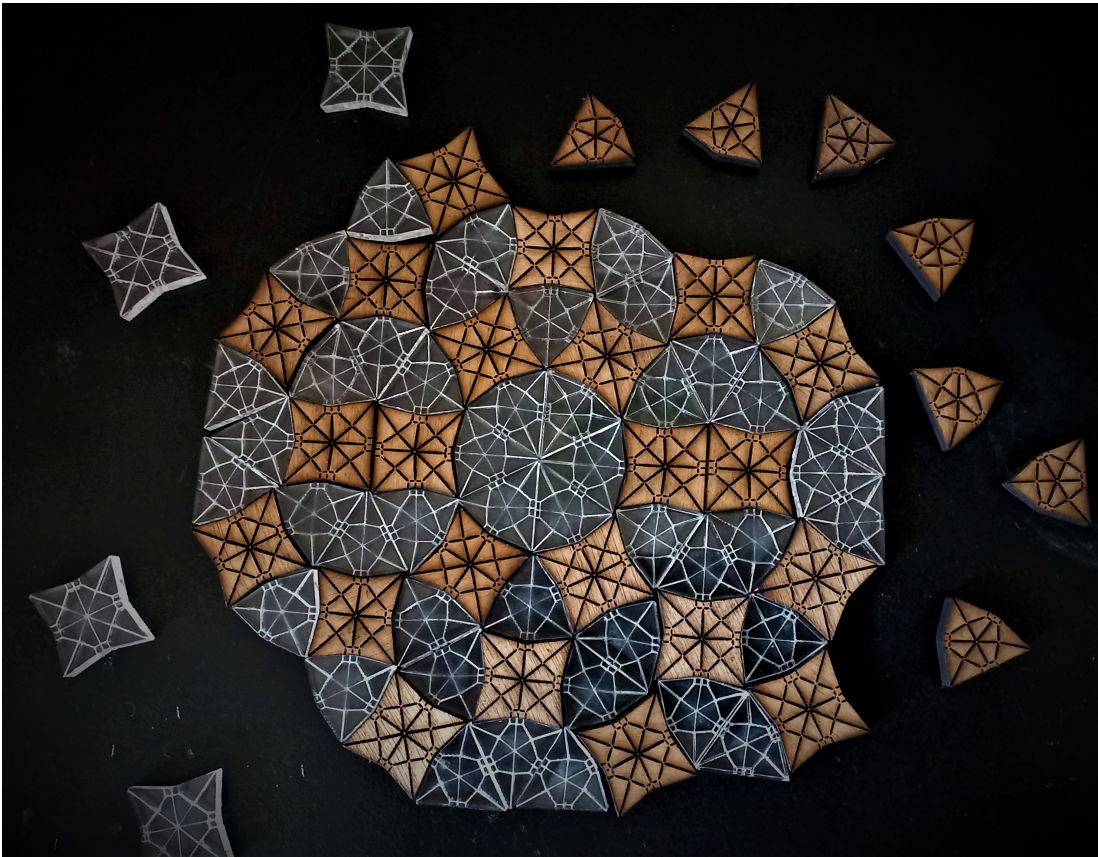
for the degree of

Doctor of Philosophy

August, 2023

Dedicated to....

Echachan, my grandfather
that common shopkeeper, who stayed my ultimate support
until his last breath.



The curvy 'square' and 'triangle' tiles produced via this thesis.

Acknowledgements

I extend my sincerest appreciation to my supervisors, Alastair Rucklidge and Daniel Read. Their steadfast support and unwavering patience have been indispensable throughout these years. I am genuinely grateful to them for everything starting from opening my mail inquiring about a PhD position to their ongoing mentorship that has nurtured my growth as a more adept researcher. Their roles as supervisors, educators, and mentors have truly been unparalleled.

I also wish to express my gratitude to Ron Lifshitz, Andrew Archer, Priya Subramanian, Steve Fitzgerald, Daniel Ratliff and Chinmay Das for their valuable discussions, which enabled me to delve into the intricacies of these fascinating patterns. I'm particularly grateful to Petra Staynova for the support, encouragement and also for cutting the tiles (on the left) and hence giving a form to my patterns. I am thankful to Jacob Kirkensgaard from Neil Bohr Institute for providing me with the DPD codes to compare my results. Furthermore, I am deeply thankful to SOFI-CDT and the School of Mathematics for the financial backing that facilitated this PhD journey.

My heartfelt thanks also extend to Katie Chicot and the entire Mathscity team for affording me the privilege of being part of their community. Their platform not only provided an avenue to cultivate a deeper appreciation for the beauty of mathematics but also enabled me to enhance my skills in science communication. A special acknowledgement goes to Alice Chandler, whose collaborative involvement in the Creative Labs project expanded my intellectual horizons in unforeseen ways.

Undertaking this PhD trajectory in the pre-COVID era and culminating it in a time when the pandemic receded from collective awareness has been a unique experience. The challenges of being an international student further accentuated the journey. However, the unwavering support from those around me, frequently echoing, "You can do this, Merin!" propelled me forward. I am equally grateful to the SOFI CDT for not only the financial provision but also for fostering a tight-knit community among cohort 5 members, with a special mention to

those in Leeds: ‘Spice Girls ft’ Jordan’. Doing a PhD and getting to the other end with my sanity intact would not have been possible without the SEE Badminton group, who welcomed my invasion with friendship and let me sharpen my badminton skills. I thank Joanna, Sijia, Christina, Rukia and Adam for the company, walks and chilled coffee breaks. To my friends back home, though physically distant, your constant encouragement spanning thousands of kilometres has been a cornerstone of my perseverance from the very start.

Lastly but most importantly, I reserve my deepest gratitude for my parents, Gigi Jose and V.H Joseph, who have been unwavering in their guidance and support. Their influence has significantly shaped my worldview and ambition. I am grateful for their and Abin’s support throughout my life which I take for granted most of the time.

Abstract

Quasicrystals are materials that display long-range order despite lacking translational periodicity. Despite it has been 41 years since its discovery, the stability of quasicrystals remains a perplexing enigma for scientists. Initially discovered in metals, these structures also appear in soft matter systems like block copolymers.

Polymer chains that contain two or more different types of monomer blocks joined together are block copolymers. They can microphase separate to form different patterns and structures in their morphology, including quasicrystals. Different morphological structures are formed depending on the block lengths and the interaction strengths. This soft matter system, akin to a designer material, can be adjusted to autonomously self-assemble into various intriguing morphologies, including quasicrystals.

This thesis proposes two methods for designing block copolymers with the potential to self-assemble into quasicrystals. The stability of morphologies in block copolymers can be determined using well-established phase separation theories: weak segregation theory (WST), self-consistent field theory (SCFT), and strong segregation theory (SST). In this study, we present design criteria for two categories of block copolymers: two-component alternating linear chains and ABC star terpolymers within the context of weak segregation limit. These criteria guide the self-assembly of structures with length-scale ratios conducive to quasicrystals. The second half of the thesis presents a novel framework in strong segregation limit where morphologies in ABC star terpolymers are compared with tiling patterns to study their stability. This framework can incorporate periodic tilings and periodic approximants of aperiodic tilings and develop the phase space for ABC star terpolymers.

The overarching aim is to make experimentally valid predictions on polymer architectures that could lead to stable 2- and 3-dimensional quasicrystals or other structures. Using the two methodologies, we find experimentally feasible composition ranges in the block copolymers we are considering in this thesis that can potentially form quasicrystal or other interesting, complex morphologies.

The candidate confirms that the work submitted is her own, except where work which has formed part of jointly authored publications has been included. The contribution of the candidate and the other authors to this work has been explicitly indicated below. The candidate confirms that appropriate credit has been given within the thesis where reference has been made to the work of others.

The work in Chapter 2 produced a jointly authored publication:

- Joseph, M., Read, D.J. and Rucklidge, A.M., *Design of linear block copolymers and ABC star terpolymers that produce two length scales at phase separation*. *Macromolecules* 2023, 56, 19, 7847–7859.

The candidate performed all the calculations and preparation of figures for the paper. MJ also wrote the initial draft of the article. AMR, DJR and MJ were involved in revising the manuscript for publication.

This copy has been supplied on the understanding that it is copyright material and that no quotation from the thesis may be published without proper acknowledgement.

Abbreviations and Nomenclatures

$k_B T$	Thermal energy
N	Total number of monomer units in a chain
χ	Flory interaction parameter
b	Kuhn Length
QC	Quasicrystal
WST	Weak Segregation Theory
SST	Strong Segregation Theory
$SCFT$	Self Consistent Field Theory
SSP	Strongly Segregated Polygons

Morphology

Natural numbers separated by dots and semicolons inside square braces indicate different patterns formed during block copolymer phase separation in terms of different coloured domains.

- $[a.b.c]$ Morphology with only one type of arrangement between three different coloured domains. This indicates a pattern formed where one coloured domain shares sides with a domains, another shares sides with b domains and the third shares sides with c domains.
- $[a.b.c;d.e.f;\dots]$ Morphology with more than one type of arrangements between three different coloured domains. In this morphology, domains of one colour have two or more different configurations. Arrangements of these domains are separated by semicolons. Domain of one colour shares sides with a domains or d domains or so on. The second coloured domain shares sides with b domains or e domains or so on. Similarly, the third coloured domain shares sides with c domains or f domains or so on. A combination of all different configurations of domains constitutes the morphology.

Tiling

This thesis considers tilings made of regular polygons (triangles, squares, etc with whose side lengths are equal). They are classified using their vertices.

- (n_1, n_2, n_3, \dots) The tiling consists of vertices around which there are n_1 -gon, n_2 -gon, n_3 -gon and so on. [\[53\]](#)

Here $n_1, n_2, n_3 \dots \in \mathbb{N}$.

Contents

1	Introduction	1
1.1	Quasicrystals in soft matter	3
1.2	Stability of soft matter quasicrystals	6
1.3	Block copolymer phase separation	8
1.3.1	Parallels between polymer phase separation and quasicrystal formation	14
1.4	ABC star terpolymer and its morphologies	14
1.5	Thesis Outline	19
2	Weak Segregation Approach for Phase Separation	23
2.0.1	Brief review of polymer statistics	24
2.1	Random Phase Approximation	25
2.1.1	RPA for a single component polymer system	26
2.1.2	RPA for incompressible polymer system with two components	33
2.1.3	RPA for 3 component system	38
2.2	Structure factor for any arbitrary chain : Review based on $(AB)_{L_b}$	41
2.3	Monodisperse two component model: $A_L(BA_S)_n$	45
2.3.1	Structure factor for $A_L(BA_S)_2$	47
2.3.2	Structure factor for $A_L(BA_S)_n$	50
2.3.3	Results	54
2.3.4	$A_LBA_S B$	59
2.3.5	Discussion	61
2.4	Two component linear chains with random assembly	62
2.4.1	RPA for linear chains with random assembly	64
2.4.2	Discussion	70
2.5	ABC star terpolymer	72
2.5.1	RPA for ABC star	73
2.5.2	Results	75
2.5.3	Discussion	79
2.6	Conclusion	80

3	Formulation of Strong Segregation Theory for <i>ABC</i> star terpolymer	83
3.1	Stretching free energy for a brush	84
3.2	Interfacial energy at block copolymer interfaces	88
3.3	Strong segregation for two-component block copolymers	89
3.3.1	Lamellar morphology	89
3.3.2	Free energy of a wedge	92
3.4	Strong Segregation Theory for <i>ABC</i> star terpolymer	100
3.4.1	Stretching free energy of brushes on curved surface	101
3.4.2	SST for hexagonal morphology in <i>ABC</i> star terpolymer	103
3.5	Strongly Segregated Polygon method	116
3.5.1	Interfacial energy in an SSP	119
3.5.2	Stretching energy in an SSP	120
3.6	Shape shifting minimisation	124
3.7	Summary	127
4	Computational tools in Strongly Segregated Polygon analysis	129
4.1	Strongly Segregated Polygon (SSP) Method: manual computation	129
4.1.1	The ‘constraint list’ and free energy minimisation	132
4.2	Constructing large tilings from SSPs	133
4.2.1	Combinatorics with monomer compositions	141
4.3	Fourier Analysis of morphologies created using <i>SSPs</i>	142
4.4	Multi-variable minimisation	145
4.5	Phase space exploration	148
5	<i>ABC</i> star terpolymers morphologies: Periodic	153
5.1	Symmetric <i>ABC</i> star terpolymers ($\nu_{AB} = \nu_{BC} = \nu_{AC} = 1$)	153
5.1.1	[6.6.6]-Hexagon	154
5.1.2	[8.8.4]-Square	157
5.1.3	[12.6.4]-Triangle	160
5.1.4	[8.6.4; 8.6.4; 8.6.6]	164
5.1.5	[10.6.4; 10.6.4; 10.6.6]	167
5.1.6	Phase space and Discussion	169
5.2	<i>ABC</i> star architectures and phase space for asymmetric interactions	174
5.2.1	Discussion on effects of asymmetric interactions in <i>ABC</i> star terpolymers.	175
5.2.2	$\nu_{AB} = \nu_{BC} = 1, \nu_{AC} < 1$	176
5.2.3	$\nu_{AB} = \nu_{BC} = 1, \nu_{AC} > 1$	180
5.2.4	$\nu_{BC} < \nu_{AB} < \nu_{AC}$	184
5.3	Discussion	187

CONTENTS

6	Periodic approximants of Square-Triangle tilings in ABC star terpolymers	191
6.1	What happens when squares and triangles are put together? . . .	192
6.2	Σ -phase	194
6.2.1	Phase spaces with asymmetric interaction strengths	198
6.3	Dodecagonal arrangements of squares and triangles	201
6.3.1	Square (a)	205
6.3.2	Square (b)	207
6.3.3	Square (c)	211
6.3.4	Triangle (a)	212
6.3.5	Triangle (b)	215
6.4	Linear phase spaces	215
6.5	Fourier analysis of square-triangle tilings	220
6.6	Discussion	224
7	Conclusion	227
7.1	Future research proposed	232
A		235
A.1	Calculation of internal energy in polymer melt of one component	235
A.2	Calculation of \widetilde{W}_q	236
B		241
B.1	Stretching free energy for a wedge	241
B.2	Input file structure	244
	References	262

CONTENTS

List of Figures

1.1	Images of first quasicrystal	2
1.2	Polymeric quasicrystal	6
1.3	Three wave interaction with 12 fold symmetry	7
1.4	Morphologies in ABC star terpolymer phase separation	9
1.5	ABC star terpolymer	15
2.1	Polymer chain model	24
2.2	Debye function	28
2.3	A schematic representation of a diblock.	36
2.4	Scattering factor for diblock	38
2.5	An arbitrary chain α of A blocks	42
2.6	$(AB)_{L_b}$ block polymer	43
2.7	Non-interacting structure factor for infinite diblock	44
2.8	An illustration of $A_L(BA_S)_n$	46
2.9	Schematic structure for $A_L(BA_S)_2$	47
2.10	Structure factor for $A_L(BA_S)_2$	49
2.11	Part II of polymer chain $A_L(BA_S)_n$	50
2.12	$S_0(Q)$ for $A_L(BA_S)_2$	55
2.13	$S_0(Q)$ for $A_L(BA_S)_7$	56
2.14	Contour plot for $A_L(BA_S)_n$	57
2.15	Illustration of monodisperse chain $A_LBA_S B$	59
2.16	Non-interacting structure factor for $A_LBA_S B$	61
2.17	Schematic representation of the polydisperse model	62
2.18	Non-interacting structure factor for random block model	68
2.19	Composition map for random assembly model.	69
2.20	Contour map for monodisperse model in terms of ν_{A_S} and ν_B	71
2.21	Schematic representation for 3-component ABC star block copolymer	72
2.22	Eigenvalues for symmetric ABC star terpolymer	76
2.23	Eigenvalue variations for $Q_r = 1.6$ and $Q_r = 2.1$ for ABC star	77
2.24	Contour space for symmetric ABC star terpolymer.	78
2.25	Composition space for different ξ values in ABC star terpolymer.	81

LIST OF FIGURES

3.1	Schematic representation of chains stretching out from an interface	84
3.2	Schematic representation of lamellar morphology at SSL	90
3.3	Free energy variation of lamellar morphology	91
3.4	Schematic representation of (a) hexagonal and (b) cylindrical morphologies for diblocks.	92
3.5	SST wedge for two component system.	93
3.6	Schematic representation of choosing wedges for hexagonal and cylindrical morphology.	96
3.7	Schematic representation of ABC star terpolymer and phase separation	101
3.8	Schematic representation of the wedge with only one type of polymer chain grafted into a core cylinder.	102
3.9	An example of hexagonal morphology in ABC star terpolymer phase separation	103
3.10	The repeating equilateral triangle in hexagonal morphology	104
3.11	The triangle patches for hexagonal morphology with two different compositions.	107
3.12	Diagram of Area I in the triangle	109
3.13	Free energy per chain for two different monomer compositions as given in triangular domain	113
3.14	Hexagonal morphologies formed from different monomer compositions	114
3.15	Free energy maps for hexagonal morphology using triangle SST	115
3.16	Structure of an SSP	117
3.17	Possible triangles in an SSP	121
3.18	Shape shifting minimisation explained using $SSPs$	125
3.19	Free energy map for hexagon using SSP	127
4.1	Illustration of the nodes in SSP methodology	130
4.2	Tiling of the periodic motif of Σ - phase.	134
4.3	Illustration of all nodes in Σ -phase for the placing of $SSPs$.	136
4.4	Flowchart describing the process of placing $SSPs$ to larger tile.	138
4.5	Illustration of placing $SSPs$ into an original tile.	139
4.6	Initial configuration for Σ -phase	140
4.7	Process of minimisation	146
4.8	Phase space labelling and exploration is explained schematically	150
4.9	Phase space exploration is demonstrated using this flow chart	151
5.1	Morphological analysis of hexagonal morphology	156
5.2	The initial configuration for the square morphology	157
5.3	Six topological varieties of square morphology	158
5.4	Free energy maps for triangle morphology	160
5.5	Initial configurations of triangle morphology	161

LIST OF FIGURES

5.6	Different topological sub-classes in triangle morphology	162
5.7	Free energy maps for six topological sub-classes of triangle morphology	163
5.8	Initial configurations of (8.6.4; 8.6.4; 8.6.6)	165
5.9	Morphologies and free energy maps of (8.6.4; 8.6.4; 8.6.6).	166
5.10	Initial configurations of (10.6.4; 10.6.4; 10.6.6) morphology	167
5.11	Morphologies of (10.6.4; 10.6.4; 10.6.6)	168
5.12	Phase space for symmetric ABC star morphology	172
5.13	Asymmetric surface tension in the domains.	175
5.14	Structure of hexagonal morphology when $\nu_{AB} = \nu_{BC} = 1, \nu_{AC} = 0.8$	177
5.15	Phase space for ABC star with interactions: $\nu_{AB} = \nu_{BC} = 1, \nu_{AC} = 0.8$	178
5.16	Morphological structures with asymmetric interactions $\nu_{AB} = \nu_{BC} = 1, \nu_{AC} = 1.4$	181
5.17	Phase space for asymmetric interactions $\nu_{AB} = \nu_{BC} = 1, \nu_{AC} = 1.4$	182
5.18	Comparison of the phase spaces	183
5.19	Comparison of morphology (6.6.6) morphology for $\nu_{AB} = 1.0, \nu_{BC} = 0.6$ and $\nu_{AC} = 1.6$	185
5.20	Phase space for the asymmetric case $\nu_{AB} = 1.0, \nu_{BC} = 0.6$ and $\nu_{AC} = 1.6$	186
5.21	Proposed SSP for lamellar morphologies.	188
6.1	Morphological analysis of H -phase	193
6.2	Morphology of Σ -phase in ABC star terpolymer	195
6.3	Phase space for ABC star terpolymer with equal interaction strength	197
6.4	Phase spaces for different asymmetric interactions	200
6.5	A dodecagon with square and triangle arrangement in them.	202
6.6	Square and rectangular arrangement of dodecagons	203
6.7	Triangular arrangement of dodecagons	204
6.8	Periodic patch with square and triangle tiles for square (a)	205
6.9	Minimised configuration for square (a)	206
6.10	Periodic patch of square (b)	207
6.11	SSP analysis of square (b)	209
6.12	Different varieties of squares and triangles obtained after minimisation	210
6.13	Periodic patch for square (c)	211
6.14	The minimised configuration for square (c)	212
6.15	Morphologies for triangle (a).	213
6.16	Morphology of the triangle (b).	214
6.17	Linear phase space for symmetric interactions.	216
6.18	Linear phase space for $\nu_{AB} = \nu_{BC} = 1, \nu_{AC} = 0.8$	218
6.19	Linear phase space for $\nu_{AB} = \nu_{BC} = 1, \nu_{AC} = 1.4$	219

LIST OF FIGURES

6.20	Linear phase space for $\nu_{AB} = 1, \nu_{BC} = 0.6, \nu_{AC} = 1.6$	219
6.21	Morphologies and their corresponding Fourier spectra.	222
7.1	Phase spaces for ABC star terpolymer in WST and SST	230
7.2	Results of DPD simulation	231

Chapter 1

Introduction

Quasicrystals are materials that exhibit long-range order despite not having translational periodicity. Until 1982, crystals were believed to be materials that are characterised by repeating a unit cell and so have spatial periodicity. This principle of crystal classification was called into question with the discovery of quasicrystals, which do not have a repeated unit cell and yet have long-range order. In crystallography, 10-, 5- and 12-fold rotational symmetry are considered forbidden as these are inconsistent with a periodic arrangement of atoms and so cannot have a single unit cell. The first quasicrystal was discovered by Dan Shechtman in 1982 in a metallic alloy of Aluminium and Manganese (fig. 1.1.(a)) [140]. The diffraction pattern of this solidifying alloy showed sharp peaks with 10-fold rotational symmetry indicating that the material had both a forbidden symmetry and long-range order as in fig. 1.1.(b). This phenomenal discovery paved way for changing the definition of a crystal to: "by crystal we mean any solid having an essentially discrete diffraction diagram, and by aperiodic crystal we mean any crystal in which three-dimensional lattice periodicity can be considered to be absent" [73]. Shechtman's discovery was awarded the Nobel Prize in Chemistry in 2011. Although these materials were first found in complex solidifying metal alloys, quasicrystalline structures have also been observed in natural systems: the diffraction pattern of a micron-sized grain of $Al_{71}Ni_{24}Fe_5$ from a Khatyrka meteorite fragment showed 10-fold rotational symmetry [21].

The quasicrystal discovered in metal alloys by Shetchman were meta-stable. When the sample was heated above a certain temperature ($350 - 400^\circ C$), the quasiperiodic arrangement of atoms did not survive and it transformed to a different phase. A stable metallic quasicrystal with icosahedral symmetry was discovered by Tsai et al. in the alloy $Al_{65}Cu_{20}Fe_{15}$ [161]. There are multiple speculations about what makes metallic quasicrystals stable [29, 148], but the stability of quasicrystals remains an open question in the scientific community.

Metallic quasicrystals have found some applications in cooking appliances and photonics [78, 95, 149].

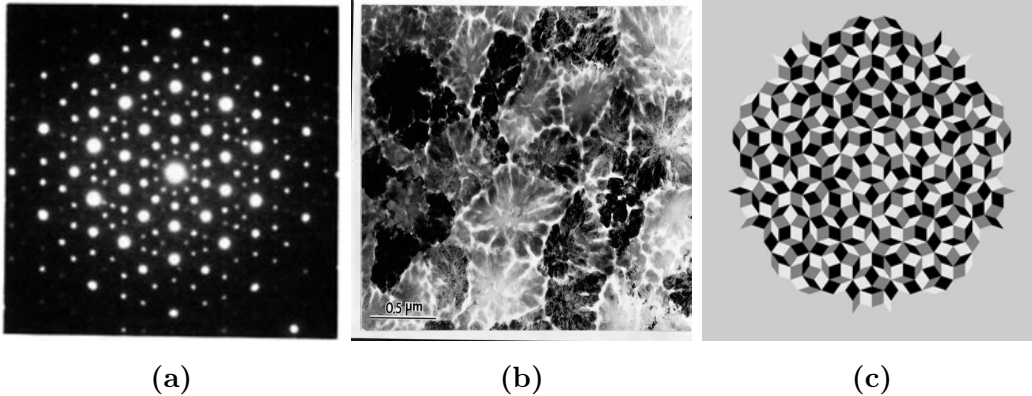


Figure 1.1: [From Left] (a) Diffraction pattern obtained for an icosahedral quasicrystal in an Aluminium and Manganese alloy, taken from [140]. (b) First view of a crystal with icosahedral symmetry, credit: Shechtman [3]. (c) A Penrose tiling with five-fold symmetry consisting two type of rhombuses [1].

While this rebellious discovery was happening in material science, this was no news for mathematicians, who had explored non-repeating structures in depth in aperiodic tilings. The problems in tilings are old as civilisation. Tiling or filling a surface with regular or non regular shapes becomes more complicated when the aim is to achieve non-repeating patterns. Similar to forbidden symmetries in crystallography, it was considered impossible to tile a plane with pentagons or shapes with five-fold symmetry. The curiosity over aperiodic tilings goes back to the time of Kepler when he tried to pack a plane with simple geometrical shapes. In this process, in 1619 he discovered 11 Archimedean tilings and some finite aperiodic arrangements that are mentioned in his book *Harmonice Mundi* [139]. Amongst Kepler’s aperiodic tilings, there is a five-fold tiling created from various shapes. This tiling inspired Roger Penrose in 1974 to solve the question of aperiodic tilings with 5-fold symmetry [122], resulting in the famous Penrose tilings, which are composed of two¹ geometrical shapes or prototiles² given in fig. 1.1.(c). Mackay had predicted the possibility of a material that would exhibit the aperiodicity of Penrose tilings [94]. Immediately after the discovery

¹The lowest number of protiles needed to make an aperiodic tiling is reduced to one with the monotile discovery [146].

²Protiles are the constituent shapes that are used in making a tiling pattern, eg two different rhombuses seen in the Penrose tile.

of quasicrystals, Steinhardt made connections between Penrose tilings and quasicrystals [88]. Henceforth aperiodic tilings with a definite diffraction pattern and long-range order became synonymous with quasicrystals.

As quasicrystals with different rotational symmetries like 8-fold, 10-fold, 12-fold, 18-fold, and so on were discovered, aperiodic tilings with corresponding rotational symmetries became more intriguing [47, 161, 166, 172]. More connections were made between aperiodic tilings of different prototiles and different rotational symmetries found in materials. In metallic alloys, quasicrystals are found with order at smaller near-atomic lengthscales. Icosahedral quasicrystal and 5-fold symmetric structures are observed more in metallic alloys. In metallic quasicrystals, aperiodicity is observed in three directions so 3D projections of the tilings are considered [88]. In later years quasicrystals have been observed in systems with mesoscopic lengthscales like soft matter or nanoplates where they exhibit other rotational symmetries. While icosahedral quasicrystals are associated with the Penrose tilings, 8-fold quasicrystals are compared to Ammann-Beenker tiling [45, 53] and 12-fold quasicrystals are mostly associated with square-triangle aperiodic tilings [14, 119]. In mesoscopic systems, observed quasicrystals are often aperiodic in two dimensions and periodic in the third dimension, so these patterns are related to 2D tilings [58]. In soft matter systems the most commonly found quasicrystals have 12-fold dodecagonal symmetry [172]. Dodecagonal aperiodic tilings can be made from squares and equilateral triangles [57, 71], but it is unknown why soft matter systems prefer these particular geometrical shapes while forming quasicrystals.

Quasiperiodic patterns can also be found in fluid systems, in the Faraday wave experiment [41]. Quasiperiodic patterns with 12-fold symmetry have been reported when exciting a layer of fluid with two frequencies that are in certain ratios. Stability of quasipatterns in these experiments is attributed to the non linear interaction between waves [130].

Even with all these observations an explanation on the causality of stable quasicrystals is missing in the research [148].

1.1 Quasicrystals in soft matter

Soft matter systems can be broadly identified as all squishy matter that has weaker interactions in them compared to solids typically such that the interaction scale is commensurate with thermal energies. These weaker interactions lead to different structural and physical properties. The first observation of quasicrystalline order in soft matter occurred when Zeng et.al discovered structures with dodecagonal symmetry in dendritic liquid crystals [172]. They observed 12 definite peaks in the X-ray diffraction patterns and hence initiated the quest for quasicrystals in all kind of soft materials. In their system, the dendritic

molecules form micelle-like structures which then align at different lattice points resulting in structures with 12-fold symmetry. Quasicrystals have subsequently been reported in soft matter systems with squishy spherical components such as colloids, micelles and diblock copolymers [46, 47, 51, 74].

In most soft matter systems quasicrystalline patterns are mostly found as metastable states where they appear during phase transitions. They can be also designed to form in systems where an external potential drives the transition: colloidal particles can be aligned to form a decagonal Penrose tiling using an energy potential produced using five polarised laser beams [103]. Such potentials can be tuned to produce periodic tilings including Archimedean tilings. Similar experiments are done on nanoparticle surfactants in colloidal solution, where an imposed potential drives the phase transition to form quasicrystals [158]. At mesoscopic lengthscales, networks formed from hard matter particles can also assemble into dodecagonal quasicrystals [163]. Other soft matter systems where 12-fold quasicrystalline structures were observed include mesoporous silica [152, 167] and mesoscopic surfactants [169]. The experiment with mesoscopic surfactants suggested that the intrinsic molecular architecture of surfactants contributes to the formation of quasicrystals and its approximants [169]. Thus the architectural design of a molecule involved is an important factor that needs to be taken into account in phase transition.

The quasicrystalline examples discussed so far are carefully synthesised with utmost control over the driving potentials, and usually only some certain specific compositions or architecture result in quasicrystals. However, Jayaraman et al. recently reported the presence of dodecagonal quasicrystals upon adding water into ionic surfactant and n-decane [74]. This development suggests that quasicrystals need not have to be always complex to synthesise with specifically tuned potential and/or composition. Instead what is required is appropriate design criteria for a given soft matter system that will induce the phase transition.

In all above discussed soft matter systems, quasicrystalline phase exhibits 12-fold rotational symmetry. Other rotational symmetries are also observed in soft matter systems. There are colloidal quasicrystals which demonstrates 18 fold rotational symmetry in its diffraction pattern [47] and nanoparticle quasicrystals with 8-fold rotational symmetry [45, 124]. The 18-fold rotational symmetry is associated with an aperiodic tiling with 4 different types of quadrilaterals (one square and 3 different rhombuses) and 8-fold rotational symmetry is associated with the Ammann-Beenker tiling, which has 2 types of quadrilaterals (a square and a rhombus). Dodecagonal rotational symmetry is usually associated with square triangle aperiodic tiling with 12 definite peaks in their diffraction pattern, [58, 71]. Complex arrangements of particles in soft matter system has an affinity to arrange themselves in squares and triangles [71]. Recently, dodecagonal quasicrystals that are assembled into aperiodic tilings with squares, triangles and trapezoidal tiles were reported [70, 170]. The soft potential and complex

interactions available in soft matter systems make the study of their structure an interesting geometrical problem.

As demonstrated so far using many examples, even though quasicrystals are no longer seen as a rarity, the parameters and conditions necessary to induce their presence are very specific. This is where the computational advances in simulations and numerical methods come to the rescue. Instead of fine-tuning the conditions in an experiment, soft matter systems can be modelled to find the required conditions to undergo a phase transition to a quasicrystalline phase. One approach is to consider hard and soft spheres with different soft potentials to replicate the formation of quasicrystals and thus study the effects of entropy and energy in the formation of quasicrystals. Quasicrystals of different rotational symmetries are observed in core-corona particles with a hard core and soft corona [120, 135, 147]. In these simulations the particles are simulated using the Monte Carlo method with a soft square potential that has step size matching the two lengthscale ratio from the Faraday wave experiments [38]. Another method of particle-based simulations is conducted using platonic solids and they are allowed to arrange themselves into some packing controlled by the overall entropy of the system [42, 55, 68]. Complex structures that are often observed in these simulations include the Frank-Kasper and Σ -phases in three and two-dimensional space respectively [64, 133, 169]. These phases are considered to be quasicrystal approximants.

Quasicrystal phases are observed in continuous systems like block copolymer melts where repulsive monomer interactions drive them to form patterns similar to tilings. Immediately following the discovery of soft matter quasicrystal in liquid crystals, polymeric quasicrystals were discovered in three-component star terpolymers. A dodecagonal quasicrystal that appears to be described by a square-triangle aperiodic tiling is observed in this block copolymer melt [57] which is shown in fig. 1.2. The diffraction pattern shows twelve distinct peaks, each in two concentric circles. This is visual evidence of the connection between the square-triangle tilings and 12-fold rotational symmetry.

Polymeric quasicrystals are observed in experiments and simulations in a variety of block copolymer including simple structures like diblocks as well as more complex architectures like tetra-blocks [51, 93, 107, 153, 174]. Some block copolymer systems consider a blend of different types of block copolymers. In a diblock melt, the initial segregation of the melt drives them to form micelles. These micelles can then arrange into different lattice positions, as in the cases of soft/hard spheres. In these simple block copolymer systems, the soft potential and polydispersity of these soft-hard core-corona structures can result in quasicrystal like morphologies [137]. In block copolymers with complex architecture like tetra-blocks, the intrinsic molecular architecture and resulting competing interactions can lead to complex morphologies [26].

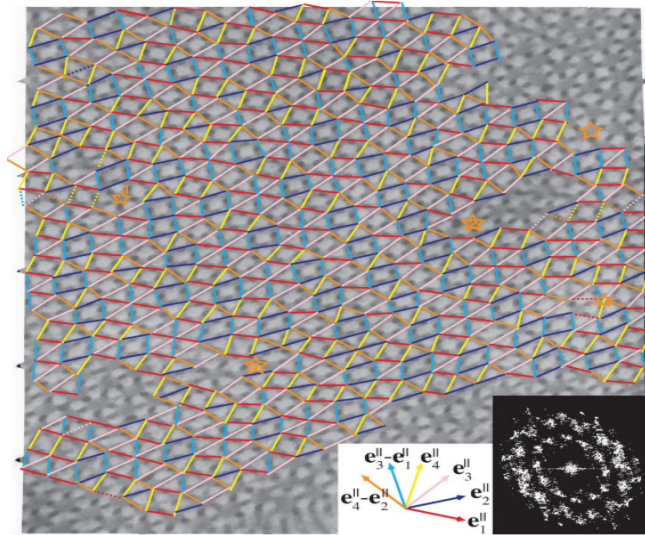


Figure 1.2: Dodecagonal quasicrystal observed in a blend of three component star terpolymer of polystyrene, polypropene and poly-iso-pyredene and the homopolymer polystyrene. This is a TEM image of the phase separated polymer blend with an attempt to overlay it with squares and triangles. The diffraction pattern obtained is given in the inserted image, which shows two concentric rings of 12 distinct peaks. Image sourced from [57].

Discovering quasicrystals in all sorts of soft matter systems makes quasicrystals not a rare phenomenon, as was perceived before 1982. But even with this abundance in occurrence, it is still unknown what makes the particles arrange themselves or the melt to segregate to form such a complex structure. Soft matter quasicrystals provide a window to learn more about the instability using the ideas from pattern formation and self-assembly of particles in driven by entropy and it is easier to understand. Soft matter quasicrystals offer the potential of developing materials with unusual photonic bandgap behavior [142, 164].

1.2 Stability of soft matter quasicrystals

Faraday wave interactions demonstrate how two frequencies can result in stable patterns that have quasicrystal-like rotational symmetries [10,12,8]. At the most basic level, the theoretical work attributes the stability of quasicrystals to the nonlinear three-wave interaction of waves of density fluctuations on two length scales. Lifshitz and Petrich identified that these wave interactions can be adapted in free energy functional to drive particles to form 12-fold quasipatterns [92].

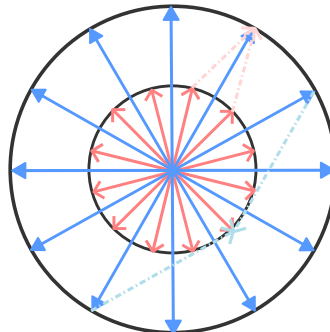


Figure 1.3: Schematic representation of two waves interacting with each other where when the radii of the circles are in ratio $(2 + \sqrt{3})^{1/2}$.

When two wave vectors are in a ratio $Q_r = 2 \cos \frac{\pi}{12} = (2 + \sqrt{3})^{1/2} \approx 1.93$, two wavevectors of the same magnitude can add up to result in the second wavevector. In fig. 1.3, red vectors indicates the twelve wavevectors spaced 30° apart in the small circle of unit radius. Given that the radius of the larger circle is $(2 + \sqrt{3})^{1/2}$, two adjacent red wavevectors give one blue vector as their sum and two blue vectors that are 150° apart add upto a short red wavevector. With this length ratio, three wave interactions can help stabilise the density distributions arranged in quasipatterns with 12-fold symmetry [16]. Similar three wave interactions contribute to the stability of periodic and quasiperiodic patterns, with a ratio of the radii within the range $1.5 - 2.5$ [25, 129]. Icosahedral symmetry, observed in elemental quasicrystals is associated with the golden ratio [76, 131, 151].

Two concentric circles with 12 equidistant Fourier peaks as in fig. 1.3 are observed in both early soft matter experimental quasicrystals [57, 172]. This encourages to design of free energy functional that can result in quasicrystals. Many studies have been done by adapting this idea into soft matter systems using phase field crystals [4, 76, 77, 134, 151, 160] and classical density functional theory of interacting particles [8, 9, 16, 125, 135, 165]. Stable quasicrystals are reported from these theoretical work as a result of tuning the free energy to have correct wavenumber ratios. Presence of two lengthscales on its own is not enough to stabilise quasicrystals but there is evident connection between emergence of two lengthscales and stability of quasicrystals [125].

Another way to look at the stability is by looking at the real space arrangement of particles. As pointed out earlier, most of the two dimensional quasicrystals in soft matter systems exhibit dodecagonal rotational symmetry. Amongst tilings, dodecagonal symmetry is associated with arrangements of squares and triangles. In most of the experimental quasicrystals, the dodecagonal arrangement originates from a seemingly random arrangement of squares and triangles. The stability of an arrangement is understood in two ways: one through the tiling

energy and the other via tiling entropy [39]. An ideal aperiodic tiling, that can be made from the inflation rules owe to lowering the energy of the particles in it [119]. But entropy- wire stability is attained from random tiling arrangements that are resultant of thermodynamic arrangement of particles [71, 118]. The stability study of soft matter quasicrystals based on these kinds of tilings is conducted using linear block copolymers [40].

It is challenging to list the factors that make a quasicrystal stable though prominent features like three wave interactions and structural arrangements are clearly important. Either one of these or both are present in most of the soft matter quasicrystals observed to date.

1.3 Block copolymer phase separation

Amongst soft matter systems, block copolymers offer structural versatility that is relatively easy to modify. Given block copolymers are used widely in many applications, it is interesting to know that complex structures like quasicrystals are present in block copolymers. Block copolymers are polymer chains that contain two or more monomer types that are connected as blocks (as in fig. 1.4.(a)). Block copolymers can be classified based on structure and variety of monomers, from the can be simplest diblocks to complex multi-branched, multi-component terpolymers. Block copolymers that are branched are commonly called terpolymers. As block copolymers contain more than one type of monomers, they have the tendency to phase separate like oil and water. The repulsive interaction between monomers of different type induces this phase separation. But unlike oil and water a complete phase separation is not possible in block copolymers as the different type of monomers are chemically attached. Instead the polymer chains can rearrange themselves such that blocks of the same type segregate together to form different structures [19, 87]. This is called microphase separation in block copolymer melts. Microphase separation results in simple structures like lamellae [87] to complex structures quasicrystals [57]. The controlling parameters for the structure formed are monomer compositions, the polymer architecture and the chemical interaction strength, all of which are easily varied compared to other systems.

Diblocks (AB), with two types of monomers A and B can form morphologies like lamallae, hexagons, cylinders, gyroids and many others by changing the proportion of A [19]. The interaction between A and B is quantified by the Flory interaction parameter χ . Diblocks also microphase separate into spheres which, depending on the solvent will have micellar behaviour. We have seen that quasicrystals can be made from such diblock micelles [33, 137].

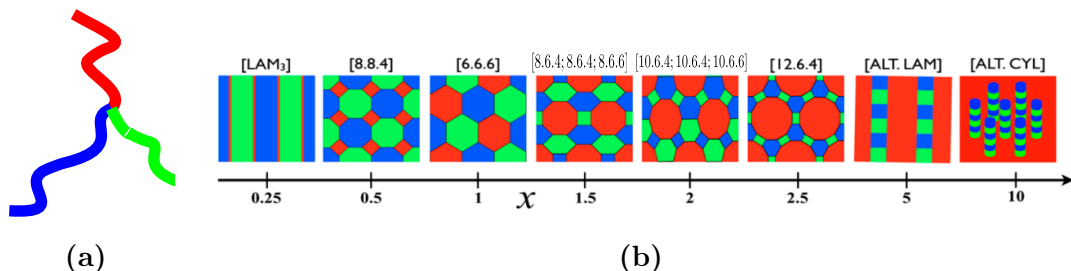


Figure 1.4: Different morphologies that are possible in ABC star terpolymer by varying composition of one component. In here A , B and C are indicated by red, blue and green. The composition of C blocks is varied with x . The morphology is indicated as in [27] from where this image was adapted.

A bit more complex block copolymer is ABC star terpolymer which has three types of monomers and branched molecular structure. Here, complexities contributed by polymer architecture and interactions lead to more complex structures, which we will discuss in detail in coming sections and chapters. Lots of morphologies are possible by changing only one parameter in this system as demonstrated in fig. 1.4 [27].

Block copolymers are a morphologically versatile system in soft matter. Bates rightfully coined the term "designer soft matter" [19] owing to the simplicity in modelling and complex morphologies that block copolymers can provide. The potential diversity of resultant mesoscale structures in block copolymer systems is explained in detail in the review by Huang et al. [65]. Along with regular periodic structures (as in fig. 1.4), they offer highly complex and interesting structures, from bicontinuous structures [30, 96, 106, 117] to the Frank-Kasper and Σ -phases [33, 86, 155] and the A15 phase [93]. All these complex morphologies have more than one prominent lengthscales. Also, Frank-Kasper in three dimensions and the Σ -phase in 2D are considered to be indicators for the presence of metastable quasicrystals. Leibler considered the possibility of 5-fold symmetry in block copolymers but then dismissed the idea since it was considered an impossible structure at that time [87].

Microphase separation in block copolymers can be studied using well established phase separation theories in polymer physics: Weak Segregation Theory (WST), Self Consistent Field Theory (SCFT) and Strong Segregation Theory (SST). These theories are applied to block copolymer melt depending on the segregation state that is being considered. The segregation state is quantified by monomer interaction strength. Brief overviews of each of these mathematical theories are provided here.

Weak Segregation Theory

Microphase separation of block copolymers (diblocks) in a homogeneous melt with weak interaction strength was studied in detail by Leibler [87]. The state at which the segregation of monomers occur is called the order-disorder transition (ODT) point. Near to the ODT, the free energy functional of the melt is determined by Landau-Ginzburg Theory as a function of the density distribution $\psi(\mathbf{q})$ in Fourier space. The wavevector \mathbf{q} corresponds to the prominent lengthscale associated with the structure [56, 87]. The free energy functional $F\{\psi(\mathbf{q})\}$ expanded to its third order term is given:

$$\begin{aligned}
 F\{\psi(\mathbf{q})\} = & \frac{1}{2!} \int_{\mathbf{q}} S^{-1}(\mathbf{q}) \psi(\mathbf{q}) \psi(-\mathbf{q}) + \\
 & \frac{1}{3!} \int_{\mathbf{q}} \int_{\mathbf{q}'} \mu(\mathbf{q}, \mathbf{q}', -\mathbf{q} - \mathbf{q}') \psi(\mathbf{q}) \psi(\mathbf{q}') \psi(-\mathbf{q} - \mathbf{q}') + \dots
 \end{aligned}
 \tag{1.1}$$

The second order term involves the structure factor $S(\mathbf{q})$ of the microphase separated structure. The third and higher order terms determine the stability of the structure formed. The three wave interactions are apparent in the third order term, since the three wavevectors \mathbf{q} , \mathbf{q}' and $-\mathbf{q} - \mathbf{q}'$, sum to zero.

The structure factor of the melt can be determined using the linear theory of Random Phase Approximation (RPA) in which the free energy functional is truncated at second order. The melt is taken as a Gaussian distribution of monomer densities which fluctuates and phase separates. The maximum of the structure factor gives the ODT point in phase separation and corresponding wavevector $\mathbf{q} = \mathbf{q}^*$ is associated with the spatial periodicity length $2\pi/\mathbf{q}^*$ of the morphology that emerges at the ODT. Thus using RPA we can predict the lengthscale that emerges from the melt without calculating the free energy functional. The cubic term μ in $F\{\psi(\mathbf{q})\}$, which is the vector function for thermodynamic potential is zero for an compositionally symmetric block copolymer system or is chosen to be positive. At the critical wavevector \mathbf{q}^* the second order term in the free energy has a minimum and ensure the structure with corresponding periodicity is stable [48, 56].

This theoretical framework was developed by Leibler for diblocks, who reported a phase space of morphologies varying the monomer composition of one block [87]. The framework can be extended to multicomponent block copolymers [79] and complex polymer architectures [110]. More complex morphologies were determined in block copolymers with two components using the RPA in weak segregation limit [83]. Nap et al. proposed that having two intrinsic lengthscales in the polymer architecture can lead to the emergence of two prominent lengthscales in the structure factor [110]. They reported linear polymer chains with alternating A and B blocks having two lengthscales in the lengthscales for

a few selected compositions. These compositions and architectures further gave morphologies that have two lengthscales like double periodic lamellar-in-lamellar using mean field calculations like SCFT [82, 109].

Weak segregation analysis of multi-component systems is more cumbersome owing to the dependence on multiple parameters. For a three component system, there will be three monomer compositions and three monomer interactions that will affect these density fluctuations. The structure factor is represented by matrices which makes the free energy analysis more complex. It can be necessary to apply constraints on the parameters. The RPA analysis of three component *ABC* block copolymers was conducted for terpolymers [23] and triblocks [43] to detect the prominent wavevectors at the ODT. Erukhimovich conducted the stability analysis of morphologies in *ABC* triblock melt in the weak segregation limit (WSL) calculating the cubic- and quartic-ordered terms in the free energy expansion [43]. So far two lengthscales in the structure factor have not been reported for three-component systems using the RPA. But the complexity and multiple interactions available in *ABC* block copolymers make these a potential system where two lengthscale phase separation might occur at the ODT.

Strong Segregation Theory

In the strong segregation limit (SSL) when the repulsive interaction strength between the different monomer types is large, and small fluctuations in monomer composition become negligible. The weak segregation framework which is based on small perturbations in the monomer distribution is not sufficient at this stage. Phase separated structures comprise domains of different monomer types separated by thin interfaces forming the morphologies. In this segregation limit, polymer chains are highly stretched such that the elastic free energy of polymer chains and interfacial surface tension due to repulsive monomer interactions both contribute to the total free energy. Semenov determined the stretching energy from a classical elastic analogy and the interfacial energy from an electrostatic analogy [138]. In the SST, the stretching of chains contributes to the total free energy as the stretching free energy F_{str} per chain as the square of the distance stretched, so

$$\frac{F_{str}}{k_B T} \sim K \frac{R_d^2}{Nb^2} \quad (1.2)$$

where R_d is the lengthscale of the domain formed. Here, each polymer chain comprises N links of step length b , so that the mean square end-to-end length of the chain is Nb^2 , as detailed in section 2.0.1. Here K is a coefficient that is dependent on the parameters of the block copolymer and the morphology being considered.

1. Introduction

The interfacial free energy is the product of the surface tension $\gamma = \chi^{1/2}b^{-2}k_B T$ and the surface area per chain.

$$F_{int} \sim \gamma \frac{Nb^3}{R_d}. \quad (1.3)$$

The interfacial energy F_{int} per chain is dependent on the Flory interaction parameter:

$$\frac{F_{int}}{k_B T} \sim Nb \frac{\chi^{1/2}}{R_d}. \quad (1.4)$$

The total free energy per chain of the phase separated structure is the sum of these two contributions.

$$\frac{F_t}{k_B T} \sim K \frac{R_d^2}{Nb^2} + Nb \frac{\chi^{1/2}}{R_d}. \quad (1.5)$$

As seen from the above expressions the stretching free energy increases with domain size and interfacial free energy decreases with domain size. Structural stability is attained when these two free energies balance and this can be found by minimising the total free energy with respect to R_d ,

$$2K \frac{R_d^2}{Nb^2} - Nb \frac{\chi^{1/2}}{R_d} = 0. \quad (1.6)$$

giving a typical domain size $R_d \sim b\chi^{1/6}N^{2/3}$ and minimum free energy $F_{min} = (N\chi)^{1/3}$. We can see that the domain size is much larger than the typical unstretched chain size \sqrt{Nb} , hence the chains are indeed strongly stretched away from the interface. In this theory the polymer chains are assumed to be tightly packed so that they completely occupy a given geometrical area. Thus with the right geometrical approach, the free energy of each given morphology can be determined. Hence the stability is assessed by determining which structure gives the lowest free energy at the minimum. Thus the free energy per chain is turned into a geometrical problem which is solved using different approaches depending on the area one is choosing. The phase space developed by Semenov for diblock in strong segregation limit (SSL)[138] fits well with Liebler's phase space in weak segregation limit (WSL)[87].

Olmsted and Milner modified the free energy calculation so that it can include more complex structures including bicontinuous morphologies [117]. In their work, they used a wedge as the structural unit to determine the stretching and interfacial energy of a small region in a given structure. Each morphology can be considered as a sum over these wedge sub-units.

The SSL analysis has its limitations when it comes to the accuracy of free energy analysis of morphologies. Bates et al. [18] recognised SST as a theory which can simplify the free energy calculation of morphologies to a geometrical problem that balances two energies. In later years Gemma et al. [50] utilises this geometrical calculation in SSL to verify the morphological analysis done using the Monte Carlo method for *ABC* star terpolymers.

Although this theory offers a simplified framework, the lack of accuracy in free energy analysis and the need to evaluate each specific geometry on a case-by-case basis led physicists to develop more general theory, self-consistent field theory (SCFT), to study polymer phase separation.

Self Consistent Field Theory

So far we discussed two extreme limits of phase separation that can be studied using the above mentioned theories. In their respective regime both these theories are valid but as it was demonstrated by Ohta et al. [115], RPA is not valid in SSL. Likewise owing to the small monomer density fluctuations which are equivalent to small perturbations in the melt, the strong segregation approach does not work in WSL. Given this Matsen and Bates developed Self Consistent Field Theory (SCFT) based on a mean field approach to unify these two regimes so as to analyse phase separated morphologies [97]. In the simplest possible terms, SCFT solves for the set of chain configurations for a polymer chain of a given structure in a potential energy field that acts on each of the monomer species in that chain. To make the theory self-consistent, the potential energy field is derived self-consistently from the polymer densities derived from the set of chain configurations. In practice, this requires an iterative loop until chain configurations and fields match one another. The SCFT framework has been the main work-horse for theoretical phase separation owing to its accuracy and validity in all segregation limits.

This theory has been extensively used by researchers in the last 2 decades to find and verify different morphologies in block copolymers. A broadly accessible platform to conduct the SCFT calculations is provided in the work by Arora et al.[11]. Nap et al. used their initial prediction from RPA to design the block copolymer structure which was then applied to SCFT to analyse the morphologies[44, 109, 132]. Quasicrystals and its approximants are also reported using SCFT technique [33, 75, 141].

1.3.1 Parallels between polymer phase separation and quasicrystal formation

Considering the theories for polymer phase separation described above, and the ideas proposed for describing quasicrystal formation in soft matter, it is possible to note some common features. There is an evident mapping between the description of pattern formation in terms of the emergence of lengthscales in a density distribution and polymer melt in weak monomer fluctuations. From various theoretical examples listed in the previous section it is understood that stable quasicrystals are possible if the free energy is designed with two emergent lengthscales in an appropriate ratio. Given that the weak segregation theory predicts the dominant lengthscale(s) for phase separation, we can potentially design block copolymers to give quasicrystal-like lengthscale ratios. In that way, we have a well-oiled framework to study the stability of the emerging morphology and also its stabilising factors.

In strong segregation limit the monomer domains fill in space to form patterns that are equivalent to tilings. The theoretical framework of SST offers the study of phase separation in a geometrical way, filling the available space with domains of one monomer type or another, which (for two-dimensional patterns) is a tiling. Since much is already known about aperiodic, quasicrystalline tilings, this framework can be utilised to compare different aperiodic tilings to phase separated patterns in block copolymers to determine a potentially stable structure.

Thus the two main frameworks for the study of quasicrystals have direct parallels in theories for polymer microphase separation. When rapid advances in polymer phase separation happened in the 1980s and '90s, there were limited resources and methods known to study complex structures. But now, at the time of writing this thesis, standing on the shoulders of giants we have at our disposal several different techniques to understand the phase separation at any scale and for any complicated block copolymer structure one can think of.

1.4 ABC star terpolymer and its morphologies

We briefly discussed the complexity and potential of multi-component block copolymers in the previous section. It is clear that even the simplest diblock offers a highly complex morphological behaviour. So it is interesting to see what happens if we add one more component to the chain. Three-component block copolymers are the simplest of the multi-component block copolymers and their morphological versatility makes them interesting for quasicrystal seekers.

A three-component block copolymer can be composed in two different ways. One is by adding a new block of type C to one end of the diblock making a linear ABC triblock chain illustrated in fig. 1.5.(b). Mogi et al.. synthesised

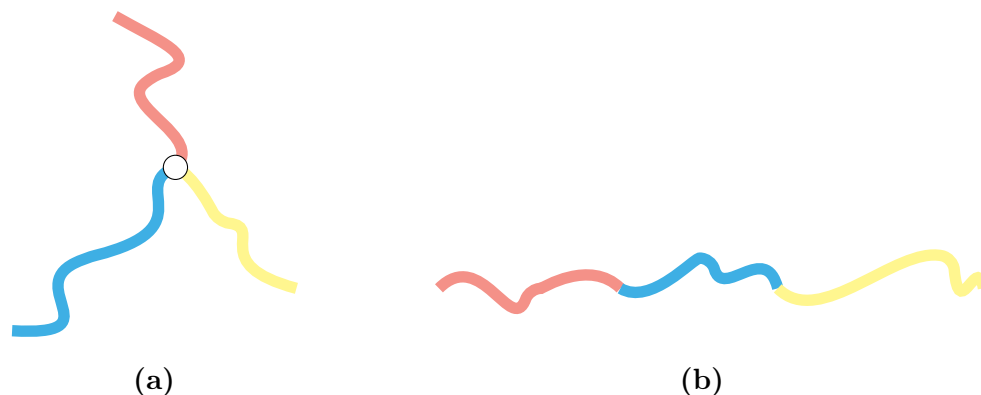


Figure 1.5: A schematic representation of (a) ABC star terpolymer and (b) ABC triblock where three different monomer types are indicated by different colours. Red: A , blue: B and yellow: C .

such a molecule for the first time in 1992 and initiated the morphological study of three-component polymer melt [105]. The phase separation of this molecule is dependent on the sequence of grafting these blocks. Block can have any of these three sequences ABC , BCA and ACB . The phase separation of this molecule has been studied theoretically using SCFT [23]: after using the RPA, the initial composition of the block copolymer knitting like patterns was found.

The second way to include a third block to a diblock is to graft a new block of type C at the same junction where the A and B blocks meet. This results in an ABC star terpolymer, a branched block copolymer, illustrated in fig. 1.5. (a). Synthesising such a polymer chain is not easy, and it was a game-changer when Fujimoto et al. [49] successfully synthesised the first ABC star terpolymer in 1992. This terpolymer was synthesised of polystyrene (PS), polydimethylsiloxane (PDMS), and polytertbutyl methacrylate (PTBMA). Many researchers subsequently reported more accessible and efficient processes for synthesising ABC terpolymers from various monomers [66, 67, 69, 85, 121, 145]. The successful synthesis of these block copolymers has motivated and enabled the exploration of different morphological structures that can be found. Hadjichristidis et al. studied star terpolymers synthesised from polystyrene (PS), 1,4-polyisoprene (1,4-PI), and 1,4-polybutadiene (PB) and reported the melt phase separating into two different microdomains that are arranged in cylinders [54, 69]. The interaction strength between dienes in this melt is weak, which resulted in the formation of only two domains during phase separation. Later, star terpolymer melts that can phase separate into morphologies containing three different microdomains were reported in the synthesis process of Sioula et al. [59, 143, 145]. In these melts, the junction point of three microdomains of A , B and C type was the resultant of the core, and this is the junction where A , B and C meets. It was noted

from these experimental studies of terpolymer phase separation that these cores tend to align in straight lines while forming the microdomains [116, 143], so these microdomains can be viewed as two-dimensional tiles.

These experimental advances piqued the interest of physicists and chemists to investigate all possible morphologies of ABC star terpolymers. These have six variables that control its properties: three monomer compositions of A , B and C blocks and three pairs of interactions between the monomers A and B , B and C and A and C . These six variables and three microdomains that can be arranged in different ways offer a plethora of possible morphologies. Here is a brief survey of the morphologies reported for this polymer system, both experimentally and theoretically.

Sioula et al. identified phase separation in hexagonal morphology in their star terpolymer of polystyrene, polyisoprene and polymethyl methacrylate [144]. In a polymer melt of ABC star synthesised from polystyrene, polybutadiene and poly(2-vinylpyridine), four different morphologies were observed by varying the compositions [66]. These four morphologies were reported as different hexagonal and tetragonal packing of cylindrical monomer domains. Today we know that these morphologies are identified as [6.6.6], [8.8.4] and [12.6.4], (this naming convention will be explained in detail in Chapter 5), morphologies, where the numbers indicate neighbouring domains [157]. The fourth morphology they reported is the lamellar phase, which was also found theoretically in the strong segregation limit [22]. Thus the single core morphologies: [6.6.6], [8.8.4] and [12.6.4] and lamellar based morphologies were observed in ABC star terpolymer synthesised from different monomer stoichiometry and chemistry.

The theoretical study of ABC star terpolymer morphologies was pioneered by Dotera et al. using a Monte Carlo (MC)- based method to search morphologies [37]. In their extensive work on ABC terpolymers using the diagonal bond method, they identified many 2D tiling-like morphologies. In their work, ABC star molecules are modelled as beads connected on a chain [37]. They conducted simulations of terpolymers varying the composition of one branch while keeping the other two the same, $1 : 1 : x$. They report two classes of morphologies, those with one type of core and those with multiple cores. They observe following morphologies: lamella+sphere (L+S), [8.8.4], [6.6.6], [8.6.4; 8.6.4; 8.6.6], [10.6.4; 10.6.4; 10.6.6], [12.6.4], perforated layer (PL), lamella+cylinder (L+C), columnar piled disk (CPD), and lamella-in-sphere (L-in-S) phases [50] similar as in fig. 1.4. In this system, strong interactions are considered between the branches so the phase separation is in SSL. They also compare their simulation results to the free energy calculated using strong segregation theory. The morphologies [6.6.6], [8.8.4] were predicted using SCFT calculations too [23].

Morphological studies became more interesting when Matsushita et al. realised that one of the cylindrical morphology observed by Sioula et al. was an

Archimedean tiling (3.4.6.4) which contains more than one type of domain combination [143, 156]. It was challenging to locate the exact polymer compositions to produce the other complex morphologies from the 1D phase space predicted theoretically by Gemma et al. so theoretical and experimental studies were combined to look for more Archimedean tiling-like morphologies. As a result of combining Monte Carlo simulations with experimental synthesis of block copolymers of polyisoprene, polystyrene, and poly(2-vinylpyridine), different Archimedean tilings, including (3.4.6.4) and (3.3.4.3.4) (the so-called Σ -phase) were discovered amongst the morphologies [58, 99, 101, 102, 156]. Closer to the composition of Σ -phase, quasicrystalline structures were predicted theoretically using the Monte Carlo method [36] and were later discovered experimentally [58]. In order to vary the composition, the homopolymer polystyrene was blended into the melt [57, 58]. Their partial phase space for the *ABC* star block copolymers, suggests that quasicrystals can be found closer to the region with Σ -phase [36].

Other combinations of monomer varieties also resulted in a single type of domain core and multiple types of domain core morphologies. The *ABC* star terpolymer melt with other monomer types, (polyisoprene, polystyrene and polyferrocenylethylmethylsilane) also produced similar morphological features to the terpolymers synthesised by Matsushita lab [5, 84, 114]. Recently *ABC* terpolymers were synthesised with polyisoprene, polystyrene and poly(methyl methacrylate) arms, which gave lamellar morphology at weak segregation and cylindrical square patterns in strong segregation limit [10]. From a physical modelling perspective, the change in monomer type is understood as the change in interaction strengths between the monomers.

Following these advances in the morphological studies of *ABC* star terpolymers, other theoretical frameworks were developed to study phase separation. Another Monte Carlo-based simulation, using dissipative particle dynamics, was employed for morphological studies which also reported the Σ -phase [27, 63, 81]. This framework enables the study of 3D morphologies like bicontinuous structures and different lamellar combinations. Another well established theoretical framework is SCFT, introduced previously. Using SCFT, all known morphologies both 2D and 3D are obtained for *ABC* star terpolymer [75, 89, 91, 168, 173]. Using SCFT elaborative phase spaces are reported for 2D morphologies in *ABC* star terpolymers with equal interactions $N\chi$ between the monomers [91]. Morphologies of *ABC* star with unequal interaction strength between monomers are also studied using SCFT and corresponding phase space is created [75].

Morphologies	Gemma and Dotera (DBM, MC) [36, 50]	Tang and Qiu (SCFT) [159]	Huang and Fang (DPD) [63]	Qui and Shi (SCFT) [91]	Kirkensgaard et al. (DPD) [81]
[6.6.6]					
[8.8.4]					
[12.6.4]					
[8.6.4;8.6.4;8.6.6]					
[10.6.4;10.6.4;10.6.6]					
[10.8.4;10.6.4] (3.3.4.3.4)					
[8.6.4;8.8.4;12.6.4;12.8.4]					
[8.6.4;10.6.4]					
[14.6.4;14.4.4]					
Lamellae + Sphere (L+S)					
Lamellae + Cylinder (L+C)					

Table 1.1: A summary of morphologies in ABC star terpolymer that have been reported using different computational methods. Green cells indicate the morphology reported by the corresponding authors.

As it has been pointed out, apart from three prominent single core morphologies: [6.6.6], [8.8.4] and [12.6.4], there are many multi-core morphologies that are observed in ABC star terpolymer phase separation. Depending on the branch composition and interaction strength, there can be many other possibilities for morphological structures. It is nearly impractical to determine the stable structure for given compositions and interaction strengths with limited options of morphologies. In order to determine the stable structure we need a catalogue of all possible topologies and geometries of three domains such that they will always

have a core shared between them. Close to this catalogue is the list of morphologies that Kirkensgaard et al. presented using the Spoke method [81]. They reported some new morphologies by considering monomer domains as foams [81] which were studied using *Evolver* [2] and using the Dissipative Particle Dynamics (DPD) method [27].

A survey of prominent morphologies observed so far in *ABC* terpolymer and the method used is listed in table 1.1.

There are many versions of phase spaces for *ABC* star morphologies. The molecule is difficult to synthesise, and simulations can also be computationally demanding if the branch lengths/monomer compositions are allowed to vary. So as a result, mainly linear phase spaces are created by constraining the compositions of two types of monomers to be equal and varying the composition of the third monomer [27, 50, 173]. There are relatively few ternary phase space calculations varying all three branches, but some examples have been reported using the SCFT formulation [75, 91].

Quasicrystals observed using different methodologies listed above ought to be metastable [36]. The calculations that reported stable quasicrystals were either driven by an external stimulus or had a finely tuned free energy potential. Experimentally quasicrystals appear with many defects in the structure, but still with diffraction patterns with 12 equidistant peaks [57]. This brings us back to the question of what makes quasicrystals stable. Dotera suggests a study of the stability of these morphological systems using a Mermin and Troian type mean field theory [34]. Even then, there are discrepancies in the stability analysis between different theoretical frameworks when it comes to multi-core morphologies. The stability of quasicrystalline structures formed in block copolymers can be assessed using different options: phase separation studies or field theories. Hence it is promising to combine the morphological features of block copolymers and question of stability starting with *ABC* star terpolymer.

While *ABC* star terpolymers makes interesting morphologies they can be utilized for different applications too. It is theoretically predicted that polymeric quasicrystals can be utilised for photonic applications [162]. The topological features of *ABC* star terpolymers are also utilised in solid-state batteries [150].

1.5 Thesis Outline

Overall the theme of this thesis is to combine the stability analysis of quasicrystals with block copolymer phase separation. As explained in the previous sections, the stability of quasicrystals is a puzzle that is yet to be explained. Block copolymer phase separation is a suitable system to apply both the two lengthscale theory and tiling theory to investigate the stability of resulting patterns. We aim to design block copolymer architectures that will self assemble into stable quasicrystalline

structures on phase separation. This thesis covers two methodologies for the study of phase separation. In the first, we study density fluctuations in block copolymer melts to check if two lengthscales emerge in them such that their ratio is favourable to form quasicrystalline structures. This is done at the point of onset of phase separation in the WSL using RPA. In the second method, morphologies formed in *ABC* star terpolymer melt are compared to 2D tilings at a strong segregation limit using a novel method we developed based on flexible polygons. The structure of the thesis is elaborated below.

In chapter 2 we look at block copolymer melts at the early stages of segregation. The polymer melt is taken as a homogeneous mixture where fluctuations between the monomers drive them into polymer phase separation. We consider two classes of block copolymers here: linear block copolymer chains with two components and three component *ABC* star terpolymers. The linear chains are composed of three types of blocks; a long block of type *A*, smaller chains of type *A* and smaller chains of type *B*. We propose two different ways to design these linear chains such that they will induce phase separation with two different lengthscales. In one method we use monodisperse alternating blocks of type *A* and *B* along with one long *A* type block in one end. In the other, we mimic polydispersity through a selective polymerising model with a random collection of these three blocks. We apply the RPA to both these families of block copolymers and to *ABC* star terpolymers, to determine the scattering factor and hence the prominent wavelengths that emerge at phase separation. For all the models, we identify the compositions for which two lengthscales emerge.

In Chapters 3-6 we focus on *ABC* star terpolymer and its morphologies in the strong segregation limit.

In Chapters 3 and 4 we introduce the concept of strong segregation theory in the context of *ABC* star terpolymers. Here combine the concept of tilings and 2D patterns with SST to study different morphologies. We introduce a flexible hexagonal motif, which we call a strongly segregated polygon (SSP), which contains three domains and their common junction point at the core. Boundary conditions and matching protocols are applied to SSPs to assemble them into the different morphologies available for *ABC* star terpolymers. We assign periodic boundary condition on the structure as a whole. The SSP contains the geometric structure of the phase separated pattern and SST allows us to calculate the free energy for a particular configuration. This free energy of the morphology depends on the monomer compositions and the interaction parameters of the terpolymer. In Chapter 3 we devise the theoretical framework for the study of phase separation using SSP. In chapter 4 we discuss the computational tools that were developed to apply the SST framework on different morphologies. From a literature survey of *ABC* star morphologies, it is clear there are inconsistencies in results reported, depending on the morphologies and methodologies used. The multi-core morphologies need to be screened in strong segregation limit to create

a complete phase space. Using our tools, the SSPs can form any morphology without any modification, and single-core structures and multi-core structures can be treated using the same method, irrespective of their periodicity.

In Chapter 5, 2D morphologies that are experimentally observed in *ABC* star terpolymer phase separation are analysed using our SSP framework. We analyse the following morphologies in this chapter to create a phase space for *ABC* star terpolymers: [6.6.6], [8.8.4], [12.6.4], [8.6.4; 8.6.4; 8.6.6] and [10.6.4; 10.6.4; 10.6.6]. For each morphology, an initial configuration is designed, which then will undergo structural variation, varying the shape of each SSP constrained by the geometry to find the optimal structure with the lowest free energy. All six variables: three monomer compositions and three interaction strengths can be varied without any constraints. Hence the stable structure is determined by comparing different morphologies at a given monomer composition and a phase space is created from the available morphologies. This chapter also covers the morphological analysis and phase space for *ABC* terpolymer melts with unequal interaction strengths between branches.

In Chapter 6, we demonstrate the versatility of our SSP framework by analysing complex morphologies involving squares and triangles that can potentially have approximate 12-fold rotational symmetry. Here we devise a systematic way to arrange dodecagons composed of squares and triangles so that they form periodic approximants to 12-fold quasicrystals. We investigate the morphological stability of the Σ -phase and six other types of square-triangle tiling arrangements. The aim is to detect their presence in the *ABC* terpolymer phase space. We compute the Fourier space of these structures to identify the lengthscales present in them.

We conclude in Chapter 7 with significant observations on phase separation from our two investigations. We report potential block copolymer architectures that can phase separate into structures with two lengthscales with quasicrystal-friendly ratios. We also report ternary phase spaces for *ABC* star terpolymer with our novel framework that agrees with existing literature. The Σ -phase is the closest to quasicrystals we find in our phase spaces. From the overall analysis, it is interesting to find that in the ternary phase spaces of *ABC* star terpolymers, the region where two lengthscales are reported in chapter 2 and the region where we find Σ -phase in chapter 6 are entirely different.

1. Introduction

Chapter 2

Weak Segregation Approach for Phase Separation

Phase separation in block copolymers is controlled by their branch lengths and monomer interactions. From extensive literature on polymer phase separation demonstrated in Chapter 1, it is obvious that phase separation is studied using different theories depending on the strength of monomer interactions [87, 98, 138]. Incompatibility between different monomer types is characterised by the Flory interaction parameter χ which quantifies these monomer interactions. In a weak segregation regime, for low χ values, monomer interactions are strong enough to amplify density fluctuations leading to phase separation.

Phase separation theory based on density fluctuations can be utilised to predict the lengthscales that will arise due to phase separation. In the quest to find the appropriate window for stable quasicrystals in block copolymers, weak segregation theory can provide a head start by predicting stabilising free energy and length scales for a given architecture. Phase separation in a polymer system is indicated by the divergence of its structure factor at the corresponding wave number. Leibler [87] demonstrated how to determine the structure factor using Random Phase Approximation (*RPA*) for diblocks. This chapter covers the technique of (*RPA*) for two-component and three-component block copolymer systems, focusing on two families of block copolymer architecture. In this chapter we are interested in developing a simplified model to predict block copolymer architectures that can phase separate in two lengthscales. Some of these resulting architecture have the potential to form quasicrystalline morphologies.

2.0.1 Brief review of polymer statistics

A polymer chain can be characterised by its end-to-end vector \mathbf{R} , the vector sum of bond lengths in a chain. A monomer unit is a section of the polymer chain with a certain number of chemical monomers less than the whole polymer chain. In a polymer chain, the angle between neighbouring bonds is fixed. For example, in polyethylene, this angle is 68° [128]. Each bond has freedom of rotation which increases by each bond along the chain. After a certain number of steps, the section of the polymer chain is highly flexible and is essentially a random walk. The number of steps required for a composite step to be random is different for different monomer types. If N_{bonds} bonds of effective bond lengths b make the chain flexible and random then the monomer unit consists of $N_{bonds} + 1$ monomers in it. A polymer chain is a long string of monomer units as shown in fig. 2.1 and its length is characterised using the end-to-end vector \mathbf{R} .

For a polymer chain indicated by α , the length of the chain is given by its end-to-end vector \mathbf{R} . Random orientations of monomer units in polymer chain result in an average of end-to-end vector over all polymer conformations ($\langle \dots \rangle$) to be zero:

$$\langle \mathbf{R} \rangle = 0. \quad (2.1)$$

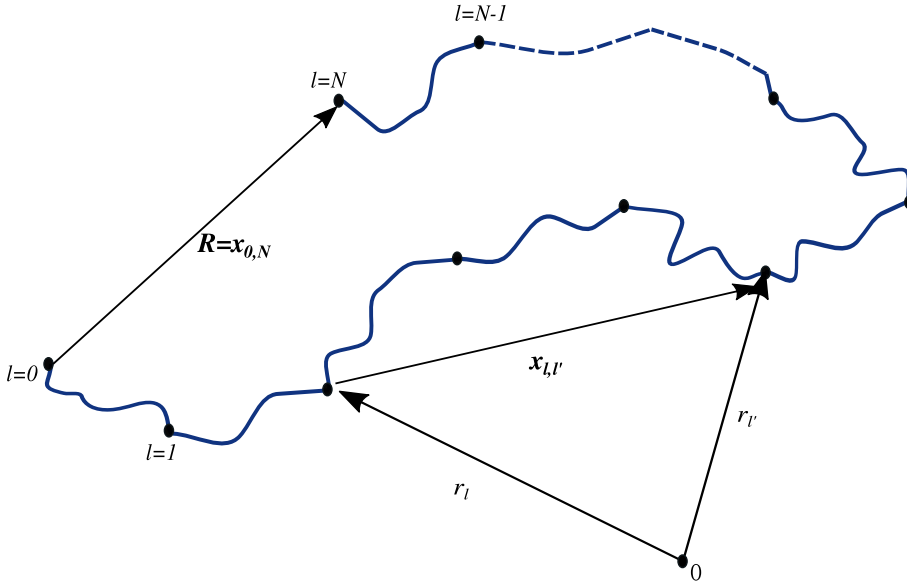


Figure 2.1: Schematic representation of a polymer chain consisting N monomer units. Each small chain between the dots represents a monomer unit and they are completely flexible to one another. The position vector of each monomer unit is given by \mathbf{r}_l and $\mathbf{x}_{l,l'} = \mathbf{r}_{l'} - \mathbf{r}_l$ is the separation vector between monomer unit l and l' .

2. Weak Segregation Approach for Phase Separation

We therefore use the root-mean-square of the end-to-end vector to characterise the polymer chain length. For a long polymer chain of N monomer units of effective bond length b root mean square of end-to-end vector [128] is

$$\langle \mathbf{R}^2 \rangle = Nb^2. \quad (2.2)$$

This expression suggests a relation between the length and number of monomer units in a polymer chain that is later used for scaling the wave number q . In the Gaussian coil model, \mathbf{r}_l ($l = 0, \dots, N$), is the position vector for each monomer unit: in fig. 2.1, the section of monomers connecting two adjacent dots is a monomer unit. To find the end-to-end vector for a chain we take two monomer units at l and l' in the chain with position vectors \mathbf{r}_l and $\mathbf{r}_{l'}$. Then the separation vector $\mathbf{x}_{l,l'} = \mathbf{r}_{l'} - \mathbf{r}_l$. From eq. (2.1) and eq. (2.2) we know that

$$\langle \mathbf{x}_{l,l'} \rangle = 0 \quad (2.3)$$

$$\langle \mathbf{x}_{l,l'}^2 \rangle = |l' - l| b^2.$$

Since $\mathbf{x}_{l,l'} = (x_{l,l'}, y_{l,l'}, z_{l,l'})$, and x , y and z obey the same statistics they each have zero mean and

$$\langle x_{l,l'}^2 \rangle = \langle y_{l,l'}^2 \rangle = \langle z_{l,l'}^2 \rangle = \frac{|l' - l| b^2}{3}. \quad (2.4)$$

The separation vector is the sum of independent random variables. Hence the probability distribution for the separation vector can be obtained from the Central Limit Theorem which will be a Gaussian distribution [32]. Thus the distribution of monomer units in a polymer melt, Φ is given by

$$\Phi(\mathbf{x}_{l,l'}) = \left(\frac{3}{2\pi |l' - l| b^2} \right)^{\frac{3}{2}} \exp \left(\frac{-3\mathbf{x}_{l,l'}^2}{2 |l' - l| b^2} \right). \quad (2.5)$$

2.1 Random Phase Approximation

The Random Phase Approximation (*RPA*) can be used to obtain scattering properties and subsequently free energy of morphologies for polymer systems. It can be used to determine the limits of stability for a homogeneous system (the spinodal) or to construct free energy which can be minimised to obtain the most stable state. The method was introduced by Pines *et al.* [113], where they dealt with coherent and incoherent electron density fluctuations. Later it was used by De Gennes [31] to extract the relation between polymer density fluctuations and

scattering. Leibler [87] used this method to explain the phase transition in block copolymer melts using diblocks. In the case of polymers, the polymer density changes in response to a potential on the monomers. This potential could either be an externally applied potential or a self-consistent potential due to the interaction between monomers themselves. The *RPA* treats the response of a polymer system to either of these potentials. Hence, *RPA* is used to calculate the structure factor for concentrated polymer solutions like polymer blends and melts which have interaction between the monomers. In *RPA* the polymer system is treated without any interaction at first and then interactions are added in a self-consistent manner. The second order term in the free energy expansion in Leibler's work gives the critical wave number \mathbf{q}^* at the phase transition which determines the dominant lengthscale. Once the transition wave number is obtained, the detailed structure and amplitude of phase separation are obtained from the higher order terms in the free energy. In this work, we are interested in finding if there are more than one critical wave number with quasicrystal-like wave number ratios at the phase transition. Hence we will only be dealing with the second order term in the weak segregation free energy term.

In addition, one can determine the structure factor of a polymer blend from its density fluctuations. In the weak segregation limit, density fluctuations due to the inter-monomer interactions drive the polymer blend toward phase separation but even before phase separation, density fluctuations are increased. The phase separation in polymer blends can be detected by scattering suitable radiations through the polymer blend, for eg: Small Angle X-ray scattering (*SAXS*) or Small Angle Neutron Scattering (*SANS*). The structure factor of the material gives structural information such as lengthscale, molecular arrangement, etc. We will discuss the calculation of structure factors for different block copolymer systems in the coming sections.

2.1.1 RPA for a single component polymer system

Polymer systems consisting of only one kind of monomer are called homogeneous. Monomer density at position \mathbf{r} from l^{th} monomer unit in the polymer chain α is defined by delta function $\delta(\mathbf{r} - \mathbf{r}_l^\alpha)$. Overall monomer density at \mathbf{r} from all chains is defined as the sum of delta functions over $l = 0, \dots, N$ and $\alpha = 1, \dots, n_c$, where n_c is the total number of chains. Monomer density $\rho(\mathbf{r})$ at position \mathbf{r} is defined as

$$\rho(\mathbf{r}) = \sum_{\alpha, l} \delta(\mathbf{r} - \mathbf{r}_l^\alpha). \quad (2.6)$$

Applying the Fourier transform, the transform of polymer density will be

$$\rho_{\mathbf{q}} = \int \exp(i\mathbf{q} \cdot \mathbf{r}) \rho(\mathbf{r}) d^3\mathbf{r} \quad (2.7)$$

2. Weak Segregation Approach for Phase Separation

which gives

$$\rho_{\mathbf{q}} = \sum_{\alpha, l} \exp(i\mathbf{q} \cdot \mathbf{r}_l^\alpha). \quad (2.8)$$

The structure factor $S(\mathbf{q})$ for wavevector \mathbf{q} is given by the second moment of the density fluctuation[32].

$$S(\mathbf{q}) = \langle \rho_{\mathbf{q}} \rho_{-\mathbf{q}} \rangle \quad (2.9)$$

Here the average is taken over all monomer units. From eq. (2.8) we get $\rho_{\mathbf{q}} \rho_{-\mathbf{q}}$ as

$$\rho_{\mathbf{q}} \rho_{-\mathbf{q}} = \sum_{\substack{\alpha, l \\ \alpha', l'}} \exp(i\mathbf{q} \cdot (\mathbf{r}_l^\alpha - \mathbf{r}_{l'}^{\alpha'})) \quad (2.10)$$

For dilute polymer solutions where the mutual interaction between the monomer units is negligible, there is no correlation between the chains α and α' . Hence,

$$\langle \exp(i\mathbf{q} \cdot (\mathbf{r}_l^\alpha - \mathbf{r}_{l'}^{\alpha'})) \rangle = 0 \quad \text{if, } \alpha \neq \alpha'. \quad (2.11)$$

because when we average over all chain positions the phases $\mathbf{q} \cdot \mathbf{r}_l^\alpha$ and $\mathbf{q} \cdot \mathbf{r}_{l'}^{\alpha'}$ are completely random. Hence the structure factor depends only on contributions from monomers in the same chain which gives

$$S(\mathbf{q}) = \langle \rho_{\mathbf{q}} \rho_{-\mathbf{q}} \rangle = \sum_{\substack{\alpha \\ l, l'}} \langle \exp(i\mathbf{q} \cdot (\mathbf{r}_l^\alpha - \mathbf{r}_{l'}^\alpha)) \rangle = \sum_{\substack{\alpha \\ l, l'}}^N \langle \exp(i\mathbf{q} \cdot \mathbf{x}_{l, l'}^\alpha) \rangle. \quad (2.12)$$

For an ideal random walk polymer by properties of Gaussian function [32]

$$\langle \exp(i\mathbf{q} \cdot \mathbf{x}_{l, l'}^\alpha) \rangle = \exp\left(-\frac{1}{2}q^2 \langle x_{l, l'}^{\alpha 2} \rangle\right). \quad (2.13)$$

We have $\langle x_{l, l'}^{\alpha 2} \rangle$ from eq. (2.4). Substituting it to the above expression we get the structure factor of a monomer unit expressed in terms of the step length and wave number,

$$S(\mathbf{q}) = \sum_{\substack{\alpha \\ l, l'}}^N \exp\left(-\frac{q^2 |l' - l| b^2}{6}\right). \quad (2.14)$$

In order to consider the structure factor in a continuous approximation the summation is converted into integration. If the function $f(l, l')$ is to be made continuous where $0 \leq l \leq N$ and $0 \leq l' \leq N$, then we introduce $x = \frac{l}{N}$ and $y = \frac{l'}{N}$.

2. Weak Segregation Approach for Phase Separation

This allows to write the summation of $f(l, l')$ as

$$\begin{aligned} \sum_{\substack{\alpha \\ l, l'}}^N f(l, l') &= n_c \int_0^N \int_0^N f(l, l') dl dl' \\ &= n_c N^2 \int_0^1 \int_0^1 f(l, l') dx dy. \end{aligned} \quad (2.15)$$

Here α is summed over the total number of chains n_c . Using this the structure factor is rewritten as

$$S(\mathbf{q}) = n_c N^2 \int_0^1 \int_0^1 \exp\left(-\frac{q^2 b^2 N |x - y|}{6}\right) dx dy \quad (2.16)$$

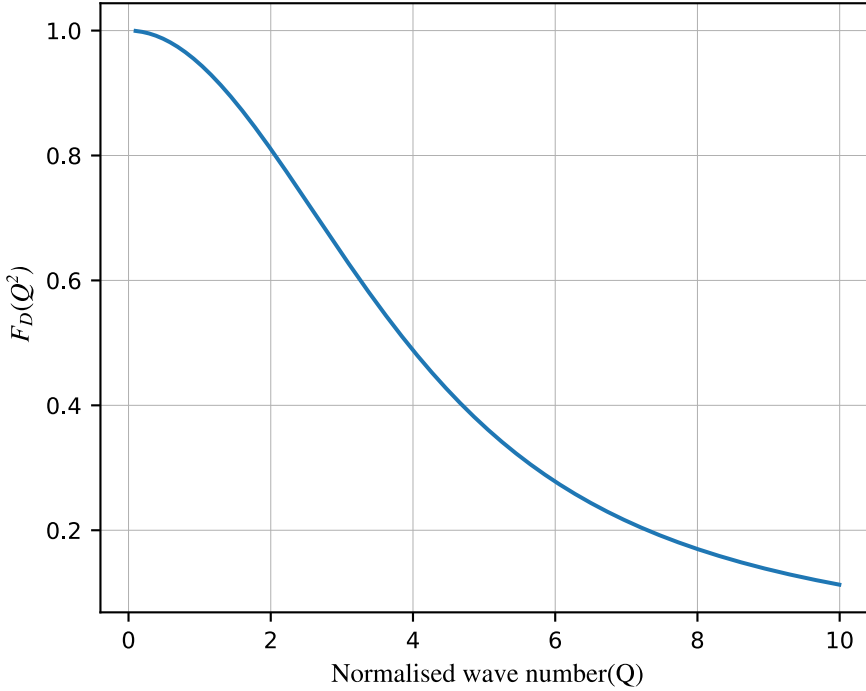


Figure 2.2: The Debye function $F_D(Q^2)$ with as a function of Q .

The dimensionless wave number Q is defined as $Q^2 = \frac{N b^2}{6} q^2$. Wave number q is scaled with the number of monomer units in a chain N and effective bond

2. Weak Segregation Approach for Phase Separation

length b over a factor of 6.

$$\begin{aligned} S(\mathbf{q}) &= n_c N^2 \int_0^1 \int_0^1 \exp(-Q^2 |x - y|) dx dy \\ &= n_c N^2 \frac{2}{Q^4} (\exp(-Q^2) + Q^2 - 1). \end{aligned} \quad (2.17)$$

In the structure factor, the quantity $n_c N^2$ can be written as $n_c N^2 = \Omega \rho N$, where Ω is the system volume and $\rho = n_c N / \Omega$ is the monomer unit density. This prefactor $\Omega \rho N$ is very common in calculations of the structure factors. The Debye function $F_D(Q^2)$ is defined as [31],

$$F_D(Q^2) = \frac{2}{Q^4} (\exp(-Q^2) + Q^2 - 1). \quad (2.18)$$

The behaviour of Debye function with respect to the normalised wavenumber Q is given in fig. 2.2. For small values of $Q < 1$ the function approaches 1 and at large Q ($Q \gg 1$) the function approaches zero ($F_D \approx \frac{2}{Q^2}$). The structure factor $S(\mathbf{q})$ is written in terms of Debye function $F_D(Q^2)$ as

$$S(\mathbf{q}) = n_c N^2 F_D(Q^2) \quad (2.19)$$

Here we are determining the structure factors for dilute, non-interacting chains. For more concentrated systems we need to include interactions. We have already mentioned that the separation vector $\mathbf{x}_{i,\nu}$ for random monomer units can be assumed to follow a Gaussian distribution as given in eq. (2.5). This is true for the case of monomer density ρ too since it is defined by the positions of monomer units.

We saw that the density distribution of monomer unit $\rho_{\mathbf{q}}$ can be expressed using the correlation between density corresponding to two monomer units. In the absence of interaction, these monomer units are free to move anywhere within the chain. It is not possible to distinguish between monomer units from the same chain or a different chain. So monomer density fluctuations can be written as,

$$\langle \rho_{\mathbf{q}} \rangle_0 = 0, \quad (2.20)$$

$$\langle \rho_{\mathbf{q}} \rho_{\mathbf{k}} \rangle_0 = \langle \rho_{\mathbf{q}} \rho_{-\mathbf{q}} \rangle_0 \delta_{\mathbf{q}\mathbf{k}}.$$

when $\mathbf{q} \neq 0$ and $\delta_{\mathbf{q}\mathbf{k}}$ is the Kronecker delta. Here \mathbf{q} and \mathbf{k} indicate wave number corresponding to two monomer units. Given there are no monomer interactions,

2. Weak Segregation Approach for Phase Separation

monomer unit distribution in the melt can be taken as a Gaussian distribution. From the constraints in eq. (2.20) the Gaussian distribution of monomer density in the second order approximation with no monomer interactions will be

$$\psi_0(\{\rho_{\mathbf{q}}\}) \propto \exp\left(-\frac{1}{2} \sum_{\mathbf{q}} \frac{\rho_{\mathbf{q}}\rho_{-\mathbf{q}}}{\langle \rho_{\mathbf{q}}\rho_{-\mathbf{q}} \rangle_0}\right). \quad (2.21)$$

This distribution is a sum over all possible configurations of the monomer density and hence this relates to the entropy of the system.

Now let us consider if there are interactions between these correlating monomer units. The internal potential energy of the system in terms of $k_B T$ is also dependent on the position of monomer units. For a homogeneous system if the potential energy between two monomer units that are separated by $\mathbf{r} = \mathbf{r}_i^\alpha - \mathbf{r}_{i'}^{\alpha'}$ is $v(\mathbf{r}) = k_B T V(\mathbf{r})$ (where k_B is Boltzmann's constant and T is the temperature). Then the total internal energy is given by

$$\begin{aligned} \frac{U\{\rho_{\mathbf{q}}\}}{k_B T} &= \frac{1}{2} \sum_{\substack{\alpha, l \\ \alpha', l'}} V(\mathbf{r}_i^\alpha - \mathbf{r}_{i'}^{\alpha'}) \\ &= \frac{1}{2\Omega} \sum_{\mathbf{q}} V_{\mathbf{q}} \rho_{\mathbf{q}} \rho_{-\mathbf{q}}. \end{aligned} \quad (2.22)$$

Detailed derivation for eq. (2.22) is given in appendix A.1.

Here, $V_{\mathbf{q}}$ is the Fourier transform for the internal energy $V(\mathbf{r})$. We have both free energies of the system due to monomer interactions and entropy of the system due to the rearranging of monomer units in Fourier space.

The potential energy associated with monomer interactions is short-ranged with $V(\mathbf{r}) \cong 0$ for $|\mathbf{r}| > a$, where a is in the order of monomer size. So, for $|\mathbf{q}| \ll \frac{1}{a}$ Fourier transform $V_{\mathbf{q}}$ is constant and independent of \mathbf{q} .

$$V_{\mathbf{q}} = \int d^3\mathbf{r} V(\mathbf{r}) \exp(i\mathbf{q} \cdot \mathbf{r}) \approx \int V(\mathbf{r}) d^3\mathbf{r} = V_0. \quad (2.23)$$

Thus total internal energy in terms of $k_B T$ is

$$U\{\rho_{\mathbf{q}}\} = \frac{1}{2\Omega} V_0 \sum_{\mathbf{q}} \rho_{\mathbf{q}} \rho_{-\mathbf{q}}. \quad (2.24)$$

Now we have the entropy of the melt from its conformations and internal energy in terms of $k_B T$ associated with it the partition function can be defined. When we define the partition function for a polymer system, a microstate (j) represents

2. Weak Segregation Approach for Phase Separation

a specific conformation formed by the chains. The partition function of this homopolymer system is given as a sum over microstates (j):

$$Z = \sum_{\text{states } j} \exp(-U(\{\rho_{\mathbf{q}}^j\})). \quad (2.25)$$

Here $\rho_{\mathbf{q}}^j$ is the Fourier transformed density in microstate j and $\{\rho_{\mathbf{q}}^j\}$ represents it for all values of wavevectors \mathbf{q} . The infinite (very large) number of chains available in the melt allows us to calculate partition function considering this as a continuous system. The free energy calculation as a function is of $\rho_{\mathbf{q}}$ is proceeded by introducing delta functions for each density field $\rho_{\mathbf{q}}$:

$$\int D\{\rho_{\mathbf{q}}\} \prod_{\mathbf{q}} \delta(\rho_{\mathbf{q}} - \rho_{\mathbf{q}}^j) = 1. \quad (2.26)$$

So the partition function Z can be written as,

$$Z = \sum_{\text{states } j} \int D\{\rho_{\mathbf{q}}\} \prod_{\mathbf{q}} \delta(\rho_{\mathbf{q}} - \rho_{\mathbf{q}}^j) \exp(-U(\{\rho_{\mathbf{q}}\})). \quad (2.27)$$

Rearranging the summation and product we get

$$Z = \int D\{\rho_{\mathbf{q}}\} \sum_{\text{states } j} \prod_{\mathbf{q}} \delta(\rho_{\mathbf{q}} - \rho_{\mathbf{q}}^j) \exp(-U(\{\rho_{\mathbf{q}}\})). \quad (2.28)$$

Here $\int D\rho_{\mathbf{q}}$ is the integral over $\rho_{\mathbf{q}}$ for all allowed \mathbf{q} . The quantity $\sum_j \prod_{\mathbf{q}} \delta(\rho_{\mathbf{q}} - \rho_{\mathbf{q}}^j)$ can be considered to be a sum which counts all the microstates j for which $\rho_{\mathbf{q}}^j = \rho_{\mathbf{q}}$ for all \mathbf{q} . This sum is equal to the total number of microstates W_s multiplied by the probability that $\rho_{\mathbf{q}}^j = \rho_{\mathbf{q}}$, which is $\psi_0(\{\rho_{\mathbf{q}}\})$ given in eq. (2.21). Hence,

$$\sum_j \prod_{\mathbf{q}} \delta(\rho_{\mathbf{q}} - \rho_{\mathbf{q}}^j) = W_s \psi_0(\{\rho_{\mathbf{q}}\}). \quad (2.29)$$

So we can write:

$$Z = W_s \int D\{\rho_{\mathbf{q}}\} \psi_0(\{\rho_{\mathbf{q}}\}) \exp(-U(\{\rho_{\mathbf{q}}^j\})). \quad (2.30)$$

where U is in terms of $k_B T$. Thus we have expressions for internal energy and monomer distribution ψ_0 . Substituting for ψ_0 eq. (2.21) and U eq. (2.22) in the above expression we get partition function for the system in terms of monomer density $\rho_{\mathbf{q}}$ in Fourier space.

2. Weak Segregation Approach for Phase Separation

$$\begin{aligned}
 Z &= W_s \int D\{\rho_{\mathbf{q}}\} \exp\left(-\frac{1}{2\Omega} \sum_{\mathbf{q}} V_0 \rho_{\mathbf{q}} \rho_{-\mathbf{q}}\right) \exp\left(-\frac{1}{2} \sum_{\mathbf{q}} \frac{\rho_{\mathbf{q}} \rho_{-\mathbf{q}}}{\langle \rho_{\mathbf{q}} \rho_{-\mathbf{q}} \rangle_0}\right) \\
 &= W_s \int D\{\rho_{\mathbf{q}}\} \exp\left(-\frac{1}{2} \left(\sum_{\mathbf{q}} \rho_{\mathbf{q}} \rho_{-\mathbf{q}} \left(\frac{V_0}{\Omega} + \frac{1}{\langle \rho_{\mathbf{q}} \rho_{-\mathbf{q}} \rangle_0} \right) \right)\right).
 \end{aligned} \tag{2.31}$$

Here $\frac{\rho_{\mathbf{q}} \rho_{-\mathbf{q}} V_0}{\Omega}$ gives the energy term and $\frac{\rho_{\mathbf{q}} \rho_{-\mathbf{q}}}{\langle \rho_{\mathbf{q}} \rho_{-\mathbf{q}} \rangle_0}$ gives the entropy of the system up to second order approximation. Now we have the expression for the partition function, the free energy functional $F\{\rho_{\mathbf{q}}\}$ is given by

$$Z = \int D\{\rho_{\mathbf{q}}\} \exp(-F\{\rho_{\mathbf{q}}\}). \tag{2.32}$$

From eq. (2.31), we get the second order terms of free energy in terms of $\rho_{\mathbf{q}}$. The partition function gives all possible distributions of monomer densities in the presence of interactions which is equivalent to the polymer distribution function with interaction $\psi_v(\{\rho_{\mathbf{q}}\})$ which we obtained in eq. (2.21).

$$\psi_v(\{\rho_{\mathbf{q}}\}) \propto \exp\left(-\frac{1}{2} \sum_{\mathbf{q}} \rho_{\mathbf{q}} \rho_{-\mathbf{q}} \left(\frac{V_{\mathbf{q}}}{\Omega} + \frac{1}{\langle \rho_{\mathbf{q}} \rho_{-\mathbf{q}} \rangle_0} \right)\right). \tag{2.33}$$

Comparing with eq. (2.21) the second moment of monomer density with interaction is $\langle \rho_{\mathbf{q}} \rho_{-\mathbf{q}} \rangle$. As we mentioned earlier average over the conformations for monomer fluctuations. the structure factor $S(\mathbf{q})$ is

$$S(\mathbf{q}) = \langle \rho_{\mathbf{q}} \rho_{-\mathbf{q}} \rangle \tag{2.34}$$

Now from eq. (2.31) in the presence of interaction, the second moment of monomer density is

$$\langle \rho_{\mathbf{q}} \rho_{-\mathbf{q}} \rangle = \frac{1}{\left(\frac{1}{\langle \rho_{\mathbf{q}} \rho_{-\mathbf{q}} \rangle_0} + \frac{V_0}{\Omega} \right)}. \tag{2.35}$$

In terms of structure factors, we have

$$S(\mathbf{q}) = \left(\frac{1}{S_0(\mathbf{q})} + \frac{V_{\mathbf{q}}}{\Omega} \right)^{-1}. \tag{2.36}$$

where $S_0(\mathbf{q}) = \langle \rho_{\mathbf{q}} \rho_{-\mathbf{q}} \rangle_0$, the structure factor in the absence of interactions. The potential energy V_0 depends upon the type of monomers. As the polymer system is homogeneous V_0 contains the monomer interactions of the same type. Now if there are more types of monomers $S(\mathbf{q})$ will change as V_0 will contain the mutual interaction between like monomers and unlike monomers.

2.1.2 RPA for incompressible polymer system with two components

When the polymer system consists of more than one type of monomers the structure factor depends on the density fluctuation of both monomer densities. We will now consider two different monomer densities, $\rho_{\mathbf{q}}^A$ for type A monomers and $\rho_{\mathbf{q}}^B$ for type B monomers. The structure factor for the polymer system is calculated using the *RPA* method as explained in the last section. From eq. (2.8) the monomer densities of A and B are given by

$$\begin{aligned}\rho_{\mathbf{q}}^A &= \sum_{\{\alpha,l\} \in A} \exp(i\mathbf{q} \cdot \mathbf{r}_l^\alpha) \\ \rho_{\mathbf{q}}^B &= \sum_{\{\alpha,l\} \in B} \exp(i\mathbf{q} \cdot \mathbf{r}_l^\alpha).\end{aligned}\tag{2.37}$$

In the absence of interactions, the monomer densities satisfy the following conditions, similar to the single component system as given in eq. (2.20). Monomer units have no correlation with themselves and since it is a homogeneous melt monomer units from different chains are indistinguishable in them. This results in three types of density fluctuations between $A - A$, $B - B$ and $A - B$.

$$\begin{aligned}\langle \rho_{\mathbf{q}}^A \rangle_0 &= 0, \\ \langle \rho_{\mathbf{q}}^B \rangle_0 &= 0, \\ \langle \rho_{\mathbf{q}}^A \rho_{\mathbf{k}}^A \rangle_0 &= \langle \rho_{\mathbf{q}}^A \rho_{-\mathbf{q}}^A \rangle_0 \delta_{\mathbf{q}\mathbf{k}}, \\ \langle \rho_{\mathbf{q}}^B \rho_{\mathbf{k}}^B \rangle_0 &= \langle \rho_{\mathbf{q}}^B \rho_{-\mathbf{q}}^B \rangle_0 \delta_{\mathbf{q}\mathbf{k}}, \\ \langle \rho_{\mathbf{q}}^A \rho_{\mathbf{k}}^B \rangle_0 &= \langle \rho_{\mathbf{q}}^A \rho_{-\mathbf{q}}^B \rangle_0 \delta_{\mathbf{q}\mathbf{k}}.\end{aligned}\tag{2.38}$$

Comparing with one component case, we can write the non-interacting structure factors from these density correlations as:

$$\begin{aligned}S_0^{AA} &= \langle \rho_{\mathbf{q}}^A \rho_{-\mathbf{q}}^A \rangle_0, \\ S_0^{BB} &= \langle \rho_{\mathbf{q}}^B \rho_{-\mathbf{q}}^B \rangle_0, \\ S_0^{AB} &= \langle \rho_{\mathbf{q}}^A \rho_{-\mathbf{q}}^B \rangle_0 = S_0^{BA}.\end{aligned}\tag{2.39}$$

2. Weak Segregation Approach for Phase Separation

The non-interacting structure factor $S_0(\mathbf{q})$ is a two by two matrix here:

$$S_0(\mathbf{q}) = \begin{bmatrix} S_0^{AA} & S_0^{AB} \\ S_0^{AB} & S_0^{BB} \end{bmatrix}. \quad (2.40)$$

This allows us to interpret the distribution function as a Gaussian for a two component system. Following the expression for monomer distribution from eq. (2.20), the expression for two component systems will be:

$$\psi_0(\{\rho_{\mathbf{q}}^A, \rho_{\mathbf{q}}^B\}) \approx \exp \left(-\frac{1}{2} \sum_{\mathbf{q}} \begin{bmatrix} \rho_{\mathbf{q}}^A & \rho_{\mathbf{q}}^B \end{bmatrix} S_0^{-1}(\mathbf{q}) \begin{bmatrix} \rho_{-\mathbf{q}}^A \\ \rho_{-\mathbf{q}}^B \end{bmatrix} \right) \quad (2.41)$$

Here also we take the Fourier transformed potential due to monomer interactions V_0 as a constant. Since there are two different monomer interactions we need to define different potentials for $A - A$, $B - B$ and $A - B$ interactions namely, V_{AA} , V_{BB} and V_{AB} . The total internal energy $U(\{\rho_{\mathbf{q}}^A, \rho_{\mathbf{q}}^B\})$ in terms of $k_B T$ is then given:

$$U(\{\rho_{\mathbf{q}}^A, \rho_{\mathbf{q}}^B\}) = \frac{1}{2\Omega} \sum_{\mathbf{q}} \begin{bmatrix} \rho_{\mathbf{q}}^A & \rho_{\mathbf{q}}^B \end{bmatrix} \begin{bmatrix} V_{AA} & V_{AB} \\ V_{AB} & V_{BB} \end{bmatrix} \begin{bmatrix} \rho_{-\mathbf{q}}^A \\ \rho_{-\mathbf{q}}^B \end{bmatrix}. \quad (2.42)$$

As the interaction energy and the distribution function are defined, the partition function is calculated to find the second order term in free energy expression. Following the procedure as in one component system, we get

$$Z = W_s \int D\rho_{\mathbf{q}}^A D\rho_{\mathbf{q}}^B \psi_0(\{\rho_{\mathbf{q}}^A, \rho_{\mathbf{q}}^B\}) \exp(-U(\{\rho_{\mathbf{q}}^A, \rho_{\mathbf{q}}^B\})). \quad (2.43)$$

where W_s indicates the total number of microstates. Here the partition function is dependent on both $\rho_{\mathbf{q}}^A$ and $\rho_{\mathbf{q}}^B$. For polymer melts we consider the incompressible state where the total monomer density is constant throughout the volume.

$$\rho^A(\mathbf{r}) + \rho^B(\mathbf{r}) = \text{const.} \quad (2.44)$$

$$\implies \rho_{\mathbf{q}}^A = -\rho_{\mathbf{q}}^B = \rho_{\mathbf{q}}. \quad (2.45)$$

After applying the constraints and substituting eq. (2.41) and eq. (2.42) to eq. (2.43) we get the partition function in terms of single monomer density $\rho_{\mathbf{q}}$, which is dependent on wavevector \mathbf{q} .

2. Weak Segregation Approach for Phase Separation

$$Z = W_s \int D\rho_{\mathbf{q}} \exp \left(-\frac{1}{2} \sum_{\mathbf{q}} \left(\rho_{\mathbf{q}} \rho_{-\mathbf{q}} \left(\frac{V_{AA} + V_{BB} - 2V_{AB}}{\Omega} + \frac{S_0^{AA} S_0^{BB} - (S_0^{AB})^2}{S_0^{AA} + S_0^{BB} + 2S_0^{AB}} \right) \right) \right) \quad (2.46)$$

For a polymer melt system if the average of the total potential is given by V and small perturbation to that potential because of the monomer interactions are $\epsilon_{AA}, \epsilon_{BB}$ and ϵ_{AB} we get

$$\begin{aligned} V_{AA} &= V + \epsilon_{AA} \\ V_{BB} &= V + \epsilon_{BB} \end{aligned} \quad (2.47)$$

$$V_{AB} = V + \epsilon_{AB}$$

Even if interaction potentials V_{AA}, V_{BB} and V_{AB} are very large $V_{AA} + V_{BB} - 2V_{AB}$ will be finite. Here the Flory interaction parameter χ is introduced, which gives the relative degree of interaction between monomers.

$$\frac{-2\chi}{\rho} = \epsilon_{AA} + \epsilon_{BB} - 2\epsilon_{AB} = V_{AA} + V_{BB} - 2V_{AB} \quad (2.48)$$

The non-interacting structure factor $S_0(\mathbf{q})$ for two component system is then

$$S_0(\mathbf{q}) = \frac{S_0^{AA} S_0^{BB} - (S_0^{AB})^2}{S_0^{AA} + S_0^{BB} + 2S_0^{AB}}. \quad (2.49)$$

When calculating structure factors such as S_0^{AA} , the result is always found to be proportional to a factor of $\Omega\rho N$, where $\Omega\rho$ is the monomer density of the melt and N is the number of monomer units in a polymer chain. It is convenient to write $S_0^{AA} = \Omega\rho N s_0^{AA}$, so that $S_0(\mathbf{q}) = \Omega\rho N s_0(\mathbf{q})$, where

$$s_0(\mathbf{q}) = \frac{s_0^{AA} s_0^{BB} - (s_0^{AB})^2}{s_0^{AA} + s_0^{BB} + 2s_0^{AB}}. \quad (2.50)$$

Thus free energy functional up to the second order in density fluctuations (in units of $k_B T$) is

$$F\{\rho_{\mathbf{q}}\} = \frac{1}{2} \sum_{\mathbf{q}} \left(\rho_{\mathbf{q}} \rho_{-\mathbf{q}} \left(\frac{-2\chi}{\Omega\rho} + \frac{1}{\Omega\rho N s_0(\mathbf{q})} \right) \right). \quad (2.51)$$

2. Weak Segregation Approach for Phase Separation

So total structure factor is then:

$$S(\mathbf{q}) = \left(\frac{1}{\Omega\rho N s_0(\mathbf{q})} - \frac{2\chi}{\Omega\rho} \right)^{-1} = \left(\frac{1}{S_0(\mathbf{q})} - \frac{2\chi}{\Omega\rho} \right)^{-1}. \quad (2.52)$$

So from the RPA of a two-component system, we get an expression similar to eq. (2.36), where instead of V_q we have $\frac{2\chi}{\rho}$, which gives quantifies the interaction between different types of monomers in the melt. In two-component cases, there are multiple monomer density fluctuations which will give rise to a critical wavevector at which phase separation emerges. When χ is increased and reaches the critical value (χ_c) in eq. (2.52), the structure factor $S(\mathbf{q})$ diverges at the critical wavevector $\mathbf{q} = \mathbf{q}^*$. This is the spinodal point at which the phase separation is initiated. As χ increases past the spinodal point phase separation occurs [128]. The spinodal point is determined from

$$N\chi_c = \frac{1}{2\max(s_0(\mathbf{q}))} \quad (2.53)$$

Non-interacting structure factor for a diblock

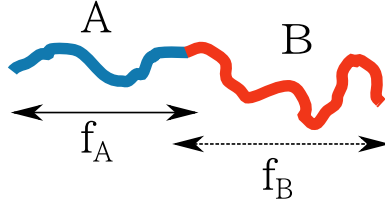


Figure 2.3: A schematic representation of a diblock copolymer. Block of A type occupies f_A , and block of B type occupies f_B of the total length.

The calculation of non-interacting structure factor and critical wave number \mathbf{q} is demonstrated considering a diblock. A diblock comprises polymer chains of two types namely, A and B joined at the centre. Let N_A and N_B be the number of monomer units in each block, occupying f_A and f_B length fractions, respectively. Here the total number of monomer units in a chain is $N = N_A + N_B$. Then length fractions are expressed as:

$$f_A = \frac{N_A}{N}; f_B = \frac{N_B}{N}. \quad (2.54)$$

In order to calculate the non-interacting structure factor $S_0(\mathbf{q})$ we need to calculate s_0^{AA} , s_0^{BB} and s_0^{AB} for this particular polymer architecture. Using the same steps used in finding the structure factor for a homogeneous system one

2. Weak Segregation Approach for Phase Separation

can calculate the structure factor for each block separately. For A block, non-interacting structure factor S_0^{AA} as a function of normalised wave number $Q^2 = \frac{q^2 N b^2}{6}$ is

$$\begin{aligned} S_0^{AA} &= \langle \rho_{-\mathbf{q}}^A \rho_{\mathbf{q}}^A \rangle = n_c N^2 \int_0^{f_A} \int_0^{f_A} \exp(-Q^2 |x - y|) dx dy \\ &= n_c N^2 f_A^2 F_D(f_A Q^2). \end{aligned} \quad (2.55)$$

This expression is similar to the structure factor for the homogeneous system $S(\mathbf{q})$ eq. (2.19) but here we are only considering the monomer density fluctuations of A type. It is indicated by length fraction f_A in S_0^{AA} . In the same manner, the non-interacting structure factor for the B block is calculated. The only difference in the expression is f_B replacing f_A . So,

$$S_0^{BB} = n_c N^2 f_B^2 F_D(f_B Q^2). \quad (2.56)$$

Due to the presence of two different types of monomers in the same chain, there will be interactions between A and B monomer units. This introduces structure factor in the absence of any external interaction S_0^{AB} , which is given by

$$S_0^{AB} = \langle \rho_{-\mathbf{q}}^A \rho_{\mathbf{q}}^B \rangle = n_c N^2 \int_0^{f_A} \int_{f_A}^1 \exp(-Q^2 |x - y|) dx dy. \quad (2.57)$$

Substituting $x = f_A - X$ and $y = f_A + Y$ and using $f_A + f_B = 1$ we get

$$\begin{aligned} S_0^{AB} &= n_c N^2 \int_0^{f_A} dX \int_0^{f_B} dY \exp(-Q^2(X + Y)) \\ &= \frac{n_c N^2}{Q^4} (\exp(-f_A Q^2) - 1)(\exp(-f_B Q^2) - 1) \\ &= n_c N^2 f_A f_B h(f_A Q^2) h(f_B Q^2). \end{aligned} \quad (2.58)$$

In this expression, a new function is defined,

$$h(x) = \frac{1}{x} (1 - \exp(-x)) \quad (2.59)$$

which will be seen and discussed in detail in later sections where we determine the structure factor for more complex architectures.

Expressions for S_0^{AA} , S_0^{BB} and S_0^{AB} are substituted into the expression for non-interacting structure factor for two-component system $S_0(Q)$ in eq. (2.49).

2. Weak Segregation Approach for Phase Separation

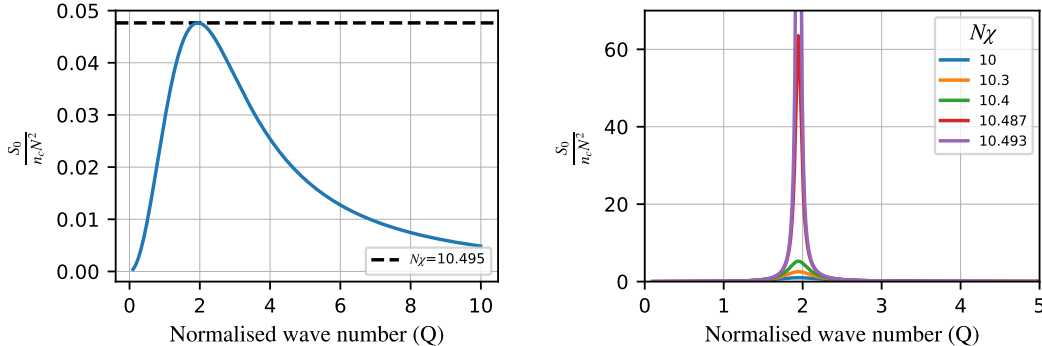


Figure 2.4: In the left the non interacting structure factor $S_0(Q)$ for AB block copolymer is varied with normalised wave vector Q for $f_A = 0.5$. The $S_0(Q)$ for a diblock has maxima at $Q = 2$ as we are considering the radius of gyration twice the size of one block. The variation of total structure factor $S(Q)$ with N_χ where $f_A = f_B = 0.5$. As the N_χ is increased the total structure factor diverges at $Q = 2$ indicating phase separation.

This will give the overall non-interacting structure factor as a function of normalised wave number Q . The non-interacting structure factor is for diblock where $f_A = 0.5$ and $f_B = 0.5$ is given in fig. 2.4.(a). The non-interacting structure factor $S_0(Q)$ has a maximum at $Q \approx Q^*$. This indicates that the melt segregates into some morphology where the prominent wave number is Q^* . The total structure factor given in eq. (2.52) will diverge at this wavevector. Hence the Flory interaction parameter N_χ of the melt during the phase formation is obtained using eq. (2.53). Total structure factor ($S(Q)$) eq. (2.52) diverges at wave number Q^* and N_χ as shown in fig. 2.4 indicating phase separation. The most common morphology for diblock with comparable A and B length fractions is lamellar. They also give other complex morphologies like quasicrystals under specific conditions[12, 33].

2.1.3 RPA for 3 component system

This section covers the same idea of phase separation but now for a three-component system. The procedure to determine the non-interacting structure factor is similar to a two-component system. The only difference is that the structure factor matrix is now 3×3 given there are three kinds of monomer densities.

For a polymer system with three components, monomer unit densities in Fourier space are ρ_q^A , ρ_q^B and ρ_q^C for A, B and C type monomers respectively.

2. Weak Segregation Approach for Phase Separation

Following the same procedure as the two-component case, first the monomer unit distribution $\psi_0(\{\rho_{\mathbf{q}}^A, \rho_{\mathbf{q}}^B, \rho_{\mathbf{q}}^C\})$ is defined in the absence of interactions. If $S_0(\mathbf{q})$ is defined as the matrix of non-interacting structure factors, the monomer unit distribution function is given as

$$\psi_0(\{\rho_{\mathbf{q}}^A, \rho_{\mathbf{q}}^B, \rho_{\mathbf{q}}^C\}) = \exp \left(-\frac{1}{2} \sum_{\mathbf{q}} \begin{bmatrix} \rho_{\mathbf{q}}^A & \rho_{\mathbf{q}}^B & \rho_{\mathbf{q}}^C \end{bmatrix} S_0^{-1}(\mathbf{q}) \begin{bmatrix} \rho_{-\mathbf{q}}^A \\ \rho_{-\mathbf{q}}^B \\ \rho_{-\mathbf{q}}^C \end{bmatrix} \right) \quad (2.60)$$

where

$$S_0(\mathbf{q}) = \begin{bmatrix} S_0^{AA} & S_0^{AB} & S_0^{AC} \\ S_0^{AB} & S_0^{BB} & S_0^{BC} \\ S_0^{AC} & S_0^{BC} & S_0^{CC} \end{bmatrix}. \quad (2.61)$$

Similar to the case of the two-component system it is convenient to take out the factor of $\Omega\rho N$ so that

$$S_0(\mathbf{q}) = \Omega\rho N \begin{bmatrix} s_0^{AA} & s_0^{AB} & s_0^{AC} \\ s_0^{AB} & s_0^{BB} & s_0^{BC} \\ s_0^{AC} & s_0^{BC} & s_0^{CC} \end{bmatrix}. \quad (2.62)$$

As we are using the inverse of the non-interacting structure factor in the expression we determine the inverse of this 3×3 matrix and each entry is identified as Γ_{ij} . The inverse of matrix $S_0(\mathbf{q})$ is given as

$$S_0^{-1}(\mathbf{q}) = \frac{1}{\Omega\rho N} \begin{bmatrix} \Gamma^{AA} & \Gamma^{AB} & \Gamma^{AC} \\ \Gamma^{AB} & \Gamma^{BB} & \Gamma^{BC} \\ \Gamma^{AC} & \Gamma^{BC} & \Gamma^{CC} \end{bmatrix}. \quad (2.63)$$

2. Weak Segregation Approach for Phase Separation

The internal energy functional $U(\{\rho_{\mathbf{q}}^A, \rho_{\mathbf{q}}^B, \rho_{\mathbf{q}}^C\})$ is of the form

$$\frac{U(\{\rho_{\mathbf{q}}^A, \rho_{\mathbf{q}}^B, \rho_{\mathbf{q}}^C\})}{k_B T} = \frac{1}{2\Omega} \sum_{\mathbf{q}} \begin{bmatrix} \rho_{\mathbf{q}}^A & \rho_{\mathbf{q}}^B & \rho_{\mathbf{q}}^C \end{bmatrix} \begin{bmatrix} V_{AA} & V_{AB} & V_{AC} \\ V_{AB} & V_{BB} & V_{BC} \\ V_{AC} & V_{BC} & V_{CC} \end{bmatrix} \begin{bmatrix} \rho_{-\mathbf{q}}^A \\ \rho_{-\mathbf{q}}^B \\ \rho_{-\mathbf{q}}^C \end{bmatrix} \quad (2.64)$$

The monomer interactions are quantified using Flory interaction parameter χ for the monomer pairs $A - B$, $B - C$ and $C - C$.

$$\begin{aligned} \frac{-2\chi_{AB}}{\rho} &= V_{AA} + V_{BB} - 2V_{AB}, \\ \frac{-2\chi_{BC}}{\rho} &= V_{BB} + V_{CC} - 2V_{BC}, \\ \frac{-2\chi_{AC}}{\rho} &= V_{AA} + V_{CC} - 2V_{AC}. \end{aligned} \quad (2.65)$$

The partition function Z is now expressed in terms of all three monomer densities.

$$Z = W_c \int D\rho_{\mathbf{q}}^A D\rho_{\mathbf{q}}^B D\rho_{\mathbf{q}}^C \psi_0(\{\rho_{\mathbf{q}}^A, \rho_{\mathbf{q}}^B, \rho_{\mathbf{q}}^C\}) \exp\left(-\frac{U(\{\rho_{\mathbf{q}}^A, \rho_{\mathbf{q}}^B, \rho_{\mathbf{q}}^C\})}{k_B T}\right). \quad (2.66)$$

Introducing incompressibility to the system reduces the dependency of partition function (Z) to two monomer densities, $\rho_{\mathbf{q}}^A$ and $\rho_{\mathbf{q}}^B$, with

$$\rho_{\mathbf{q}}^C = -(\rho_{\mathbf{q}}^A + \rho_{\mathbf{q}}^B). \quad (2.67)$$

Elimination and rearrangement of non-interacting scattering factor matrix $S_0(\mathbf{q})$ and interaction potential matrix to a 2×2 matrix ($W_{\mathbf{q}}$) is discussed in detail in appendix A.2. The partition function is then function of $\rho_{\mathbf{q}}^A$, $\rho_{\mathbf{q}}^B$, $N\chi_{AB}$, $N\chi_{BC}$, $N\chi_{AC}$, Γ^{AA} , Γ^{BB} , Γ^{CC} , Γ^{AB} , Γ^{BC} and Γ^{AC} .

$$Z = W_c \int D\rho_{\mathbf{q}}^A D\rho_{\mathbf{q}}^B \exp\left[-\frac{1}{2} \sum_{\mathbf{q}} \begin{bmatrix} \rho_{\mathbf{q}}^A & \rho_{\mathbf{q}}^B \end{bmatrix} W_{\mathbf{q}} \begin{bmatrix} \rho_{-\mathbf{q}}^A \\ \rho_{-\mathbf{q}}^B \end{bmatrix}\right] \quad (2.68)$$

where

$$W_{\mathbf{q}} = \Omega\rho N\widetilde{W}_{\mathbf{q}} = \left\{ N\Omega\rho \begin{bmatrix} -2\chi_{AC} & \chi_{AB} - \chi_{BC} - \chi_{AC} \\ \chi_{AB} - \chi_{BC} - \chi_{AC} & -2\chi_{BC} \end{bmatrix} + \begin{bmatrix} \Gamma^{AA} + \Gamma^{CC} - 2\Gamma^{AC} & \Gamma^{AB} - \Gamma^{BC} - \Gamma^{AC} + \Gamma^{CC} \\ \Gamma^{AB} - \Gamma^{BC} - \Gamma^{AC} + \Gamma^{CC} & \Gamma^{BB} + \Gamma^{CC} - 2\Gamma^{BC} \end{bmatrix} \right\} \quad (2.69)$$

Using *RPA*, the second order term $\widetilde{W}_{\mathbf{q}}$ will indicate the phase transition. As $\widetilde{W}_{\mathbf{q}}$ is a symmetric matrix, its geometric nature and stability are determined by its eigenvalues $\lambda_1(\mathbf{q})$ and $\lambda_2(\mathbf{q})$. For a two-component system, it was easier to extract the non-interacting structure factor, but here it is a bit complicated to extract the total structure factor. Analogous to the two-component system, the point of instability is determined where monomer density fluctuations diverge and phase separation occurs. We need to find the point of transition from a stable to an unstable state where either one of the eigenvalues becomes less than zero. So the wavevector \mathbf{q} for which the lowest eigenvalue first changes from positive to negative given by the minima in the eigenvalue plot. This will give the wavevector at which phase transition occurs.

2.2 Structure factor for any arbitrary chain : Review based on $(AB)_{L_b}$

It is obvious from the *RPA* formulations discussed in the previous section 2.1 that all that we need to calculate is the non-interacting structure factor. This section is a review of the method to calculate the structure factor for any arbitrary block copolymer which was formulated by Read [126]. The structure factor for any block polymer, including branched copolymers, can be determined using this method, provided there are no loops in the polymer architecture. In Read's method, a polymer chain α is split into different 'blocks', which is indicated by γ as shown in fig 2.5. Each block is considered flexible to adjacent blocks, that is, which makes them free to rotate and select any random orientations with respect to the rest of the chain. Thus the polymer chain has high flexibility. These blocks are treated individually first to find their contribution to $S_0(\mathbf{q})$. The normalised wave number Q_γ is defined for each block which is dependent on its step length b and number of monomer units (N_γ). For the sake of simplicity, we consider the same step length (b) for blocks of all monomer types.

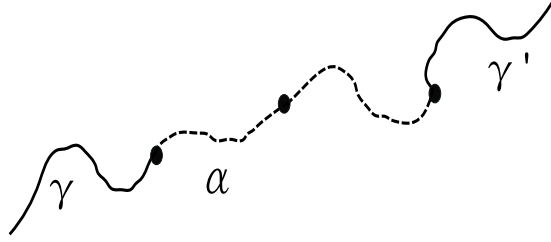


Figure 2.5: An arbitrary chain α of A blocks

$$Q_\gamma^2 = \frac{q^2 b^2 N_\gamma}{6}. \quad (2.70)$$

Each block is associated with a ‘self term’ J_γ , a ‘co-term’ H_γ and a ‘propagator term’ G_γ [126].

$$\begin{aligned} J_\gamma &= N_\gamma^2 j_\gamma & \text{where, } j_\gamma &= \frac{2}{Q_\gamma^4} (\exp(-Q_\gamma^2) - 1 + Q_\gamma^2) \\ H_\gamma &= N_\gamma h_\gamma & \text{where, } h_\gamma &= \frac{1}{Q_\gamma^2} (1 - \exp(-Q_\gamma^2)) \\ G_\gamma &= \exp(-Q_\gamma^2) \end{aligned} \quad (2.71)$$

The ‘self-term’ J_γ defined in eq. (2.71) is the Debye function that is seen as the structure factor term for a homogeneous system in eq. (2.18).

When calculating structure factors for a given polymer chain, we always require a double sum over pairs of monomers in that chain. This gives rise to two types of terms in the sum, either (i) the monomer pair lies in the same block, or (ii) the monomer pair lies in two different blocks. Summing over monomer pairs in the same block gives the ‘self-term’ J_γ to the structure factor. The ‘self term’ J_γ gives the contribution of each block that represents monomer density fluctuations within each block γ . The ‘co-term’ H_γ gives the contribution from block γ when the other monomer unit is on a different block γ' and ‘propagator term’ G_γ gives the contribution of structure between block γ and block γ' . Summing over monomer pairs in two different blocks γ and γ' gives a contribution of form $H_\gamma H_{\gamma'} \prod_\eta G_\eta$ (η represents the block labelling for blocks between γ and γ') where the product of propagators G_η gives the contribution from the unique connecting path between γ and γ' . Hence, the sum over monomer pairs becomes a sum over block pairs.

To demonstrate this procedure, we are considering a long chain of diblocks connected end-to-end, $(AB)_{L_b}$ as shown in fig. 2.6. Given the number of A monomer

2. Weak Segregation Approach for Phase Separation

units and B monomer units are N_A and N_B , respectively, the total number of monomer units $N = N_A + N_B$. Here the length fraction of A is $f_A = \frac{N_A}{N}$ and that of B is $f_B = \frac{N_B}{N}$.

The normalised wave number for A and B blocks are:

$$\begin{aligned} Q_A^2 &= \frac{q^2 b^2 N_A}{6} = f_A Q^2, \\ Q_B^2 &= \frac{q^2 b^2 N_B}{6} = f_B Q^2 = (1 - f_A) Q^2. \end{aligned} \quad (2.72)$$

Now ‘self-term’, ‘co-term’ and ‘propagator terms’ are defined in terms of normalised wave number Q . Here L_b is a large number that denotes the number of diblock (AB) included in this polymer architecture. We first calculate S_0^{AA} for

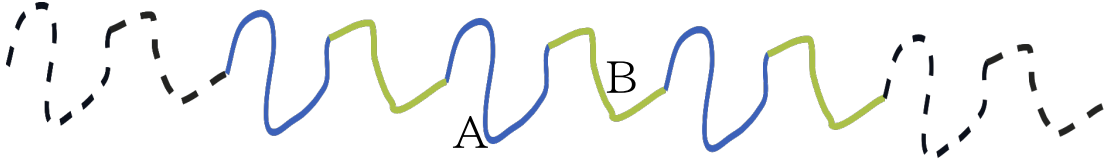


Figure 2.6: Schematic representation of $(AB)_{L_b}$ polymer chain

n_c chains of this architecture. In $(AB)_{L_b}$ there are L_b blocks of A type. This gives the first term in eq. (2.73), which is the sum of all self terms corresponding to A blocks. Taking one A block as a reference, looking to the right, this block is connected to the next A block with one B block in between. This will give the term $H_A H_A G_B$ in eq. (2.73). Likewise, the second A block to the right will give $H_A H_A G_B G_A G_A$ due to the $B - A - B$ blocks between two A blocks. This pattern continues until we reach last A block in the right side. There are same pattern of blocks to the left of the reference A block. Thus the entire summation is multiplied by two in the second term of eq. (2.73). Approximating the number of blocks to the right and left to be infinite gives S_0^{AA} as an infinite geometric progression.

$$\begin{aligned} S_0^{AA} &= n_c (L_b J_A + 2L_b (H_A H_A G_B + H_A H_A G_B G_A G_B + \\ &\quad H_A H_A G_B G_A G_B G_A G_B + \dots)), \\ &= n_c (L_b J_A + 2L_b H_A^2 G_B (1 + G_A G_B + (G_A G_B)^2 + \\ &\quad (G_A G_B)^3 + \dots)). \end{aligned} \quad (2.73)$$

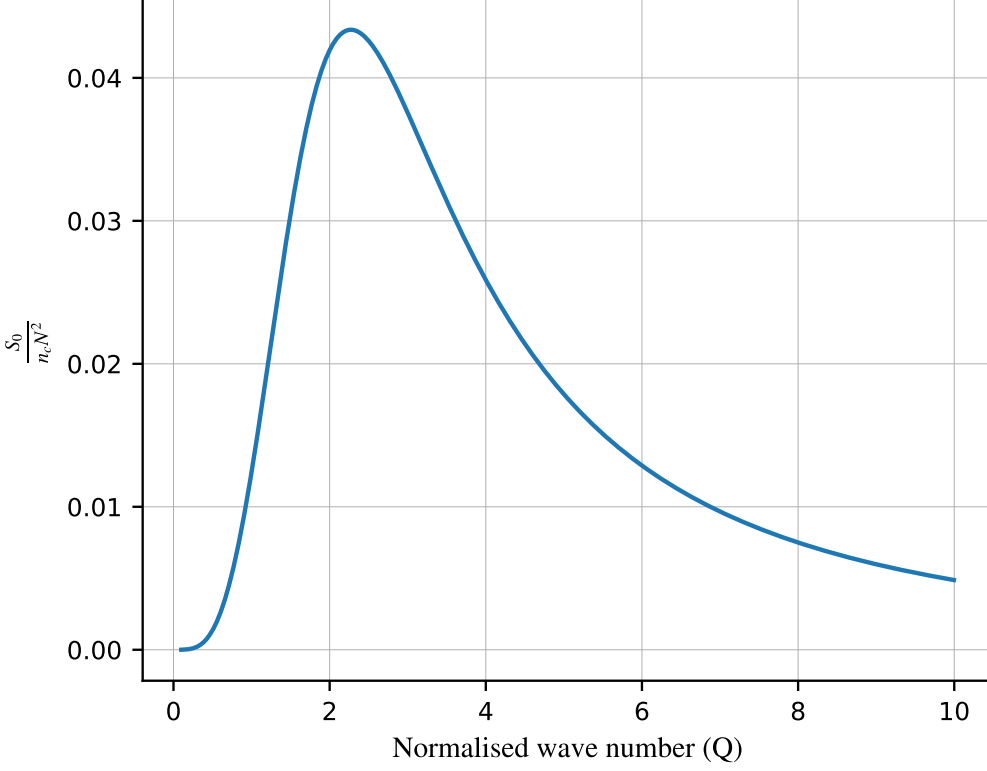


Figure 2.7: The non-interacting structure, $S_0(Q)$ for infinite linear $(AB)_{L_b}$ block copolymer is given where the length fraction of A block $f_A = 0.5$.

Explicitly summing the geometric progression an expression for S_0^{AA} is derived.

$$S_0^{AA} = n_c \left(L_b J_A + 2L_b H_A^2 G_B \left(\frac{1}{1 - G_A G_B} \right) \right). \quad (2.74)$$

The calculation for S_0^{BB} is exactly the same since the number of B blocks are the same as the number of A blocks. The B blocks are also found in polymer architecture alternating with A . The ‘self term, ‘co-term’ and ‘propagator term’ for A blocks in eq. (2.74) are replaced by ‘self term, ‘co-term’ and ‘propagator term’ for B blocks.

$$S_0^{BB} = n_c \left(L_b J_B + 2L_b H_B^2 G_A \left(\frac{1}{1 - G_A G_B} \right) \right). \quad (2.75)$$

In order to calculate S_0^{AB} consider blocks of different monomer types (A and B). Taking one A block as a reference looking to the right, reference A block is

connected to the adjacent B block which will give the term, $H_A H_B$. Looking for the next B block, there are $(B - A)$ blocks between the reference A block and this B block. This will add the term $H_A H_B G_A G_B$ to the expression. Pattern will go on infinitely (L_b is a large number) giving a geometric progression. The same pattern of calculation is done to the left of reference A which introduces a multiple of two in the expression. Taking the block number as infinite, the above calculation is true from any reference A in the chain giving a multiple of L_b in the expression.

$$\begin{aligned} S_0^{AB} &= 2n_c L_b (H_A H_B + H_A H_B G_B G_A + H_A H_B G_B G_A G_B G_A + \dots) \\ &= 2n_c L_b H_A H_B \left(\frac{1}{1 - G_A G_B} \right) \end{aligned} \tag{2.76}$$

From these expressions for S_0^{AA} , S_0^{BB} and S_0^{AB} , eq. (2.74), eq. (2.75) and eq. (2.76), the non-interacting structure factor $S_0(\mathbf{q})$ for this two component system is determined using eq. (2.50). The variation of the non-interacting structure factor as a function of normalised wave number Q is shown in fig. fig. 2.7. From the previous discussions on phase separation, a single maximum indicates the prominent wave number that emerges in the phase separation and hence the length scale. Since the structure factor only has one maximum it only has a single lengthscale in its phase separated structure.

The structure factor for any block polymer, including branched copolymers, can be calculated in this manner, provided there are no loops in the structure.

With all these tools discussed so far, we are proposing three designs of block copolymers that can potentially give two lengthscaled phase separation. We have two models within the two-component system: a monodisperse $A_L(BA_S)_n$ chain and a polydisperse model which contains three types of blocks (A_L , B and A_S) in a mixture. As for the third model, we are considering a monodisperse model of ABC star terpolymer in the weak segregation limit. Each case is discussed in detail in the coming sections.

2.3 Monodisperse two component model: $A_L(BA_S)_n$

The first polymer we are considering is a linear chain polymer with two different types of monomers. The design of the model is such that there will be two distinct critical lengthscales emerging at phase separation in its non-interacting structure factor.

The proposed polymer architecture $A_L(BA_S)_n$ is illustrated in fig. 2.8. It has a long block A_L of A type monomers followed by n alternating BA_S diblocks. The incompatibility and difference in block lengths will induce two different phase

2. Weak Segregation Approach for Phase Separation

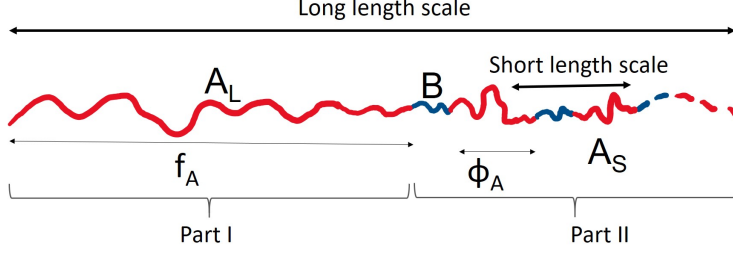


Figure 2.8: Schematic representation of the linear chain $A_L(BA_S)_n$. Blocks indicated in red are of type A and blue blocks are of type B . The dashed part represents the continuation of BA_S diblock up to n . Length fraction of the long red block A_L , short red blocks A_S and blue blocks B are f_A , ϕ_A and $\phi_B = 1 - \phi_A$ respectively.

separations. Incompatibility between A type monomer units in A_L and $(BA_S)_n$ gives rise to one lengthscale. Another lengthscale emerges from the incompatibility between A -type and B type monomers within the tailing $(BA_S)_n$. Since there are the same A -type monomers in both A_L and A_S , the incompatibility between the $(BA_S)_n$ tail and the A_L block will be smaller relative to incompatibility within the $(BA_S)_n$ tail. However, phase separation at smaller lengthscales within the $(BA_S)_n$ tail requires greater elastic energy from chain deformation (as compared to phase separation at the larger scale of the whole molecule). These two effects compensate one another, giving the possibility of phase separation at both lengthscales occurring at the same point.

Building on this hypothesis we look for two different length scales indicated by two peaks in the non-interacting structure factor. The non-interacting structure factor is calculated in the same way as in section 2.2. In the infinite linear chain discussed earlier, all A type blocks are considered to have the same length fraction. But in this new model, we have two types of A blocks which makes the calculation slightly different from the previous case, requiring two intermediate steps. The whole polymer chain is considered into two parts: part I consists the long A_L block and part II contains the the tailing $(BA_S)_n$ blocks. First composite self terms J_{AA}^{II} , J_{BB}^{II} and J_{AB}^{II} for part II , $(BA_S)_n$ tail is determined as detailed below. These are then used by considering $(BA_S)_n$ tail as a single block in a diblock where the adjacent block is A_L .

From the illustration of the polymer chain part I with A_L block is of length fraction f_A . The rest of the chain, part II $(BA_S)_n$ will have length fraction $(1 - f_A)$. Considering one BA_S block as one unit, the length fraction of A_S block is ϕ_A . Then length fraction of B block in BA_S diblock is $1 - \phi_A$. The part II consists of n such diblocks. Given total number of monomer units is N number of monomer



Figure 2.9: Schematic structure for $A_L(BA_S)_2$ where A_L is tailed by BA_SBA_S .

units in each block is determined to be:

$$\text{Number of monomer units in } A_L = f_A N, \quad (2.77)$$

$$\text{Number of monomer units in } A_S = \frac{1}{n}(1 - f_A)\phi_A N, \quad (2.78)$$

$$\text{Number of monomer units in } B = \frac{1}{n}(1 - f_A)(1 - \phi_A)N. \quad (2.79)$$

Normalised wave numbers are now defined for the polymer melt for A_L , A_S and B blocks as Q_{A_L} , Q_{A_S} and Q_B respectively using eq. (2.70). If we define normalised wave number $Q^2 = \frac{Nb^2}{6}q^2$, then normalised wave numbers for each block is defined. The wave numbers corresponding to each block is expressed in terms of length fractions of the blocks and normalised wave number Q .

$$\begin{aligned} Q_{A_L}^2 &= f_A \frac{Nb^2 q^2}{6} = f_A Q^2, \\ Q_{A_S}^2 &= \frac{1}{n}(1 - f_A)\phi_A \frac{Nb^2 q^2}{6} = \frac{(1 - f_A)\phi_A}{n} Q^2, \\ Q_B^2 &= \frac{q^2 b^2 \left(\frac{(1 - f_A)(1 - \phi_A)N}{n} \right)}{6} = \frac{(1 - f_A)(1 - \phi_A)}{n} Q^2. \end{aligned} \quad (2.80)$$

Now all parameters necessary to determine the non-interacting structure factor are defined.

2.3.1 Structure factor for $A_L(BA_S)_2$

In order to demonstrate the calculation consider the case where $n = 2$. We have a polymer chain of structure $A_L - B - A_S - B - A_S$ as shown in fig. 2.9. The composite self-terms are determined first.

Composite self terms for part II (BA_S)₂

Composite ‘self terms’ to be determined are: J_{AA}^{II} , J_{BB}^{II} and J_{AB}^{II} which gives the contributions from A_S blocks, B blocks and $A_S - B$ interactions within part II.

2. Weak Segregation Approach for Phase Separation

The composite self term for A type monomer units in part II is J_{AA}^{II} . There are two A_S blocks in the chain which give the first term in the self term J_{AA}^{II} , J_{A_S} multiplied by a factor of two. In addition to the same type of monomer interactions within blocks, there is the same type of monomer interactions between alternating A_S blocks. These interactions results in the second term which is the product of the ‘co-term’ of the first A_S block, propagator terms for the block in between (B) and co-term of the second A type block A_S : $H_{A_S}G_BH_{A_S}$. There is the same interaction contribution in reverse order too which gives a factor of two to the term. Together, the composite self term J_{AA}^{II} gives

$$J_{AA}^{II} = 2J_{A_S} + 2H_{A_S}G_BH_{A_S}. \quad (2.81)$$

The composite self term for B blocks J_{BB}^{II} is determined in same manner. There are two B arranged in the same fashion as A_S in part II. In between two B blocks there is an A_S block, thus the composite self term for B blocks is

$$J_{BB}^{II} = 2J_B + 2H_BG_{A_S}H_B. \quad (2.82)$$

Next, we consider the composite self term that corresponds to $A-B$ interaction in $(BA_S)_n$. Again, starting from B connected to A_L , the interaction between each B and A_S along the chain is represented by their product of co-terms and propagator terms if there are any blocks separating B and A_S blocks. It is demonstrated as:

$$\begin{aligned} J_{AB}^{II} &= H_BH_{A_S} + H_BG_{A_S}G_BH_{A_S} + H_{A_S}H_B + H_{A_S}H_B, \\ &= 3H_{A_S}H_B + H_BG_{A_S}G_BH_{A_S}. \end{aligned} \quad (2.83)$$

The same expression is obtained if you consider each A_S block in turn and the connected B blocks.

Non-interacting structure factor $S_0(Q)$ for $A_L(BA_S)_2$

The non-interacting structure factor for the whole chain is obtained by including A_L in the calculation. This will introduce self interactions in part I, J_{AA}^I and interactions between other two blocks: $A_L - A_S$ and $A_L - B$.

$$J_{AA}^I = J_{A_L}. \quad (2.84)$$

The expression for the non-interacting structure factor in ?? requires the calculation of S_0^{AA} , S_0^{BB} and S_0^{AB} as seen in the previous section. With the addition of A_L , $A-A$ interactions within A_L , A_S blocks and between $A_L - A_S$ blocks will contribute to S_0^{AA} .

$$S_0^{AA} = J_{AA}^I + J_{AA}^{II} + 2H_{A_L}G_BH_{A_S} + 2H_{A_L}G_BG_{A_S}G_BH_{A_S}. \quad (2.85)$$

2. Weak Segregation Approach for Phase Separation

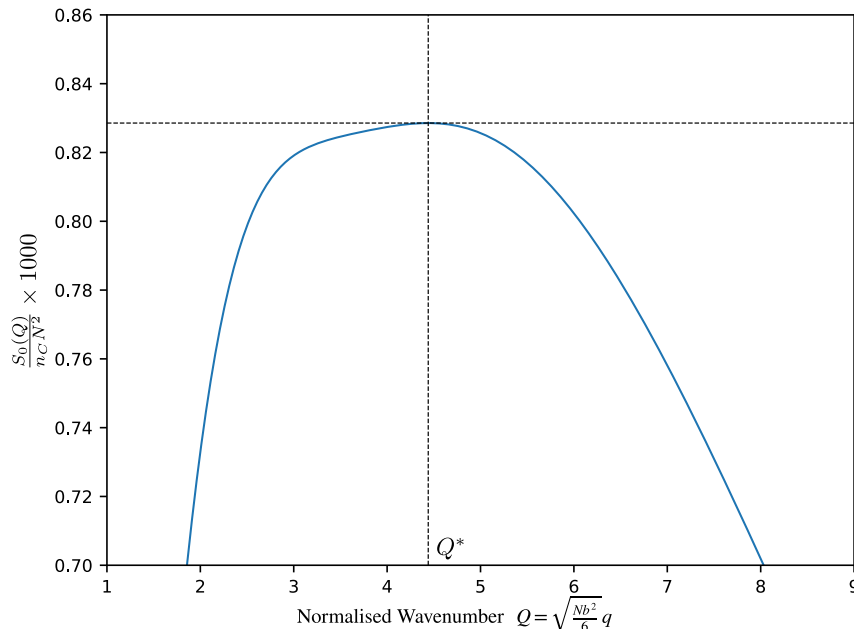


Figure 2.10: The non-interacting structure factor $S_0(Q)$ for $A_L(BA_S)_2$ where length fraction of A_L and A_S are $f_A = 0.8725$ and $\phi_A = 0.6085$ is given. The maximum is indicated by the vertical line at Q^* .

The contribution from B type monomers is J_{BB}^{II} as it is since there are no additional B monomer units in the chain.

$$S_0^{BB} = J_{BB}^{II}. \quad (2.86)$$

Now AB interactions, contributing to S_0^{AB} are formulated in the same way as before starting from A_L and ending in B blocks. This will also have the AB interaction contributed from $(BA_S)_n$. Which gives:

$$S_0^{AB} = J_{AB}^{II} + H_{A_L} H_B + H_{A_L} G_B G_{A_S} H_B \quad (2.87)$$

With S_0^{AA} , S_0^{BB} and S_0^{AB} now obtained, the non-interacting structure factor can be calculated using eq. (2.49) for one chain. The structure factor can be plotted for a range of Q as given in fig. 2.10. It is evident from the plot that the scattering factor is quite broad compared to those in fig. 2.4 and fig. 2.7 for diblock and infinite diblock respectively. There is only one intrinsic length scale in the molecular structure of the diblock and infinite diblock. In $A_L(BA_S)_2$ there are two intrinsic lengthscales indicated in fig. 2.9. There are coupling interactions between different types of blocks with A type monomer units. All this results in a broader peak.

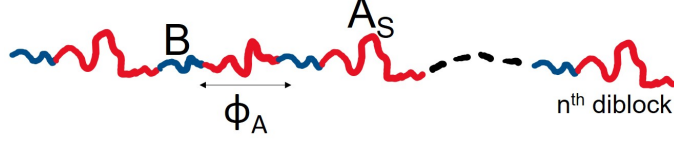


Figure 2.11: Part II of polymer chain $A_L(BA_S)_n$ given in fig. 2.8.

2.3.2 Structure factor for $A_L(BA_S)_n$

The calculation of non-interacting structure can be generalised for any value of n which is the number of BA_S tails in the chain. The structure factors, S_0^{AA} , S_0^{BB} and S_0^{AB} will be in the form of geometric progression. Similar to the case of $n = 2$, the whole chain is split into two parts to determine the non-interacting structure factor for n BA_S diblocks in part II. The composite self term corresponding to $A - A$ interactions in $(BA)_n$ is given as:

$$\begin{aligned}
 J_{AA}^{II} = & nJ_{A_S} + \\
 & ((H_{A_S}H_{A_S}G_B + H_{A_S}H_{A_S}G_BG_{A_S}G_B + \cdots + H_{A_S}H_{A_S}G_B(G_{A_S}G_B)^{n-2}) + \\
 & (2H_{A_S}H_{A_S}G_B + H_{A_S}H_{A_S}G_BG_{A_S}G_B + \cdots + H_{A_S}H_{A_S}G_B(G_{A_S}G_B)^{n-3}) + \\
 & \cdots \\
 & + (H_{A_S}H_{A_S}G_B + H_{A_S}H_{A_S}G_BG_{A_S}G_B + \cdots + H_{A_S}H_{A_S}G_B(G_{A_S}G_B)^{n-2})).
 \end{aligned} \tag{2.88}$$

To simplify this expression $2H_{A_S}^2G_B$ can be factorised out of the second term which results in the following expression involving sums of geometric series.

$$\begin{aligned}
 J_{AA}^{II} = & nJ_{A_S} + 2(H_{A_S})^2G_B (1 + (1 + G_{A_S}G_B) + (1 + G_{A_S}G_B + (G_{A_S}G_B)^2) + \\
 & \cdots + (1 + G_{A_S}G_B + (G_{A_S}G_B)^2 + \cdots + (G_{A_S}G_B)^{n-2})).
 \end{aligned} \tag{2.89}$$

Using the expression for the sum of the geometric progressions, the above expression is further rewritten as

2. Weak Segregation Approach for Phase Separation

$$\begin{aligned}
J_{AA}^{II} &= nJ_{A_S} + \\
& 2(H_{A_S})^2 G_B \left[\frac{(1 - G_{A_S} G_B)}{(1 - G_{A_S} G_B)} + \frac{1 - (G_{A_S} G_B)^2}{(1 - G_{A_S} G_B)} + \dots + \frac{1 - (G_{A_S} G_B)^{n-1}}{(1 - G_{A_S} G_B)} \right] \\
&= nJ_{A_S} + \\
& 2(H_{A_S})^2 G_B \left[\frac{n - 1 - (G_{A_S} G_B + (G_{A_S} G_B)^2 + \dots + (G_{A_S} G_B)^{n-1})}{(1 - G_{A_S} G_B)} \right] \tag{2.90}
\end{aligned}$$

After summing the final sum of the geometric series generalised expression for J_{AA}^{II} for any n is obtained.

$$J_{AA}^{II} = nJ_{A_S} + 2(H_{A_S})^2 G_B \left[\frac{n(1 - G_{A_S} G_B) - (1 - (G_{A_S} G_B)^n)}{(1 - G_{A_S} G_B)^2} \right] \tag{2.91}$$

The composite self term for $B - B$ interaction also has the same form as it was shown for the case of $n = 2$.

$$J_{BB}^{II} = nJ_B + 2(H_B)^2 G_{A_S} \left[\frac{n(1 - G_{A_S} G_B) - (1 - (G_{A_S} G_B)^n)}{(1 - G_{A_S} G_B)^2} \right]. \tag{2.92}$$

The third composite self-term required is J_{AB}^{II} . Counting through $A_S - B$ interactions in the $(BA_S)_n$ tail J_{AB}^{II} will be

$$\begin{aligned}
J_{AB}^{II} &= H_B H_{A_S} + H_{A_S} H_B G_{A_S} G_B + \dots + H_B H_{A_S} (G_{A_S} G_B)^{n-2} + H_B H_{A_S} (G_{A_S} G_B)^{n-1} \\
&+ H_B H_{A_S} + H_{A_S} H_B G_{A_S} G_B + \dots + H_B H_{A_S} (G_{A_S} G_B)^{n-2} + H_{A_S} H_B + \\
&\dots + H_B H_{A_S} + H_B H_{A_S} (G_{A_S} G_B)^{n-2} + \dots + H_{A_S} H_B G_{A_S} G_B + H_{A_S} H_B. \tag{2.93}
\end{aligned}$$

Taking the common factor $H_B H_{A_S}$ out, the expression is rewritten as sums of geometric series. These sums are simplified by a similar process as for J_{AA}^{II} to obtain the generalised condensed expression for J_{AB}^{II} .

2. Weak Segregation Approach for Phase Separation

$$\begin{aligned}
J_{AB}^{II} = & H_{A_S} H_B \left[1 + G_{A_S} G_B + (G_{A_S} G_B)^2 + \cdots + (G_{A_S} G_B)^{n-2} + (G_{A_S} G_B)^{n-1} + \right. \\
& 1 + G_{A_S} G_B + (G_{A_S} G_B)^2 + \cdots + (G_{A_S} G_B)^{n-2} + 1) \quad + \\
& 1 + G_{A_S} G_B + \cdots + (G_{A_S} G_B)^{n-3} + G_{A_S} G_B + 1) \quad + \\
& \cdots + (1 + G_{A_S} G_B + (G_{A_S} G_B)^{n-3} \dots + G_{A_S} G_B + 1) \\
& \left. (1 + (G_{A_S} G_B)^{n-2} \dots \dots + G_{A_S} G_B + 1) \right].
\end{aligned} \tag{2.94}$$

On calculating the sum of two sets of sums of geometric series J_{AB}^{II} is given by

$$\begin{aligned}
J_{AB}^{II} = & H_{A_S} H_B \left[\left(\frac{1 - (G_{A_S} G_B)^n}{1 - G_{A_S} G_B} + \frac{1 - (G_{A_S} G_B)^{n-1}}{1 - G_{A_S} G_B} + \right. \right. \\
& \left. \left. \cdots + \frac{1 - (G_{A_S} G_B)^2}{1 - G_{A_S} G_B} + \frac{1 - (G_{A_S} G_B)}{1 - G_{A_S} G_B} \right) + \right. \\
& \left. \left(\frac{1 - (G_{A_S} G_B)^{n-1}}{1 - G_{A_S} G_B} + \frac{1 - (G_{A_S} G_B)^{n-2}}{1 - G_{A_S} G_B} + \right. \right. \\
& \left. \left. \cdots + \frac{1 - (G_{A_S} G_B)^2}{1 - G_{A_S} G_B} + \frac{1 - (G_{A_S} G_B)}{1 - G_{A_S} G_B} \right) \right]
\end{aligned} \tag{2.95}$$

And so:

$$J_{AB}^{II} = H_{A_S} H_B \left(\frac{(2n+1)(1 - G_{A_S} G_B) - 2 + (G_{A_S} G_B)^n + (G_{A_S} G_B)^{n+1}}{(1 - G_{A_S} G_B)^2} \right). \tag{2.96}$$

Once the composite self terms for the tail $(BA_S)_n$ are determined the total structure factor for n_c chains, $S_0(q)$ is obtained from S_0^{AA} , S_0^{BB} and S_0^{AB} . Following the procedure from $n = 2$ case the contribution to the structure factor from the overall $A - A$ interaction is S_0^{AA} . This will be the sum self term of A_L block, composite self terms of J_{AA}^{II} and interactions between A_L and A_S blocks given by products of co-terms and propagator terms.

$$\begin{aligned}
S_0^{AA} = & n_c \left(J_A^I + J_{AA}^{II} + H_{A_L} H_{A_S} G_B + H_{A_L} H_{A_S} G_B G_{A_S} G_B + \right. \\
& \left. \cdots + H_{A_L} H_{A_S} G_B (G_{A_S} G_B)^{n-1} \right).
\end{aligned} \tag{2.97}$$

2. Weak Segregation Approach for Phase Separation

On simplifying,

$$\begin{aligned} S_0^{AA} &= n_c (J_A^I + J_{AA}^{II} + 2H_{AL}H_{AS}G_B (1 + G_{AS}G_B + \dots + (G_{AS}G_B)^{n-1})) \\ &= n_c \left(J_A^I + J_{AA}^{II} + 2H_{AL}H_{AS}G_B \left(\frac{1 - (G_{AS}G_B)^n}{1 - G_{AS}G_B} \right) \right) \end{aligned} \quad (2.98)$$

Again $B - B$ interaction is all from the tail blocks, so

$$S_0^{BB} = n_c J_{BB}^{II} \quad (2.99)$$

Overall $A - B$ interactions is quantified by S_0^{AB} given by

$$\begin{aligned} S_0^{AB} &= n_c (J_{AB}^{II} + H_{AL}H_B (1 + G_{AS}G_B + \dots + (G_{AS}G_B)^{n-1})) \\ &= n_c \left(J_{AB}^{II} + H_{AL}H_B \left(\frac{1 - (G_{AS}G_B)^n}{1 - G_{AS}G_B} \right) \right) \end{aligned} \quad (2.100)$$

With S_0^{AA} , S_0^{BB} and S_0^{AB} , total non-interacting structure factor $S_0(Q)$ is determined using eq. (2.49).

The non-interacting structure factor for this model is dependent on three parameters: length fraction of long A block f_A , length fraction of small A block ϕ_A and number of BA_S diblocks, n . Varying these parameters we can obtain different polymer chain architectures which can have different non-interacting structure factors. This polymer architecture can have one or more peaks in its structure factor. For each value of $n \in [1, 14]$, we plot resulting $S_0(Q)$ for all values of f_A and ϕ_A varying from 0 to 1. If there are two peaks, they will in general have different heights, with the higher one indicating the wavenumber that will appear first in phase separation. We define the ratio of wavenumbers $Q_r = Q_2/Q_1$, with $Q_1 < Q_2$. The height of the structure factor indicates the dominance of the corresponding wavenumber in phase separation. Hence we are interested in peaks of the same height. Here Q_1 and Q_2 indicate the wavevector corresponding to the emerging lengthscales. The shorter wavelength Q_1 is set by the size of smaller blocks BA_S and the larger wavelength Q_2 corresponds to the overall length of the polymer which increases with n . We are screening over all possible parameters to pick out the region which gives two prominent wavenumbers and hence two lengthscaled phase separations. As happens in other systems with transitions between one and two length scales, the boundary between the regions in parameter space separating one from two length scales are cusp-shaped [20, 83, 110] More detailed discussion on obtained structure factors and suitable composition space is in the following sections.

2.3.3 Results

The non-interacting structure factor of the polymer structure as a function of normalised wave number Q is plotted for all possible values of f_A and ϕ_A , with $1 \leq n \leq 10$. A broad peak is observed in non-interacting structure factor $S_0(Q)$ for $A_L(BA_S)_2$ in fig. 2.10. If block lengths are changed this peak gets broadened and for some specific block lengths even two peaks are observed as seen in fig. 2.12. For a specific value f_A and ϕ_A , the peak gets broadened such that it looks like two peaks of equal height are merged as seen in fig. 2.12 (c). At this point, the structure factor has a single quartic maximum. A schematic representation of the polymer structure that gives the quartic maximum is given in fig. 2.12.(a). It is to be noted that B blocks indicated by blue are extremely small here. As we further vary the block fractions, two peaks are observed for $A_L(BA_S)_2$ as seen in fig. 2.12 (d) and (e). The structure factors where peaks are at wave number ratios $Q_r = 1.2$ and $Q_r = 1.6$ are given in fig. 2.12 (d) and (e) respectively. The tentative polymer structure given in fig. 2.12 (b) gives the structure factor with two peaks given in fig. 2.12 (e) that have wavenumber ratio $Q_r = 1.6$. In the polymer architecture that gives two lengthscale structure factors A type monomers over-weigh in composition. This results in the competing $A - B$ interactions that will give multiple lengthscaled phase separation. As mentioned previously the presence of two peaks in a non-interacting structure factor indicates phase separation in two lengthscales. The vertical lines in fig. 2.12 indicate the wave numbers of phase separation.

Following this example, the non-interacting structure factor $A_L(BA_S)_n$ for any n can be determined. Another example of a linear two-component chain we are presenting is a long polymer chain $A_L(BA_S)_7$. In this model, there are more B - type blocks to contribute towards phase separation.

The non-interacting structure factor for $A_L(BA_S)_7$ for different block fractions are determined in the same manner as for $n = 2$ varying f_A and ϕ_A . Resulting structure factors are given in fig. 2.13. Similar to the previous case, here also a quartic is observed in fig. 2.13 (c). The quartic maximum indicates that there is a divergence from the single-peaked structure factor to the double-peaked structure factor. The schematic polymer structure in fig. 2.13.(a) corresponds to the quartic structure factor. Compared to $n = 2$ case the quantity of B blocks is now comparable with the composition of A_S blocks. Structure factors with two distinct peaks are given in fig. 2.13 (d), (e) and (f), which indicates simultaneous phase separation in two lengthscales. All the scattering functions shown here are for approximately the same peak heights. The ratio of wave numbers at the two peaks given in these plots is in the quasicrystal favourable range (1.5 – 2.1). The schematic diagram of the polymer chain in fig. 2.13.(b) gives the structure factor in fig. 2.13.(f) which has wavenumber ratio $Q_r = 2.1$.

2. Weak Segregation Approach for Phase Separation

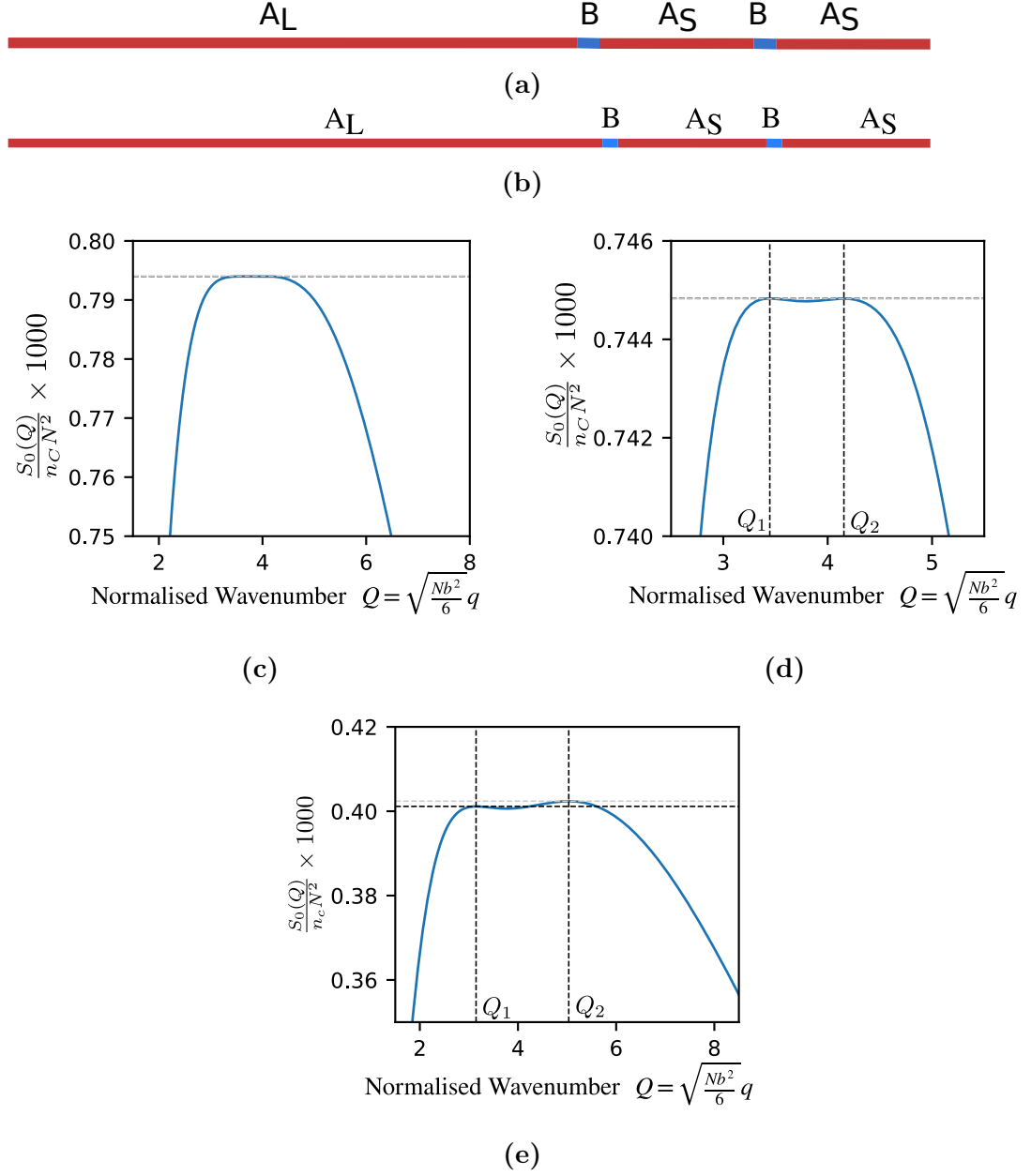


Figure 2.12: Non-interacting structure factor $S_0(Q)$ for different branch lengths for $A_L(BA_S)_2$ is plotted along with a representation of molecule architecture. The non-interacting structure factors are given for (c) $f_A = 0.6185$ and $\phi_A = 0.873$, (d) $f_A = 0.6215$ and $\phi_A = 0.876$ and (e) $f_A = 0.6445$ and $\phi_A = 0.906$. The polymer architecture given in (a) corresponds to (c), that has $Q_r = 1$ and the one in (b) corresponds to (e) with $Q_r = 1.6$ are given

2. Weak Segregation Approach for Phase Separation

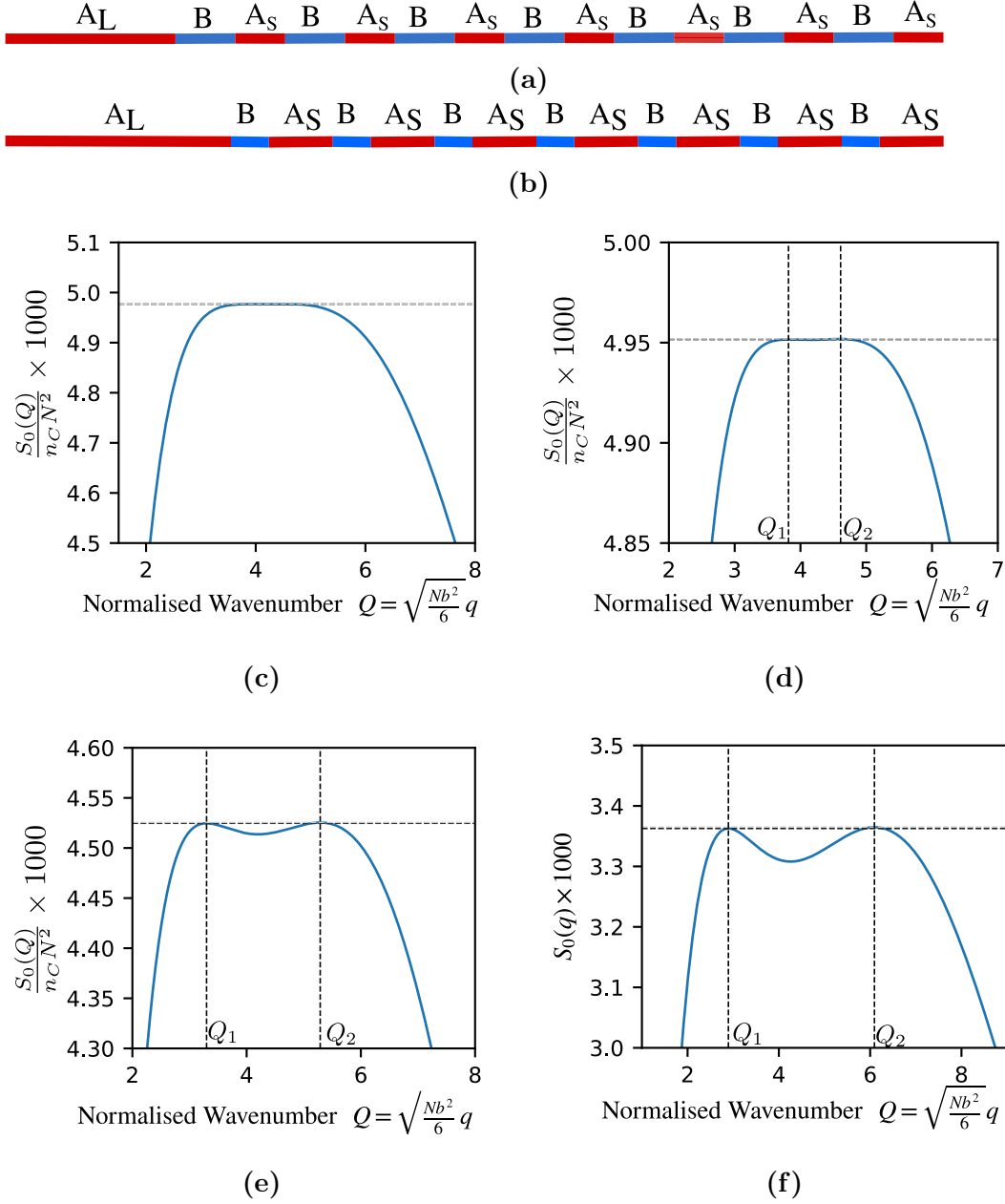


Figure 2.13: Non-interacting structure factor $S_0(Q)$ for different branch lengths for $A_L(BA_S)_7$ is plotted along with polymer structure for $Q_r = 1$ in (a) and $Q_r = 2.1$ in (b). The $S_0(Q)$ for (c) $f_A = 0.181$ and $\phi_A = 0.455$, (d) $f_A = 0.183$ and $\phi_A = 0.460$, (e) $f_A = 0.202$ and $\phi_A = 0.518$ and (f) $f_A = 0.240$ and $\phi_A = 0.628$ are plotted. In here structure (a) corresponds to $S_0(Q)$ in (c) and (b) corresponds to $S_0(Q)$ in (f).

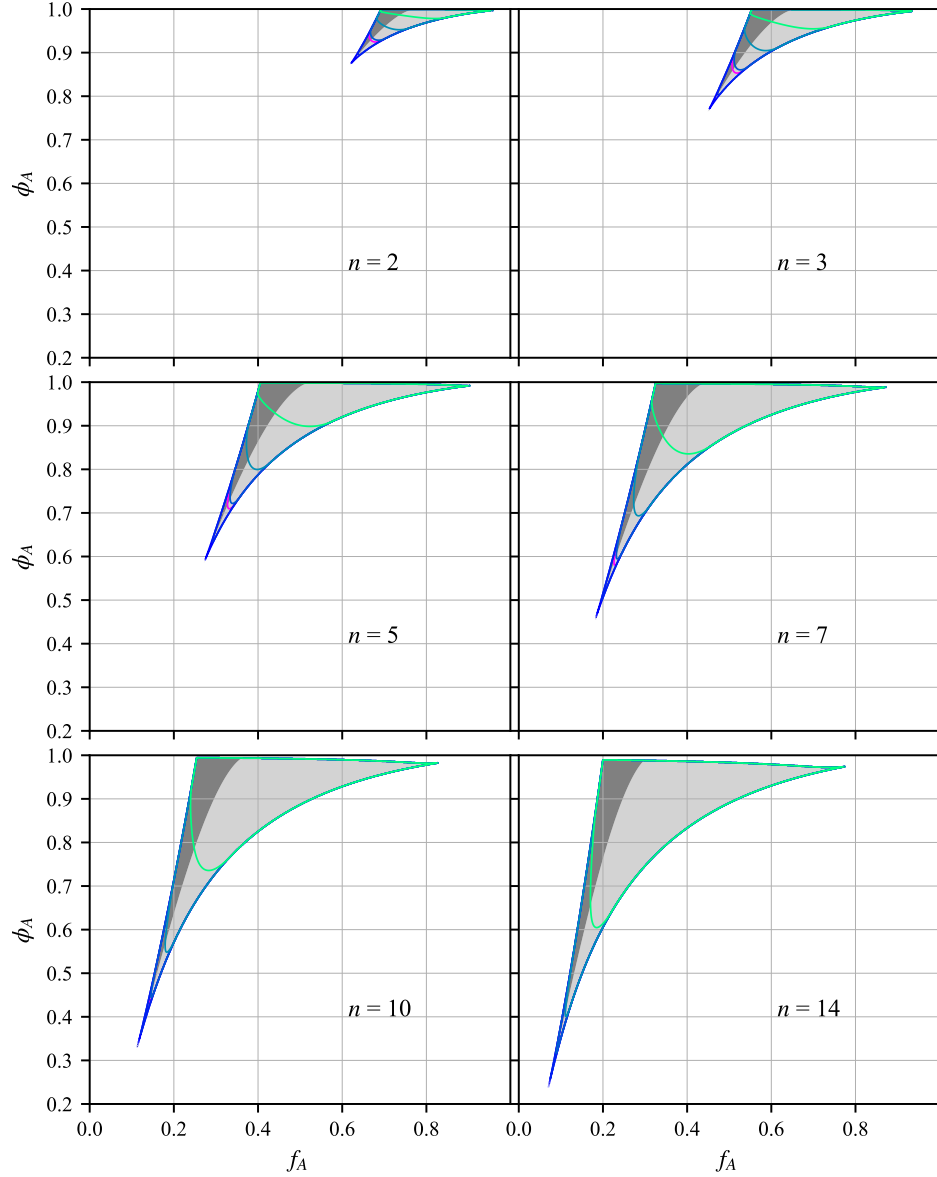


Figure 2.14: Contour plots of block fraction map for $n = 2, 3, 5, 7, 10$ and 14 are given with Q-ratios and height ratios. The dark shaded region is where the smaller wave number has a higher peak and the light shaded region is where the bigger wave number has a higher peak. Coloured lines across the cusp indicate the wavenumber ratios as indicated in the legend on top. Each line indicated wave number ratios $Q_r = 1.2, 1.5, 2.0, 2.5, 3.5$ starting from the cusp where $Q_r = 1$. The line in magenta indicates wave number ratio $Q_r = 1.93$, which corresponds to 12-fold rotational symmetry.

2. Weak Segregation Approach for Phase Separation

From fig. 2.12 and fig. 2.13 it is evident that there is a window of block fractions for which the chain get phase separated in two lengthscales for each choice of n .

In fig. 2.12 and 2.13 the fraction of A blocks (f_A and ϕ_A) are varied for both A_L and $(BS_S)_n$ tail. For smaller values of A_L fractions f_A , A_L block gets comparable to A_S and it leads to phase separation in one lengthscale giving one peak, as in fig. 2.10. When f_A is increased there is enough A type monomers to increase the incompatibility from A_L block to introduce another lengthscale. This is observed in schematic figures in fig. 2.12 (a) and (b) and fig. 2.13 (a) and (b).

In order to screen out all probable parameters that can give two lengthscaled phase separation, we need to check for all synthesis-able values of n . This will give a composition map with feasible monomer compositions f_A and ϕ_A . In fig. 2.12 and 2.13 it is observed that for a specific compositions it has a quartic peak, and that for other compositions the ratio of peak heights can vary. As indicated earlier the strcture factor gives a transition from one lengthscaled phase separation to two lengthscaled phase separation which is often observed in cusps. For a given n from plotting the non-interacting structure factor all valid f_A and ϕ_A , we can map the region which gives two lengthscales. In each structure factor that have two peaks the ratio of larger wavenumber to smaller wavenumber is determined. Simultaneously the height ratios (H_r) are also calculated. The composition maps for each n are created by plotting the region with two lengthscales as shaded. The wavenumber ratios (Q_r) and height ratios H_r are overlaid on this shaded region to indicate the exact value in which they may phase separate.

The polymer structure for $n = 1$, is A_LBA_S and it does not indicate any two lengthscaled phase separation by varying block length fractions. So we are interested in polymer structures starting from $n = 2$. The resulting contour plots for polymer chains with $n = 2, 3, 5, 7, 10$ and 14 are given in fig. 2.14. As expected, there are cusp shapes that separate from the two lengthscaled region and one lengthscaled region. The composition space that has two lengthscales in their structure factor is the shaded region. The white region indicates the compositions that give one lengthscale. In this model, $n = 2$: $A_LBA_SBA_S$ is the smallest polymer chain that have a valid two lengthscaled region. The wave number ratios Q_r are indicated by the coloured lines that are plotted across the shaded region. The wave number ratio varies from 1.2 to 3.5, with one along the cusp being 1. Among the lines indicating wavenumber ratios, the magenta line indicates the ratio $Q_r = 1.93$, which is associated with 12-fold rotational symmetry. This line is present in the composition space for $n = 2, 3, 5$ and 7 evidently giving valid compositions. For $n = 10$ and 14 , the lines for lower wavenumber ratios are closer to the cusp. It is observed that the area of cusps increases as n . The maximum ratio between the two length scales increases as well. This is because the short length scale is set by the size of the BA_S blocks, while the long length scale is set by the overall size of the polymer, which increases

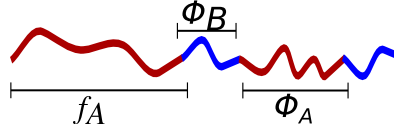


Figure 2.15: Illustration of monodisperse chain $A_L B A_S B$.

with n . When n increases the competing $N\chi_{AB}$ interaction between $A_L - B$ and $A_S - B$ is more prominent. This results in more compositions having monomer fluctuations that can result in two lengthscaled phase separation.

2.3.4 $A_L B A_S B$

In the family of $A_L(BA_S)_n$, the chain architecture with $n = 2$ is the smallest monodisperse linear chain that gives two lengthscale phase separation. This instigates the question of which is the smallest linear chain with only two components that can phase separate in two lengthscale. The architecture $n = 1$, with three blocks, does not have two lengthscales in its phase separation. As the difference between the two structures is just two blocks, the architecture $A_L B A_S B$ which we are considering as $n = 1.5$ is also a valid candidate for two lengthscale phase separation. The structure factor is calculated in a similar manner for $A_L(BA_S)_n$. Since the structure does not quite belong to the $A_L(BA_S)_n$ family the non-interacting structure factor is determined separately using self-terms, co-terms and propagator terms. The number of monomer units in each chain is defined using which normalised wavenumber is also defined. As in the previous case, the length fraction of the block A_L is f_A and that of block A_S is ϕ_A . In accordance with the previous parameterisation of length fractions, block fraction of B , ϕ_B is $1 - \phi_A$. Given the total number of monomer units is N , the number of monomer units in A_L , A_S and B blocks are:

$$\text{Number of monomer units in } A_L, N_{A_L} = f_A N$$

$$\text{Number of monomer units in } A_S, N_{A_S} = (1 - f_A)\phi_A N$$

$$\text{Number of monomer units in } B, N_B = \frac{1}{2}(1 - f_A)(1 - \phi_A)N.$$

2. Weak Segregation Approach for Phase Separation

Given the monomer composition the normalised wave numbers Q_{A_L} , Q_{A_S} and Q_B are determined in terms of Q as seen previously. Here,

$$\begin{aligned} Q_{A_L}^2 &= f_A Q^2, \\ Q_{A_S}^2 &= (1 - f_A) \phi_A Q^2, \\ Q_B^2 &= \frac{1}{2} (1 - f_A) (1 - \phi_A) Q^2. \end{aligned} \tag{2.101}$$

The self term, co-term and propagator term are determined for each block in $A_L B A_S B$. The non interacting structure factors S_0^{AA} , S_0^{BB} and S_0^{AB} corresponding to correlations between $A - A$, $B - B$ and $A - B$ monomers are determined in terms of normalised wave number Q .

$$\begin{aligned} S_0^{AA} &= n_c (J_{A_L} + J_{A_S} + 2H_{A_L} G_B H_{A_S}), \\ S_0^{BB} &= n_c (2J_B + 2H_B G_{A_S} H_B), \\ S_0^{AB} &= n_c (H_{A_L} H_B + H_{A_L} G_B G_{A_S} H_B + 2H_B H_{A_S}). \end{aligned} \tag{2.102}$$

On substituting these in eq. (2.49) the non-interacting structure factor $S_0(Q)$ is determined for all valid monomer compositions of (f_A, ϕ_A) .

For specific values of f_A and ϕ_A , the incompressible structure factor has two peaks at Q_1 and Q_2 . An example is given in fig. 2.16.(a) for $f_A = 0.710$ and $\phi_A = 0.87$ where there are two peaks with the same height. While we vary the monomer compositions we find a cusped region given in fig. 2.16.(b) with where two lengthscaled phase separation occurs. Lines across the cusp region indicate wavenumber ratios in the range 1.5 – 3.5. The ratio corresponding to 12- fold rotational symmetry, 1.93 is indicated by the magenta line across the cusp. In comparison with the cusp region of $A_L(BA_S)_2$, the cusp corresponding to $A_L B A_S B$ has a larger area. In the latter, the presence of B monomers are more prominent and it increases the $A_S - B$ and $A_L - B$ incompatibilities. So there are more compositions that will give two lengthscaled phase separation.

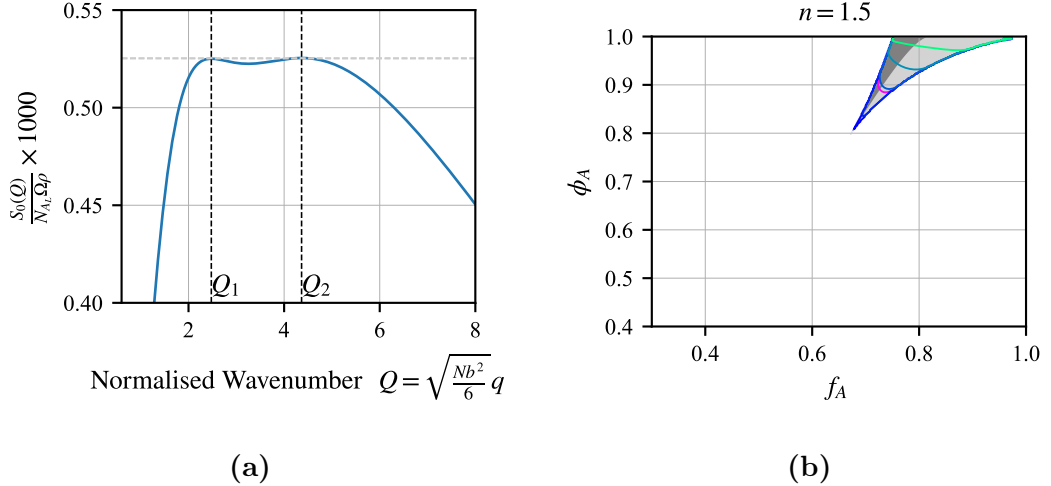


Figure 2.16: The non-interacting structure factor S_0 against normalised wave number is shown in (a). Two peaks are observed when monomer fractions are $f_A = 0.71$ and $\phi_A = 0.87$. The region in (f_A, ϕ_A) space where two lengths are observed is given in (b). The region is cusp shaped and lines across the shaded region indicate the wave number ratios starting at the cusp from 1. The magenta line indicates a wavenumber ratio 1.93.

2.3.5 Discussion

From the above results, it is evident that the linear chain family of $A_L(BA_S)_n$ can phase separate in two lengthscales when $(BA_S)_n$ tail has $n > 1$. The result obtained is consistent with our assumption that if we design a block copolymer which can induce the incompatibilities desired, then there will be two lengthscaled phase separation.

The two lengthscale scale phase separation in linear molecules that have two intrinsic lengthscales in their polymer architecture has been reported by Nap et al. [83, 109, 110]. They invested in polymer architecture similar to $A_L(BA_S)_n$ restricting monomer compositions such that the length of smaller A blocks and B blocks are equal. With that restriction, they obtain cusp shaped region in their composition space [110].

Our work builds on this observation that polymer chain structures with two or more intrinsic lengthscales can phase separate in two lengthscales. In addition, we have no restrictions in our composition space. The smallest polymer chain in the $A_L(BA_S)_n$ family that has two lengthscale phase separation is $A_L(BA_S)_2$ with 5 blocks. We are also presenting $A_LBA_S B$ which is the smallest possible linear chain with two components that can phase separate in two lengthscales. These

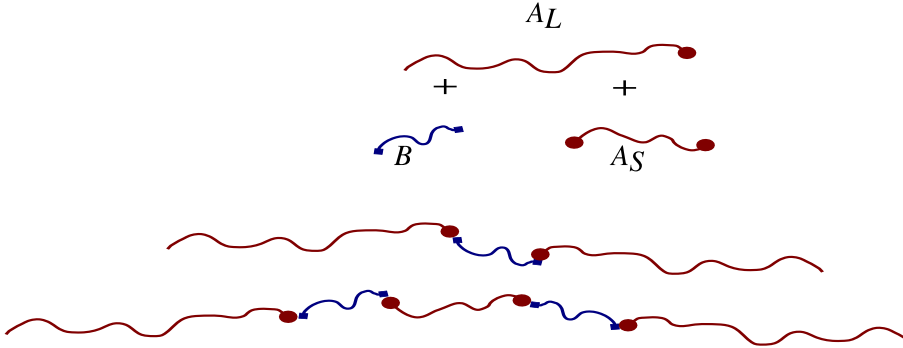


Figure 2.17: Schematic representation of the polydisperse model. Starting with a mixture of A_L , A_S and B (top), the final mixture (bottom) will contain polymer chains of architecture A_LBA_L , $A_LBA_SBA_L$, etc.

polymer chains A_LBA_SB and $A_L(BA_S)_2$ are easier to synthesise and have phase separation at the length scale ratio 1.93 that favours twelve-fold quasicrystals. Double periodic lamellar structures and gyroids are reported in similar polymer models using SCFT [109, 175]. There are many other compositions suggested in our work but their synthesis can be a bit more complex.

As mentioned in the introduction the presence of two lengthscales in certain ratios favours towards stable quasicrystalline structure. The cusps reported in this work give a wide range of two lengthscale ratios (1.6 – 2.6). Soft matter quasicrystals [57, 172] mostly show 12-fold dodecagonal symmetry with a wave number ratio $Q_r = 1.932$. We are reporting many suitable compositions (f_A, ϕ_A) along the magenta lines in our cusps in fig. 2.14 that can phase separate accordingly. In addition, 8-fold and 18-fold symmetries are found in soft matter quasicrystals [25, 45, 47]. Wavenumber ratios corresponding to these rotational symmetries are also available in our composition space.

2.4 Two component linear chains with random assembly

Polymer chains discussed until now are all monodispersed. In a realistic block copolymer synthesis, it is not possible to synthesise all the blocks in a chain to be of the same length. Polydispersity is unavoidable. So we are proposing another model for the two-component block copolymer where the block copolymer system exhibits polydispersity by considering a mixture of chains with random lengths. This is a theoretical equivalent to the polycondensation process where the reaction starts with an exact amount of reactants and a mixture of linear chains is formed

2. Weak Segregation Approach for Phase Separation

from them at the end of the reaction. Theoretical equivalence of the process is achieved using the Markov chain process to a mixture of blocks proposed by Read [127].

At the start, the mixture consists of a fixed amount of individual blocks: long A type block A_L , short A type block A_S and short B type block B as given in fig. 2.17. These blocks have reactive ends which drive the polycondensation process. The reactive ends indicated by $\text{---}\bullet$, are α reactive ends of A type blocks and those at the end of B type blocks $\text{---}\blacksquare$ are β reactive ends in fig. 2.17. During polymerisation, α reactive end connects with the β reactive end. We are discussing the case where at the end of the polycondensation there will not be any free-reacting ends left. At the end of polycondensation, assuming a complete reaction and stoichiometry, the mixture will contain only chains that have A_L blocks at both ends and different lengths of $BA_S \dots A_S B$ blocks in between, for example, $A_L B A_L$, $A_L B A_S B A_L$, etc., as illustrated in Figure 2.17. Given there are n_{blocks} of blocks in the melt, there are $n_{blocks}\beta_{A_L}$ α ends from A_L , $2n_{blocks}\beta_{A_S}$ α blocks from A_S and $2n_{blocks}\beta_B$ β blocks from B blocks.

If total number of blocks are n_{blocks} , then block fraction of A_L is β_{A_L} . Similarly the block fraction of A_S and B blocks are β_{A_S} and β_B respectively. All these block fractions should add up to 1.

$$\beta_{A_L} + \beta_{A_S} + \beta_B = 1. \quad (2.103)$$

The blocks A_{A_L} , A_S and B have N_{A_L} , N_{A_S} and N_B monomer units in them. The monomer units in A_S and B are quantified with respect to those in A_L as follows.

$$N_{A_S} = \nu_{A_S} N_{A_L}, \quad (2.104)$$

$$N_B = \nu_B N_{A_L}.$$

Upon complete polycondensation number of β ends are equal to the number of α ends, so

$$2n_{blocks}\beta_B = n_{blocks}\beta_{A_L} + 2n_{blocks}\beta_{A_S}. \quad (2.105)$$

Eliminating β_B from eq. (2.103) and eq. (2.105), we get the condition for complete reaction:

$$3\beta_{A_L} + 4\beta_{A_S} = 2. \quad (2.106)$$

In this model, monomer compositions are defined in terms of the block fraction of A_L : β_{A_L} and monomer fractions ν_{A_S} and ν_B . Given the total number of monomer units involved in the process is $N = \Omega\rho$ is then,

$$N = \Omega\rho = n_{blocks}(\beta_{A_L} N_{A_L} + \beta_{A_S} N_{A_S} + \beta_B N_B). \quad (2.107)$$

2. Weak Segregation Approach for Phase Separation

In terms β_{A_L} and monomer fractions ν_{A_S} and ν_B the above expression is:

$$\Omega\rho = n_{blocks}N_{A_L}(\beta_{A_L} + \nu_{A_S}\beta_{A_S} + \nu_B\beta_B). \quad (2.108)$$

Rearranging,

$$n_{blocks}N_{A_L} = \frac{\Omega\rho}{\beta_{A_L} + \nu_{A_S}\beta_{A_S} + \nu_B\beta_B}. \quad (2.109)$$

The monomer units in different blocks are quantified in terms of N_{A_L} , the number of monomer units in A_L block in this model. With this parameterisation, we can do RPA in this model to calculate its structure factor.

2.4.1 RPA for linear chains with random assembly

The structure factor is determined for the normalised wave vector Q using in this model using the above parameterisation. Unlike the monodisperse melt, in this model, there are different architectures of polymer chains in this melt, which makes the structure factor calculation a bit more complex. In the case of random reaction in addition to the architectural component from self terms, co-terms and propagator terms [126], the probability of the architecture formed is determined using the Markov chain method. The normalised wave vector for each block γ , $Q_\gamma = \sqrt{\frac{N_\gamma b^2}{6}}q$, for a given wave vector \mathbf{q} . The normalised wave vectors for the blocks: A_L , A_S and B are:

$$\begin{aligned} Q_{A_L} &= \sqrt{\frac{N_{A_L} b^2}{6}}q \\ Q_{A_S} &= \sqrt{\frac{N_{A_S} b^2}{6}}q = \sqrt{\frac{\nu_{A_S} N_{A_L} b^2}{6}}q = \sqrt{\nu_{A_S}}Q_{A_L} \\ Q_B &= \sqrt{\frac{N_B b^2}{6}}q = \sqrt{\frac{\nu_B N_{A_L} b^2}{6}}q = \sqrt{\nu_B}Q_{A_L}. \end{aligned} \quad (2.110)$$

Accounting for the random reaction that can occur, the probability matrix for a chain of architecture $A_L - B - A_S - B \cdots - B - A_L$ is defined. As none of the same blocks follows itself or blocks of the same type, the diagonal elements of the matrix will be 0. The probability that a B block will be followed by A_L block is $P_{A_L B} = \frac{\beta_{A_L}}{2\beta_B}$. The probability for a B block will be followed by A_S block is $P_{A_S B} = \frac{\beta_{A_S}}{\beta_B}$. The probability of a B block following A_S or A_L is 1. Thus the

2. Weak Segregation Approach for Phase Separation

probability matrix P is:

$$P = \begin{bmatrix} 0 & 0 & P_{A_L B} \\ 0 & 0 & P_{A_S B} \\ 0 & 1 & 0 \end{bmatrix}. \quad (2.111)$$

In this model, the chain structure from one block to another in the same chain is traced by the propagators. Here the propagators for each block type are given in a diagonal matrix.

$$G = \begin{bmatrix} G_{A_L} & 0 & 0 \\ 0 & G_{A_S} & 0 \\ 0 & 0 & G_B \end{bmatrix}. \quad (2.112)$$

For m blocks to follow in the chain, the propagator should be given by $P \cdot (G \cdot P)^{m-1}$ [126]. The sum in m is in the form of a geometry progression similar to what is observed in the calculation of definite linear chains. The contribution of propagators to the structure factor from the random mixture formed is determined by the product of both matrices: $G \cdot P$.

$$G \cdot P = \begin{bmatrix} 0 & 0 & P_{A_L B} \\ 0 & 0 & P_{A_S B} \\ 0 & G_B & 0 \end{bmatrix}. \quad (2.113)$$

Now the self-terms and co-terms are defined for the blocks as J_{A_L} , J_{A_S} , J_B , H_{A_L} , H_{A_S} and H_B .

The non-interacting structure factor from $A_L - A_L$ interactions $S_{A_L A_L}$ is determined. The correlation between A_L blocks will be at different ends if you go from left to right in the chain as the reactive end is in the opposite ends for both chains. This leads to choosing the second element to be 1 in the column matrix.

$$S_{A_L A_L} = n_{blocks} \beta_{A_L} \left(J_{A_L} + H_{A_L}^2 \begin{bmatrix} 1 & 0 & 0 \end{bmatrix} P \cdot (1 - G \cdot P)^{-1} \begin{bmatrix} 0 \\ 1 \\ 0 \end{bmatrix} \right). \quad (2.114)$$

2. Weak Segregation Approach for Phase Separation

The propagator matrix $P \cdot (1 - G \cdot P)^{-1}$ will be there for all correlations between the blocks analogous to the geometric sum term in the monodisperse model.

$$P \cdot (1 - G \cdot P)^{-1} = \begin{bmatrix} 1 & \frac{G_B P_{A_L B}}{1 - P_{A_S B} G_{A_S} G_B} & \frac{P_{A_L B}}{1 - P_{A_S B} G_{A_S} G_B} \\ 0 & \frac{1}{1 - P_{A_S} G_B} & \frac{P_{A_S B}}{1 - P_{A_S} G_{A_S} G_B} \\ 0 & \frac{1}{1 - P_{A_S} G_B} & \frac{G_{A_S} P_{A_S B}}{1 - P_{A_S} G_B} \end{bmatrix}. \quad (2.115)$$

The total number of monomers could be factorised from each term of in $S_{A_L A_L}$. On matrix multiplication the expression for $S_{A_L A_L}$ is obtained.

$$\begin{aligned} S_{A_L A_L} &= n_{blocks} \beta_{A_L} N_{A_L}^2 \left(j_{A_L} + h_{A_L}^2 \begin{bmatrix} 1 & 0 & 0 \end{bmatrix} P \cdot (1 - G \cdot P)^{-1} \begin{bmatrix} 0 \\ 1 \\ 0 \end{bmatrix} \right), \\ &= n_{blocks} \beta_{A_L} N_{A_L}^2 \left(j_{A_L} + h_{A_L}^2 \frac{P_{A_L B} G_B}{1 - P_{A_S B} G_{A_S} G_B} \right), \\ &= N_{A_L} \Omega \rho \frac{\beta_{A_L}}{\beta_{A_L} + \nu_{A_S} \beta_{A_S} + \nu_B \beta_B} \left(j_{A_L} + h_{A_L}^2 \frac{P_{A_L B} G_B}{1 - P_{A_S B} G_{A_S} G_B} \right). \end{aligned} \quad (2.116)$$

Likewise, the structure factor contribution from all block interactions is determined. Consider the correlation of A_L block with A_S blocks which occur in both directions. The structure factor corresponding to this $S_{A_L A_S}$ is

$$\begin{aligned} S_{A_L A_S} &= n_{blocks} \beta_{A_L} H_{A_L} H_{A_S} \begin{bmatrix} 0 & 1 & 0 \end{bmatrix} P \cdot (1 - G \cdot P)^{-1} \begin{bmatrix} 0 \\ 1 \\ 0 \end{bmatrix}, \\ &\equiv 2n_{blocks} \beta_{A_S} H_{A_L} H_{A_S} \begin{bmatrix} 1 & 0 & 0 \end{bmatrix} P \cdot (1 - G \cdot P)^{-1} \begin{bmatrix} 0 \\ 1 \\ 0 \end{bmatrix}. \end{aligned} \quad (2.117)$$

2. Weak Segregation Approach for Phase Separation

These expressions will be simplified to $S_{A_L A_S}$ as

$$\begin{aligned} S_{A_L A_S} &= n_{blocks} \beta_{A_L} N_{A_L} N_{A_S} h_{A_L} h_{A_S} \frac{P_{A_S B} G_B}{1 - P_{A_S B} G_{A_S} G_B}, \\ &= N_{A_L} \Omega \rho \frac{\nu_{A_S} \beta_{A_L}}{\beta_{A_L} + \nu_{A_S} \beta_{A_S} + \nu_B \beta_B} h_{A_L} h_{A_S} \frac{P_{A_S B} G_B}{1 - P_{A_S B} G_{A_S} G_B}. \end{aligned} \quad (2.118)$$

In the same manner, expressions for contribution to structure factor from interactions between A_L blocks and B blocks: $S_{A_L B}$, A_S blocks and A_S blocks: $S_{A_S A_S}$, A_S blocks and B blocks: $S_{A_S B}$ and B blocks and B blocks: $S_{B B}$ are determined. The rest of the structure factors are listed below.

$$\begin{aligned} S_{A_L B} &= N_{A_L} \Omega \rho \frac{\nu_B \beta_{A_L}}{\beta_{A_L} + \nu_{A_S} \beta_{A_S} + \nu_B \beta_B} h_{A_L} h_B \frac{1}{1 - P_{A_S B} G_{A_S} G_B}, \\ S_{A_S A_S} &= N_{A_L} \Omega \rho \frac{\nu_{A_S}^2 \beta_{A_S}}{\beta_{A_L} + \nu_{A_S} \beta_{A_S} + \nu_B \beta_B} \left(j_{A_S} + 2h_{A_S}^2 \frac{P_{A_S B} G_B}{1 - P_{A_S B} G_{A_S} G_B} \right), \\ S_{A_S B} &= N_{A_L} \Omega \rho \frac{\nu_{A_S} \nu_B \beta_{A_S}}{\beta_{A_L} + \nu_{A_S} \beta_{A_S} + \nu_B \beta_B} 2h_{A_S} h_B \frac{1}{1 - P_{A_S B} G_{A_S} G_B}, \\ S_{B B} &= N_{A_L} \Omega \rho \frac{\nu_B^2 \beta_B}{\beta_{A_L} + \nu_{A_S} \beta_{A_S} + \nu_B \beta_B} \left(j_B + 2h_B^2 \frac{P_{A_S B} G_{A_S}}{1 - P_{A_S B} G_{A_S} G_B} \right). \end{aligned} \quad (2.119)$$

These non-interacting structure factors collectively obtained from above constitutes S_0^{AA} , S_0^{BB} and S_0^{AB} .

$$\begin{aligned} S_0^{AA} &= S_{A_L A_L} + 2S_{A_L A_S} + S_{A_S A_S}, \\ S_0^{BB} &= S_{B B}, \\ S_0^{AB} &= S_{A_L B} + S_{A_S B}. \end{aligned} \quad (2.120)$$

2. Weak Segregation Approach for Phase Separation

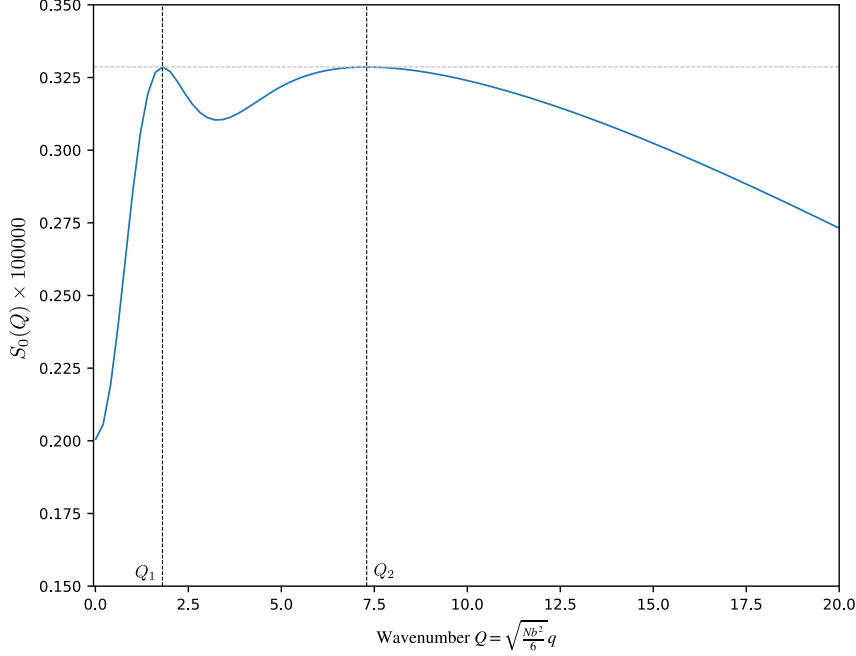


Figure 2.18: The non-interacting structure factor for the random assembly linear model is given. This plot is obtained when $\beta_{A_L} = 0.4$, $\nu_{A_S} = 0.265$ and $\nu = 0.002$. Two maxima are observed at wavenumber Q_2 and Q_1 as indicated by vertical lines.

The non-interacting structure factor $S_0(Q)$ for this polymer model with two components is then determined using the expression in eq. (2.49). The expression is rewritten here:

$$S_0 = \frac{S_0^{AA}S_0^{BB} - (S_0^{AB})^2}{S_0^{AA} + S_0^{BB} + 2S_0^{AB}} \quad (2.121)$$

The structure factor for a given range of Q is plotted for a chosen value of ν_{A_S} , ν_B and β_L . Similar to the monodisperse case, for a given β_{A_L} specific values of ν_{A_S} and ν_B the structure factor gives two maxima. These two maxima appear simultaneously at wave numbers Q_1 and Q_2 where $Q_2 > Q_1$. There will be a window of two maxima in this case too. An example of the structure factor is given in fig. 2.18.

2. Weak Segregation Approach for Phase Separation

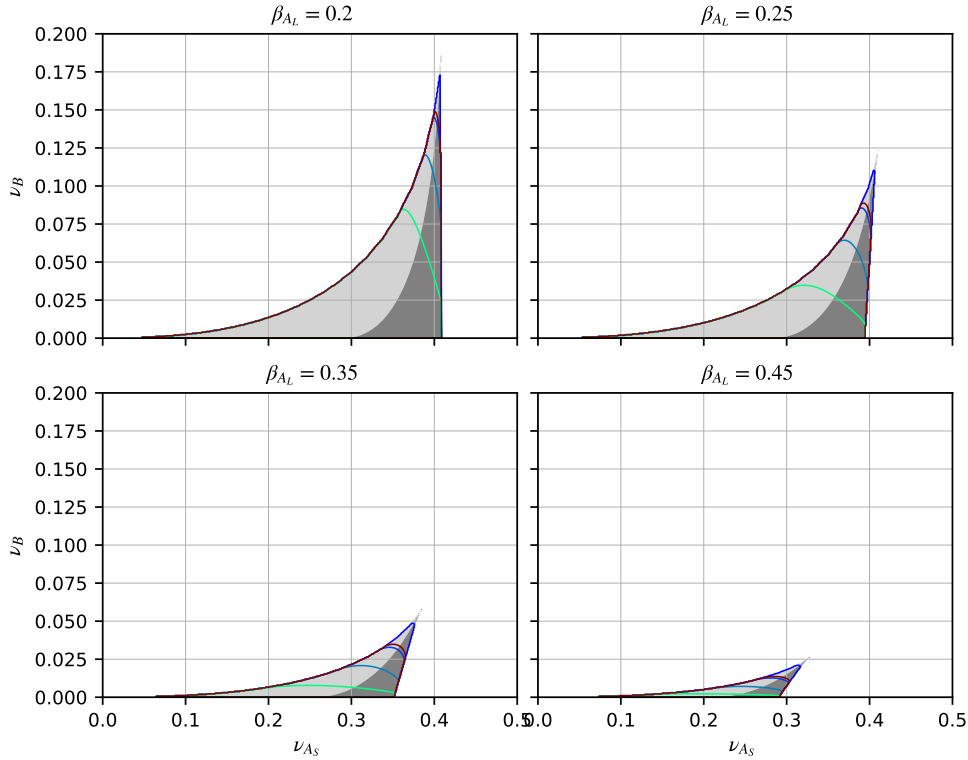


Figure 2.19: Regions of single maxima (white) and two maxima (shaded) as a function of ν_{A_S} and ν_B with $\beta_{A_L} = 0.2, 0.25, 0.35$ and 0.45 , for the two-component linear chain with random assembly. In the shaded regions, the darker (resp. lighter) areas are where the maximum with the smaller (resp. larger) wavenumber is higher. The solid contour lines across the cusp indicate wavenumber ratios from $Q_r = 1.5$ to $Q_r = 3.5$ from the cusp to the broader region. The maroon line indicates where the wavenumber ratio is 1.93.

As we mentioned earlier, the block composition is measured in terms of the composition of A_L block in the melt. Thus the block fraction of A_L , β_{A_L} is equivalent to n from the monodisperse model. Varying the monomer composition of A_S and B , the compositions that give two peaks are categorised and plotted. Analogous to varying n , the block fraction of A_L is varied and we get different composition maps as shown in fig. 2.19.

For fixed β_{A_L} , the regions of (ν_{A_S}, ν_B) where there are two maxima in the structure factor are cusp-shaped (see fig. 2.19 for $\beta_{A_L} = 0.2, 0.25, 0.35$ and 0.45). The lines across the shaded part of the cusps indicate the ratio between the

wavenumbers where the two peaks occur. In this parameterisation, cusps are seen at the bottom of the composition map, unlike the monodisperse model, where parameters are in length fractions. When β_{A_L} is 0.2 (with $\beta_{A_S} = 0.35$ and $\beta_B = 0.45$), there are more A_S and B blocks than A_L block so that the polymer will form longer chains, and the region for two length scale phase separation is considerably larger than with $\beta_{A_L} = 0.45$ ($\beta_{A_S} = 0.1625$ and $\beta_B = 0.3875$). In both these cases, the length scale ratio corresponding to 12-fold symmetry is present in the composition space. The maroon line indicates it.

2.4.2 Discussion

In this model, we offer a better synthesis-friendly block copolymer architecture that can phase separate in two lengthscales with desired wavenumber ratios. An example of block composition that can give two lengthscale phase separation is 20% A_L , 35% A_S and 45% B , where the lengths of the three chains are in a ratio $A_L : A_S : B = 1 : 0.39 : 0.14$.

In this model, the regions indicating two lengthscale phase separation in fig. 2.19 have a lower composition of B blocks than the A_L blocks. This agrees with the results from the monodisperse case, where the B block lengths were comparably smaller. In the structure factor in fig. 2.18, the second peak is broader than the first peak. This indicates that the intensity of diffraction is sharper from the structure, which results in a shorter length scale.

Map $A_L(BA_S)_n$ in (ν_{A_S}, ν_B) space

A direct mapping between the monodisperse fixed n and polydisperse random assembly versions of the two-component linear chain models is not possible because of the range of chain lengths possible in the second case and because of the difference in architecture. But to comparison the monodisperse model $A_L(BA_S)_n$, can be plotted in (ν_{A_S}, ν_B) space. If there are N monomer units in a monodisperse polymer chain, then the number of monomer units in A_L and A_S will be:

$$\begin{aligned} N_{A_L} &= f_A N, \\ N_{A_S} &= \frac{(1 - f_A)}{n} \phi_A N, \\ N_B &= \frac{(1 - f_A)}{n} (1 - \phi_A) N. \end{aligned} \tag{2.122}$$

2. Weak Segregation Approach for Phase Separation

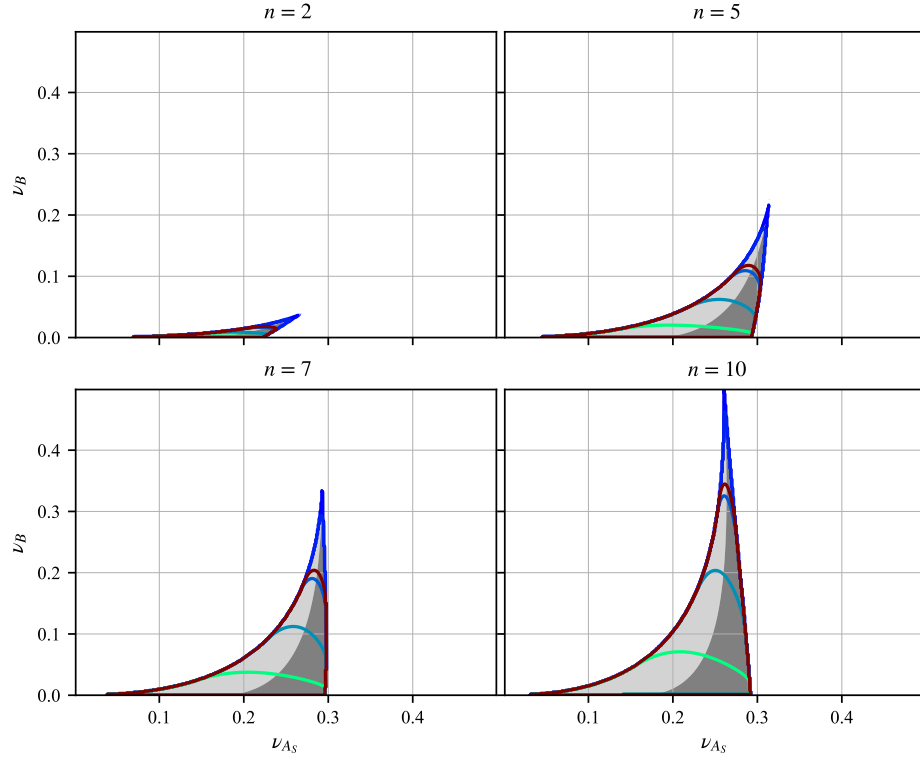


Figure 2.20: We plot the results for the monodisperse versions with $n = 2, 5, 7$ and $n = 10$ in terms of equivalent values of ν_{A_S} and ν_B

So the monomer fractions of the blocks with respect to A_L , ν_{A_S} and ν_B are then $\frac{N_{A_S}}{N_{A_L}}$ and $\frac{N_B}{N_{A_L}}$ respectively.

$$\begin{aligned}\nu_{A_S} &= \frac{(1 - f_A)\phi_A}{nf_A}, \\ \nu_B &= \frac{(1 - f_A)(1 - \phi_A)}{nf_A}.\end{aligned}\tag{2.123}$$

After rearranging, the length fraction of A blocks (f_A, ϕ_A) are expressed relative to monomer fractions (ν_{A_S}, ν_B, n). Thus the composition space with two length-scales is determined for $A_L(BA_S)_n$ model in terms of (ν_{A_S}, ν_B, n). The region is again cusps at the bottom of the composition space as given in fig. 2.20. As n is equivalent to β_{A_L} , the cusps are found for the monodisperse model at the bottom

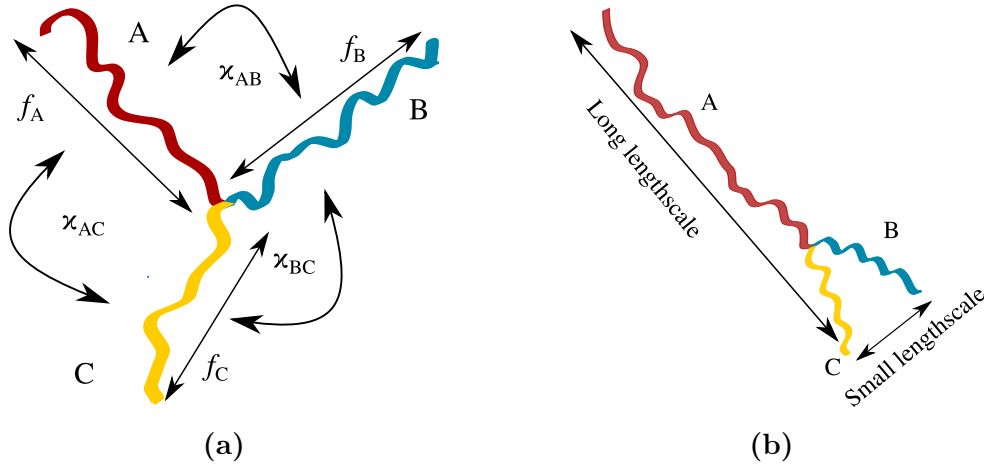


Figure 2.21: Schematic representation ABC star terpolymer is given in (a). Interaction parameters between different branches are also shown. Different length-scales generated during phase separation for a molecule with a longer A block are shown in (b).

of the composition space. As n increases, the block fraction of A_L decreases. The cusp area increases with n .

2.5 ABC star terpolymer

Another polymer model subjected to the same analysis in this chapter is the 3-component ABC star terpolymer. The ABC star terpolymer introduced in Chapter 1 has three blocks connected at a junction. This architecture opens up options for a wide variety of morphologies such as hexagonal, square, triangular, cylindrical, and different Archimedean tilings [50]. Moreover, dodecagonal QCs were discovered in three component star polymer and homopolymer blend [57]. In this section, we use RPA to detect if ABC star terpolymers can be designed in a similar manner as the linear chains such that there is phase separation in two length-scales simultaneously. For an ABC star block copolymer there are six determining parameters, three branch lengths and three interaction parameters between the branches $A - B$, $B - C$ and $A - C$. It is possible to see how phase separation could be simultaneously attained at two length-scales by considering a star in which A block is substantially longer than B or C blocks. There can be two possible microphase separation in this system. One between A and BC where incompatibility between A and $B + C$ combined drives phase separation at a long lengthscale (length of molecule). The elastic energy penalised for such

phase separation is low and the phase separation is due to the coupling of χ_{AC} and χ_{AB} . A second phase separation is between B and C , due to the incompatibility between B and C blocks. Here the elastic energy penalty is higher, so a large χ_{BC} is required to drive the separation. Different degrees of incompatibilities in the structure promise a variety of morphologies. Applying a similar linear theory as in the two component system we will look for a two length scale phase separation region in the parameter space for a 3 component star block copolymer.

2.5.1 RPA for ABC star

Non-interacting structure factor for the ABC star terpolymer can be calculated using Read's method [126]. This calculation is more straightforward compared to the previous long chains with two components. Similar to what was done for the two component case, a normalised wave number Q_γ is defined for each block. Given that the polymer chain has N monomer units in total and the branch fraction for A , B and C are f_A , f_B and f_C respectively, where $f_A + f_B + f_C = 1$. The number of monomer units in each block is then

$$\begin{aligned} \text{Number of monomers in } A \text{ block: } N_A &= f_A N, \\ \text{Number of monomers in } B \text{ block: } N_B &= f_B N, \\ \text{Number of monomers in } C \text{ block: } N_C &= f_C N = (1 - f_A - f_B)N. \end{aligned} \tag{2.124}$$

Normalised wavenumbers for each block are then,

$$\begin{aligned} Q_A^2 &= f_A Q^2, \\ Q_B^2 &= f_B Q^2, \\ Q_C^2 &= f_C Q^2 = (1 - f_A - f_B)Q^2. \end{aligned} \tag{2.125}$$

where $Q^2 = \frac{Nb^2}{6}q^2$. As discussed in section 2.1.3 phase separation in ABC star system is indicated by the behaviour of $W(Q)$ in eq. (2.68). This two-by-two matrix $W(Q)$ contains inverse of structure factor terms ($\Gamma_{AA}, \dots, \Gamma_{CC}$) and interaction terms $\chi_{AB}, \chi_{AB}, \chi_{AB}$ in it. So the problem is reduced to determining the non-interacting structure factors $S_0^{AA}, S_0^{BB}, S_0^{CC}, S_0^{AB}, S_0^{AC}$ and S_0^{BC} . Noting that $N_A = f_A N$ and $nN^2 = \Omega\rho N$ we write

$$S_0^{AA} = \Omega\rho N f_A^2 j_A = N_A^2 j_A. \tag{2.126}$$

Similarly, all other structure factors are also parameterised. The self-terms and co-terms for the polymer system are defined: j_A, j_B, j_C, h_A, h_B and h_C for three

2. Weak Segregation Approach for Phase Separation

branches A , B and C . The self-terms associated with each block constitute the non-interacting structure factor of each block:

$$\begin{aligned} S_0^{AA} &= n_c J_A = N_A^2 j_A, \\ S_0^{BB} &= n_c J_B = N_B^2 j_B, \\ S_0^{CC} &= n_c J_C = N_C^2 j_C. \end{aligned} \tag{2.127}$$

The correlation between different branches results in three non-interacting structure factors with co-terms: S_0^{AB} , S_0^{BC} and S_0^{AC} .

$$\begin{aligned} S_0^{AB} &= n_c H_A H_B = N_A N_B h_A h_B, \\ S_0^{BC} &= n_c H_B H_C = N_B N_C h_B h_C, \\ S_0^{AC} &= n_c H_A H_C = N_A N_C h_A h_C. \end{aligned} \tag{2.128}$$

Here, for a given value of f_A , f_B , χ_{AB} , χ_{BC} and χ_{AC} , the matrix $W_{\mathbf{q}}$ is expressed as a function of normalised wavenumber Q : $W(Q)$. With $W(Q)$ defined, the quadratic form in eq. (2.68) is positive definite when eigenvalues of $W(Q)$ are both positive. Phase separation occurs when the smallest eigenvalue λ of $W(Q)$ changes from positive to negative. The phase separation lengthscale is determined from the minimum of the smallest eigenvalue where for wave number Q^* , $\lambda(Q^*) = 0$. If the phase separation was in a single lengthscale, at the corresponding wavenumber $Q = Q^*$, the smallest eigenvalue will have,

$$\lambda(Q^*) = 0; \quad \frac{d\lambda}{dq} \Big|_{Q=Q^*} = 0. \tag{2.129}$$

In this model, we are again looking for phase separation at two wavenumbers, one long and another short. To achieve this there must be two wave numbers Q_1 and Q_2 at which the lowest eigenvalue $\lambda_1(Q)$ of $W(Q)$, changes sign simultaneously as explained earlier. That is,

$$\begin{aligned} \lambda(Q_1) &= 0; & \lambda(Q_2) &= 0; \\ \frac{d\lambda(Q)}{dQ} \Big|_{Q_1} &= 0; & \frac{d\lambda(Q)}{dQ} \Big|_{Q_2} &= 0. \end{aligned} \tag{2.130}$$

2. Weak Segregation Approach for Phase Separation

For fixed architectural parameters of a polymer chain, if there exist two length-scales at phase separation the above equations will be satisfied for Q_1 and Q_2 . For this model, there are too many parameters to calculate the eigenvalue for a range of these parameters. Instead, by solving the above equation for the architectural parameters, we get the composition and $N\chi$ s that will give two lengthscales. For ABC star terpolymer, the variable space is quite complex with six parameters. But given that $f_C = 1 - f_A - f_B$, we can reduce then into five parameters: f_A , f_B , $N\chi_{AB}$, $N\chi_{BC}$ and $N\chi_{AC}$. We consider the case where the A branch is longer. In this case, interactions between A and C and A and B are comparable. For such a chain the branch lengths of B and C are comparable. Thus we let

$$\begin{aligned}\frac{f_B}{f_C} &= \mu, \\ \frac{\chi_{AC}}{\chi_{AB}} &= \xi.\end{aligned}\tag{2.131}$$

This will help to further reduce the number of parameters. Now block fractions of branch C , f_C and B , f_B are given as

$$\begin{aligned}f_C &= \frac{1 - f_A}{1 + \mu}, \\ f_B &= \mu \frac{1 - f_A}{1 + \mu}.\end{aligned}\tag{2.132}$$

Thus variables to analyse this model are now reduced to f_A , $N\chi_{AB}$ and $N\chi_{BC}$ for a range of values of μ and ξ . Even then, determining eigenvalues for a range of wave numbers is not straightforward. The parameters μ and ν can control the composition and interaction strength. For a fixed value of ξ and μ , the set of equations in section 2.5.1 are solved for Q_1 , Q_2 , f_A , $N\chi_{AB}$ and $N\chi_{BC}$. We are looking for two minima simultaneously at Q_1 and Q_2 , where $Q_2 > Q_1$ where $Q_r = \frac{Q_2}{Q_1}$ is a quasicrystal friendly ratio. By fixing the values of $Q_r = [1.5, 2.2]$, we are further reducing the parameters that are required to determine the polymer architecture to four: Q_1 , f_A , $N\chi_{AB}$ and $N\chi_{BC}$. We are plotting eigenvalues $\lambda_1(Q)$ and $\lambda_2(Q)$ for thus obtained given polymer parameters where $\lambda_1 < \lambda_2$. To simplify the model further to start the composition space exploration, we take $\mu = 1$ and $\xi = 1$, and determine the smallest eigenvalue as a function of Q , constraining $Q_1 = Q_2$. Later this value is taken as the initial condition of the numerical procedure we followed in the exploration.

2.5.2 Results

For this model, we are first looking at a special case, a symmetric ABC star terpolymer, which has the same lengths for all three branches and their interaction

2. Weak Segregation Approach for Phase Separation

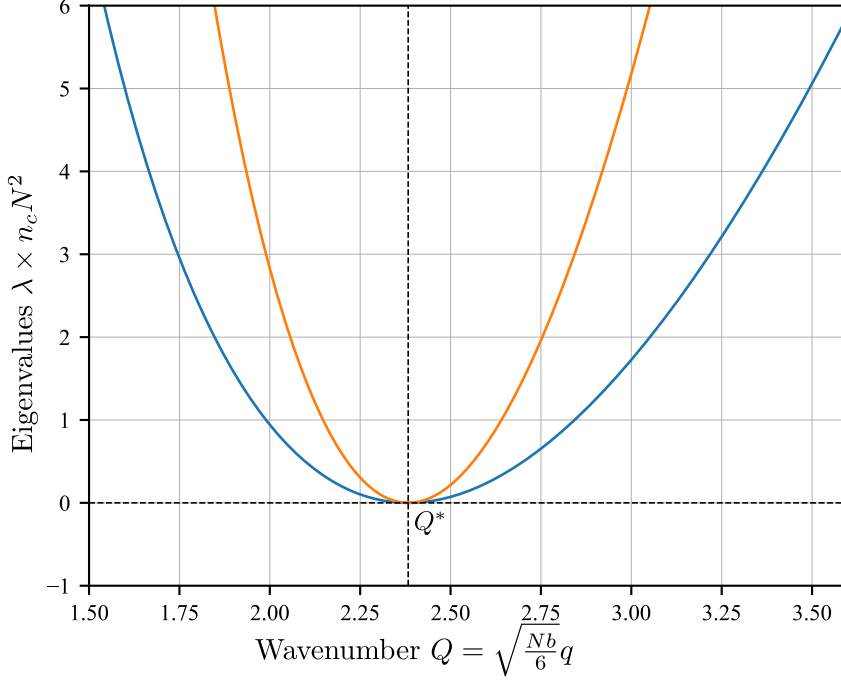


Figure 2.22: Eigenvalues λ_1 (blue) and λ_2 (orange) are plotted as function of Q for symmetric ABC star with same branch length, $f_A = f_B = f_C = 1/3$ and interaction parameters $N\chi_{AB} = N\chi_{BC} = N\chi_{AC} = 23.61$. The wave number ratio $Q_r = 1$ in this case

in pairs is also the same. This is when $\mu = 1$ and $\xi = 1$. With these parameters, we look for the cusp equivalent point where the $Q_r = 1$. The equations in section 2.5.1 are solved with these constraints. The eigenvalues hence plotted have one minimum at $Q = Q^*$ as given in fig. 2.22. The minima of both eigenvalues coincide at $Q = Q^*$. The smallest eigenvalue has a quartic minimum at $Q = Q^*$ ($\lambda_1 \propto (Q - Q^*)^4$), similar to composition corresponding to $Q_r = 1$ in two-component models which is the tip of the cusps in fig. 2.14.

Now retaining $\mu = 1$ and $\xi = 1$ and using $Q_r = 1$ as the initial parameters we explore the eigenvalue behaviour when $Q_r > 1$. For each value of Q_r we solve the equations in section 2.5.1 for f_A , $N\chi_{AB}$ and $N\chi_{BC}$ at some Q_1 (with $Q_2 = Q_r Q_1$). The eigenvalue variation with Q for $Q_r = 1.6$ and $Q_r = 2.1$ are given in fig. 2.23.(a) and (b) respectively. There are two minima in the smallest eigenvalue (blue line) at Q_1 and Q_2 . Two minima indicate two simultaneous phase separation for the given composition in two lengthscales.

2. Weak Segregation Approach for Phase Separation

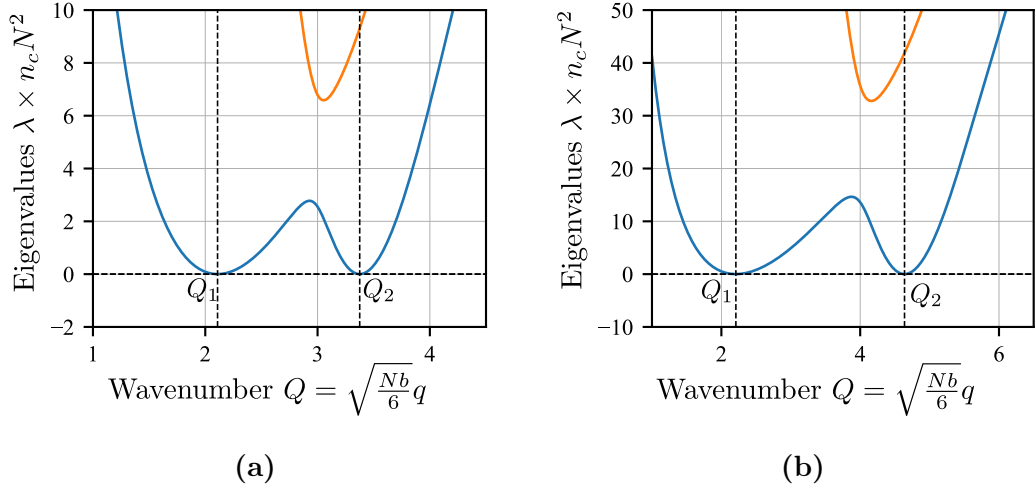


Figure 2.23: Eigenvalue variation for $Q_r = 1.6$ is given in (a) and $Q_r = 2.1$ is given in (b). Both plots are for the case where $\mu = 1$ and $\xi = 1$. The lowest eigenvalue λ_1 is given in blue and the other eigenvalue λ_2 is in orange. In fig.(a) the eigenvalue is plotted for ABC star with $f_A = 0.67$, $N\chi_{AB} = 39.3$ and $N\chi_{BC} = 95.1$ and fig.(b) is for ABC star with $f_A = 0.82$, $N\chi_{AB} = 117$ and $N\chi_{BC} = 339.2$.

In the plots in fig. 2.23, we demonstrate that it is possible to obtain phase separation at two lengthscales given the right value of block lengths and interaction parameters. The plots in fig. 2.22 and 2.23 are for the case where B and C have same branch length, $\mu = 1$ and $A - B$ and $A - C$ interactions are same $\xi = 1$ for two values of Q_r . We can vary Q_r , μ and ξ to obtain the monomer compositions and interactions that will give two lengthscales.

For some ξ and Q_r , if we vary μ , we will obtain the compositions with a prominent A block that will give two lengthscale phase separation. If we try to plot thus obtained compositions in a composition space one will obtain one of the teal lines given in fig. 2.24. The composition space for an ABC star terpolymer is an equilateral triangle given in fig. 2.24.(a). Here all possible values of (f_A, f_B, f_C) are available to vary. The labels A , B and C in the triangle represent the corner where the compositions are maximum: $(1, 0, 0)$, $(0, 1, 0)$ and $(0, 0, 1)$ respectively. The line connecting A to the centre of the triangle $(\frac{1}{3}, \frac{1}{3}, \frac{1}{3})$, is where $\mu = 1$ with $f_B = f_C$.

For a symmetric ABC star terpolymer with $\xi = 1$, the contour lines that will give two lengthscale phase separations are given in fig. 2.24. For $Q_r = 1.2$ you obtain the outer most line in fig. 2.24.(a) and (b). Both plots are the same fig. 2.24.(b) is a focused version of the corner with larger composition of A . When

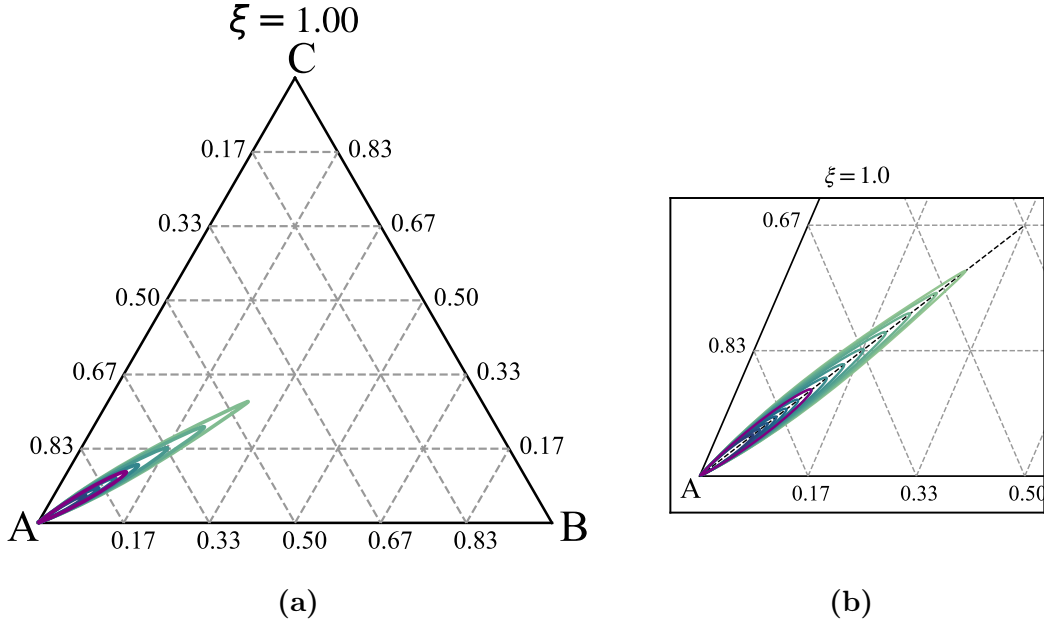


Figure 2.24: Block fractions for ABC star architecture that can give two length-scale phase separation are given in a triangular composition plot (ternary phase space) given in (a). The green contour lines give the block fractions for which the eigenvalues have two minima. Wave number ratio, Q_r varies from 1.2 near the centre to 2.5 near A in steps of 0.2 in (a). The lines are symmetric with respect to the dotted line in (b) indicating $\mu = 1$, where Q_r is varied in steps of 0.1. The purple contour is $Q_r = 1.93$.

we increase the value of Q_r , one will obtain the lines on the inside if you vary μ . For the sake of clarity the lines in fig. 2.24.(a) represent Q_r ratios starting from 1.2 with a step size 0.2 up to 2.5. In the fig. 2.24.(b), there are more lines as the step size is 0.1. The purple contour line indicates where $Q_r = 1.93$. The contour lines for the symmetric interaction $\xi = 1$ ($N_{\chi_{AB}} = N_{\chi_{AC}}$) is found to be mirror symmetric with the line $\mu = 1$. On varying ξ , more composition spaces can be obtained in a similar manner. When ξ is varied the interaction strength between $A-B$ and $A-C$ is no more equal. There will be an affinity between either $A-B$ or $A-C$, which can contribute towards phase separation. We varied the values of ξ from 0.7 to 1.3 and obtained contour lines in the composition spaces given in fig. 2.25. It is observed that when $\xi < 1$, that is when $N_{\chi_{AC}}$ is smaller than $N_{\chi_{AB}}$ the contour lines tilt upwards. This is where the composition of C is more which indicates that A is more compatible with more C during phase separation. The contour lines tilt downwards towards B when $\xi > 1$. Here A is compatible with

B. The tilt is proportional to the increase or decrease of ξ . In all composition spaces, the contour lines are well spaced for the lower value of Q_r and they appear crowded as Q_r is increased. It is to be noted that desirable wavenumber ratios for stable quasicrystals are present in the observed contour regions. The purple line in all these composition spaces indicates compositions that can give phase separation with a wavenumber ratio of 1.93, which corresponds to 12-fold rotational symmetry.

2.5.3 Discussion

From the results, there exist certain compositions of f_A , f_B and f_C branch lengths where two lengthscales phase separation is observed. The linear theory of *RPA* is used to identify two lengthscales regimes for a *ABC* star terpolymer. To our knowledge, this is the first presentation of phase separation with two length scales in the *ABC* star terpolymer system. The phase separation study in weak segregation limit [43] and *RPA* [23] for *ABC* terpolymer were attempted previously. There is no mention of two lengthscaled phase separation in these two works.

The curves obtained for the model with equal *AB* and *AC* interactions have a mirror symmetry with the line $f_A = f_B$. This indicates that the morphologies will obey this mirror symmetry in the phase space for this block copolymer. When $\xi > 1$, we have a down tilt in the contour lines indicating polymer chains with a longer *B* block are preferred when the incompatibility between *AC* is large. Likewise, when $\xi < 1$, the tilt is towards *C*, preferring longer *C* chains. For the first case, the branch length order is $f_A > f_B > f_C$; for the latter, it is $f_A > f_C > f_B$. Similar analysis can be done for the other *ABC* star models: terpolymer with long *B*, by controlling χ_{AB} and χ_{BC} and terpolymer with long *C* controlled by χ_{AC} and χ_{BC} .

The obtained results support that it is possible to design *ABC* star terpolymers by tuning their lengths and interactions to produce two lengthscales phase separation. Most phase separation studies on *ABC* star terpolymers, [50, 101, 159] id done using *SCFT* as mentioned in chapter 1. These methods are computationally heavy and need an initial parameter screening process depending on the morphology seeking. We are providing a substantial window of compositions and interaction strengths for *ABC* star terpolymer with a lower segregation limit. In fig. 2.24 and 2.25 the region with $1.6 < Q_r < 2.1$ occupy more compositions compared to the two component models. These Q_r values are already seen in stable soft matter quasicrystals, hence we can expect to see quasicrystalline morphologies within these compositions.

The exploration of block fraction maps is limited by the choice of ξ and μ . For specific values the matrix $W(Q)$ becomes singular. Also, along the corner of the triangle, one branch will be long and others will be small compared to the long chain. At these compositions star polymers behave similarly to diblocks.

When the segregation strength is lower there is a fair chance that there won't be phase separation. More detailed analysis of the stability and morphologies of the terpolymer melt at these compositions can be done using WST.

2.6 Conclusion

In this chapter, two lengthscale theory from pattern formation is successfully combined with *RPA* for polymers to predict polymer chains that can self-assemble into morphologies with more than one lengthscales. We have investigated the length scales that emerge at the point of phase separation in two classes of block copolymer models: two component linear chains and three component terpolymers. In both cases, we find that as well as having a single length scale at phase separation, it is possible to design the polymers so that two length scales emerge. The transition from one to two length scales occurs at a point (a cusp) in the parameter space when the length scale ratio is one. Beyond this cusp, the length scale ratio can be made much larger than one. The lengthscale ratios obtained here complement the rotational symmetries observed in quasicrystal systems. We have predicted compositions that can phase separate in lengthscales corresponding to 12-fold rotational symmetry in both block copolymer classes and sub-classes ($A_L(BAS_S)_n$, random block model and *ABC* star terpolymer). This rotational symmetry is often associated with square-triangle based dodecagonal quasicrystals that are observed in soft matter systems.

We have provided the initial screening of parameters in this chapter. To continue the study of morphologies we need to consider the interaction strength ($N\chi$) to decide on the methodology with which we proceed. The composition space defined in this work using linear theory can be adapted using SCFT or MC to study the morphologies. In principle we are providing a generalised technique that will give initial parameter space for any block copolymer depending on the morphologies one is looking for. Our work provides this information and so should provide useful starting parameter values with two-length scale phase separation, which should be a good place to start a search for quasicrystals or their approximants, experimentally or using more sophisticated theoretical methods.

2. Weak Segregation Approach for Phase Separation

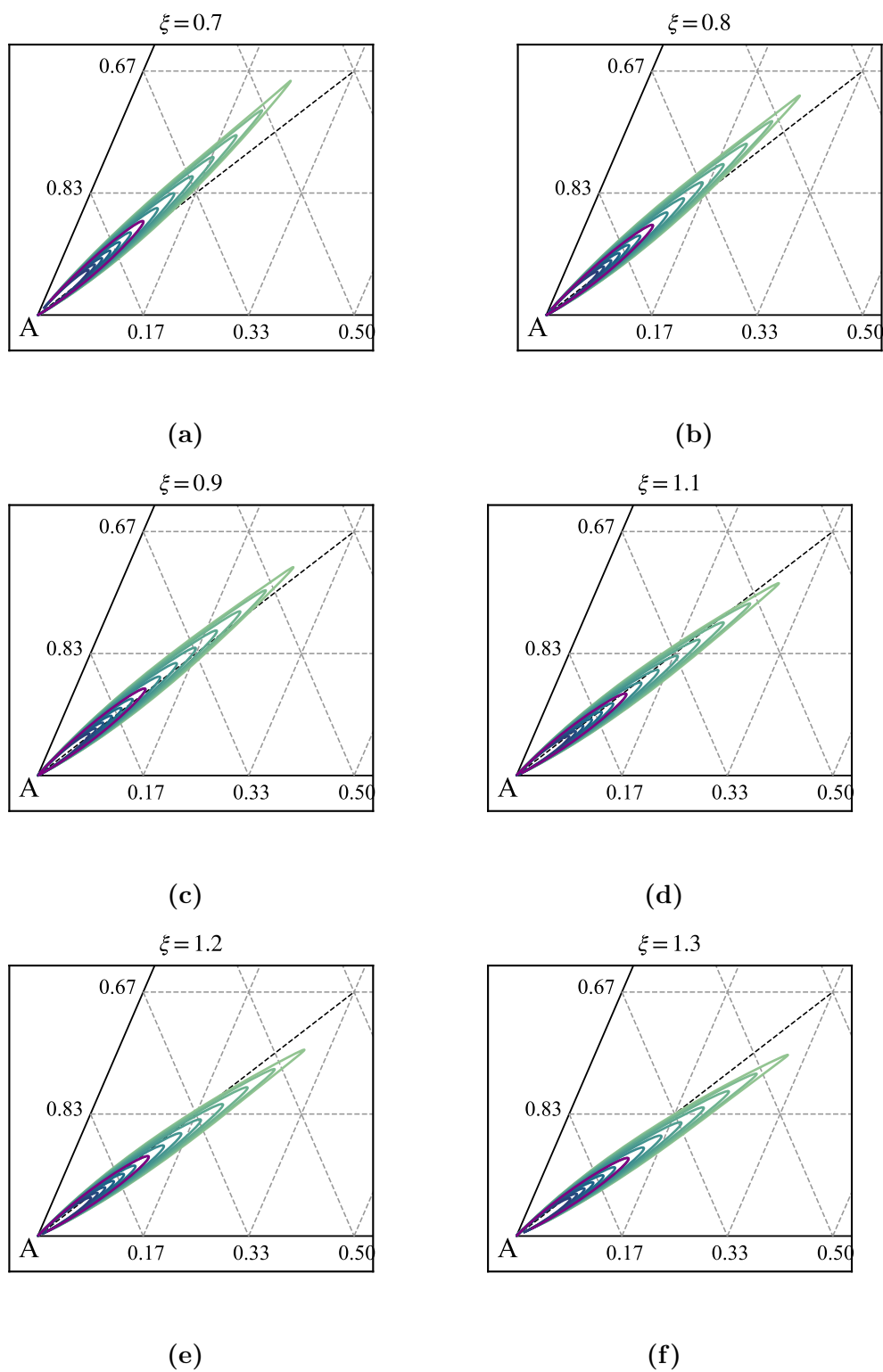


Figure 2.25: Composition space for different ξ values are given. For cases where $\xi < 1$, (a)-(c), there is an upper tilt with respect to the $\mu = 1$ line. When $\xi > 1$, there lines are tilted downwards as given in (d)-(f).

2. Weak Segregation Approach for Phase Separation

Chapter 3

Formulation of Strong Segregation Theory for ABC star terpolymer

In this chapter, we present an alternative theoretical approach towards describing phase separation in block copolymers. In the limit of strongly phase-separated domains with well defined interfaces, the patterns formed resemble "tiled" patterns. In their work on morphologies of ABC stars, Hayashida et al. [57] reports phase separated structures arranged in aperiodic tiling of squares and triangles. The phase separated structure in [57] exhibits 12 fold dodecagonal symmetry which is a feature of quasicrystals. As aperiodic tilings, (specifically square triangle aperiodic tilings [71]) often appear in soft matter quasicrystals (as discussed in Chapter 1), this suggested a route towards the investigation of quasicrystalline patterns in block copolymer phase separation. Among available polymer phase separation theories, the Strong Segregation Theory (SST) facilitates the theoretical framework for this concept. The SST was developed by Semenov [138] where polymer chains are strongly stretched across the interfaces. This stretching along with the strong incompatibility between the monomers results in microphase separation of monomers into domains, resulting in tiling-like morphologies in 2D. This chapter will give a review of the strong segregation approach developed by Olmsted and Milner [117] for diblocks depending on the geometry of the morphologies. In the latter part of the chapter, we will discuss implementing a similar approach for ABC star terpolymer.

Semenov developed the phase separation theory for block copolymer with high monomer incompatibility in diblocks[138]. By incompatibility, we are referring to interactions between different monomer types that is quantified by $N\chi$ as referred in chapter 2. The basis of strong segregation theory is that when stretching free energy and interfacial free energy of a system of block copolymers balances, the resulting phase separated domain is a stable structure. The work resulted

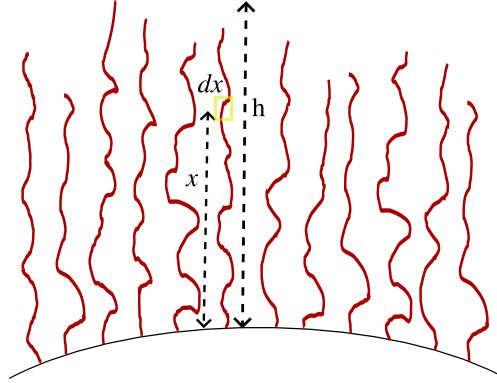


Figure 3.1: Schematic representation of chains stretching out from an interface. Here h is the length of the phase separated domain and x is the distance from the interface to a section of chain dx .

in a phase space that complemented the phase space from weak segregation approach [87]. This was later verified using a unified formulation of Self-Consistent Field Theory (SCFT) [97].

The *SST* formulation was extended by Olmsted et al. [117] to incorporate different geometrical features of the domains, which we are revisiting in detail in the next section. The majority of the chapter will discuss how this formulation was adapted to include different geometries for ABC star morphologies.

3.1 Stretching free energy for a brush

In order to determine the stretching energy of the polymer chains in a phase separated block copolymer, the chains are taken as brushes grafted to the interfaces. The stretching free energy is evaluated following the methodology developed by Ball et al. [15]. In a polymer melt in the absence of any solvent, the length of the chains is proportional to the volume of the melt. Stretching of a subsection of the chain of length Δx will result in a change in the volume of the melt, Δv . The stretching energy consumed here is Δf_{str_m} :

$$\Delta f_{str_m} = \frac{3}{2} \frac{v}{b^2} \left(\frac{\Delta x}{\Delta v} \right)^2 k_B T, \quad (3.1)$$

where b and v are the Kuhn length and volume of the chain, respectively. The subscript m indicated the monomer type. Taking the chain as continuous, the stretching free energy f_{str_m} of the entire chain, forming a domain of volume V in

3. Formulation of Strong Segregation Theory for ABC star terpolymer

terms of $k_B T$ is:

$$f_{str_m} = \int_0^V dv \frac{3v}{2b^2} \left(\frac{dx}{dv} \right)^2. \quad (3.2)$$

Given it is an incompressible melt where the entire volume is filled with monomer units, the volume $v(x)$ of the domain is related to the number of monomer units $n(x)$ in the melt at height x as,

$$n(x)v = v(x). \quad (3.3)$$

Thus,

$$dn = \frac{dv}{v_m}. \quad (3.4)$$

Rewriting the stretching energy due to chain extension in terms of the number of monomer units,

$$f_{str_m} = \int_0^N dn \frac{3}{2b^2} \left(\frac{dx}{dn} \right)^2. \quad (3.5)$$

In addition to the stretching from the chain, work is required to insert a section δv into the polymer melt at height $x(n)$. This work is the chemical potential $\mu(x(n))$ required for inserting a single monomer unit at height $x(n)$ multiplied by the number of monomers inserted. Thus the total energy F is a combination of the elastic energy due to the chain stretch and the work due to chain interactions.

$$F = \int_0^N dn \left(\frac{3}{2b^2} \left(\frac{dx}{dn} \right)^2 + \mu(x(n)) \right). \quad (3.6)$$

We now find the optimal path for a chain $x(n)$, which starts at the interface $x = 0$ and ends at some height $x = X$, that lies within the brush of height h , i.e. $0 < X < h$, which is a variational problem. That is to find the optimal path of the chain that minimises the free energy F . Applying the least action, the action for the stretching energy $J(F)$ from a fluctuation $\delta x(n)$ in the chain is given by,

$$\begin{aligned} J(F) &= F + \delta F, \\ &= \int_0^N dn \left(\frac{3}{2b^2} \left[\left(\frac{dx}{dn} \right)^2 + \frac{\partial x}{\partial n} \frac{\partial}{\partial n} \delta x \right] + \mu(x(n)) + \delta x \frac{d\mu}{dx} \right). \end{aligned} \quad (3.7)$$

Taking the small change in the length δx outside, we get the minimum variation in the length using the Euler-Lagrange (E-L) equation. The path of the chain satisfies the E-L equation for minimum stretching free energy.

$$\frac{3}{b^2} \frac{d^2 x}{dn^2} = \frac{d\mu}{dx}. \quad (3.8)$$

3. Formulation of Strong Segregation Theory for ABC star terpolymer

The above expression is analogous to a particle subjected to Newtonian motion. The path of the chain from x to interface is equivalent to a particle-free falling from rest with a potential: $-\mu(x)$. The chain has a free end at $x(0) = X$ and it reaches the interface at $x(N)$ through N monomer units in that chain. The boundary conditions are then

$$x(0) = X, \quad (3.9)$$

$$x(N) = 0, \quad (3.10)$$

$$\left. \frac{dx}{dn} \right|_0 = 0. \quad (3.11)$$

Now we try to solve for $x(n)$ and μ at optimal free energy. Assuming that there are free ends at all distances from the interface, the chemical potential $\mu(x)$ is a quadratic function of x [154]. So

$$\frac{d\mu}{dx} = -Ax. \quad (3.12)$$

where A is a constant. Using eq. (3.8), the expression is rewritten as

$$\frac{3}{b^2} \frac{d^2x}{dn^2} = -Ax. \quad (3.13)$$

A general solution that satisfies all the boundary conditions for the above ODE is

$$x = X \cos \frac{\pi n}{2N}. \quad (3.14)$$

Substituting x to eq. (3.13) will give expression for the constant A .

$$A = \frac{3\pi^2}{4N^2b^2}. \quad (3.15)$$

The differential equation in eq. (3.12) is rewritten by substituting for A as

$$\frac{d\mu}{dx} = -\frac{3\pi^2}{4N^2b^2}x. \quad (3.16)$$

This is now solvable by the variable separable method to find the chemical potential μ at a given height x . On the free end, the potential μ is zero. Solving the equation eq. (3.16) we get the contribution of the chemical potential of the chains $\mu(x)$ at height x .

$$\int_h^x \mu d\mu = -\frac{3\pi^2}{4N^2b^2} \int_h^x x dx, \quad (3.17)$$

$$\mu(x) = \frac{3\pi^2}{8N^2b^2} (h^2 - x^2).$$

3. Formulation of Strong Segregation Theory for ABC star terpolymer

Using the expressions for x and $\mu(x)$, the free energy for a chain at a height X is obtained from eq. (3.6). Thus the free energy F is

$$F = \int_0^N \left(\frac{3}{2b^2} \left(\frac{X\pi}{2N} \right)^2 \sin^2 \left(\frac{\pi n}{2N} \right) + \frac{3\pi^2}{8N^2b^2} \left(h^2 - X^2 \cos^2 \left(\frac{\pi n}{2N} \right) \right) \right) dn. \quad (3.18)$$

On rearranging the above expression the sines and cosines can be brought together.

$$F = \int_0^N \frac{3X^2\pi^2}{8N^2b^2} \left(\sin^2 \left(\frac{\pi n}{2N} \right) - \cos^2 \left(\frac{\pi n}{2N} \right) \right) dn + \int_0^N \frac{3\pi^2}{8N^2b^2} h^2 dn. \quad (3.19)$$

When we solve the integral, the first term will be zero. Thus the free energy associated with a single chain attached to an interface in the domain is

$$F = \int_0^N \frac{3\pi^2}{8N^2b^2} h^2 dn, \quad (3.20)$$

$$= \frac{3\pi^2}{8Nb^2} h^2.$$

Here the energy is dependent only on the height of the chain, which also indicates the size of the domain formed in phase separation. So, irrespective of where a chain is inserted in the domain, the free energy associated with the change in the chain conformations is the same.

If n polymer chains are grafted to an interface whose area is S , then free energy associated with the displacement of chains will result in the stretching free energy F_{str} at a height h . This height h can also be the radius of the domain formed by these chains. Free energy associated with an interface of area S is,

$$F = \frac{3\pi^2\Omega^2 n^2}{8Nb^2S^2}. \quad (3.21)$$

Here, Ω is the volume of a chain and $n\Omega = hS$. Given that a domain contains n_c chains, the free energy will be,

$$F = \int_0^{n_c} \frac{3\pi^2\Omega^2}{8Nb^2S^2} n^2 dn, \quad (3.22)$$

$$= \frac{\pi^2\Omega_m^2 n_c^3}{8Nb^2S^2}.$$

3. Formulation of Strong Segregation Theory for ABC star terpolymer

In terms of the domain height h , $h = \frac{\Omega n_c}{S}$ overall free energy contribution due to n_c chains is:

$$F = \frac{n_c \pi^2 h^2}{8Nb^2}. \quad (3.23)$$

The free energy per chain f for brushes grafted to a surface is given by $\frac{F}{n_c}$ which is

$$f_c = \frac{\pi^2 h^2}{8Nb^2}. \quad (3.24)$$

At the strong segregation limit, this overall free energy due to stretching and pressure is highly elastic and contributes to the stretching of the chains. Thus for a flat interface grafted with brushes, the stretching free energy $f_{str} = f_c$.

$$f_c = \frac{\pi^2 h^2}{8Nb^2} = f_{str}. \quad (3.25)$$

Here a single monomer type is considered. The free energy of different block copolymer models can be computed using this free energy as the stretching free energy. We will demonstrate the free energy calculation of the morphologies in diblocks in brief. Later in the chapter, we will adapt the theory for ABC star terpolymers.

3.2 Interfacial energy at block copolymer interfaces

If there is more than one type of monomer in the polymer melt, then interfaces are formed due to their incompatibility. The incompatibility between monomers results in the interfacial tension γ between the domains [60]. The energy associated with this surface tension is quantified using the product of the Flory interaction parameter and the number of monomer units $N\chi$. For a polymer melt of total density ρ , the interfacial tension γ is

$$\gamma = \left(\frac{\chi}{6}\right)^{\frac{1}{2}} \rho b k_B T. \quad (3.26)$$

From the extensive literature available, the strong segregation limit is considered when $N\chi \geq 60$. So we are scaling the surface tension with $N\chi = 60$. The interfacial in terms of $k_B T$ is then $\gamma \approx 10^{\frac{1}{2}}$. Given there are n_c polymer chains of volume Ω , the interfacial energy F_{int} at a domain surface of area S is

$$F_{int} = \gamma S = \frac{\gamma n_c \Omega}{h} \quad (3.27)$$

where h is the radius of the domains formed. The interfacial energy per chain f_{int} is

$$f_{int} = \frac{\gamma\Omega_m}{h}. \quad (3.28)$$

We have the free energy consumed by chains for stretching (eq. (3.25)) and at the interfaces of monomer domains eq. (3.28). When we combine these two we get the overall free energy expense in a polymer melt at strong segregation limit. It is possible to determine the total free energy associated with different block copolymer models. First, we will discuss the simpler case of two-component block copolymers using diblocks and their morphologies. Later in this chapter, we will develop the free energy calculation for ABC star terpolymers and their morphologies.

3.3 Strong segregation for two-component block copolymers

The simplest two-component block copolymer is a diblock with two blocks: AB . This gives two types of polymer brushes at both sides of the AB interface. One side will have brushes of monomer type A and the other will have brushes of B . The stretching of these brushes and resulting interfacial strength constitute the free energy of phase separated morphologies.

The most common morphology found for symmetric diblocks is lamellar [87, 138]. Here is a review for determining the total free energy of the lamellar phase at strong segregation limit based on the work done by Olmsted and Milner [117].

3.3.1 Lamellar morphology

When the composition of A and B blocks are comparably equal diblocks form stable lamellar structures [87, 97, 138]. In this morphology, the diblocks are arranged such that the connecting points of A and B blocks will form a surface resulting in A and B branches stretching in opposite directions. The arrangement of A and B blocks results in the stretching free energy and the tension due to this stretching at the interface results in the interfacial free energy.

3. Formulation of Strong Segregation Theory for ABC star terpolymer



Figure 3.2: Schematic representation of lamellar morphology. The type A domain is given in red with height h_A and the type B domain is given in blue with height h_B .

In diblock morphologies, the domain height is dependent on its monomer compositions, ϕ_A for A type and ϕ_B for B type monomers. The height of A brush $h_A = \phi_A h$ and that of B brush is $h_B = \phi_B h$ as shown in fig. 3.2.

We consider a lamellar structure as shown in fig. 3.2 with A and B type blocks occupying the domain of height h_A and h_B , respectively. The compositions of A and B monomers in the lamellar structure of domain size are $\phi_A = \frac{h_A}{h}$ and $\phi_B = \frac{h_B}{h}$. Considering N_A monomer units in the A block and N_B monomer units in the B block of a chain, resulting stretching free energy f_{str} is,

$$\begin{aligned} f_{str} &= \frac{\pi^2}{8} \left\{ \frac{h_A^2}{N_A b_A^2} + \frac{h_B^2}{N_B b_B^2} \right\}, \\ &= \frac{\pi^2}{8} \left\{ \frac{\phi_A^2}{N_A b_A^2} + \frac{\phi_B^2}{N_B b_B^2} \right\} h^2 \\ &= M h^2. \end{aligned} \tag{3.29}$$

where $M = \frac{\pi^2}{8} \left\{ \frac{\phi_A^2}{N_A^2 b_A^2} + \frac{\phi_B^2}{N_B^2 b_B^2} \right\}$. Here M has the architectural details of the chains in the melt. The surface energy at the AB interface for a lamellar morphology is

$$f_{int} = \frac{\gamma \Omega}{h}. \tag{3.30}$$

where Ω is the total volume of the A and B brushes.

3. Formulation of Strong Segregation Theory for ABC star terpolymer

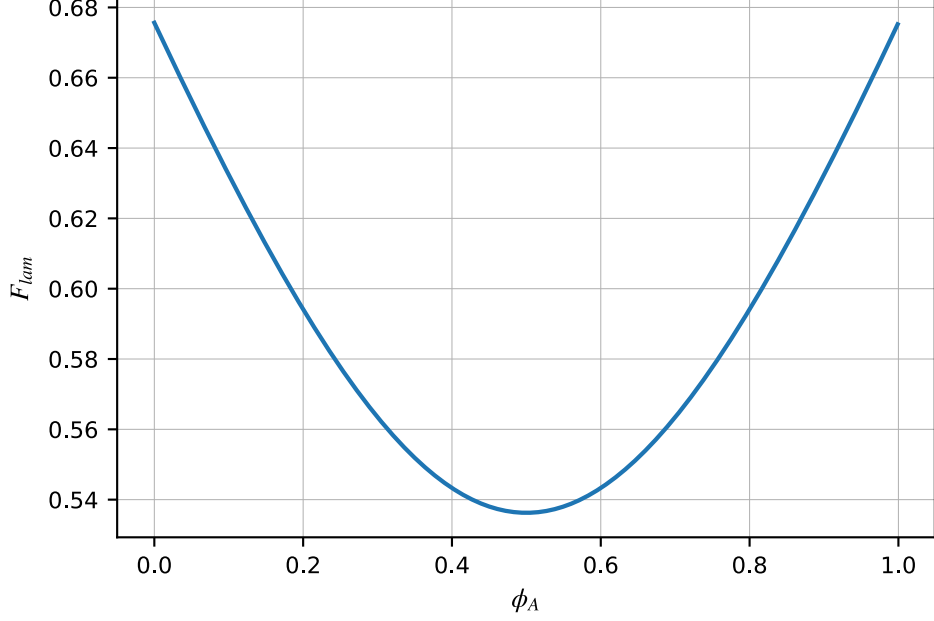


Figure 3.3: Total free energy determined from strong segregation analysis for lamellar morphology is varied with the monomer composition ϕ_A .

The total free energy associated with the lamellar morphology, F_{lam} is then,

$$\begin{aligned} F_{lam} &= f_{str} + f_{int} \\ &= Mh^2 + \frac{\gamma\Omega}{h} \end{aligned} \quad (3.31)$$

The total free energy F_{lam} varies with the lengthscale of the morphology h . The stretching energy increases with the domain size or brush length and interfacial energy decreases with the domain size. So at a specific lengthscale $h = h_0$ the stretching and interfacial tension balances and the morphology will be in equilibrium. The total free energy F_{lam} will have a minimum at h_0 satisfying,

$$\begin{aligned} \frac{dF_{lam}}{dh} \Big|_{h_0} &= 0, \\ -\frac{\gamma\Omega}{h_0^2} + 2Mh_0 &= 0 \end{aligned} \quad (3.32)$$

Solving for h_0 we get

$$h_0 = \left(\frac{\gamma\Omega}{2M} \right)^{\frac{1}{3}}. \quad (3.33)$$

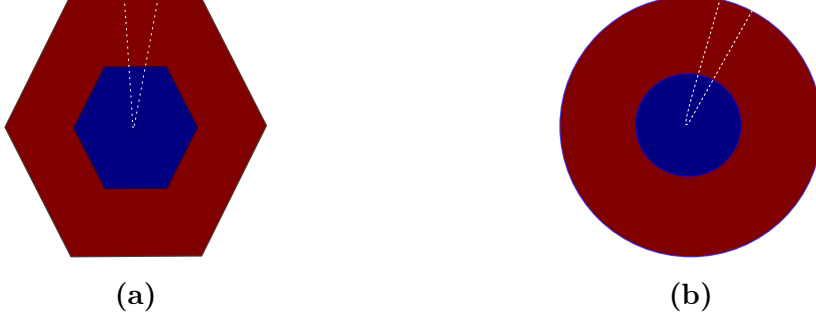


Figure 3.4: Schematic representation of (a) hexagonal and (b) cylindrical morphologies for diblocks. The white outline in both figures gives the different wedges that can be considered for these morphologies.

The free energy lamellar structure is then obtained by substituting h_0 in eq. (3.31). Thus we get,

$$\begin{aligned}
 F_{lam} &= 2^{\frac{1}{3}} \frac{3}{2} (\gamma\Omega)^{\frac{2}{3}} M^{\frac{1}{3}} = \left\{ \frac{27\pi^2}{32} \right\}^{\frac{1}{3}} (\gamma\Omega)^{\frac{2}{3}} \left\{ \frac{\phi_A^2}{N_A b_A^2} + \frac{\phi_B^2}{N_B b_B^2} \right\}^{\frac{1}{3}}, \\
 &= \left\{ \frac{27\pi^2}{32} \right\}^{\frac{1}{3}} (\gamma\Omega)^{\frac{2}{3}} \left\{ \frac{\phi_A^2}{N_A b_A^2} + \frac{(1 - \phi_A)^2}{N_B b_B^2} \right\}^{\frac{1}{3}},
 \end{aligned} \tag{3.34}$$

which is now in terms of the monomer compositions ϕ_A and $\phi_B = 1 - \phi_A$.

The total free energy is plotted by varying monomer compositions of A , ϕ_A as given in fig. 3.3 taking $N_A = N_B = N$ and $b_A = b_B = b$. When $\phi_A = \phi_B = \frac{1}{2}$, the free energy of lamellar morphology is the lowest as it was predicted in various phase separation studies [17, 87, 117, 138].

3.3.2 Free energy of a wedge

In lamellar morphology, the AB interface is a flat surface. When the compositions of A and B blocks are varied there emerge other morphological structures like hexagonal or cylindrical phases. In these structures, the interfaces are not flat throughout the melt. They form circles or hexagons as shown in fig. 3.4 at their interfaces. There are many other different morphologies that are formed in diblock melts. To determine the free energy of different morphologies of various geometrical shapes Olmsted et al. divided these morphologies into small wedges as indicated by the white outline in fig. 3.4. The total free energy of this wedge is determined which then is added up to calculate the total free energy of the given morphology.

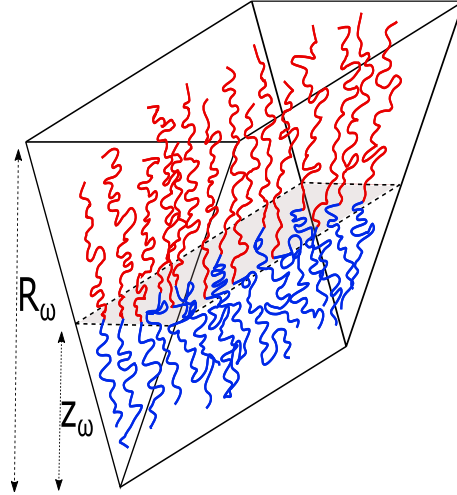


Figure 3.5: Wedge which adds up to form the diblock morphologies. The interface is at the height z_w .

In a wedge that is considered in a AB phase-separated structure, the narrow-ended side will be occupied by monomers of one type (A , red) and the broader is occupied by the other monomer type (B , blue) making an interface AB somewhere in between. The height of this interface varies with the composition. A parameter $\beta = \frac{z_w}{R_w}$ is defined to determine the interfacial height z_w variation with respect to the radius of the wedge (R_w).

$$\beta = \frac{z_w}{R_w} \quad (3.35)$$

With this scaling that can relate between the compositional change and geometry of the morphology the total free energy of the wedge is determined. Here, the interfacial free energy is determined first and then the stretching free energy per chain associated with the wedge is obtained.

The cross-sectional area of the interface $a(\beta)$ is defined as [117]

$$a(\beta) = \beta. \quad (3.36)$$

With the cross sectional area defined, the volume below the cross-section is then determined. The interfacial free energy for a wedge at the AB interface for a given morphology is determined. The area occupied by n_w chains in the wedge is $\frac{\Omega a(\beta)}{v(1)R}$ [117]. Given the surface tension at the interface is γ , the interfacial energy contributed to the

3. Formulation of Strong Segregation Theory for ABC star terpolymer

morphology due to the wedge is

$$\begin{aligned}
 f_{int} &= \gamma \times \text{Area of the interface occupied by the chains,} \\
 &= \frac{\gamma \Omega a(\beta)}{v(1)R_w}, \\
 &= \frac{W}{R_w}.
 \end{aligned} \tag{3.37}$$

where $W = \frac{\gamma \Omega a(\beta)}{v(1)}$. This constant contains the architectural characteristics of the polymer chain in the melt like the $N\chi$, its density and the shape of the interface formed. The stretching energy in a wedge is to be determined. The number of chains per cross-section, $\sigma_A = \frac{N_A}{a(\beta)}$ changes with the height. Thus the height is a function of the number of chains per area. The stretching energy due to A type monomers in the red part of the wedge given in fig. 3.5 is

$$f_{stretch_A} = \int_0^{N_A} \frac{3\pi^2 h^2(\sigma_A)}{8N_A b_A^2} dn. \tag{3.38}$$

The number of monomer units varies from 0 to N_A as we consider the chain from the AB interface to the broad end of the wedge. We have to consider the stretching below the interface caused by the B blocks. The stretching energy contribution from the B blocks is

$$f_{stretch_B} = \int_0^{N_B} \frac{3\pi^2 h^2(\sigma_B)}{8N_B b_B^2} dn. \tag{3.39}$$

The total stretching energy will be the sum of these two stretching energies. On solving the integral we get the simplified expression for total stretching energy. The detailed derivation is given in appendix B.1. We obtain the expression for stretching free energy given below:

$$\begin{aligned}
 f_{str} &= \frac{3\pi^2 R_w^2}{8v(1)} \left[\int_0^\beta \frac{y^2 a(\beta - y)}{R_A^2 \phi_A} dy + \int_0^{1-\beta} \frac{y^2 a(\beta + y)}{R_B^2 \phi_B} dy \right], \\
 &= \frac{3\pi^2 R_w^2}{8v(1)} \left[\frac{I_A}{R_A^2 \phi_A} + \frac{I_B}{R_B^2 \phi_B} \right], \\
 &= MR_w^2.
 \end{aligned} \tag{3.40}$$

Here I_A and I_B give the geometric contribution from the domains formed by A and B blocks. These two constants depend on the interfacial surface that

3. Formulation of Strong Segregation Theory for ABC star terpolymer

is formed. We assign $M = \frac{3\pi^2}{8v(1)} \left[\frac{I_A}{R_A^2 \phi_A} + \frac{I_B}{R_B^2 \phi_B} \right]$, which shows that in the end stretching energy is depend on the square of domain radius.

Now, as expression for stretching free energy and interfacial free energy are obtained, the total free energy per chain for the wedge is

$$F_w = MR_w^2 + \frac{W}{R_w}. \quad (3.41)$$

This is the format of total free energy expression irrespective of the morphologies or polymer structure.

The diblocks can form different morphologies which are composed of straight interfaces or curved interfaces. In order to determine the free energy expense a morphology is divided into appropriate wedges. Using this the free energy of hexagonal and cylindrical morphologies are determined as examples.

Hexagonal morphology

In a hexagonal morphology like the one given in fig. 3.6.(a) blocks of monomer type B (blue) form cylindrical hexagons that are embedded in domains formed by blocks of monomer type A (red) in 2D. Wedges are chosen for this morphology such that on putting them together, you get the hexagonal morphology. The morphology is divided into six identical triangles which are then divided into smaller wedges. The interfacial energy is determined for the wedge in a hexagon. Considering the simple case where AB interface is a straight line. In the case of a hexagon this interface will be a rectangle (refer to fig. 3.5). Here, the interface is not perpendicular to the horizontal height of the wedge R_w . Instead there is a slight inclination which is indicated by the angle ψ . By scaling the height of the chain with the height of the interface using the previously mentioned β , the area of the interface A_{int} is determined.

$$A_{int} = a(\beta) \cos \psi \quad (3.42)$$

The expression for interfacial energy is then,

$$\begin{aligned} f_{hex_{int}} &= \frac{\gamma \Omega a(\beta) \cos \psi}{v(1) R_h \cos \psi} \\ &= \frac{W}{R_h} \end{aligned} \quad (3.43)$$

where W is $\frac{\gamma \Omega a(\beta)}{v(1)}$. Here W has the chemical characteristics of the polymer chain including the monomer interactions and chain lengths.

Next is to determine the stretching energy of the chains in the hexagonal morphology. For this, a wedge of width dl is considered in the hexagon at a

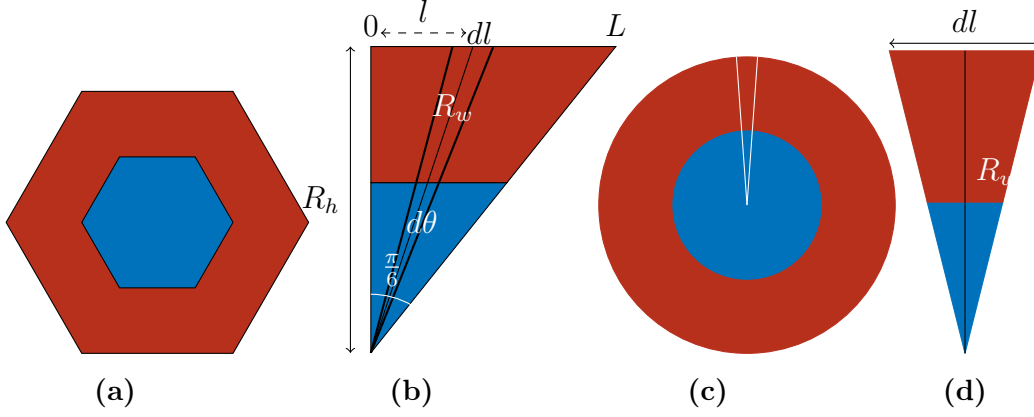


Figure 3.6: Schematic representation of wedges for hexagonal and cylindrical morphology in diblocks are given in (a) and (c). The red indicates the A type and the blue indicates B type monomers. In (b) the $\frac{1}{12}^{th}$ portion of the hexagon is given where the wedge is indicated in black outlines. The wedge for cylindrical morphology is given in (d) where the radius of the cylinder is the height of the wedge.

distance l from the perpendicular height R_h of the hexagon as shown in fig. 3.6. (b). In order to apply the expression for stretching energy from the wedge, the radius is determined in terms of the height of the hexagon R_h .

$$R_w^2 = R_h^2 + l^2, \quad (3.44)$$

$$R_w^2 = R_h^2(1 + x^2).$$

The stretching energy of the chains in the triangle in fig. 3.6.(a) is determined by integrating f_{str} for the wedge over $0 \rightarrow L$, which is $0 \rightarrow \frac{1}{\sqrt{3}}$. So the stretching free energy $f_{hex(str)}$ associated with the chains in the triangle in fig. 3.6.(a) that is $\frac{1}{12}$ th of a hexagon is

$$\begin{aligned} f_{hex(str)} &= \frac{\int_0^{\frac{1}{\sqrt{3}}} f_{str} dV_w}{\int_0^{\frac{1}{\sqrt{3}}} dV_w}, \\ &= \sqrt{3} \int_0^{\frac{1}{\sqrt{3}}} f_{str} dx. \end{aligned} \quad (3.45)$$

The cross-sectional area varies with height in a hexagon as $a(\beta) = \beta$. The stretching energy per chain for the hexagonal morphology in the expanded form

3. Formulation of Strong Segregation Theory for ABC star terpolymer

is

$$f_{hex(str)} = \sqrt{3} \int_0^{\frac{1}{\sqrt{3}}} \left(\frac{3\pi^2 R_w^2}{8v(1)} \left[\int_0^\beta \frac{y^2 a(\beta - y)}{R_A^2 \phi_A} dy + \int_0^{1-\beta} \frac{y^2 a(\beta + y)}{R_B^2 \phi_B} dy \right] \right) dx \quad (3.46)$$

The terms in the square bracket depend on the composition of the polymer chains and the interfacial cross-sections formed. Consider these terms as ζ where,

$$\zeta = 3 \int_0^\beta \frac{y^2 a(\beta - y)}{R_A^2 \phi_A} dy + 3 \int_0^{1-\beta} \frac{y^2 a(\beta + y)}{R_B^2 \phi_B} dy. \quad (3.47)$$

Now the stretching free energy in hexagonal morphology can be written as,

$$\begin{aligned} f_{hex(str)} &= \sqrt{3} \int_0^{\frac{1}{\sqrt{3}}} \frac{\pi^2}{8v(1)} \zeta R_h^2 (1 + x^2) dx \\ &= \frac{10}{9} \frac{\pi^2}{8v(1)} \zeta R_h^2 \end{aligned} \quad (3.48)$$

where $R_w = R_h \sqrt{1 + x^2}$. The stretching energy is evaluated by solving the integral eq. (3.46). The final expression can be written as

$$f_{hex(str)} = \frac{10}{9} M R_h^2, \quad (3.49)$$

by taking $\frac{3\pi^2}{8v(1)} \zeta = M$. Now the stretching energy is in the familiar form where it is proportional to the square of the domain height R_h . The parameter M contains the chemical and architectural features of the diblocks like monomer composition and domain lengths.

The total free energy is determined by combining the interfacial energy in eq. (3.43) and the stretching free energy eq. (3.49).

$$F_{hex} = \frac{10}{9} M R_h^2 + \frac{W}{R_h}. \quad (3.50)$$

Similar to the total free energy expression of lamellar morphology in eq. (3.31), the expression for the total free energy of the hexagon also has the same structure. In this expression, the M contains ζ which describes the morphological structure that is formed. The interfacial area and thus the monomer-monomer interactions are considered through W . These two constants vary with the morphology we are considering, monomer composition and interaction strength. Here the scaling length is R_h , the height of the hexagon. Morphology gets stable at lengthscale

3. Formulation of Strong Segregation Theory for ABC star terpolymer

R_h when there is an equilibrium state due to the balance between the stretching energy which encourages entropy (conformational change) and interfacial energy that pulls the chains back to the domains. The lengthscale for stable morphology is obtained when the total free energy is at its minimum. That is when $\frac{dF_{hex}}{dR_h} |_{R_{h_0}} = 0$. The stable lengthscale is then

$$R_{h_0} = \left(\frac{9}{20} \frac{W}{M} \right)^{\frac{1}{3}}. \quad (3.51)$$

Now the total free energy is rewritten by substituting R_h with the stable lengthscale R_{h_0} . So the minimum free energy of hexagonal morphology for a given monomer composition of ϕ_A and ϕ_B is

$$\begin{aligned} F_{hex_{min}} &= \left(\frac{10}{9} \right)^{\frac{1}{3}} \left(\frac{27}{4} \right)^{\frac{1}{3}} M^{\frac{1}{3}} W^{\frac{2}{3}}, \\ &= \left(\frac{10}{9} \right)^{\frac{1}{3}} \left(\frac{27}{4} \right)^{\frac{1}{3}} \left(\frac{3\pi^2 \zeta}{8v(1)} \right)^{\frac{1}{3}} \left(\frac{\gamma \Omega \beta}{v(1)} \right)^{\frac{2}{3}}. \end{aligned} \quad (3.52)$$

Cylinder

We can analyse morphologies with curved interfaces using the wedge method. If we consider a cylindrical morphology as given in fig. 3.6. (c), then the morphology can be divided into infinitesimally small wedges such that the interface is mostly straight. Here the radius of the wedge is uniform all around the cylinder as demonstrated in fig. 3.6.(d). Following the procedures as the hexagonal case, the interfacial energy and the stretching free energy are determined.

The interfacial energy for the cylinder will be

$$f_{cyl_{int}} = \frac{\gamma \Omega a(\beta)}{v(1) R_w}, \quad (3.53)$$

where the area of cross section $a(\beta) = \beta$ as the cross section for the wedge in the cylinder is also rectangular. Again taking $W = \frac{\gamma \Omega a(\beta)}{v(1)}$ the interfacial energy for a wedge in a cylindrical morphology is

$$f_{cyl_{int}} = \frac{W}{R_w}. \quad (3.54)$$

The stretching free energy for the wedge across the circle of radius R_w is given by

$$f_{cyl(str)} = \frac{\int_0^{2\pi R_w} f_{str(w)} dV_w}{\int_0^{2\pi R_w} dV_w}, \quad (3.55)$$

3. Formulation of Strong Segregation Theory for ABC star terpolymer

where the volume of wedge $dV_w = \frac{R_w dl}{2}$. The stretching free energy per chain is then,

$$\begin{aligned} f_{cyl(str)} &= \frac{\int_0^{2\pi R_w} f_{str(w)} R_w dl}{\int_0^{2\pi R_w} R_w dl}, \\ &= \frac{1}{2\pi R_w} \frac{3\pi^2 R_w^2}{8v(1)} \int_0^{2\pi R_w} \left[\int_0^\beta \frac{y^2 a(\beta - y)}{R_A^2 \phi_A} dy + \int_0^{1-\beta} \frac{y^2 a(\beta + y)}{R_B^2 \phi_B} dy \right] dl. \end{aligned} \quad (3.56)$$

As the cross sectional area for cylinder is again $a(\beta) = \beta$, the ζ for cylindrical morphology is the same as in hexagon (eq. (3.47)). The final expression for stretching free energy will be:

$$\begin{aligned} f_{cyl(str)} &= \frac{1}{2\pi R_w} \frac{3\pi^2 R_w^2}{8v(1)} \zeta \int_0^{2\pi R_w} dl, \\ &= \frac{3\pi^2 R_w^2}{8v(1)} \zeta, \\ &= MR_w^2. \end{aligned} \quad (3.57)$$

The stable radius R_{w_0} is obtained by determining the minimum of the overall free energy $F_{cyl} = f_{cyl(str)} + f_{cyl(int)}$ with respect to R_w . Thus the minimum free energy $F_{cyl_{min}}$ is

$$F_{cyl_{min}} = \left(\frac{27}{4}\right)^{\frac{1}{3}} \left(\frac{3\pi^2 \zeta}{8v(1)}\right)^{\frac{1}{3}} \left(\frac{\gamma \Omega \beta}{v(1)}\right)^{\frac{2}{3}} \quad (3.58)$$

Thus by choosing the appropriate β and $a(\beta)$, the free energy of different morphologies can be determined at strong segregation limit. We demonstrated the idea for diblocks here. More morphologies are analysed for diblocks using this method in the work done by Olmsted and Milner [117]. Through this method, the problem of phase separation is converted into a geometrical problem in 2D. In their work with diblocks, Olmsted et al. also extend the theory to include bicontinuous morphologies in 3D. This theory has the potential to be extended to other block copolymer systems like ABC star terpolymer.

From here on, in this thesis we will demonstrate the versatile framework to study phase separation in ABC star terpolymers and its application to various morphologies.

3.4 Strong Segregation Theory for ABC star terpolymer

The phase separation and the morphologies formed in ABC star terpolymer are dependent on six variables, the three monomer compositions and three interaction strengths, of the chain. In an incompressible melt of ABC star terpolymers this reduces to five: ϕ_A, ϕ_B with $\phi_C = 1 - \phi_A - \phi_B$ and the chemical incompatibilities between each monomer types: $N\chi_{AB}, N\chi_{AC}$ and $N\chi_{BC}$. Varying these parameters, there are a plethora of morphologies that could be formed for this polymer system as mentioned in Chapter 1. Previous works done on ABC star terpolymers explore the morphologies at strong segregation limit using *SCFT* [62, 91, 159], Dissipative Particle Dynamics *DPD* [27, 80, 81] and Monte Carlo method [50, 156].

In this work we are proposing a simpler yet powerful methodology to determine stable morphologies based on strong segregation theory. The technique follows the same principle as discussed above for diblock morphologies. A preliminary analysis of this type was made by Gemma et al. [50] who developed a strong segregation theory for the prominent 2D periodic morphologies to complement their lattice-based molecular Monte Carlo simulations. In their work, Gemma et al. report their results along a 1D slice through the two dimensional composition space. In our work, we go significantly beyond the work of Gemma et al. by developing a generalised computational framework which can encapsulate a wide range of morphological structures and which then can be utilised to study 2D morphologies including quasicrystals.

The ABC star terpolymer chain contains three branches of different monomer types joined together at a point as shown in fig. 3.7.(a). When these terpolymers rearrange themselves to form different morphologies, these junction points align themselves in a line in a third dimension giving different domains in the two dimensions of the page. In order to fit within any morphology, the chains must stretch into the domains away from the unique points where the three colours meet, as shown in fig. 3.7. (b). A line formed by such unique points is called ‘core’ in this work. In any phase-separated structures, the three branches stretch around this core forming monomer domains around it. Thus we are dealing with polymer branches that stretch from a curved surface of a very small radius. The chain distribution within the core is not well defined [50]. In *DPD* calculations [81], the core is taken as a sphere of the fourth type, which facilitates the architectural and spatial restriction of an unknown entity. But this doesn’t efficiently resolve the role of the core in terpolymer phase separation.

In this work, we are considering the core as a convex cylinder in 3D of radius $R_c \approx b$, where b is the Kuhn length. The three branches are grafted to the convex side of this cylinder as shown in fig. 3.7. (b). Thus same type branches can

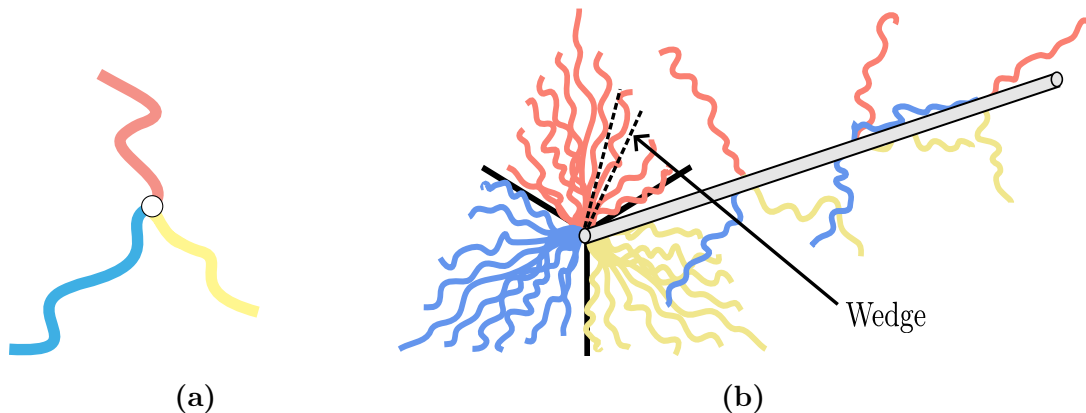


Figure 3.7: A schematic representation of ABC star terpolymer is shown in (a). The red, blue and yellow branches indicate monomer types A , B and C respectively. In (b), the domain formation from the stretching of branches around the core line is demonstrated.

assemble in a way to give a tiling like arrangement as shown in fig. 3.9. So the stretching we are concerned for this system is due to the brushes being grafted to convex surfaces.

3.4.1 Stretching free energy of brushes on curved surface

In order to evaluate the stretching energy of the branches in terpolymers the 2D morphologies are divided into wedges as shown in fig. 3.7.(b). In this case, wedges contain branches of the same monomer type. Each domain can be split into a set of wedges, but interfaces between domains are not included inside the wedge-like diblock wedges. The stretching energy for brushes grafted on a convex surface of radius of curvature R_c is reported by Ball et al. in their work on brushes grafted on surfaces [15]. They give stretching energy per unit area $F(\sigma)$ in the units of $k_B T$ in terms of packing fraction $a = \frac{3v_m}{b}$ and chains per unit area σ for monomer unit of volume v_m . When the radius of the surfaces is sufficiently small, the stretching energy is dependent on the leading term which is,

$$F(\sigma) = \frac{aR_c\sigma^2}{4} \log \frac{\sigma\Omega}{R_c}, \quad (3.59)$$

where R_c is the radius of the cylindrical surface.

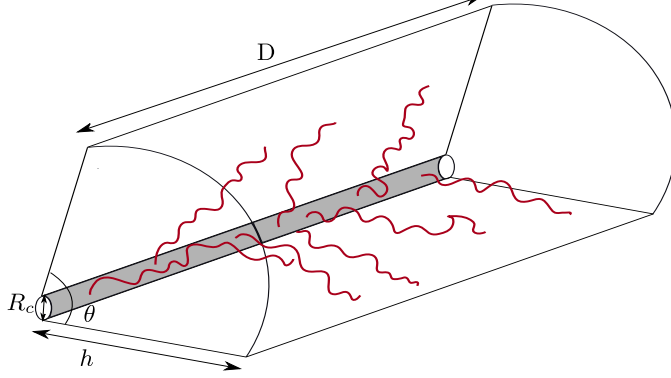


Figure 3.8: Schematic representation of the wedge with only one type of polymer chain grafted into a core cylinder.

Now we consider a wedge in which the polymer branches are grafted to a core cylinder of radius $R_c \sim b$ as given in fig. 3.8. The stretching free energy per chain $f_w = \frac{F(\sigma)}{\sigma}$ is,

$$f_w = \frac{aR_c\sigma}{4} \log \frac{\sigma\Omega}{R_c}. \quad (3.60)$$

For a wedge of sectional angle θ , radius h and depth D as given in fig. 3.8, the volume of the wedge will be $\theta h^2 D$. This is equivalent to the volume of monomer melt in the wedge: $\rho\Omega D$ where ρ is the monomer density and Ω is the volume of a monomer unit. The chains per unit area (σ) in the wedge the ratio of total chains in the wedge ρD to the cross-sectional area $R_c\theta D$

$$\sigma = \frac{\rho D}{R_c\theta D} = \frac{h^2}{R_c\Omega}. \quad (3.61)$$

where $\Omega = Nv_m$ with N being the number of monomer units and v_m , the volume of a monomer unit. Substituting for σ and a in eq. (3.60) we get the stretching free energy in terms $k_B T$ for a wedge of radius h ,

$$f_w = \frac{3}{4} \frac{h^2}{Nb^2} \log \frac{h^2}{R_c^2}. \quad (3.62)$$

The expression for stretching energy here is comparable to the diblock wedges given in eq. (3.40) as both depend on the square of the domain radius, h . Here in the case of this wedge with a core, the expression has a logarithmic correction dependent on the ratio $\frac{h}{R_c}$. Now following the procedures from the diblock case, each morphology is split up into a set of wedges to determine the overall stretching free energy per chain in units of $k_B T$.

Utilising this, we will now develop the theoretical and computational framework for hexagonal morphology in ABC star terpolymers. The interfacial energy is determined separately for ABC star terpolymer melts in a strong segregation limit, which will be discussed in the following section using an example morphology.

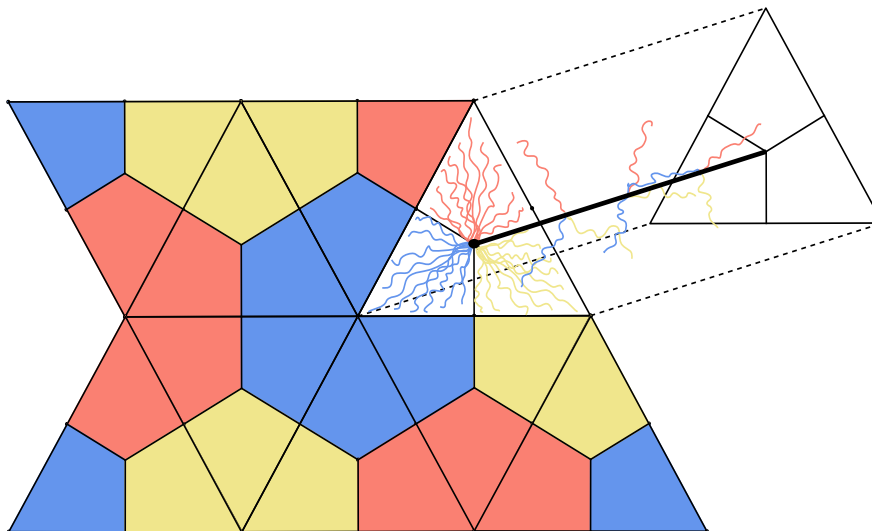


Figure 3.9: The phase separated state of ABC star terpolymer to form hexagonal morphology is shown here. The chains given in the triangle stretch out and align themselves to form domains that are arranged in a honeycomb.

3.4.2 SST for hexagonal morphology in ABC star terpolymer

The simplest morphology to consider for ABC star terpolymer is hexagon. In a symmetric ABC star terpolymer melt where the all blocks have the same monomer composition and equal interaction strengths, the domains formed have a honeycomb structure which is the hexagonal morphology as shown in fig. 3.9. As we can see the polymer branches stretch away from the core cylinder forming hexagonal domains of the same monomer type. The red, blue and yellow domain contains A , B and C monomer types respectively. We will be using this monomer-colour convention throughout this thesis. While forming these domains they also form interfaces with hexagons of two other monomer types. This results in three interfacial surfaces between A and B , B and C and A and C .

The repeating unit for hexagonal morphology is an equilateral triangle that is indicated with polymer branches in fig. 3.9. In the case of diblocks, the change

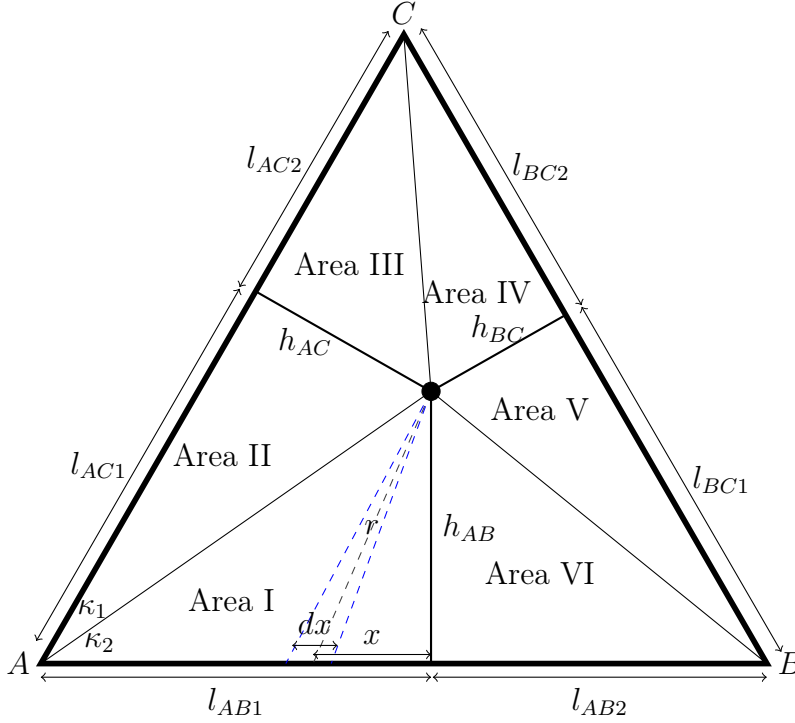


Figure 3.10: Schematic representation of the equilateral triangle that will form hexagons. In here all length parameters are indicated. Areas I and II is occupied A type, areas III and IV are occupied by C type and areas V and area VI is occupied by B type monomer. The wedge is marked by dashed lines.

in monomer composition was reflected in the height of the interface which was controlled using the variable β (eq. (3.35)). In the case of ABC star terpolymer, the composition changes the position of the core in this equilateral triangle and can control the size of the domains. The position of the core is hence dependent on the monomer compositions ϕ_A , ϕ_B and $\phi_C = 1 - \phi_A - \phi_B$.

The core divides the equilateral triangle into three regions each with one type of monomer in it. In order to apply the method of wedges the three domains are determined in terms of monomer compositions. So we need to express the geometry of the hexagonal morphology in terms of monomer compositions ϕ_A , ϕ_B and ϕ_C . A geometrical interpretation of this equilateral triangle is given in fig. 3.10.

The three regions in the triangle assigned to different monomer types are further divided into two right angled triangles as shown in fig. 3.10. Thus the regions with A type are Area I and II, regions with C type are Area III and IV and regions with B type are Area V and VI. The monomer composition is then

3. Formulation of Strong Segregation Theory for ABC star terpolymer

defined as,

$$\begin{aligned}\phi_A &= \frac{\text{Area I} + \text{Area II}}{\text{Total Area}}, \\ \phi_C &= \frac{\text{Area III} + \text{Area IV}}{\text{Total Area}}, \\ \phi_B &= \frac{\text{Area V} + \text{Area VI}}{\text{Total Area}}.\end{aligned}\tag{3.63}$$

Since the area of the triangles is known from the length of their sides, the composition fraction is defined in terms of these lengths. We write all lengths as dimensionless parameters by scaling with the side length l of the triangle. The lengths from the corner to interfaces l_{IJ} and interface heights h_{IJ} which are written in dimensionless form as $l_{IJ} = lL_{IJ}$ and $h_{IJ} = lH_{IJ}$. Thus the monomer compositions in terms of the domain lengths are

$$\begin{aligned}\phi_A &= \frac{2}{\sqrt{3}}(L_{AB1}H_{AB} + L_{AC1}H_{AC}), \\ \phi_B &= \frac{2}{\sqrt{3}}(L_{AB2}H_{AB} + L_{BC1}H_{BC}), \\ \phi_C &= \frac{2}{\sqrt{3}}(L_{AC2}H_{AC} + L_{BC2}H_{BC}).\end{aligned}\tag{3.64}$$

Our goal is now to invert these equations so that we can obtain the geometry of the domains (i.e. the lengths and heights of the triangles) from the composition (ϕ_A, ϕ_B) . Using simple trigonometry, we first get two relations between H_{IJ} and L_{IJ} . The relation between interfacial heights and side lengths is established considering the corner A of fig. 3.10. We know that for an equilateral triangle $\angle A = 60^\circ$. As we divide the triangle into six triangular regions, $\angle A = \kappa_1 + \kappa_2$, as indicated in fig. 3.10. So,

$$\begin{aligned}\tan A &= \tan(\kappa_1 + \kappa_2) = \frac{\tan \kappa_1 + \tan \kappa_2}{1 - \tan \kappa_1 \tan \kappa_2}, \\ \tan 60 &= \sqrt{3} = \frac{\frac{H_{AC}}{L_{AC1}} + \frac{H_{AB}}{L_{AB1}}}{1 - \frac{H_{AC}}{L_{AC1}} \frac{H_{AB}}{L_{AB1}}},\end{aligned}\tag{3.65}$$

$$\sqrt{3}\{L_{AC1}L_{AB1} - H_{AC}H_{AB}\} = L_{AB1}H_{AC} + L_{AC1}H_{AB}.$$

Also for the right angled triangles that contain κ_1 and κ_2 ,

$$H_{AB}^2 + L_{AB1}^2 = H_{AC}^2 + L_{AC1}^2.\tag{3.66}$$

3. Formulation of Strong Segregation Theory for ABC star terpolymer

Solving the two equations in eq. (3.65) and eq. (3.66) for L_{AB1} and L_{AC1} the side lengths are expressed in terms of interfacial heights only.

$$\begin{aligned} L_{AB1} &= \frac{\sqrt{3}(H_{AB} + 2H_{AC})}{4}, \\ L_{AC1} &= \frac{\sqrt{3}(H_{AC} + 2H_{AB})}{4}. \end{aligned} \quad (3.67)$$

This is done for all the corners and every side length in fig. 3.10 is expressed in terms of the interfacial heights. Substituting for all L_{IJS} in section 3.4.2 monomer compositions are now in terms of interfacial heights.

$$\begin{aligned} \phi_A &= \frac{2}{3}(H_{AB}^2 + H_{AC}^2 + 4H_{AB}H_{AC}), \\ \phi_B &= \frac{2}{3}(H_{AB}^2 + H_{BC}^2 + 4H_{AB}H_{BC}), \\ \phi_C &= \frac{2}{3}(H_{BC}^2 + H_{AC}^2 + 4H_{BC}H_{AC}). \end{aligned} \quad (3.68)$$

Solving these equations using numerical methods we get H_{AB} , H_{BC} and H_{AC} in terms of some ϕ_A and ϕ_B and $\phi_C = 1 - (\phi_A + \phi_B)$. It should be noted that the core is should always be inside the triangle and it should form domains that are physically valid. However, not all values of ϕ_A and ϕ_B lead to physically valid geometry. For example if $H_{AB} \leq 0$, $H_{BC} \leq 0$ and $H_{AC} \leq 0$, the domains formed are physically invalid. If $H_{AB} = 0$, then

$$\begin{aligned} \phi_A &= \frac{2}{3}H_{AC}^2 \\ H_{AC} &= \sqrt{\frac{3}{2}}\sqrt{\phi_A} \end{aligned} \quad (3.69)$$

and

$$H_{BC} = \sqrt{\frac{3}{2}}\sqrt{\phi_B}. \quad (3.70)$$

Also for an equilateral triangle of side l , the perpendiculars to the sides obey

$$h_{ab} + h_{bc} + h_{ac} = \frac{\sqrt{3}}{2}l \quad (3.71)$$

where l is the total length of the sides. That gives,

$$H_{BC} + H_{AC} = \frac{\sqrt{3}}{2}. \quad (3.72)$$

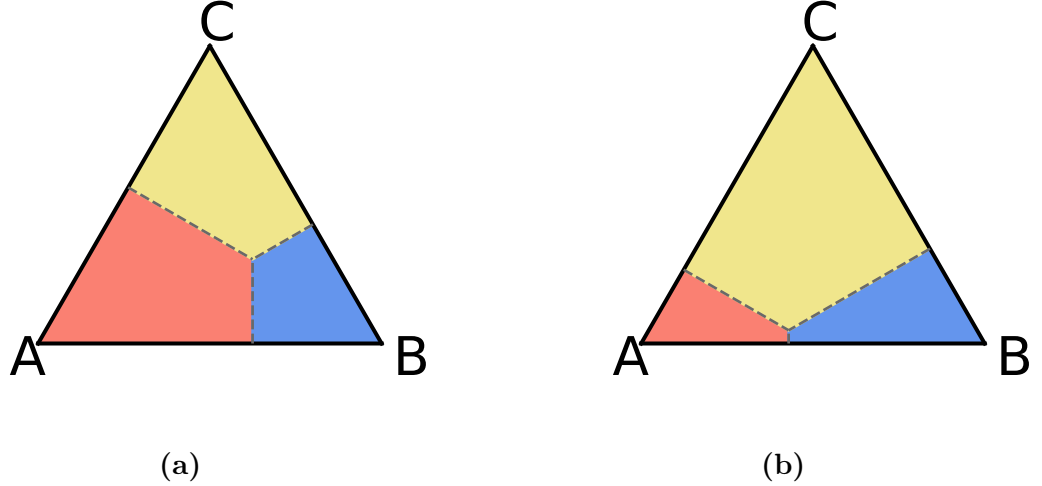


Figure 3.11: These triangles demonstrate how changing monomer compositions alter domains. In (a) $\phi_A = 0.43$ and $\phi_B = 0.20$ and in (b) $\phi_A = 0.12$ and $\phi_B = 0.20$.

And so $\sqrt{\phi_A} + \sqrt{\phi_B} = \frac{1}{\sqrt{2}}$. This forms one boundary on the region of validity. Considering all such boundaries, we conclude that the compositions ϕ_A , ϕ_B and ϕ_C that obey

$$\begin{aligned}
 \sqrt{\phi_A} + \sqrt{\phi_B} &\geq \frac{1}{\sqrt{2}}, \\
 \sqrt{\phi_B} + \sqrt{\phi_C} &\geq \frac{1}{\sqrt{2}}, \\
 \sqrt{\phi_A} + \sqrt{\phi_C} &\geq \frac{1}{\sqrt{2}},
 \end{aligned} \tag{3.73}$$

will give physically valid phase separated domains. Thus for given monomer compositions ϕ_A and ϕ_B we can tell how the equilateral triangle with domains and hence the morphology will look like. Two examples of triangles with different compositions are given in the fig. 3.11. We can see that the composition change affects the domain according to the above formulation. Different domains mean different phase separation patterns within the same morphology. Now we can consider the interfacial energy and stretching energy in terms of the geometry of the triangle.

Interfacial free energy

There are three interfacial planes, each between A and B , B and C and A and C . The interfacial energy is defined in terms of surface tension $\gamma = \left(\frac{\chi}{6}\right)^{\frac{1}{2}} \rho b k_B T$ [60]. For the given triangular domain interfacial energy in the units of $k_B T$ will be

$$F_{int} = \gamma_{AB} a_{AB} + \gamma_{BC} a_{BC} + \gamma_{AC} a_{AC} \quad (3.74)$$

where a_{AB} , a_{BC} and a_{AC} are the interfacial areas. If the depth of the domain is D , the area of the triangle is $A_T = \frac{\sqrt{3}l^2}{4}$ and the volume per chain is Ω then, the number of chains in the triangle is $\frac{A_T D}{\Omega}$ and area of each interfacial plane will be $h_{IJ} D$. So the interfacial energy per chain in units of $k_B T$ is

$$\begin{aligned} f_{int} &= \frac{(\gamma_{AB} h_{AB} D + \gamma_{BC} h_{BC} D + \gamma_{AC} h_{AC} D) \Omega}{A_T D} \\ &= \frac{4(\gamma_{AB} H_{AB} + \gamma_{BC} H_{BC} + \gamma_{AC} H_{AC}) \Omega}{\sqrt{3} L R} \end{aligned} \quad (3.75)$$

where we have introduced a dimensionless triangle side length $L = \frac{l}{R}$ scaled by the chain random walk length $R = \sqrt{N} b$. In eq. (3.75), we can introduce a scaled surface tension $\xi_{IJ} = \frac{\gamma_{IJ} \Omega}{R k_B T}$. On substituting for γ_{IJ} as in [60] we get

$$\begin{aligned} \xi_{IJ} &= \frac{\left(\frac{\chi_{IJ}}{6}\right)^{\frac{1}{2}} \rho_0 b \Omega}{R} = \frac{\left(\frac{\chi_{AB}}{6}\right)^{\frac{1}{2}} \left(\frac{1}{v_0}\right) b (N v_0)}{N^{\frac{1}{2}} b}, \\ &= \sqrt{\frac{N \chi_{IJ}}{6}}. \end{aligned} \quad (3.76)$$

From [50, 98] it is clear that SST is valid when $N \chi \geq 60$ giving a lower limit of $\xi_{IJ} = \sqrt{10}$. For convenience, we scale ξ_{IJ} again to maintain $N \chi_{IJ}$ in strong segregation limit and also to control interaction between monomers. For this, ξ_{IJ} is expressed in terms of ν_{IJ} :

$$\xi_{IJ} = \sqrt{10} \nu_{IJ} \quad (3.77)$$

Collecting all this together, the interfacial free energy per chain in the units of $k_B T$ in this triangle is

$$f_{int} = \frac{4\sqrt{10}}{\sqrt{3} L} (\nu_{AB} H_{AB} + \nu_{BC} H_{BC} + \nu_{AC} H_{AC}) \quad (3.78)$$

Thus small change in ν_{IJ} will reflect the changes in monomer interaction in a strong segregation limit. It is to be noted that the interfacial energy per chain is still inversely proportional to L , as it was observed in diblock cases.

Stretching free energy

The stretching energy for the equilateral triangle is determined from the sum of the stretching energies of six right-angle triangles. Taking one of the small triangles, for example, Area I occupied by A type blocks, the stretching energy is determined from the sum of stretching energies of the wedges. The stretching energy per a chain in the units of $k_B T$ in a wedge with core of radius R_c and domain height r using eq. (3.62) is,

$$f_w(r) = \frac{3}{4} \frac{r^2}{N_A b_A^2} \log \frac{r^2}{R_c^2}. \quad (3.79)$$

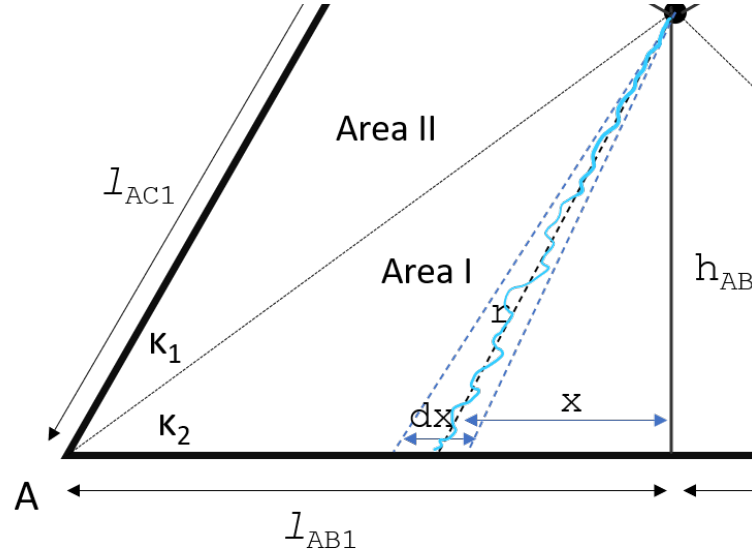


Figure 3.12: A closer diagram of Area I in the triangle. We consider a small wedge of width dw to determine the stretching energy.

Area I is occupied by A type monomers and the the chain random walk length R of A block is $R^2 = Nb^2$. For simplicity, we assume all monomer step lengths to be the same and equal to the Kuhn length b , $b_A = b_B = b_C = b$. In terms of monomer fraction, the stretching energy per chain in the units of $k_B T$ is

$$f_w(r) = \frac{3}{4} \frac{r^2}{\phi_A N b^2} \log \frac{r^2}{R_c^2}. \quad (3.80)$$

For a wedge of given width dx as given in fig. 3.12, the stretching free energy of the wedge is given by the number of chains in the wedge times the stretching free

3. Formulation of Strong Segregation Theory for ABC star terpolymer

energy per chain f_c . The free energy of the wedge df_w ,

$$df_w = f_w(r) \frac{h_{AB} D dx}{2\Omega_A} \quad (3.81)$$

where $\frac{1}{2}h_{AB}Ddx$ is the volume of the wedge and Ω_A is the volume of the A block of one chain. Given the stretching energy of the wedge for a type of monomer, it is integrated over the length of Area I, l_{AB1} to determine the stretching energy contributed by Area I. So the stretching energy of Area I will be,

$$F_I = \int_0^{l_{AB1}} f_w(r) \frac{h_{AB} D dx}{2\Omega_A} \quad (3.82)$$

We know that $r^2 = x^2 + h_{AB}^2$. Taking $y = \frac{x}{l_{AB}}$ we can write $dx = l_{AB} dy$ and the limits also change from $0 \rightarrow l_{AB1}$ to $0 \rightarrow 1$. Thus,

$$r^2 = (yl_{AB})^2 + h_{AB}^2. \quad (3.83)$$

So eq. (3.82) becomes,

$$\begin{aligned} F_I &= \int_0^1 f_w(r) \frac{h_{AB} D l_{AB1} dy}{2\Omega_A} \\ &= \frac{D h_{AB} l_{AB1}}{2\Omega_A} \int_0^1 f_w \left(\sqrt{(yl_{AB1})^2 + h_{AB}^2} \right) dy \end{aligned} \quad (3.84)$$

The total number of chains is given by dividing the total volume of A chains, $\phi_A A_T D$ by the volume of a single chain Ω_A . Here A_T is the total area of the triangle. So contribution to the total stretching free energy per chain from Area I, f_I will be

$$f_I = \frac{F_I}{n_t} = \frac{\frac{D h_{AB} l_{AB1}}{2\Omega_A}}{\frac{\phi_A A_T D}{\Omega_A}} \int_0^1 f_w \left(\sqrt{(yl_{AB1})^2 + h_{AB}^2} \right) dy \quad (3.85)$$

But we know that area of Area I given by $\frac{1}{2}h_{AB}l_{AB1} = A_I$. Thus,

$$f_I = \frac{A_I}{\phi_A A_T} \int_0^1 f_w \left(\sqrt{(yl_{AB1})^2 + h_{AB}^2} \right) dy \quad (3.86)$$

On expanding for $f_w(r)$, the above equation becomes,

$$f_I = \frac{A_I}{\phi_A A_T} \int_0^1 \frac{3}{4} \frac{(yl_{AB1})^2 + h_{AB}^2}{\phi_A N b^2} \log \frac{(yl_{AB1})^2 + h_{AB}^2}{R_c^2} dy \quad (3.87)$$

3. Formulation of Strong Segregation Theory for ABC star terpolymer

All lengths associated with the equilateral triangle (l, h_{IJ}, l_{IJ}) are scaled to the chain random walk length $R = \sqrt{Nb}$ using the dimensionless triangle side length $L = \frac{l}{R}$. So the stretching free energy per chain for area I is

$$f_I = \frac{A_I}{\phi_A^2 A_T} \int_0^1 \frac{3 L^2 R^2 ((yL_{AB1})^2 + H_{AB}^2)}{4 R^2} \log \frac{L^2 R^2 ((yL_{AB1})^2 + H_{AB}^2)}{R_c^2} dy \quad (3.88)$$

The ratio of the chain random walk length to the radius of the core is defined as $R_D = \frac{R}{R_c}$. The equation in eq. (3.88) will become

$$f_I = \frac{3}{4} \frac{A_I}{\phi_A^2 A_T} \int_0^1 L^2 ((yL_{AB1})^2 + H_{AB}^2) \log (L^2 R_D^2 ((yL_{AB1})^2 + H_{AB}^2)) dy \quad (3.89)$$

The integral in this expression is analytically solvable. In order to solve it we write the general form of the integral in terms of (X, Y) . The integral is of the form

$$I = G(X, Y) = \int_0^1 (Xy^2 + Y) \log(c(Xy^2 + Y)) \quad (3.90)$$

where $X = L^2 L_{AB1}^2$, $Y = L^2 H_{AB}^2$ and $c = R_D^2$. The integration is executed in two steps, first by integration by parts and then using long division. Using integration by parts the solution of the integral for region Area I is,

$$I_I = \left[\log(c(Xy^2 + Y)) \left(\frac{Xy^3}{3} + Yy \right) \right]_0^1 - \int_0^1 \frac{2Xy}{(Xy^2 + Y)} \left(\frac{Xy^3}{3} + Yy \right) dy \quad (3.91)$$

Thus solution of the integral I_I is

$$I_I = G(X, Y) = \log(c(X + Y)) \left(\frac{X}{3} + Y \right) - \left(\frac{2X}{9} + \frac{4Y}{3} - \frac{4Y}{3} \sqrt{\frac{Y}{X}} \arctan \sqrt{\frac{X}{Y}} \right) \quad (3.92)$$

The integration is verified using analytical mathematical tools like REDUCE and MAPLE. Similar analysis is done for the rest of the regions: Area II, Area III, Area IV, Area V and Area VI with their respective monomer fractions. The contribution of stretching energy per unit chain from each of them results in an integral of the same structure with its corresponding length parameters and monomer types. Contributions of the rest of the regions to stretching free energy

3. Formulation of Strong Segregation Theory for ABC star terpolymer

per chain are listed below.

$$f_{II} = \frac{3}{4} \frac{A_{II}}{\phi_A^2 A_T} G(L^2 L_{AC1}^2, L^2 H_{AC}^2) \quad (3.93)$$

$$f_{III} = \frac{3}{4} \frac{A_{III}}{\phi_C^2 A_T} G(L^2 L_{AC2}^2, L^2 H_{AC}^2) \quad (3.94)$$

$$f_{IV} = \frac{3}{4} \frac{A_{IV}}{\phi_C^2 A_T} G(L^2 L_{BC2}^2, L^2 H_{BC}^2) \quad (3.95)$$

$$f_V = \frac{3}{4} \frac{A_V}{\phi_B^2 A_T} G(L^2 L_{BC1}^2, L^2 H_{BC}^2) \quad (3.96)$$

$$f_{VI} = \frac{3}{4} \frac{A_{VI}}{\phi_B^2 A_T} G(L^2 L_{AB2}^2, L^2 H_{AB}^2) \quad (3.97)$$

On solving the integrals they will also give the same analytical solution but with different length parameters. In terms of the integral solutions I_I , I_{II} , I_{III} , I_{IV} , I_V and I_{VI} the stretching energy per chain in the units of $k_B T$ in the triangle with ABC star in it is

$$\begin{aligned} f_{stretch} = & \frac{3}{4} \frac{A_I}{\phi_A^2 A_T} I_I + \frac{3}{4} \frac{A_{II}}{\phi_A^2 A_T} I_{II} + \frac{3}{4} \frac{A_{III}}{\phi_C^2 A_T} I_{III} \\ & + \frac{3}{4} \frac{A_{VI}}{\phi_C^2 A_T} I_{VI} + \frac{3}{4} \frac{A_V}{\phi_B^2 A_T} I_V + \frac{3}{4} \frac{A_{VI}}{\phi_B^2 A_T} I_{VI} \end{aligned} \quad (3.98)$$

From the general structure of the stretching energy, after replacing X s and Y s, a factor of L^2 is found in all the terms. The overall stretching energy is again in the format ML^2 which we saw for diblock structures. Here also, M has all the geometrical properties that arise from the monomer composition and morphological structure. Thus the total free energy expense per chain f_c in the units of $k_B T$ to form a hexagonal morphology by ABC star terpolymers is

$$\begin{aligned} f_c = & f_{int} + f_{stretch} \\ = & \frac{4\sqrt{10}}{\sqrt{3}L} (\nu_{AB} H_{AB} + \nu_{BC} H_{BC} + \nu_{AC} H_{AC}) + \\ & \frac{3}{4A_T} \left(\frac{A_I I_I + A_{II} I_{II}}{\phi_A^2} + \frac{A_{III} I_{III} + A_{IV} I_{IV}}{\phi_C^2} + \frac{A_V I_V + A_{VI} I_{VI}}{\phi_B^2} \right) \end{aligned} \quad (3.99)$$

The free energy per chain for the triangular patch of a hexagon is now completely in terms of the monomer compositions ϕ_A , ϕ_B and interactions, ν_{AB} , ν_{BC} and ν_{AC} . The core radius is included in the constant $R_D = \frac{R}{R_c}$. We fix this constant

3. Formulation of Strong Segregation Theory for ABC star terpolymer

$R_D = 10$ throughout the calculations. The core radius is taken to be smaller than the random walk chain length. With this, we can look at the different patterns formed in hexagonal morphology.

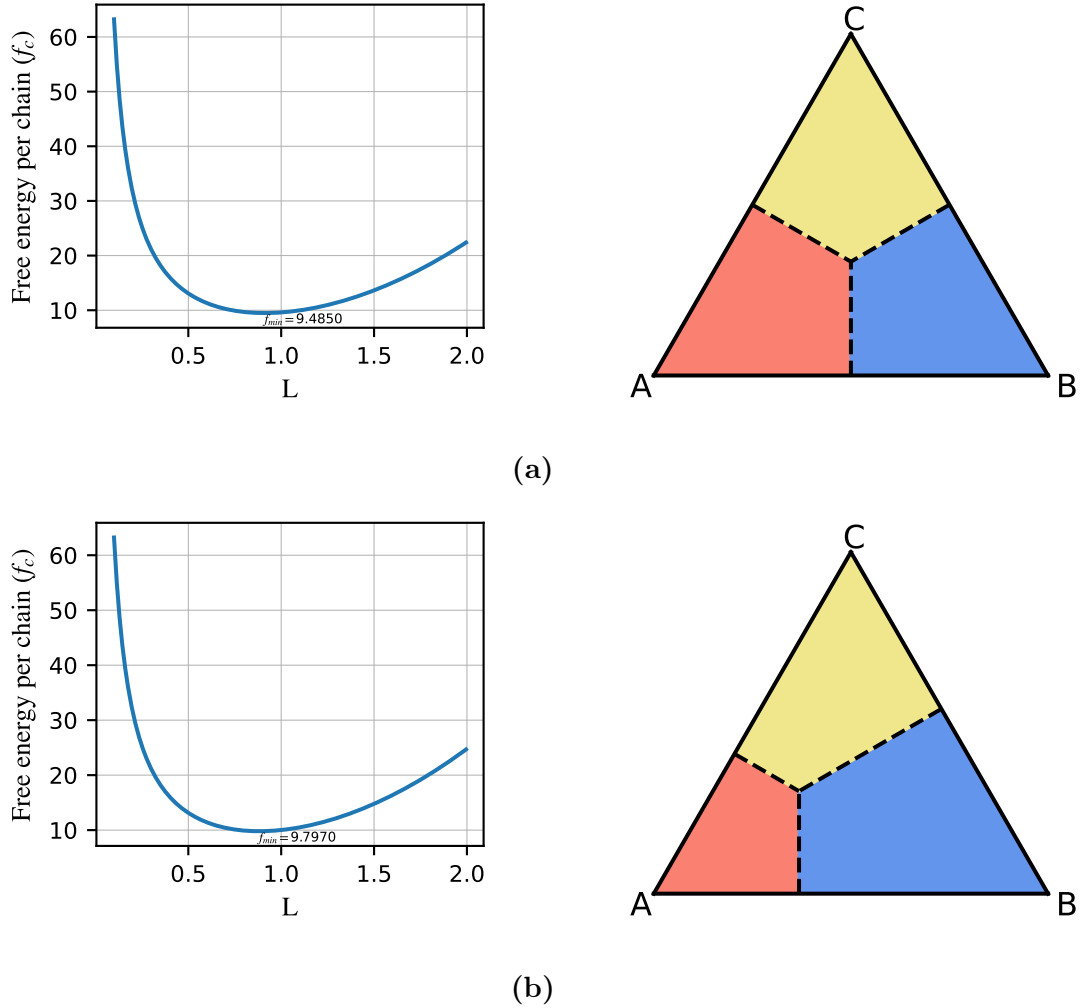


Figure 3.13: Free energy per chain for two different monomer compositions as given in triangular patch. The plots on top (a) are for the compositional symmetric case where $\phi_A = \frac{1}{3}$, $\phi_B = \frac{1}{3}$ and $\phi_C = \frac{1}{3}$ and bottom ones (b) are for $\phi_A = 0.20$, $\phi_B = 0.45$ and $\phi_C = 0.35$. The interaction between branches are equal, $\nu_{AB} = \nu_{BC} = \nu_{AC} = 1$ here. The stretching free energy varies with the dimensionless length of the equilateral triangle $L = \frac{l}{R}$. The stretching of chains and interfacial tension varies with L .

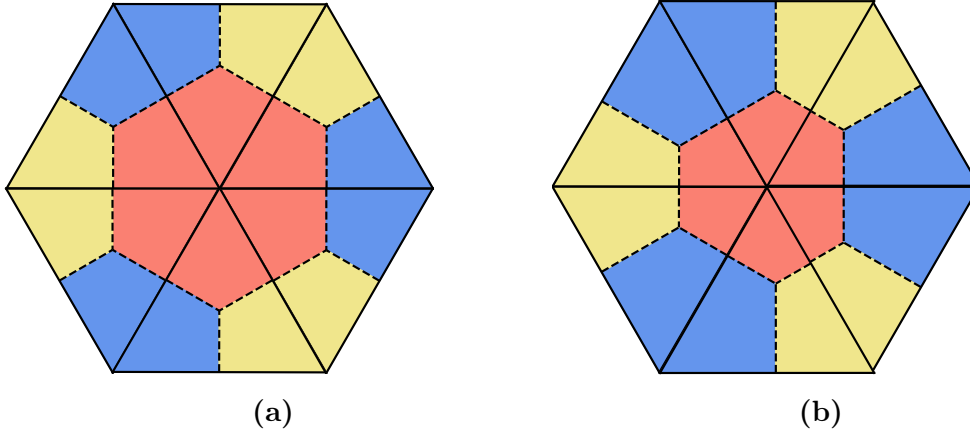


Figure 3.14: Hexagonal morphology patterns formed from tiling the triangles together. The morphology in (a) corresponds to the monomer compositions $\phi_A = \frac{1}{3}$, $\phi_B = \frac{1}{3}$ and $\phi_C = \frac{1}{3}$ and (b) occurs when $\phi_A = 0.20$, $\phi_B = 0.45$ and $\phi_C = 0.35$. These images are made by aligning previous triangles in image processing software. The interaction strength between branches are equal, $\nu_{AB} = \nu_{BC} = \nu_{AC} = 1$ here.

The expression for total free energy per chain again has two terms that are dependent on the lengthscale of the triangular patch. When the length of the triangle increases the polymer chains are able to stretch more and hence the stretching energy increases. When the length of the triangle L decreases the chains are less stretched and interfacial tension increases. At an equilibrium length $L = L^*$, the free energy will be lowest and we get the stable triangle pattern for hexagonal morphology for a given set of monomer compositions, (ϕ_A, ϕ_B, ϕ_C) . The stable triangle patch and the free energy per chain variation with the length L for two different sets of compositions are given in fig. 3.13. In both free energy plots there is a minimum which indicates the side length at which the morphology is stable for a given monomer composition. The value of minimum free energy depends on the monomer composition. The topology of this morphology remains unchanged with any change in monomer composition, that is the neighbours of the domains remains same. But geometry of these domains changes with monomer composition. An example of a complete periodic hexagon image from two triangular domains given in fig. 3.13 is shown in fig. 3.14. For the symmetric case with the same monomer compositions, all coloured domains are regular hexagons. Whereas, when monomer compositions are unequal we will get a combination of irregular hexagons. So to find the monomer compositions with hexagons with the lowest free energy, we find the free energy per chain for all valid (ϕ_A, ϕ_B, ϕ_C) .

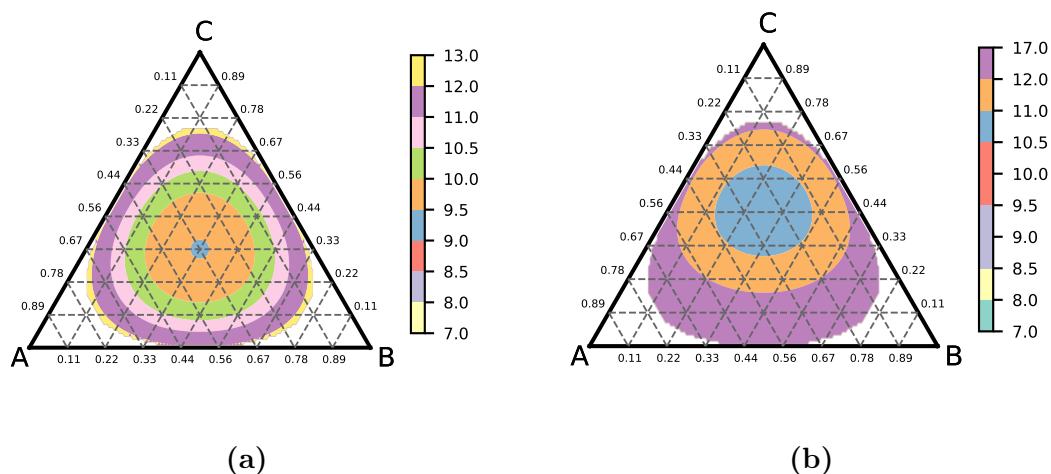


Figure 3.15: Minimum free energy variation with polymer composition for hexagonal morphology using equilateral triangle tile for ABC star architecture with (a) symmetric interactions $\nu_{AB} = \nu_{BC} = \nu_{AC} = 1$ and (b) asymmetric interactions $\nu_{AB} = 1.6$, $\nu_{BC} = \nu_{AC} = 1$.

Now we are in a position to explore the composition space where (ϕ_A, ϕ_B, ϕ_C) will give a valid structure. This space is a triangular space similar to the composition space in chapter 2, fig. 2.24. The compositions of A , B and C will be 1 at the corners and all other values are available inside the triangle. Here we have indicated the compositions between 0 and 1 with a step size of 0.11. The minimum values of free energy per chain for an ABC star terpolymer with equal interaction strengths $\nu_{AB} = \nu_{BC} = \nu_{AC} = 1$, between $A - B$, $B - C$ and $A - C$ is plotted as contours in fig. 3.15.(a). In fig. 3.15.(b) the contours for terpolymer with unequal interaction strengths $\nu_{AB} = 1.6$, $\nu_{BC} = \nu_{AC} = 1$ are plotted. When the interaction strengths between the branches are equal, the monomer compositions at the centre of the ternary plot have hexagons with the lowest free energy. As we move away from the centre of the composition triangle, the value of minimum free energy increases symmetrically. These results agree with previously obtained results in [50, 159] that hexagonal morphologies have lower free energy when all the branches have the same length for compositionally symmetric case.

From our formulation of free energy, the block copolymer system can be made asymmetric in interaction strength by varying the values of ν_{IJ} 's. Using the same computational method for the symmetric case monomer composition space for this polymer melt where $\nu_{AB} = 1.6$ is evaluated and is given in fig. 3.15.(b). This change in interaction favours more $A - C$ and $B - C$ interface compared to the $A - B$ interface. Thus the polymer architectures with a greater fraction of

C type have lower values for free energy and the free energy contour is no longer symmetric in all directions in the composition space. There is a mirror symmetry in the contours along the line $\phi_A = \phi_B$.

Our SST formulation using triangles facilitates easier evaluation of free energy compared to other methods like SCFT, Monte Carlo and DPD. This method also allows a simple and powerful way to play with the monomer interactions. But if we want to analyse a variety of morphologies then we are required to construct different triangles or orbifolds for each morphologies and figure out a way to align them together. An orbifold is the smallest unit within a pattern from which we can form the entire pattern when we apply symmetry operations like mirroring, rotation, translation and sliding. The orbifold for the hexagonal morphology is the equilateral triangle we analysed. For simpler morphologies observed in ABC star terpolymer like hexagons [6.6.6], squares [8, 8, 4] and triangles [12, 6, 4], the orbifold will be simple triangles. As the morphology gets complex their orbifolds also get complex and can contain more than one core in it. Instead of making morphologies from one type of triangle (an equilateral triangle for a hexagon), the orbifolds will be made of a single type of triangle or a combination of different triangles. With the ambition of investigating for aperiodic tilings that are found in quasicrystals, we need a more generalised formulation that can facilitate free energy analysis for a variety of morphologies.

In addition, free energy analysis of different morphologies is often done by normalising with respect to the free energy of a symmetric structure as was demonstrated in the diblocks case. The presence of the log and arctan functions in the free energy expression due to the core makes this normalisation complicated process for ABC star terpolymer structures. The triangle formulation does not allow us to visualise the geometrical effect of monomer interactions on the interfaces in the minimised pattern. These reasons call for a more generalised and powerful formulation to analyse the phase separation in ABC star. Hence we introduce the method of $SSPs$ which can overcome all these issues and also facilitate as a powerful tool in free energy analysis for most of the $2D$ morphologies. A detailed formulation of $SSPs$ is discussed in the next section.

3.5 Strongly Segregated Polygon method

In the previous section, we discussed how many regular, periodic phase separated structures can be treated by using a triangular structure as the orbifold. However, if we are to treat more complicated structures, such as periodic approximants to quasicrystals, we need a more general formulation of the strong segregation theory. In this section we are introducing a novel structure, Strongly Segregated Polygon (SSP), which encapsulates the free energy per chain and geometry of the morphology irrespective of their orbifolds. By choosing different alignments for

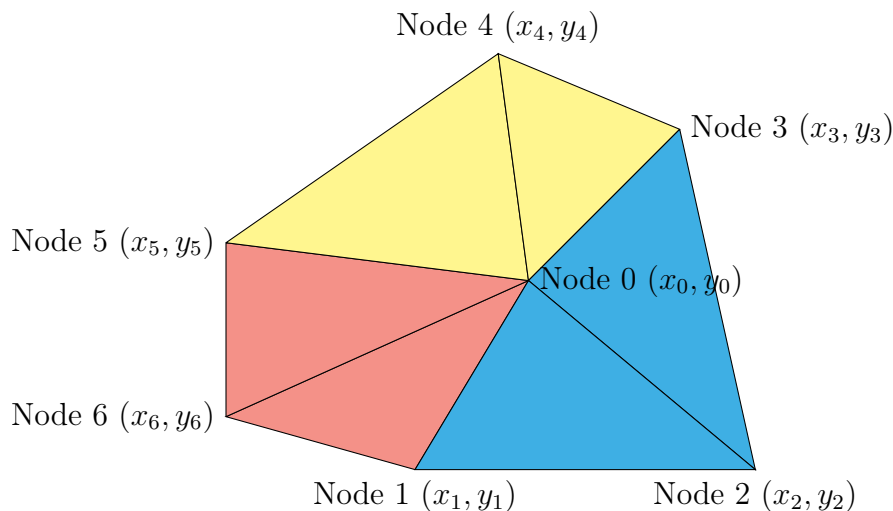


Figure 3.16: The structure of an SSP with seven nodes is given here. All the nodes Node i and their position coordinates are also given. Here again, we assign red, blue and yellow regions as domains of A , B and C monomer types.

$SSPs$, a variety of morphologies can be analysed using the same basic structure. Although we perform the analysis here only for a hexagonal structure, which is sufficient for our purposes, the formulation can be generalised to higher-order polygons or three-dimensional structures.

The Strongly Segregated Polygon (SSP) method uses the same idea as in the equilateral triangle above but allows more degrees of freedom to the vertices. The hexagonal SSP which is the basic unit in this calculation is given in fig. 3.16 with seven nodes. The polygon is divided into three regions as indicated by different colours in fig. 3.16 where each region is assigned to different monomer types. The colour map is again: red for A , blue for B and yellow for C throughout the focus of this thesis. The seven nodes in this polygon have the freedom to move around anywhere as long as they make a valid polygon containing ABC star terpolymers. Each node is defined by its x and y coordinates. The free energy per chain for ABC stars within the SSP is to be determined uniquely by the position of the nodes, and so free energy minimisation can be performed by adjusting the node positions. These seven nodes allow flexibility to the domains via which they can be assembled into a wide variety of structures. In this section first, we determined the free energy per chain in an SSP using the interfacial energy and stretching free energy. We then discuss how $SSPs$ can be assembled together, and periodic boundary conditions applied to form a phase-separated structure. Here we will use the hexagonal morphology as an example, allowing us to make a comparison with the results of the previous section.

3. Formulation of Strong Segregation Theory for ABC star terpolymer

The SSP is divided into six triangles in a similar manner as the equilateral triangle in the previous section. Although fig. 3.16 indicates there are seven nodes, in practice the monomer composition of the stars uniquely determines the position of node 0 at the core of the polygon, once the position of the other six nodes is specified. We first determine and sum the stretching energies of the 6 triangles : $\Delta 016$, $\Delta 065$, $\Delta 054$, $\Delta 043$, $\Delta 032$ and $\Delta 021$ indicated in fig. 3.16. The interfaces are line segments between nodes 0 and 1, nodes 0 and 3 and nodes 0 and 5. So, given we know the position of the core, the interfacial energy can be determined.

We first consider the monomer composition, and how we can determine the position of node 0. The monomer compositions are related to the node positions through the areas as follows.

$$\begin{aligned}\phi_A &= \frac{\text{Area}(\Delta 016) + \text{Area}(\Delta 065)}{A_T} = \frac{A_{016} + A_{065}}{A_T}, \\ \phi_B &= \frac{\text{Area}(\Delta 012) + \text{Area}(\Delta 023)}{A_T} = \frac{A_{012} + A_{023}}{A_T}, \\ \phi_C &= \frac{\text{Area}(\Delta 034) + \text{Area}(\Delta 045)}{A_T} = \frac{A_{034} + A_{045}}{A_T}.\end{aligned}\tag{3.100}$$

The area of the triangles and the total area of the polygon A_T are expressed in terms of the node coordinates in vector form. The position vector of the node i with respect to the core (node 0) is \vec{r}_{0i} . Following this labelling convention, the areas are:

$$\begin{aligned}A_{016}^{\vec{}} &= \frac{1}{2}(\vec{r}_{01} \times \vec{r}_{06}); & A_{012}^{\vec{}} &= \frac{1}{2}(\vec{r}_{02} \times \vec{r}_{01}) \\ A_{023}^{\vec{}} &= \frac{1}{2}(\vec{r}_{03} \times \vec{r}_{02}); & A_{034}^{\vec{}} &= \frac{1}{2}(\vec{r}_{04} \times \vec{r}_{03}) \\ A_{065}^{\vec{}} &= \frac{1}{2}(\vec{r}_{06} \times \vec{r}_{05}); & A_{045}^{\vec{}} &= \frac{1}{2}(\vec{r}_{05} \times \vec{r}_{04})\end{aligned}\tag{3.101}$$

$$\begin{aligned}A_T &= \frac{1}{2}((x_1y_2 - x_2y_1) + (x_2y_3 - x_3y_2) + \\ &\quad (x_3y_4 - x_4y_3) + (x_4y_5 - x_5y_4) + \\ &\quad (x_5y_6 - x_6y_5) + (x_6y_1 - x_1y_6))\end{aligned}$$

The area defined above is defined in a "clockwise sense" for all triangles, i.e. all triangle areas in the polygon of fig. 3.16 would be positive. In any phase-separated structure, it is also necessary to have polygons defined in the opposite

sense (i.e. so that the order of red, yellow and blue on travelling clockwise around the core is an odd permutation from fig. 3.16). For such a polygon, all areas would be negative. However, any polygon in which some areas are positive and some negative is invalid: it implies a nonphysical polygon structure which would be impossible to fill with star polymers

The three equations in eq. (3.100) can be solved for (x_0, y_0) with the constraint $\phi_A + \phi_B + \phi_C = 1$, to determine the position of the core as a function of monomer compositions and known coordinates of other six nodes. Solving the position of the core is

$$\begin{aligned}
 x_0 &= \frac{(2(1 - \phi_A - \phi_B)A_T - x_3y_4 - x_4y_5 + x_4y_3 + x_5y_4)(x_1 - x_5)}{(y_3 - y_5)(x_1 - x_5) - (y_5 - y_1)(x_5 - x_3)} - \\
 &\quad \frac{(2\phi_A A_T + x_6y_5 + x_1y_6 - x_5y_6 - x_6y_1)(x_5 - x_3)}{(y_3 - y_5)(x_1 - x_5) - (y_5 - y_1)(x_5 - x_3)}, \quad (3.102) \\
 y_0 &= \frac{2\phi_A A_T + x_6y_5 + x_1y_6 - x_5y_6 - x_6y_1 - x_0(y_5 - y_1)}{(x_1 - x_5)}.
 \end{aligned}$$

The core, which is given by node 0 should always be inside the SSP. Any node combinations that agree with these conditions are considered physically valid. This statement is equivalent to the statement above that all triangle areas should have the same sign. For a given value of ϕ_A and ϕ_B (and $\phi_C = 1 - \phi_A - \phi_B$), and for some positions of nodes 1-6, it is possible that the core node position given in eq. (3.102) does not satisfy this constraint: this would mean that the nodes 1-6 are arranged in an invalid configuration. Hence it is necessary to test for validity of the configuration.

If the position of the core is known, the interfacial lengths can be obtained using straightforward coordinate geometry. Thus the interfacial energy is determined in the same way as for the equilateral triangle case. While the stretching energy calculation requires a bit more geometrical manipulation via this method.

3.5.1 Interfacial energy in an SSP

Interfacial energy, f_{int} will have the same expression as in the equilateral triangle method. The interface lengths between the domains are obtained from nodes between them. In the *SSP*, interfacial lengths are between the nodes 0 and 1: l_{01} , nodes 0 and 3: l_{03} and nodes 0 and 5: l_{05} . These lengths in terms of node

coordinates are :

$$l_{01} = \sqrt{(x_0 - x_1)^2 + (y_0 - y_1)^2}, \quad (3.103)$$

$$l_{03} = \sqrt{(x_0 - x_3)^2 + (y_0 - y_3)^2}, \quad (3.104)$$

$$l_{05} = \sqrt{(x_0 - x_5)^2 + (y_0 - y_5)^2}. \quad (3.105)$$

Consider that this polygon will extend along the axis of the core in a third dimension into the page with depth D . The interfacial energy at each surface (IJ : between chains of type I and J) will be the surface tension γ_{IJ} times the area of the surface. So the interfacial energy in the units of $k_B T$ is,

$$F_{int} = \gamma_{AB}A_{AB} + \gamma_{BC}A_{BC} + \gamma_{AC}A_{AC} \quad (3.106)$$

where A_{AB} , A_{BC} and A_{AC} are the interfacial areas. The interfacial area per chain f_{int} in the units of $k_B T$ is then,

$$\begin{aligned} f_{int} &= \frac{(\gamma_{AB}l_{03}D + \gamma_{BC}l_{03}D + \gamma_{AC}l_{05}D) \Omega}{A_T D} \\ &= \frac{(\gamma_{AB}L_{03} + \gamma_{BC}L_{03} + \gamma_{AC}L_{05}) \Omega}{RA_T} \end{aligned} \quad (3.107)$$

where we have introduced a dimensionless triangle side length $L_{0i} = \frac{l_{0i}}{R}$ scaled by the chain random walk length $R = \sqrt{N}b$ and Ω is the volume per chain. The i in the subscript indicates the node. In eq. (3.75), we can introduce a scaled surface tension $\xi_{IJ} = \frac{\gamma_{IJ}\Omega}{Rk_B T}$. We introduced a new scaling of $\nu_{IJ} = \frac{\xi_{IJ}}{\sqrt{10}}$ to maintain the strong segregation limit in eq. (3.77). Thus, the final expression for interfacial energy per chain in the units of $k_B T$ for an SSP is

$$f_{int} = \frac{\sqrt{10}}{A_T} (\nu_{AB}L_{03} + \nu_{BC}L_{03} + \nu_{AC}L_{05}) \quad (3.108)$$

The interfacial energy per chain is now in terms of the position coordinates of the nodes. As long as we have a valid polygon interfacial energy per chain of domains of any shape can be obtained.

3.5.2 Stretching energy in an SSP

The stretching free energy is determined for each triangle separately and then added up to find the total stretching energy per chain in an SSP . The method is

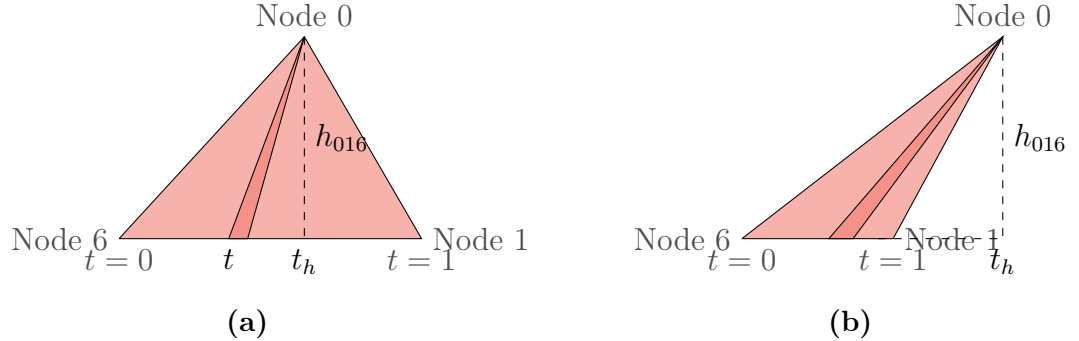


Figure 3.17: Example of two different possible geometries of $\Delta 016$ is given. The side length is parameterised by t . The height h_{016} of the triangle is marked in both cases which intersects the side length at t_h .

the same as in the case of a triangular patch of the hexagonal morphology. The triangles under concern in an *SSP* are not right-angled, so a bit more geometrical calculations are needed here. The node 0 is where the core of the *ABC* star terpolymer is placed and this gives the logarithmic correction to the stretching free energy. We are demonstrating the calculation of stretching free energy per chain by taking the triangle $\Delta 016$.

The $\Delta 016$ can be any arbitrary triangle with acute or obtuse angles. It can be broad with the height of the triangle placed inside the triangle as shown in fig. 3.17.(a) or narrow with height placed outside the triangle as in fig. 3.17.(b). If these triangles are divided into small wedges, then the length of the side is determined by adding the wedges from nodes 1 and 6. The stretching free energy of the wedge is determined which is then integrated over the length l_{06} to determine the total free energy per chain in the triangle. For the equilateral triangle patch, the height of the triangle and side length are obtained easily through simple coordinate geometry. We usually write the radius of the wedge r in terms of the perpendicular distance from the core to the triangle. Here the distance of the wedge from the point of intersection of triangle height, h_{016} and side length l_{16} can be either in positive or negative direction depending on the reference node we are choosing: (1 or 6). So the length of the triangle along nodes 1 and 6 is parameterised using a variable t that can take values from 0 to 1 between node 1 and 6. Thus the distance of the wedge from the intersection point is always positive as a length should be. In vector notation the nodes are written as $\vec{r}_0 = [x_0, y_0]^T$, $\vec{r}_1 = [x_1, y_1]^T$ and $\vec{r}_6 = [x_6, y_6]^T$. The perpendicular from node 0 intersects the line between node 1 and 6 at \vec{r}_h which is at t_h distance from the reference node, say node 1. Since $(\vec{r}_h - \vec{r}_0)$ is perpendicular to $(\vec{r}_6 - \vec{r}_1)$ the dot product should

3. Formulation of Strong Segregation Theory for ABC star terpolymer

result in zero. This gives the distance of the interaction point, t_h from node 1.

$$t_h = \frac{(\vec{r}_1 - \vec{r}_0) \cdot (\vec{r}_6 - \vec{r}_1)}{(\vec{r}_6 - \vec{r}_1)^2}. \quad (3.109)$$

Now that t_h is obtained in terms of the available nodes, heights of the triangle will be $h_{016} = |\vec{r}_h - \vec{r}_0|$, which agrees with the following equation:

$$\vec{r}_h - \vec{r}_0 = \vec{r}_1 - \vec{r}_0 + t_h (\vec{r}_6 - \vec{r}_1). \quad (3.110)$$

Thus the triangle height, h_{016} is

$$h_{016} = \sqrt{(\vec{r}_h - \vec{r}_0) \cdot (\vec{r}_h - \vec{r}_0)}. \quad (3.111)$$

The side length of the triangle is also obtained from nodes as

$$l_{016} = \sqrt{(x_6 - x_1)^2 + (y_6 - y_1)^2}. \quad (3.112)$$

Here these two lengths obtained from the given nodes as shown above are the key information needed to calculate the stretching free energy for $\Delta 016$. With t_h obtained from the given nodes, the radius of the wedge r at any t is then

$$r = \sqrt{((t - t_h)l_{016})^2 + h_{016}^2} \quad (3.113)$$

On substituting this wedge radius for r in stretching free energy for the wedge in eq. (3.80), we get the stretching energy of the wedge in $\Delta 016$. The stretching free energy per chain in a triangle will have a similar expression as in eq. (3.86), where the stretching free energy is divided by the number of chains in the triangle. To determine the total stretching energy per chain from $\Delta 016$ the free energy of the wedge in the units of $k_B T$ is integrated over the parameterised side length.

$$f_{016} = \frac{A_{016}}{\phi_A A_T} \int_0^1 f_c \left(\sqrt{((t - t_h)l_{016})^2 + h_{016}^2} \right) dt. \quad (3.114)$$

On expanding the free energy expression as in eq. (3.80), we get

$$f_{016} = \frac{A_{016}}{\phi_A A_T} \int_0^1 \frac{3}{4} \frac{((t - t_h)l_{016})^2 + h_{016}^2}{\phi_A N b^2} \log \frac{((t - t_h)l_{016})^2 + h_{016}^2}{R_c^2} dt. \quad (3.115)$$

As mentioned earlier all lengths are scaled with the random walk chain step length as: $L_{016} = \frac{l_{016}}{R}$ and $H_{016} = \frac{h_{016}}{R}$. All lengths are normalised with R and the final integral will have the form

$$f_{016} = \frac{3}{4} \frac{A_{016}}{\phi_A^2 A_T} \int_0^1 \left(((t - t_h)L_{016})^2 + H_{016}^2 \right) \log \left(R_D^2 \left(((t - t_h)L_{016})^2 + H_{016}^2 \right) \right) dt. \quad (3.116)$$

3. Formulation of Strong Segregation Theory for ABC star terpolymer

where $R_D = \frac{R}{R_c}$ which was defined in previous section. We choose $R_D = 10$ in the calculations. The contribution of stretching free energy from $\Delta 016$ is obtained by solving the above integral.

The above integral is of the general form,

$$I_{0ij} = G(X, Y) = \int_0^1 (X(t - t_h)^2 + Y) \log(c(X(t - t_h)^2 + Y)) dt, \quad (3.117)$$

where $X = L_{0ij}^2$, $Y = H_{0ij}^2$ and $c = R_D^2$ and can be solved analytically. On substituting $t - t_h = u$, integral I_{0ij} becomes

$$I_{0ij} = \int_{-t_h}^{1-t_h} (Xu^2 + Y) \log(c(Xu^2 + Y)) du. \quad (3.118)$$

The integral in eq. (3.118) is now in the same form as the integral in eq. (3.90), which is the stretching energy in the triangular region in the equilateral triangle patch for a hexagon. The analytical solution of I_{0ij} is

$$\begin{aligned} I_{0ij} = & \log(c(X(1 - t_h)^2 + Y)) \left(\frac{X(1 - t_h)^3}{3} + Y(1 - t_h) \right) + \\ & \log(c(Xt_h^2 + Y)) \left(\frac{Xt_h^3}{3} + Yt_h \right) - \frac{2X}{9} ((1 - t_h)^3 + t_h^3) - \frac{4Y}{3} \\ & + \frac{4Y}{3} \sqrt{\frac{Y}{X}} \left(\arctan \sqrt{\frac{X}{Y}}(1 - t_h) + \arctan \sqrt{\frac{X}{Y}}t_h \right). \end{aligned} \quad (3.119)$$

When $t_h = 0$, the length of the height will be along one of the sides $\bar{0}1$ or $\bar{0}6$, which is then a right-angled triangle.

$$I_{t_h=0} = \log(c(X + Y)) \left(\frac{X}{3} + Y \right) - \frac{2X}{9} - \frac{4Y}{3} + \frac{4Y}{3} \sqrt{\frac{Y}{X}} \arctan \sqrt{\frac{X}{Y}}. \quad (3.120)$$

The analytical solution is the same as that for the equilateral triangle case given in eq. (3.92). This verifies that the analytical solution is valid and the equilateral triangle is a special case of the more generalised SSP formulation.

Hence, for the triangle $\Delta 016$, the stretching free energy per chain in the units of $k_B T$ due to any triangle formed between nodes 0, 1 and 6 is

$$f_{016} = \frac{3}{4} \frac{A_{016}}{\phi_A^2 A_T} I_{016}. \quad (3.121)$$

For total stretching energy per chain of an SSP , we determine the stretching energy for the other 5 regions. Here is the list of stretching free energies for the

rest of the triangles. Each of them is in terms of the respective nodes indicated by the second and third positions in the subscript. The characteristic lengths and monomer types are different for each triangle.

$$\begin{aligned}
 f_{065} &= \frac{3}{4} \frac{A_{065}}{\phi_A^2 A_T} G(L_{065}^2, H_{065}^2), \\
 f_{045} &= \frac{3}{4} \frac{A_{045}}{\phi_C^2 A_T} G(L_{045}^2, H_{045}^2); \quad f_{034} = \frac{3}{4} \frac{A_{034}}{\phi_C^2 A_T} G(L_{034}^2, H_{034}^2), \\
 f_{023} &= \frac{3}{4} \frac{A_{023}}{\phi_B^2 A_T} G(L_{023}^2, H_{023}^2); \quad f_{012} = \frac{3}{4} \frac{A_{012}}{\phi_B^2 A_T} G(L_{012}^2, H_{012}^2).
 \end{aligned} \tag{3.122}$$

This will result in six integrals : I_{016} , I_{065} , I_{045} , I_{034} , I_{023} and I_{012} . The solutions of all these will have the same expression as in eq. (3.119). The values of X and Y vary with the chosen triangle as indicated above. The stretching free energy of an SSP in the units of $k_B T$, f_{str} is obtained by summing the stretching energy contributions from all six triangles.

$$\begin{aligned}
 f_{str} &= \frac{A_{016}}{\phi_A A_T} I_{016} + \frac{A_{065}}{\phi_A A_T} I_{065} + \frac{A_{045}}{\phi_C A_T} I_{045} + \\
 &\quad \frac{A_{034}}{\phi_C A_T} I_{034} + \frac{A_{023}}{\phi_B A_T} I_{023} + \frac{A_{012}}{\phi_B A_T} I_{012}.
 \end{aligned} \tag{3.123}$$

Thus we have the stretching free energy eq. (3.123) and interfacial free energy eq. (3.108) of the polygon defined by coordinates of 6 nodes and two monomer compositions (ϕ_A, ϕ_B) , with $\phi_C = 1 - \phi_A - \phi_B$. The expression for stretching energy is complicated but it is analytically solvable given we know the nodes. Thus, the total free energy per chain for an SSP f_c in the units of $k_B T$ is,

$$f_c = f_{int} + f_{str} \tag{3.124}$$

For a given monomer composition and morphology, the nodes will take the position coordinates to lower the free energy per chain.

3.6 Shape shifting minimisation

Using the SSP method established in the previous section the total free energy per chain for any 2D morphology in ABC star terpolymer melt can be determined. We only need to know the repeating unit of the morphology and its node coordinates. The nodes in $SSPs$ are free to move in order to find a stable configuration. For a given monomer composition and morphology, the stable configuration is the one which has the lowest value for free energy per chain. We can

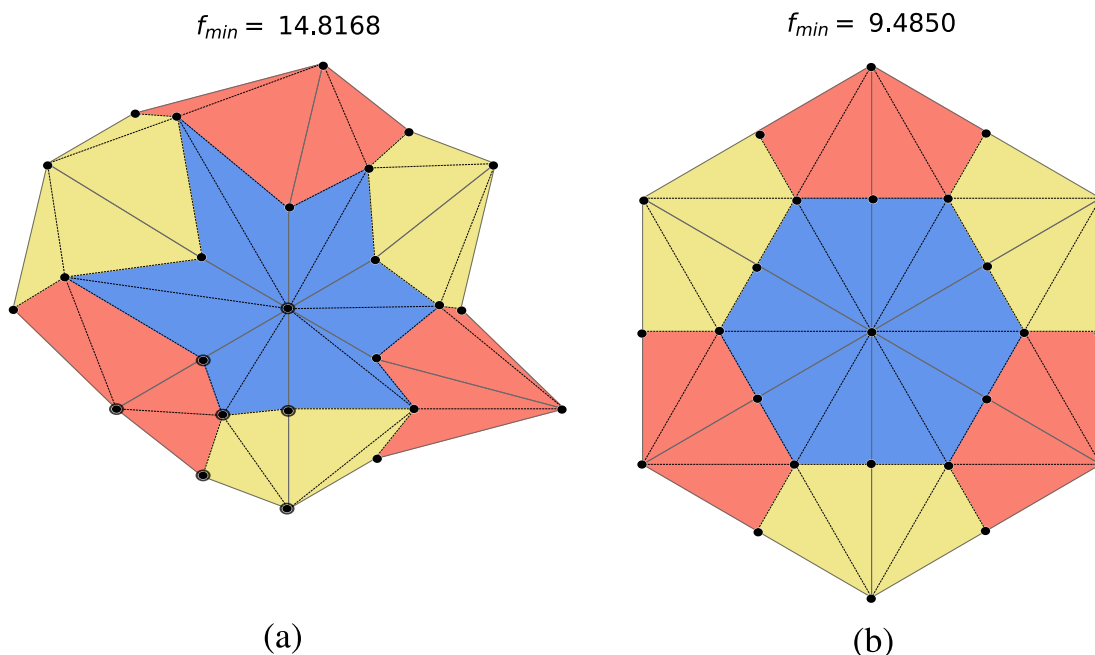


Figure 3.18: Shape shifting minimisation explained using SSPs. The initial combination of six SSPs for hexagonal morphology is given in (a). Highlighted dots represent an SSP. The remaining SSPs are placed according to ABC star matching rules. In (b) the end result after shape shifting minimisation is given. All the nodes align to form a perfect hexagon when $\phi_A = \phi_B = \phi_C$.

minimise the configuration by varying the nodes by applying some constraints. The constraints are chosen with respect to the morphology. As the process of finding a stable structure involves changing the shape of the SSP , we call this process shape shifting minimisation.

This minimisation process is explained here by taking the hexagonal morphology as an example. The structure of the SSP and the free energy map obtained through this process must agree with the equilateral triangle case.

The morphologies in ABC star architecture follow matching rules for tiling from its chain structure. Any coloured domain will be surrounded by alternating combinations of the other two coloured domains. For example, the blue domain will be surrounded by alternating red and yellow domains as shown in fig. 3.18. The same is true for red and yellow domains.

In the hexagonal morphology, all domains are surrounded by six alternating domains, hence in topological nomenclature, they are identified as $[6, 6, 6]$. So the constraints are chosen such that $SSPs$ align together to form $[6, 6, 6]$ as given in fig. 3.18.(a). The constraints are (i) the monomer compositions and

3. Formulation of Strong Segregation Theory for ABC star terpolymer

(ii) the periodicity of the domains. The length at which a domain is repeated again is unique for each morphology. By deciding the length and direction of the appearance of the next domain we can get the stable configuration for a given set of monomer compositions.

The free energy of an SSP is dependent on 17 variables: $x_1, y_1, x_2, y_2, \dots, x_6, y_6$, the monomer compositions ϕ_A, ϕ_B and the interaction strengths ν_{AB}, ν_{BC} and ν_{AC} . If we fix the terpolymer parameters (monomer compositions and interaction strengths), the minimum value of free energy is determined by varying the 12 position variables. As mentioned, the topology is fixed by aligning the $SSPs$ according to the periodicity in the morphology. Thus 6 $SSPs$ of random shapes are aligned together as given in fig. 3.18.(a). In a hexagonal morphology, the centre of the red domains are at equal distances. This will be the periodic constraint applied to the structure fig. 3.18.(a). The configuration in (a) is varied by repositioning the nodes in order to agree with the constraints and hence decrease the total free energy per chain. The nodes of one SSP are indicated in bigger black dots in fig. 3.18.(a).

The total free energy per chain becomes a function of all the nodes present in the arrangement. The nodes of one SSP are indicated in bigger black dots in fig. 3.18.(a) and the rest are in smaller black dots. All black dots are rearranged through different SSP configurations during the minimisation process. A numerical multi-variable minimisation method that takes smaller step sizes between the variables is needed for shape shifting minimisation to find the valid, stable configuration of $SSPs$. More details on the numerical minimisation are in Chapter 4.

In the case of the initial SSP configuration with hexagonal constraints in fig. 3.18.(a), the final stable configuration obtained after minimisation is given in fig. 3.18.(b). The value of the free energy per chain for hexagonal morphology using SSP is the same as the minimum free energy per chain obtained for hexagonal morphology using equilateral triangle analysis in fig. 3.13.(a). Both these configurations corresponds to the monomer compositions $\phi_A = \phi_B = \phi_C = \frac{1}{3}$.

Now we are in a position to vary the monomer compositions to explore other patterns in the same morphology. The monomer composition is varied over all possible combinations of ϕ_A and ϕ_B to obtain the free energy map. The resultant map is given in fig. 3.19. Free energy contours in this plot are identical to that of fig. 3.15 which was obtained using the equilateral triangle patch. The free energy map in fig. 3.19 explores more space in the composition triangle. The symmetric composition where $\phi_A = \phi_B = \phi_C = \frac{1}{3}$ has the lowest free energy per chain value. The free energy per chain values increase symmetrically in the composition map as we move away from the centre. The free energy maps of unequal monomer interactions can be obtained using the same method. A more detailed morphological analysis using $SSPs$ is in chapter 5.

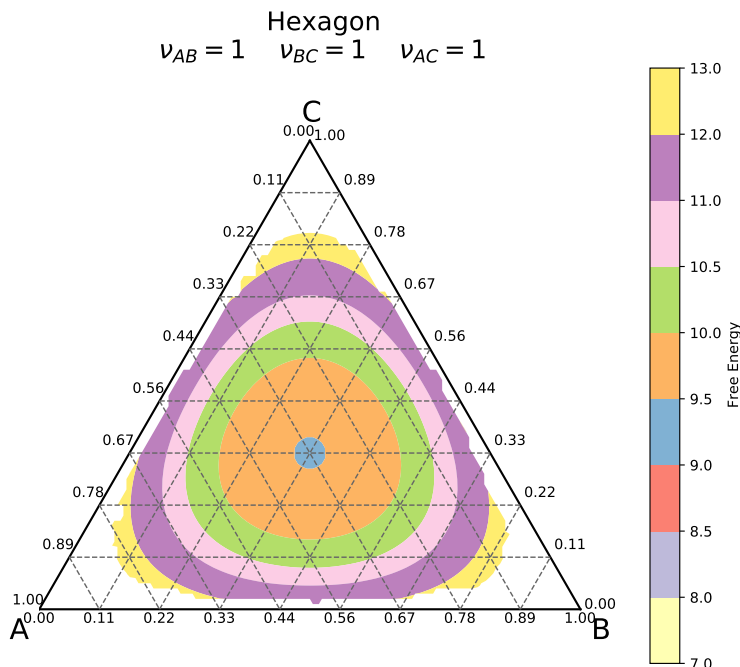


Figure 3.19: Free energy map for hexagonal morphology determined using shape-shifting minimisation of $SSPs$ is given. The contours are exactly the same as fig. 3.15.

3.7 Summary

In this chapter, we developed a versatile SST framework to study different morphologies in ABC star terpolymer. The SST analysis for diblocks was reviewed and inspirations were drawn from it to develop a similar analysis for ABC star architecture. This chapter introduced the concept of $SSPs$ and shape shifting minimisation. The SSP for ABC star terpolymer is a hexagonal structure with three domains sharing a unique core where three branches intersect. The SSP method is more generalised and versatile compared to the triangle based SST analysis done by Gemma et al.[50].

This theoretical framework can be extended for more complex 2D morphologies with more than one type of core. We will be demonstrating the usage of this method in chapters 5 and 6 using different complex morphologies available in ABC star terpolymer melt. Morphologies like lamellar+ cylinder and other 3D morphologies that appear in ABC star terpolymers [50] cannot be analysed using

3. Formulation of Strong Segregation Theory for ABC star terpolymer

this method. The theory can be extended for $3D$ morphologies by considering the core backbone to be a curve or by considering a similar idea with a packing of modified Kelvin cell or truncated octahedron [28].

More morphological analysis and qualitative discussion will follow in Chapter 5. This method gives free energy of a morphology as a function of multiple variables which raises certain computational challenges. The computational methods used to facilitate a rigorous analysis of morphologies are explained in Chapter 4.

Chapter 4

Computational tools in Strongly Segregated Polygon analysis

This chapter introduces the tools that are used in this thesis to analyse a variety of morphologies with a wide range of complexities. Here we take the theory from the previous chapter and construct efficient and versatile algorithms. Hexagonal domains formed from tiling the triangles together that we can use to model a wide number of different patterns.

4.1 Strongly Segregated Polygon (SSP) Method: manual computation

The irregular hexagonal strongly segregated polygon, *SSP* introduced in the previous chapter is the building block for all complex tiling patterns that will be discussed in this thesis. In the previous chapter six *SSPs* were placed together to form the hexagonal morphology [6.6.6], where each coloured domain is surrounded by six other domains of alternating colours. Such tiling is attained by defining *SSPs* when vertices and areas of these six *SSPs* are rearranged in small steps to reflect geometrical and free energy changes in the polymer melt. One *SSP* takes six nodes, three monomer compositions (ϕ_A, ϕ_B, ϕ_C) and scaled interactions strengths ($\nu_{AB}, \nu_{BC}, \nu_{AC}$) as input and the total free energy per chain of each polygon is obtained as output.

We can place many *SSPs* together to construct the desired morphology. For example, hexagonal and square morphologies can be formed by placing six *SSPs* and eight *SSPs* together respectively. All coloured domains should be matched while placing them together. All red, yellow and blue corners should be placed

together in order to form morphologies that are feasible for an ABC star terpolymer. Periodic morphologies are defined by taking a repeating patch within that morphology and reconstructing that patch using $SSPs$.

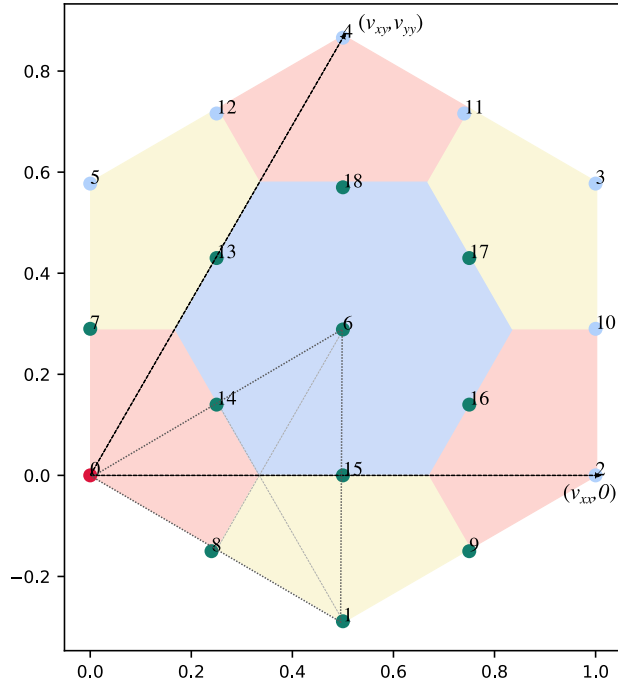


Figure 4.1: An illustration of the nodes in SSP methodology for the representation of a hexagonal morphology.. The red dot is the reference node, green dots are the free nodes and light blue dots are the periodic nodes. The black arrows indicate the periodicity, $[v_{xx}, v_{xy}, v_{yy}]$ of the repeating patch. One SSP is indicated by dashes lines across the nodes 0, 14, 6, 15, 1 and 8.

In the hexagonal morphology, the repeating patch is a hexagon with one of the coloured domains in the middle, surrounded by six domains of alternating colours. For a symmetric morphology ($\phi_A = \phi_B = \phi_C = \frac{1}{3}$), all these domain are regular hexagons. For example, in the hexagons previously mentioned in this thesis, the repeating patch is a hexagon with a blue hexagon at the centre and red and yellow half-hexagons surrounding them as in fig. 3.18. For simpler morphologies which have one core, like hexagons and squares, reconstructing the patch using polygons can be done manually.

The $SSPs$ are constructed for a given repeating patch using ‘free nodes’, ‘periodic nodes’ and the spatial periodicity of the morphology. Once the repeating patch is defined by placing $SSPs$ on it, all vertices within the patch are assigned

into three categories: reference node, free node and periodic node. The reference node is the one that is fixed in space. The reference node for the hexagonal morphology is given by the red dot in the illustration in fig. 4.1. Normally, we place the reference node at the origin $(0, 0)$. Free nodes are those vertices which can move anywhere in the space. Green dots in fig. 4.1 indicate the free nodes for the hexagonal morphology. The spatial periodicity of the pattern is defined by periodicity vectors such that the whole morphology can be recreated by shifting the patch by multiples of those vectors. For two-dimensional patterns there will be two such vectors, and these are shown for the hexagonal morphology by two dotted arrows in fig. 4.1. The position of two vertices $(v_{xx}, 0)$ and (v_{xy}, v_{yy}) at the end of these arrows gives the periodicities of the patch. The periodic nodes are those vertices at the edge of the patch which are located at a position that can be reached by adding integer multiples of the periodic vectors to the position of a free node (i.e. they represent the periodic copies of that free node). Given a free node (x_1, y_1) , it is related to a periodic node (p_{x_1}, p_{y_1}) positioned at given periodicity by

$$\begin{aligned} p_{x_1} &= x_1 + lv_{xx} + mv_{xy}, \\ p_{y_1} &= y_1 + mv_{yy}. \end{aligned} \tag{4.1}$$

Here l and m are integers which give the direction of the periodic node with respect to the reference node. We choose two values for l and m to indicate their direction with respect to the free node: $+1$ for positive x or y directions and -1 for negative x or y directions.

In the hexagonal morphology shown in fig. 4.1 the light blue dots are periodic nodes. These periodic nodes are connected to some of the green free nodes by spatial periodicity. In fig. 4.1 pairs of free node and periodic node are $(7, 10)$, $(0, 2)$, $(0, 4)$, $(8, 11)$, $(1, 3)$, $(1, 5)$ and $(9, 12)$. Thus any spatial change in the free nodes is reflected in the periodic nodes. So entire patch can be defined by its periodicities and free nodes. The seven free nodes in the centre: 6, 13, 14, 15, 16, 17 and 18 are not related to any periodic nodes.

The six vertices labelled 0, 14, 6, 15, 1 and 8 in fig. 4.1 form one *SSP*, as indicated by grey dotted lines in fig. 4.1. The order of these nodes is synchronised with the colour and direction of domains. The indicated polygon vertices in the order of colour will be: red centre, red/blue, blue centre, blue/yellow, yellow centre and yellow/red and this ordering of nodes with respect to the colours needs to be consistent across all the defined polygons. So next polygon will be defined with nodes in the order: 2, 16, 6, 15, 1 and 9. The ordering makes coloured domains match together and avoid overlapping between domains. In this way, six *SSPs* are defined to make a repeating patch of hexagonal morphology using

nineteen vertices. Once the morphology is defined in this way, any spatial change in these vertices will be reflected within the *SSPs* as a change in configurational energy.

The morphologies of *ABC* star containing a single core and multi-core periodic patches can be constructed in a similar manner. Once the patch which exhibits translational periodicity is identified from a 2D morphological pattern, it is manually divided into several subunits. Each subunit should contain one core. Thus these subunits will give an initial estimate towards the coordinate positions of *SSPs* when this is adapted in a graphing/drawing software. Coordinates thus identified are taken as the initial condition after making sure it gives a valid *SSP* configuration.

4.1.1 The ‘constraint list’ and free energy minimisation

The repeating patch of any periodic morphology (including periodic approximants to quasicrystals) can be defined in a similar way. Once the repeating patch is defined, with all free nodes and periodic nodes specified, the configuration of the repeating patch will depend on its periodicities and the position of the free nodes. These parameters can be collected together to form the "constraint list", which is simply a list of all the free parameters in the patch. In our computational framework, we construct the constraint list from the three parameters that indicate periodicity vectors (given one vector is aligned along the x-axis) followed by the coordinates of all free nodes. The constraint list will have a structure as follows:

$$\text{Constraint list} = [v_{xx}, v_{xy}, v_{yy}, x_1, y_1, x_2, y_2, \dots, x_n, y_n]. \quad (4.2)$$

This list of periodicity and vertices can specify (and control) the configuration of a repeating patch. Depending on the morphology, this list can be of any size. The morphology configuration that has the lowest free energy is obtained by varying the entries of the constraint list. Thus the minimisation of a particular morphology is carried out by varying the entries in this constraint list.

In practice, during numerical minimisation, it is helpful if the parameters are varied in small step sizes. This will prevent from the formation of invalid *SSPs* that will tamper and slow down the minimisation. Hence we define an intermediate list called the "interim-constraint list". This intermediate list contains the small changes on the corresponding entries of the constraint list. The interim-constraint list is defined as

$$\text{Interim-constraint list} = [\epsilon_{xx}, \epsilon_{xy}, \epsilon_{yy}, dx_1, dy_1, dx_2, dy_2, \dots, dx_n, dy_n]. \quad (4.3)$$

Here $\epsilon_{xx}, \epsilon_{xy}, \epsilon_{yy}, dx_1, dy_1, dx_2, dy_2, \dots, dx_n, dy_n$ which are zero in the initially defined configuration of the system. The initial constraint list is given by

$$\text{constraint list} = [v_{xx0}, v_{xy0}, v_{yy0}, x_{10}, y_{10}, x_{20}, y_{20}, \dots, x_{n0}, y_{n0}], \quad (4.4)$$

then the updated constraint list entries will be

$$\begin{aligned}
 v_{xx} &= (1 + \epsilon_{xx})v_{xx0}, \\
 v_{xy} &= (1 + \epsilon_{xx})v_{xx0} + \epsilon_{xy}v_{yy0}, \\
 v_{yy} &= (1 + \epsilon_{yy})v_{yy0},
 \end{aligned}
 \tag{4.5}$$

$$(x_i, y_i) = ((1 + \epsilon_{xx})(x_{i0} + dx_i) + \epsilon_{xy}(y_{i0} + dy_i), (1 + \epsilon_{yy})(y_{i0} + dy_i)).$$

Here i varies from 1 to n , where n is the number of free nodes. Hence, the first three entries of the displacement list control change in the large scale periodicity of the structure, and represent a global strain on the system. The remaining entries represent perturbations of the free nodes about this strained configuration.

This procedure helps numerical minimisation routines to converge because the constraint list will not be updated in random big step irrespective of the minimisation routine used. This also helps in increasing the efficiency of minimisation procedure.

To summarise we introduced a node-based tiling scheme in which 2D morphologies of *ABC* star terpolymer are represented by a periodically repeating patch. This scheme produces a list of parameters which one can use to explore different spatial configurations. Repeating patches of any size can be analysed using this technique. Following the methodology, deformations of the repeating patch can be tracked by varying the elements of a constraint list, allowing free energy minimisation to be performed.

4.2 Constructing large tilings from SSPs

The *SSP* methodology discussed above can be applied to any morphology by identifying the nodes manually. When the tiling is large and has more than one basic geometrical motif or cores involved the process of identifying nodes manually is a cumbersome task. Although there are single-cored morphologies in *ABC* phase separation that could be explained using simple geometrical motifs, from table 1.1, it is evident that there are also many multi-core morphologies. In the case of quasicrystal relating tilings, for a perfect quasicrystal, there won't be any repeating motifs and the periodic approximant can be arbitrarily large. So it is convenient to have an automated procedure for generating large tiling patterns and representing them with *SSPs*. Thus we are presenting another methodology to tile in *SSPs* into already existing tilings in an automated way.

In the process of discovering a free energy functional compatible with the bronze mean tiling[35], Rucklidge et al. [7] developed the Python script to tile geometric shapes into aperiodic tilings. In their work, the tiling is done using two different types of triangles and one type of rectangle. In contrast, tilings involving squares and triangles ("square-triangle tilings") have been observed in *ABC* star terpolymer in many investigations, both in experiments [57] and in simulations [27, 50, 91]. Its prominence in soft matter quasicrystals and dodecagonal symmetry is explained in Chapter 1. The molecular architecture of *ABC* star block copolymer is inclined to form symmetric shapes like squares or triangles. Thus the above tiling script is modified to produce square-triangle tilings.

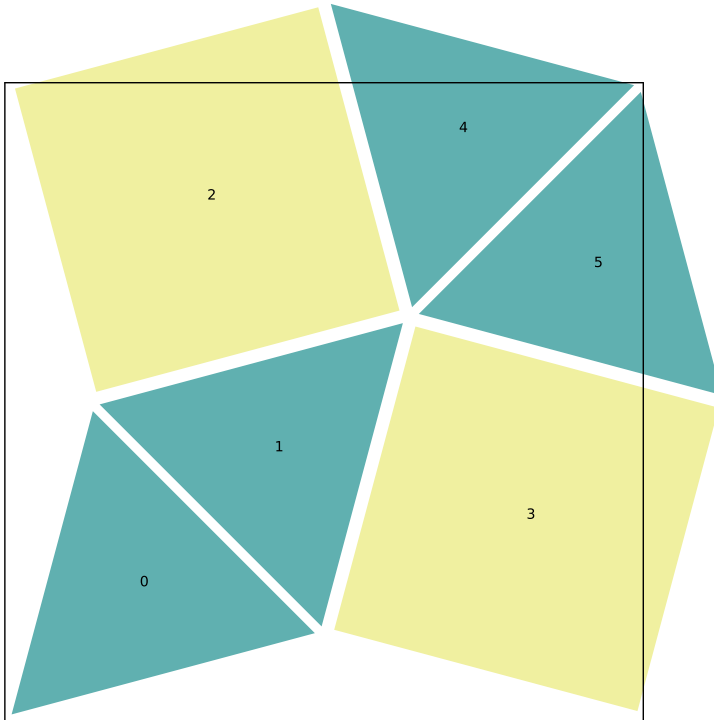


Figure 4.2: The initial tiling of Σ -phase is given. The tiles are numbered in the order they were placed. The solid black line indicates the periodicity of the repeating patch.

Given a tiling pattern of squares and triangles, we now describe a methodology for embedding *SSPs* within the structure. The process is done in three stages. The first is the tiling, where the shapes are aligned in a chosen arrangement to form a periodic patch. Additional nodes are added in the second stage

to the existing tiling creating the skeleton to embed *SSPs*. At this stage, all available nodes are sorted into reference node, free nodes and periodic nodes and the constraint list is made. Finally, *SSPs* are matched with these nodes in an ordered fashion so that they are in a physically compatible format for ABC star terpolymers.

(a).Tiling

Tiling, as the term suggests, is filling the space with shapes such that there are no free spaces or overlapping of shapes. The procedure is demonstrated using the a square- triangle tiling, known as the Σ -phase. The repeating patch of this tiling contains two squares and four triangles of the same side length as given in fig. 4.2. The tiling is done using above mentioned script.

In order to make this tiling first a triangle is placed at the origin. In fig. 4.2, the first tile, the green triangle is labelled 0. The orientation of these tiles can be controlled. The orientation of the first triangle is fixed and the rest of the tiles are placed with respect to this orientation. To make a Σ -phase there should be another triangle at one side of the triangle 0. Both sides of the second triangle labelled 1 are shared by two squares (yellow), labelled 2 and 3. The two triangles (4 and 5) that share a common side are placed between these squares such that they share one of their remaining side with one square each. This patch, when repeated in all directions, forms an infinite tiling.

When a tile is placed all the necessary information regarding the geometry of that tile is obtained. This includes the number of vertices and edges each tile has, edges and vertices that are shared between different tiles, and neighbour tiles. The information is updated whenever a new tile is placed. The vertices and edges in these tiles are independent entities. The tiling script takes in the vertices and edges to make a tile.

Once the tiling is created the periodicity can be identified. The periodicity for the given Σ -phase is given by the black lines in fig. 4.2. Here the repeating patch has a square periodicity that starts from the green triangle's free vertex to the yellow square's free vertex in vertical and horizontal directions.

Now there is enough information on the tiling and an initial tiling to start placing *SSPs* in the structure.

(b).Inserting additional nodes and creating the constraint list

The next challenge is to connect the basic tiling to an *SSP* tiling. The first part of this requires classifying nodes into reference, free and periodic nodes. If an Euclidean geometrical shape has d sides, then it can contain $2d$ *SSPs* to

form a valid ABC -star terpolymer morphology. The $SSPs$ are placed such that the monomer domain of one type/colour will be placed at the centre of each tile. The two other monomer types will occupy the domain space around this domain alternately, with one colour at the vertices and the other occupying the centre of the edges. Thus the squares will have eight $SSPs$ in them and triangles will have six $SSPs$ in them. To include $SSPs$, the existing tiling needs more nodes. The additional nodes must be placed carefully so a skeleton of a valid morphology is obtained. The symmetric case of $\phi_A = \phi_B = \phi_C = \frac{1}{3}$ is chosen as the initial case. In a morphology corresponding to a block copolymer with compositionally symmetric architecture, all domain areas will be equal and nodes can be positioned exactly halfway along all sections of these edges.

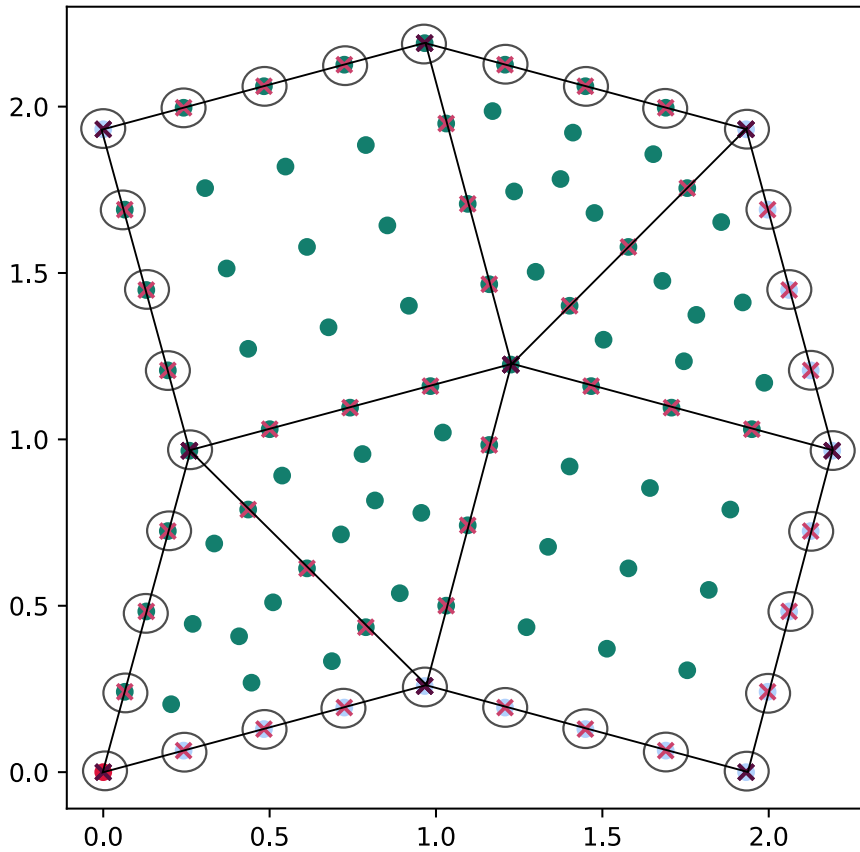


Figure 4.3: Illustration of all nodes in Σ -phase. The green dotted ones are the free nodes and light blue are the periodic nodes. Nodes with maroon crosses are vertices from the original tiling indicated by solid lines. Those with red crosses are new nodes that are placed on the edges. All non-crossed green nodes are new.

The method to add new nodes and sort them into different classifications is now discussed based on the Σ -phase. The original tiled Σ -phase (formed from squares and triangles) has nine vertices indicated by black crosses in fig. 4.3. To insert *SSPs* in this tiling it requires 97 vertices overall. The initial nodes in the tiling skeleton is placed such that it is guaranteed to be suitable for a *ABC* star terpolymer melt where $\phi_A = \phi_B = \phi_C = \frac{1}{3}$. It is easier to choose this composition as the area covered by each colour/monomer type will be equal. Three vertices are added on all the edges of each tile. On each edge in the Σ -phase, three nodes are added at positions 0.25, 0.5 and 0.75 of the edge length (as a fraction of the total length), indicated by red crosses in fig. 4.3. Additional vertices are added inside the tiles. There need to be 7 vertices inside every triangle tile and 9 vertices inside every square tile as each triangle and square tile will have localised [12.6.4] and [8.8.4] pattern respectively. These are shown as green dots inside the tiles in fig. 4.3. One node is added at the centroid of all available tiles. One set of inside nodes is placed at the midpoint between the centroid and the nodes halfway along each edge. Another set of inside nodes is placed at the midpoint between the centroid and each vertex of the tile. Thus all nodes that are needed for the *SSP* skeleton are placed as given in fig. 4.3.

Now that all necessary nodes are placed at suitable positions the next step is to sort them into reference, free or periodic nodes. This classification will create the desired constraint list. The periodicity is obtained from the original tiling stage from the solid black edges in fig. 4.2. This provides the first three entries of the constraint list. The node at the origin is taken as the fixed node, indicated in red in fig. 4.3. With known periodicity, the nodes that are periodic to each other are now identified. These will be positioned on the outer edges of the patch. From the obtained information on the original tiling, the edges that are not shared by more than one tile are identified. These must necessarily be the outer edges. There are five nodes connected to each outer edge, two at the end and three on the edges. Taking each node connected to the outer edge, we look for nodes positioned at the given periodicity in all directions. If the search finds nodes at the given periodicity, the first node is identified as a free node and the periodically located node/nodes that are found will be periodic nodes. Once a node is identified as free or periodic, it is marked as classified and is not considered again in the search. The node is identified as free if no nodes are found at the given periodicity. So, in this way, by considering all the outer edges, all the nodes connected to them (circled nodes in fig. 4.3) are sorted into either free or periodic nodes. All the remaining (internal) nodes (non-circled) are free nodes. Whenever a node is identified as a free node, it is added to the constraint list. So through this process, all parameters that control the configuration of morphology are collected in the constraint list. The procedure is elaborated in the flowchart fig. 4.4.

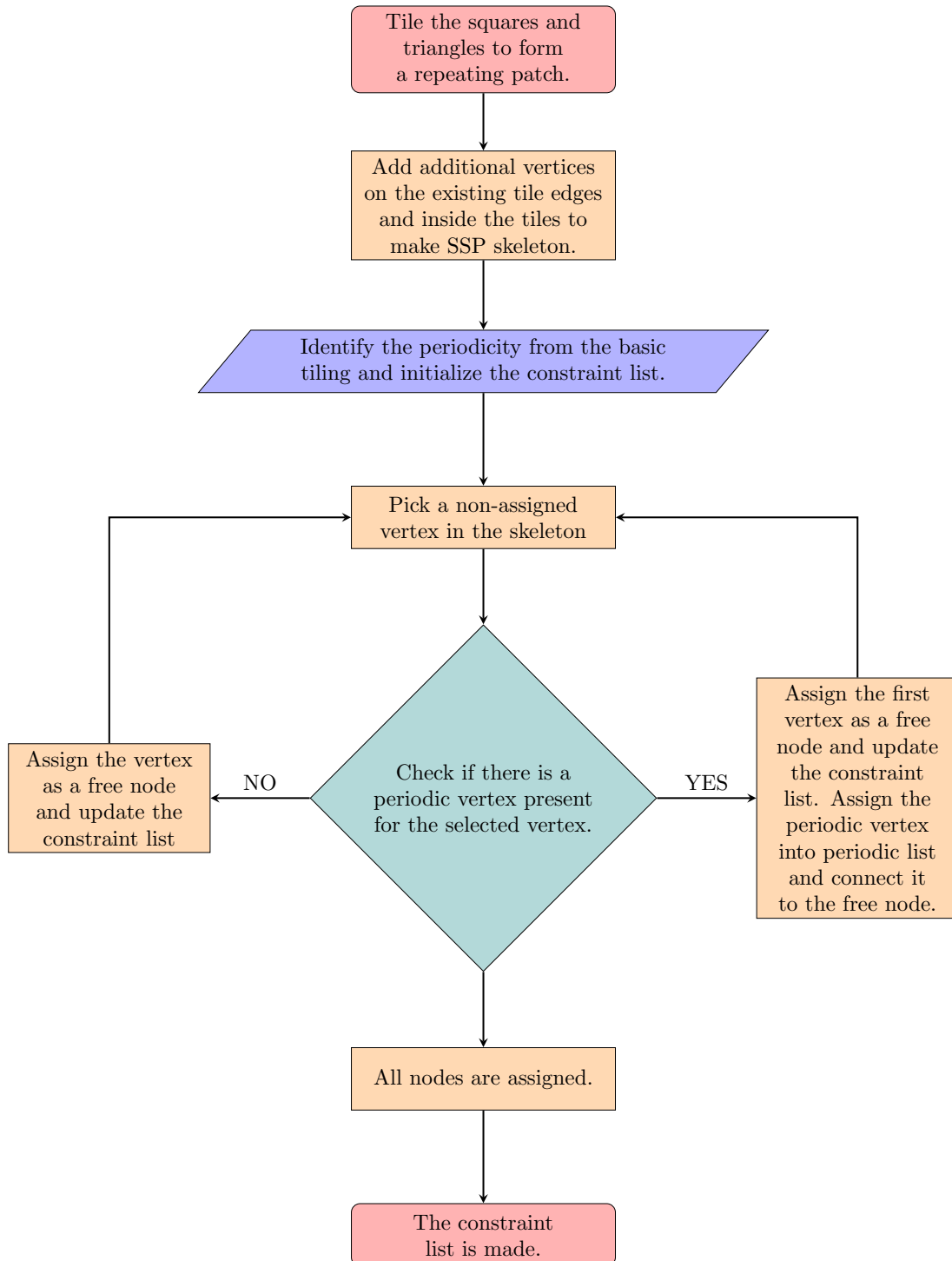


Figure 4.4: The process of inserting new nodes and creating the constraint list is elaborated in this flowchart.

Following the above procedure, the constraint list can be created for a periodic tiling of any type or size. This flexibility is particularly useful for large tilings, such as those that will be introduced in Chapter 6.

(c).Placing *SSPs* into the skeleton

The previous two stages provide us with a nodal skeleton and a constraint list. The relation between the nodes and *SSPs* is yet to be established. The *SSPs* have to be placed in a systematic order so that each colour (red, blue and yellow in our diagrams, representing different monomer types) is matched at the boundaries between neighbouring *SSPs*. While placing *SSP* into larger tiles this ordering has to be consistent and valid throughout the tiling. This kind of matching requires another set of procedures so that overlapping edges and incorrect matching of *SSPs* are avoided.

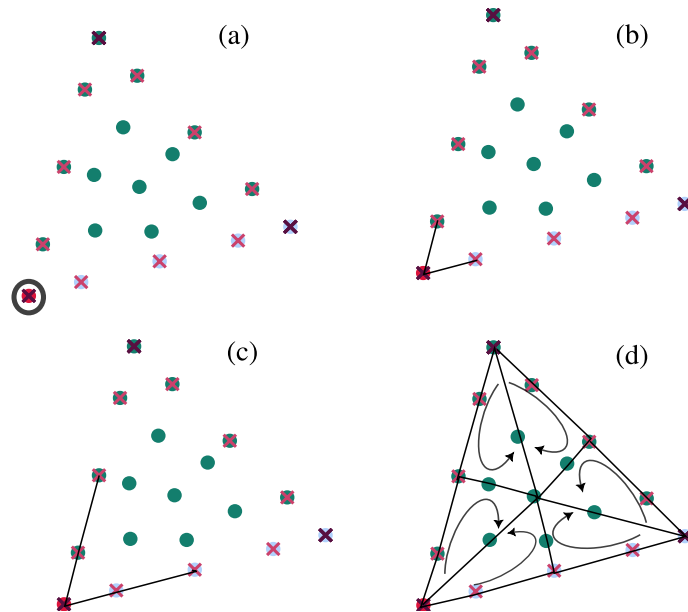


Figure 4.5: We are demonstrating different stages of placing an *SSP* into a tile with an example of a triangle tile. This process will result in the *SSP* node list. The polygons enclosed by bold lines are *SSPs*. The arrows inside the lines, show the direction in which nodes are selected.

In order to place an *SSP* into the tile we need six nodes from the tile skeleton that can form a valid *SSP*. The procedure for selecting these six nodes and placing the *SSP* in them is demonstrated using a triangle tile labelled 0 in fig. 4.2. We will place two *SSPs* simultaneously, so there will be two *SSP* node lists

denoted as $SSP-1$ and $SSP-2$. From the original triangle tile, one of its vertices is chosen as the starting node and this will be the first node for each of the two $SSPs$. The procedure for choosing the remaining nodes for $SSP-1$ and $SSP-2$ is illustrated in fig. 4.5.(b)-(d). For $SSP-1$ next two nodes are chosen from the lower edge of the triangle and for $SSP-2$ from the left hand edge as shown in fig. 4.5.(b) and (c). The rest of the three nodes each for $SSP-1$ and $SSP-2$ are chosen so the polygon will be closed. For this, the nodes are chosen via the centre of the triangle, back to the starting node while adding the nodes found en-route to the lists as shown in fig. 4.5. (d). On repeating this procedure for the other two vertices of the triangle we get six $SSPs$. The ordering of the nodes is indicated by the arrows in fig. 4.5.(d). The ordering of nodes alternates between clockwise and anticlockwise for adjacent $SSPs$. This ensures that the "colouring" of the $SSPs$ with monomer types is consistent for connected $SSPs$ that share nodes.

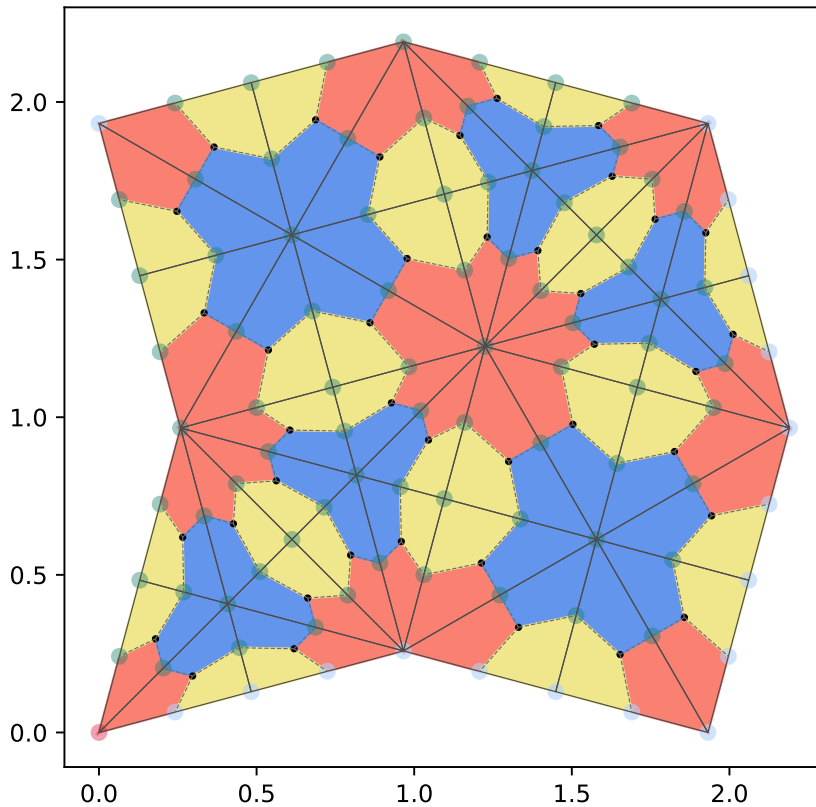


Figure 4.6: Initial configuration for Σ -phase with $SSPs$ embedded in them. The tiling skeleton is indicated by the points on the tiling. The interaction strength between three branches is taken to be equal $\nu_{AB} = \nu_{BC} = \nu_{AC} = 1$.

A similar procedure is applied to square tiles for which there will be eight *SSPs*. All the tiles in the repeating patch in fig. 4.2 undergo this procedure to produce 40 *SSPs* in total. Following this method we can avoid any invalid polygons, that may appear while manually picking the initial configuration.

The final result with *SSPs* embedded in the Σ -phase is given in fig. 4.6. At the end of this methodology, the constraint list made in the procedure (b) is connected to the *SSPs*. So now any change in constraint list or polymer parameters ϕ_A , ϕ_B , ϕ_C , ν_{AB} , ν_{BC} and ν_{AC} will reflect in the energy calculations in *SSP*. The procedure explained here can be adapted to a repeating patch of any size and we produced code that automates all steps above.

4.2.1 Combinatorics with monomer compositions

The embedded Σ -phase created in the above methodology is topologically called [10, 8, 4; 10, 6, 4]. The numbers in the square bracket represent the number of domains sharing the boundary with one domain. All red domains share sides with 10 other domains where 5 of them are yellow and other 5 are blue. All yellow domains share sides with 4 other domains, 2 red and 2 blue. There are two types of blue domains, one that shares its sides with 8 other domains and another that has 6 neighbouring domains. So the entire tiling is formed of topological combinations that are given in the square bracket.

For any given tiling pattern it is possible to produce six different structures by permutation of the monomer "colours" (i.e. red, yellow, and blue in our figures). That is the black dots (the core of *ABC* star) in fig. 4.6 will have three different domains around them in any order. Of course, for a given monomer composition and set of interaction parameters, each permutation will have a different free energy. If the colour and topology combined notations for the configuration in fig. 4.6 is given as [10*R*, 8*B*, 4*Y*; 10*R*, 6*B*, 4*Y*] other combinations are: [10*R*, 8*Y*, 4*B*; 10*R*, 6*Y*, 4*B*], [10*B*, 8*R*, 4*Y*; 10*B*, 6*R*, 4*Y*], [10*B*, 8*Y*, 4*R*; 10*B*, 6*Y*, 4*R*], [10*Y*, 8*R*, 4*B*; 10*Y*, 6*R*, 4*B*] and [10*Y*, 8*B*, 4*R*; 10*Y*, 6*B*, 4*R*]. Here *R*, *B* and *Y* indicated domain colours red, blue and yellow which map to monomer type *A*, *B* and *C* respectively.

We need to consider all the combinations possible for a given set of monomer compositions. All the combinations can be created simply by changing the order of nodes in the *SSP* list made in stage (c). This change in the order should be consistent throughout the tiling to avoid invalid combinations.

The initial configuration obtained is stored in a readable '.txt' file. In this readable input file, all the vertices in final tiling, periodic nodes, free nodes, relation between free node and periodic nodes, number of polygons and list of polygons are stored. An example of the input file for the Σ -phase is given in appendix B.2.

4.3 Fourier Analysis of morphologies created using *SSPs*

The structure of a material can be studied quantitatively using its diffraction patterns. These diffraction patterns provide the intensity distribution of waves as a function of the wavevectors at which the particles are found. The diffraction pattern of solids gives sharp peaks indicating the arrangement of atoms within. From these peaks, the lengthscale and the rotational symmetry associated with the structure are obtained. Theoretically, the diffraction pattern is obtained from the Fourier analysis of the particle or patterns.

In our *ABC* star terpolymer melt, the phase separated structures can be of different lengthscales and rotational symmetries. The pattern formed here is a tiling instead of an arrangement of particles as in solids. The lengthscale is decided by the arrangement of different domains in the defined space. These domains are categorised by area and monomer type/colour. So we need a Fourier analysis framework to determine the lengthscales in the patterns formed by putting *SSPs* together. The *SSP* can be arranged in any format such that the sides with the same colours are joined together. Thus we can theoretically build periodic, aperiodic or random patterns. We have seen hexagonal patterns in *ABC* star terpolymers in this chapter in which all the red domains of the stable structure have the same area. There can be other morphologies with domains of the same monomer type/colour having different areas. In order to determine the dominant lengthscales in such patterns formed we use the Fourier analysis based on the area density.

Since the position vector \mathbf{r} in the simulations are dimensionless, scaled by the length $R = \sqrt{N}b$, the wavevectors are also given in dimensionless form as $\mathbf{Q} = \sqrt{N}b\mathbf{q}$ where \mathbf{q} is the dimensional wavevector. We consider the area density $\rho(\mathbf{r})$ is periodic in the 2D space with periodicities $\mathbf{v}_1 = [v_{xx}, 0]^T$ and $\mathbf{v}_2 = [v_{xy}, v_{yy}]^T$ which is the periodicity of the patch. So for any integers $(n_1, n_2) \in \mathbb{Z}$, we can write:

$$\rho(\mathbf{r} + n_1\mathbf{v}_1 + n_2\mathbf{v}_2) = \rho(\mathbf{r}). \quad (4.6)$$

The periodic patches we are considering for *ABC* star terpolymers are not always necessarily in square periodicity. Thus we need to define the wavevector space (reciprocal space) customary for each periodic patch depending on their periodicity. In order to create a Fourier pattern, we are defining a wavevector space with a range of possible \mathbf{Q} consistent with that periodicity. This implies that the phase of the wave \mathbf{Q} at equivalent locations in any periodic patch must be identical, up to integer multiples of 2π , i.e.

$$\mathbf{Q} \cdot (\mathbf{r} + n_1\mathbf{v}_1 + n_2\mathbf{v}_2) = \mathbf{Q} \cdot \mathbf{r} + 2M\pi, \quad (4.7)$$

where M is an integer. This is achieved by writing \mathbf{Q} in terms of base vectors \mathbf{Q}_1 and \mathbf{Q}_2 as $\mathbf{Q} = m_1\mathbf{Q}_1 + m_2\mathbf{Q}_2$ for any $(m_1, m_2) \in \mathbb{Z}$. The constraints on the base vectors that allow to form the appropriate reciprocal lattice are,

$$\mathbf{Q}_1 \cdot \mathbf{v}_1 = 2\pi; \quad \mathbf{Q}_1 \cdot \mathbf{v}_2 = 0, \quad (4.8)$$

$$\mathbf{Q}_2 \cdot \mathbf{v}_2 = 2\pi; \quad \mathbf{Q}_2 \cdot \mathbf{v}_1 = 0$$

so that

$$\mathbf{Q} \cdot (\mathbf{r} + n_1\mathbf{v}_1 + n_2\mathbf{v}_2) = \mathbf{Q} \cdot \mathbf{r} + 2\pi(n_1m_1 + n_2m_2). \quad (4.9)$$

We can ensure that $\mathbf{Q}_1 \cdot \mathbf{v}_2 = \mathbf{Q}_2 \cdot \mathbf{v}_1 = 0$ by writing,

$$\mathbf{Q}_1 = A(\mathbf{v}_2 \times \hat{\mathbf{k}}), \quad (4.10)$$

$$\mathbf{Q}_2 = B(\hat{\mathbf{k}} \times \mathbf{v}_1).$$

where $\hat{\mathbf{k}}$ is the unit vector perpendicular to the 2D plane, for some constants A and B . On solving for A and B in eq. (4.10) using eq. (4.8), we can define the wavevector \mathbf{Q} only using the periodicity vectors \mathbf{v}_1 and \mathbf{v}_2 of a morphology motif.

$$\mathbf{Q} = m \left(\frac{2\pi}{(\mathbf{v}_2 \times \hat{\mathbf{k}}) \cdot \mathbf{v}_1} (\mathbf{v}_2 \times \hat{\mathbf{k}}) \right) + n \left(\frac{2\pi}{(\hat{\mathbf{k}} \times \mathbf{v}_1) \cdot \mathbf{v}_2} (\hat{\mathbf{k}} \times \mathbf{v}_1) \right). \quad (4.11)$$

Now that \mathbf{Q} is defined, the Fourier transform of the area density will become:

$$\rho_{\mathbf{Q}} = \int d\mathbf{r} \rho(\mathbf{r}) e^{i(m_1\mathbf{Q}_1 + m_2\mathbf{Q}_2) \cdot \mathbf{r}} \quad (4.12)$$

for a range of $(m_1, m_2) \in \mathbb{Z}$, where the integral is taken over a single periodic patch.

The above integral can be computed as a sum over the contributions from individual *SSPs*. When we consider an *SSP*, as we have established it has three different domains. We divided it into six smaller triangles in section 3.5 to determine their individual stretching energy. These smaller triangles contain only one type of monomer/colour in them. The contribution to the Fourier transform integral of one such triangle Δ_{0ij} of type $I \in \{A, B, C\}$, located between the position vectors $\mathbf{r}_0 = [x_0, y_0]^T$, $\mathbf{r}_i = [x_i, y_i]^T$ and $\mathbf{r}_j = [x_j, y_j]^T$, is given by

$$\rho_{0ij}(\mathbf{Q}) = \rho_I \int \int_A e^{i(m_1\mathbf{Q}_1 + m_2\mathbf{Q}_2) \cdot \mathbf{r}} dx dy. \quad (4.13)$$

where the integral is over the 2D area A of the triangle. The constant ρ_I is the scattering density within phase I . For convenience, it is chosen to be 1 or 0 depending on the patterns we need to highlight in the real space. The position vector of a point within the triangle Δ_{0ij} , parameterised as

$$\begin{aligned}\mathbf{r} &= \mathbf{r}_0 + \alpha(\mathbf{r}_i - \mathbf{r}_0) + \beta(\mathbf{r}_j - \mathbf{r}_0), \\ &= \mathbf{r}_0 + \alpha(\mathbf{l}_i) + \beta(\mathbf{l}_j)\end{aligned}\tag{4.14}$$

for some α and β . The integral for eq. (4.13) is further solved by writing in terms of the parameters α and β .

$$\begin{aligned}\rho_{\Delta_{0ij}}(\mathbf{Q}) &= \rho_I \int_0^1 \int_0^{1-\alpha} e^{i\mathbf{Q}\cdot\mathbf{r}} |x_i y_j - x_j y_i| d\alpha d\beta, \\ &= \rho_I |x_i y_j - x_j y_i| \int_0^1 \int_0^{1-\alpha} e^{i\mathbf{Q}\cdot(\mathbf{x}_0 + \alpha(\mathbf{l}_i) + \beta(\mathbf{l}_j))} d\alpha d\beta, \\ &= \rho_I |x_i y_j - x_j y_i| e^{ia_0} \left(\frac{a_1(e^{ia_2} - 1) + a_2(1 - e^{ia_1})}{a_1 a_2 (a_1 - a_2)} \right).\end{aligned}\tag{4.15}$$

Here in the final expression we have assigned $a_0 = \mathbf{Q}\cdot\mathbf{r}_0$, $a_1 = \mathbf{Q}\cdot\mathbf{l}_i$ and $a_2 = \mathbf{Q}\cdot\mathbf{l}_j$. Now we have the contribution to the Fourier transform at a given wavevector \mathbf{Q} in terms of the nodal coordinates of the triangle Δ_{0ij} and ρ_I . When computing with this result, we need to consider the special limiting cases listed below:

1. When $\mathbf{Q} = 0$.

$$\rho_{\Delta_{0ij}}(\mathbf{Q}) = \rho_I \frac{|x_i y_j - x_j y_i|}{2}.\tag{4.16}$$

2. When $\mathbf{Q}\cdot(\mathbf{l}_i - \mathbf{l}_j)$, $a_1 = a_2$, i.e., when \mathbf{Q} is perpendicular to one edge of the triangle:

$$\rho_{\Delta_{0ij}}(\mathbf{Q}) = \rho_I |x_i y_j - x_j y_i| \frac{e^{ia_0} (e^{ia_1} (1 - ia_1) - 1)}{a_1^2}.\tag{4.17}$$

3. When \mathbf{Q} is perpendicular to \mathbf{l}_i , i.e $a_1 = 0$:

$$\rho_{\Delta_{0ij}}(\mathbf{Q}) = \rho_I |x_i y_j - x_j y_i| \frac{e^{ia_0} (ia_2 + 1 - e^{ia_2})}{a_2^2}.\tag{4.18}$$

4. When \mathbf{Q} is perpendicular to \mathbf{l}_j , i.e $a_2 = 0$:

$$\rho_{\Delta_{0ij}}(\mathbf{Q}) = \rho_I |x_i y_j - x_j y_i| \frac{e^{ia_0} (ia_1 - 1 + e^{ia_1})}{a_1^2}.\tag{4.19}$$

As we have mentioned the value of ρ_I is chosen depending on the domain that we need to highlight in our reciprocal space. For example if we need a pattern highlighting only the A regions, then the choice of ρ_I values will be: $\rho_A = 1$, $\rho_B = 0$ and $\rho_C = 0$. We can have any desired combinations of these depending on the pattern we are looking for.

The Fourier spectrum for a given morphology is determined by summing $\rho_{\Delta_{0ij}}(\mathbf{Q})$ over all triangles in all $SSPs$ for a given \mathbf{Q} . This is done for all valid wavevectors within a reasonable range, and finally, the intensity is calculated as $|\rho(\mathbf{Q})|^2$. We will be looking at the Fourier spectrum of different patterns in chapter 6.

4.4 Multi-variable minimisation

The initial morphology's nodal configuration is obtained either manually or computationally using the two methodologies mentioned earlier in this chapter. In order to find the stable configuration the lowest free energy for a given composition is obtained. This free energy is a multivariable function whose variables are given in the constraint list. Since the free energy is a multivariable function it is not straightforward to find the minima analytically. Identifying the global minima is also not easy for such a function. Hence we use numerical minimisation routines to identify the most suitable local minima. The python `scipy` library offers a variety of inbuilt minimisation routines. We prefer a search-based minimisation routine here. In this work minimisation is conducted using Broyden-Fletcher-Goldfarb-Shanno (BFGS) algorithm [112]. In the fig. 4.7, we are showing some intermediate stages during the numerical minimisation. As we have shown, during the minimisation there can be invalid SSP combinations. We have manually assigned comparably higher values for the free energy per chain for invalid $SSPs$. When we used a gradient-based minimisation algorithm, the occurrence of invalid $SSPs$ from certain initial conditions tricked the algorithm into searching for local minima with incorrect initial conditions. This is avoided in search-based numerical minimisation algorithms such as BFGS. The BFGS algorithm uses a quasi-Newton method that uses first derivatives.

We are demonstrating the efficiency of different minimisation methods and their tolerances using the constraint list of Σ -phase morphology. The minimisation of Σ -phase of monomer compositions $\phi_A = 0.575$, $\phi_B = 0.381$ and $\phi_C = 0.044$ and equal interaction strengths, using different inbuilt `scipy` minimisation functions and tolerances are listed in table 4.1. The composition and interaction strengths are given the 4 lines of appendix B.2. The constraint list for the Σ -phase contains 161 parameters. Three different initial conditions are chosen where the first few entries are different. The minimum free energy is obtained for three different initial parameters: CL_1 , CL_2 and CL_3 listed below. The

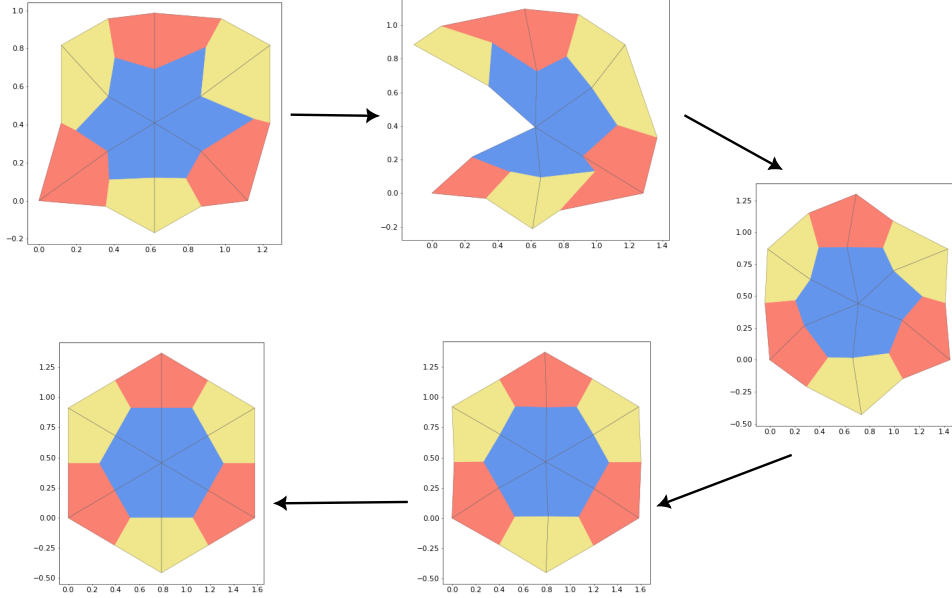


Figure 4.7: This shows some intermediate stages during the minimisation of a periodic patch of hexagonal morphology with *SSPs*. The minimisation starts with a ‘wonky’ hexagon which then goes through different configurations including invalid *SSPs* and reaches the final stable configuration with the lowest free energy per chain.

constraint list CL_1 corresponds to the input file presented in appendix B.2. The first three entries in CL_1 are the periodicities as indicated in the input file. The coordinates of the nodes that are listed as the free nodes are then listed in CL_1 following the periodicities. On slightly changing the value of v_{xx} , (the first entry) we get CL_2 and CL_3 which will reflect that change in all the periodic nodes.

$$CL_1 = [3.33876, -0.00001, 3.33876, 0.48918, 1.66938, 1.66937, \dots]$$

$$CL_2 = [3.37216, -0.00001, 3.47232, 0.78270, 1.66938, 1.66938, \dots] \quad (4.20)$$

$$CL_3 = [3.47232, -0.00001, 3.60587, 0.91478, 1.66938, 1.66938, \dots]$$

The free energy function is minimised using the BFGS method with these different initial parameters. As reported in table 4.1, the final minimised function value matches up to 9 significant digits starting with these initial conditions. Thus the value of free energy per chain is verified.

4. Computational tools in Strongly Segregated Polygon analysis

Initial parameters	Method	xtol	ftol	gtol	Time(s)	Number of function evaluations	Minimised function value
CL_1	BFGS	N/A	N/A	$\approx 10^{-5}$	256.926	20088	8.97422816
CL_2	BFGS	N/A	N/A	$\approx 10^{-5}$	251.139	19926	8.97422816
CL_3	BFGS	N/A	N/A	$\approx 10^{-5}$	287.604	23166	8.97422816
CL_1	BFGS	N/A	N/A	10^{-3}	107.760	7614	8.97423333
CL_1	BFGS	N/A	N/A	10^{-2}	48.222	4374	8.97428506
CL_1	Powell	$\approx 10^{-5}$	$\approx 10^{-5}$	N/A	181.428	14855	8.97507610
CL_1	Powell	10^{-2}	10^{-2}	N/A	39.720	3522	9.04737591
CL_1	Nelder-Mead	$\approx 10^{-5}$	$\approx 10^{-5}$	N/A	370.752	32200	Unsuccessful minimisation

Table 4.1: Minimisation for the free energy function is obtained for given initial parameters CL_1 , CL_2 and CL_3 . Each function evaluation takes 161 parameters as arguments. Minimisation is carried over using different methodologies, tolerance and initial parameters to obtain the most efficient process. The grey-shaded region indicates the method and tolerance used for minimisation in this thesis.

As indicated in the table 4.1 minimisation efficiency has been checked between three inbuilt methods, BFGS, Powell and Nelder-Mead. All these methods have a search-based minimisation algorithm. Using CL_1 as the initial set of parameters, the routine couldn't find a suitable minimum value when Nelder-Mead was used. The Powell method led to a successful minimisation. The minimised function value agrees with other minimised result to three significant digits. However, upon reducing the tolerance, the Powell method failed to produce the desired minimised value. While using the BFGS method the minimum value matches the desired value up to 5 significant digits even when the tolerance is increased. The Powell method is a bit faster than BFGS but the minimum value to a certain

accuracy is important to decide if the final morphology is correct. Thus the BFGS method with $\approx 10^{-5}$ tolerance is chosen as the preferred minimisation routine for all our morphological studies.

For tilings with a large constraint list, combinations of the above methods are used to get a better initial condition. Then the intermediate initial condition is used with the selected methodology.

4.5 Phase space exploration

We are now equipped with two algorithms where one will create an initial configuration and another gives an efficient method to find the stable configuration. Each configuration is defined for a given monomer composition (ϕ_A, ϕ_B, ϕ_C) and interaction strength $(\nu_{AB}, \nu_{BC}, \nu_{AC})$. A phase space is a map of the most stable morphology for each composition within the desired parameter range. In order to build a phase space, all possible combinations of ϕ_A , ϕ_B and ϕ_C need to be explored. All possible monomer compositions are obtained by varying ϕ_A and ϕ_B from 0 to 1 in an appropriate step length. The values of ϕ_A and ϕ_B should satisfy the condition $\phi_C = 1 - \phi_A - \phi_B$, where $\phi_C < 1$. We introduced the ternary composition space in chapter 2 and briefly in chapter 3. In this tri-axis composition space, the composition of A , B and C monomers are varied on the three sides of a triangle.

At any given composition, when performing the free energy minimisation it is helpful to have a good initial guess for the configuration. This is particularly important because some configurations of the nodes will result in invalid polygons, which makes minimisation difficult. The usual method for exploration of composition space would be to traverse the space in multiple linear cuts, via nested loops. For example, if we consider there are the two compositions $\phi_A = (0 \dots, 1]$ and $\phi_B = (0, \dots, 1]$, a nested iteration loop will take the first element from ϕ_A then consider rest of the values in ϕ_B and then in next iteration choose next entry in ϕ_A . However, a good initial guess for the structure is not available at the start of each linear traversal of the phase space. Using linear traversing next monomer composition may have a completely different geometrical configuration to adjacent initial parameters. For example, at the end of the first nested iteration, the composition space will be $(0.01, 0.99)$. The morphological configuration then will have a large B domain and a small A domain. The next composition from the nested loop will be $(0.02, 0.01)$, which is a completely different configuration from the previous structure. This will result in invalid *SSPs* and hence incomplete phase space. To address this problem, we devised a method, which we call ‘spiral’ traversing, as it can ‘grow’ from any point we choose from. Using this method we start from a good, well-minimised structure in the phase space and work outwards from there.

In the spiral traversing method, the ternary space is divided into a hexagonal array of points representing different compositions. Initially, each point is marked with a "1" to indicate that no attempt has been made to find a minimised structure at that point. We keep track of which points have been visited and whether a successful minimisation was performed there by changing this label. We mark the first composition with a "2" as given in fig. 4.8.(a). Here the initial composition marked is the symmetric composition where $(\phi_A, \phi_B, \phi_C) = (\frac{1}{3}, \frac{1}{3}, \frac{1}{3})$. Often the initial constraint list is created at this monomer composition. The procedure searches for composition labelled "2" to start the minimisation process. On successful minimisation of this composition with the given initial constraint list, the composition is labelled with a 4. If the minimisation was unsuccessful then we need to restart the procedure with a modified initial constraint list. The starting need not be an architecturally symmetric composition. It can be any valid point in the ternary plot and this procedure will work. Finally, for reasons that will become clear below, the "4" in the initial composition is replaced by a "3".

The monomer composition of a given geometry is obtained from the geometry file in appendix B.2. The slot corresponding to this monomer composition is marked as "2". On successful minimisation of morphology at the composition marked 2, we look at slots that are labelled with 4s and replace all 4s with 3's. In our method, 3 indicates successful and complete minimisation. In the next search, the algorithm looks for slots marked with 1's that have at least one slot marked 3's as a neighbour. In the illustration of phase space given in fig. 4.8.(d), there are six slots (marked with pink circles). Each composition in these marked slots is minimised by taking a minimised constraint list of slots marked 3. If the minimisation is successful the slot is marked 4 and if it is unsuccessful the slot is marked with a 5 as given in fig. 4.8.(e). At the end of the iteration, all 4's are replaced by 3's. In the next iteration, the algorithm searches for slots marked 1's or 5's that have 3's as neighbours. These slots are marked in pink in fig. 4.8.(f). The slots with 1's are minimised in the same way explained before. The slots marked 5 use the minimised constraint list from another 3 slot that is different from the previous attempt. On successful minimisation, the slot is marked 4. If the minimisation is unsuccessful again the minimisation is attempted again using the constraint list from a new 3 neighbour. At the end of each iteration, all 4's are replaced by 3's. If the slot has unsuccessful minimisation despite trying with all valid neighbour constraint lists it is marked as non-minimisable and that composition won't be tried again. An example of final space is given in fig. 4.8.(g).

4. Computational tools in Strongly Segregated Polygon analysis

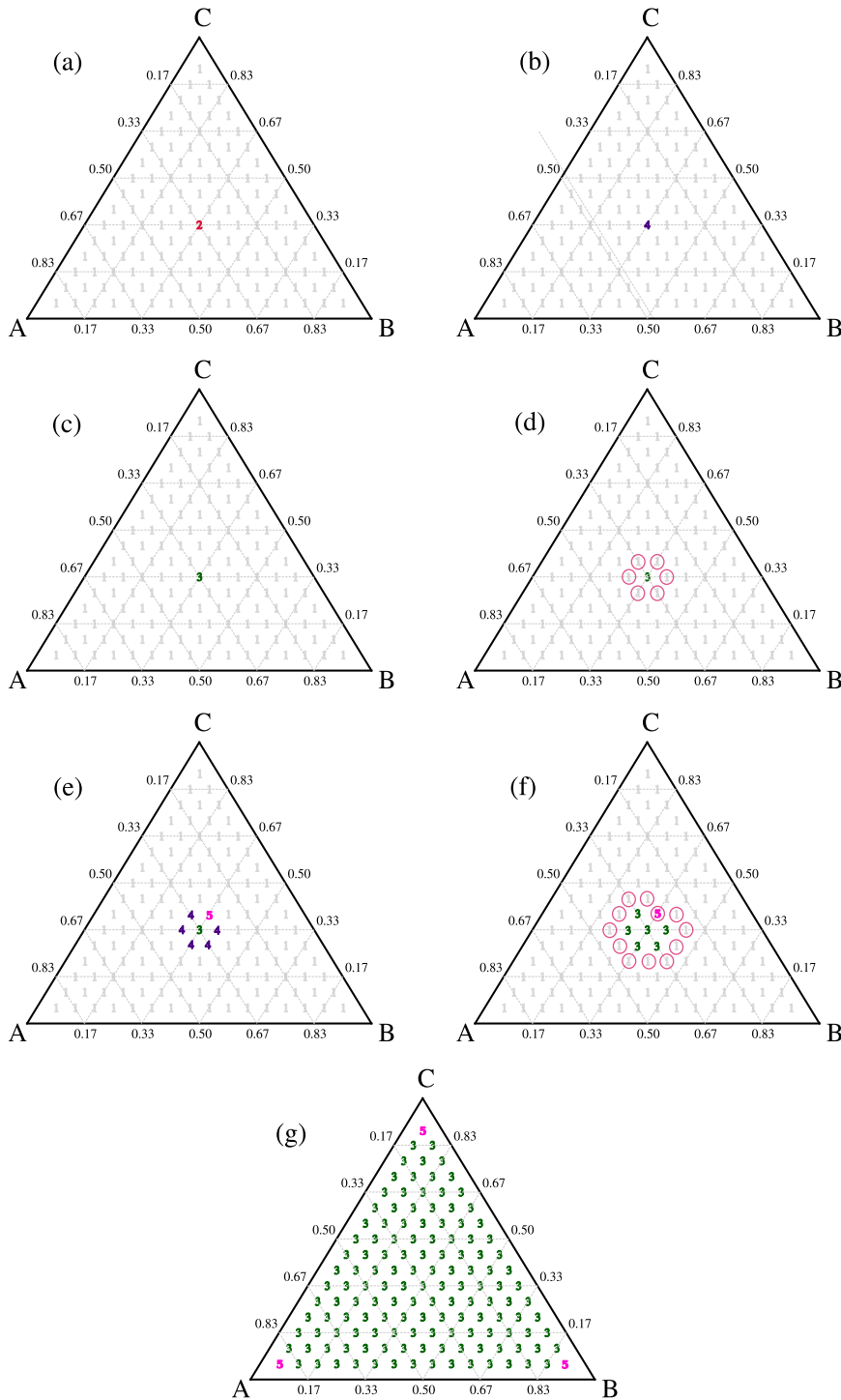


Figure 4.8: Phase space labelling and exploration is explained schematically. The end space where all available compositions are minimised is given in (g). The slots marked 1 and 2 are the valid compositions. On successful minimisation, the marker is replaced by a 4. Unsuccessful minimisation is indicated by 5. Successful complete minimisation is indicated by 3.

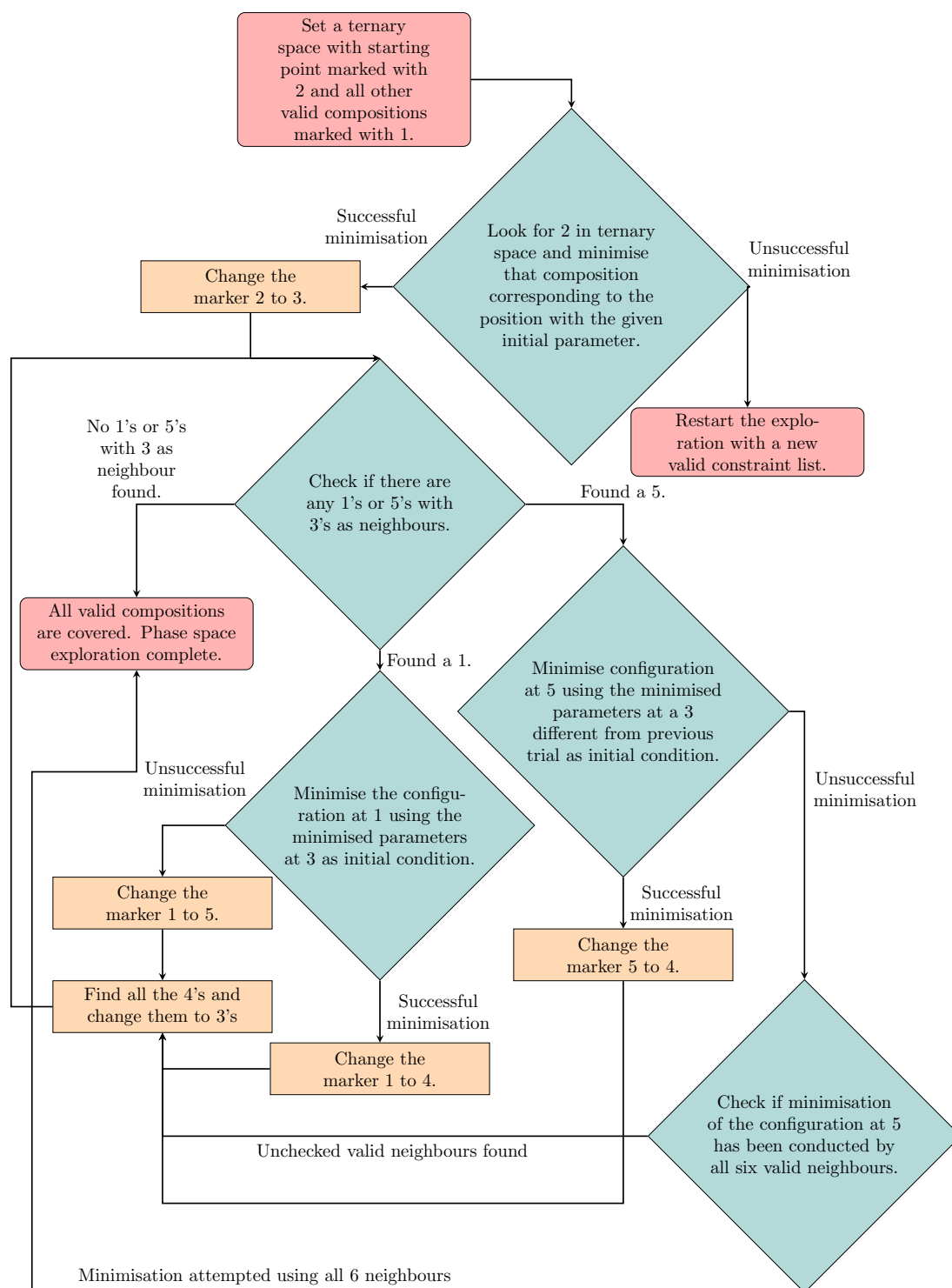


Figure 4.9: Phase space exploration is demonstrated using this flow chart.

The current version of the script that conducts this phase space exploration is versatile enough to include as many data points as needed. In the occurrence of an incomplete phase space exploration, following this numerical convention, the phase space exploration can be continued from the last iteration. The ARC4 in Leeds will only allow 48 hours to execute a script in it. When the morphology becomes complex and large the phase space exploration takes weeks, which is conducted with ease using the above procedure.

The procedure is explained using the flowchart in fig. 4.9 Each morphology is explored over the ternary space with the aim of finding the morphology that carries the lowest free energy, which we consider to be the most stable morphology.

The tools introduced in this chapter are used to analyse different morphologies in the following chapters. These tools can handle most of the 2D morphologies that are observed in *ABC* terpolymer. They can also be used without any modification for larger morphologies that are not yet observed experimentally in *ABC* terpolymers.

Chapter 5

ABC star terpolymers morphologies: Periodic

In this chapter, we will take the strong segregation methodology and techniques introduced in chapter 3 and chapter 4 to analyse different periodic morphologies possible for *ABC* star block copolymers. We aim to create a phase space with 2D morphologies which will locate the stable morphology from available varieties at each specific composition. We will analyse two main classifications of *ABC* star block copolymer melt: one with symmetric interactions where the monomer interactions between all three monomer types are equal; and one with asymmetric interactions, where the interaction between monomer types are different. The morphologies considered in this chapter are introduced in the symmetric case along with their geometric characteristics.

5.1 Symmetric *ABC* star terpolymers ($\nu_{AB} = \nu_{BC} = \nu_{AC} = 1$)

By symmetric *ABC* star terpolymer, we assume the melt contains terpolymer molecules which have equal interaction strengths between all three branches. The interaction between the monomers is measured in terms of Flory interaction parameter $N\chi$ in units of $k_B T$. As mentioned in Chapter 3, with reference to the literature, the Flory interaction parameters for a symmetric strongly segregated melt are chosen to be $N\chi_{AB} = N\chi_{BC} = N\chi_{AC} = 60$. This is scaled using parameters $\nu_{AB} = \nu_{BC} = \nu_{AC} = 1$.

The most common 2D morphologies observed in *ABC* star block copolymers: [6.6.6], [8.8.4], [12.6.4], [8.6.4; 8.6.4; 8.6.6] and [10.6.4; 10.6.4; 10.6.6] are analysed in this work as detailed below, where we define each morphology in turn.

5.1.1 [6.6.6]-Hexagon

The hexagonal morphology was introduced in Chapter 3, where the *SSP* methodology is explained. The spatial configuration of the morphology and free energy phase space was briefly described there. Here is a quick review of the hexagonal morphology and its analysis using the standardised *SSP* methodology. Topologically, the hexagonal morphology is identified as [6.6.6]. This nomenclature indicates the number of neighbouring domains for each domain within the hexagonal tiling. The nomenclature also gives information on the type of core or type of *SSP* necessary to describe the tiling. In order to model the hexagonal morphology in *ABC* star melt, one type of *SSP*, which has a core shared by three domains, each bordering six different domains is used. Different topological subclasses of the morphology formed by permutations of domains and monomers are equivalent to each other as

$$\begin{aligned}
 [6A.6B.6C] &\equiv [6A.6C.6B] \equiv [6B.6A.6C] \\
 &\equiv [6B.6C.6A] \equiv [6C.6A.6B] \equiv [6C.6B.6A].
 \end{aligned}
 \tag{5.1}$$

Thus only one topological sub-class [6A.6B.6C] is constructed for the analysis of the morphology.

The initial parameters for the periodic patch are picked manually for the configuration $(\phi_A, \phi_B, \phi_C) = (\frac{1}{3}, \frac{1}{3}, \frac{1}{3})$. The initial configuration designed using the geometric graphing software Geogebra is shown in fig. 5.1.(a). From this initial design, 19 nodes are identified. The origin $(0, 0)$ is taken as the fixed node, which is indicated in red. The remaining 18 nodes are classified into periodic and free nodes, as explained in Chapter 4. For this configuration, there are 7 periodic nodes and 11 free nodes for the chosen periodic patch. Using these nodes 6 *SSPs* are constructed which collectively defines the periodic patch necessary for [6.6.6] morphology as shown in fig. 5.1.(b). The constraint list is defined when we create the *SSP* periodic patch. The constraint list here consists of 25 elements, with the first three indicating the periodic repeat vectors of the patch. This initial configuration undergoes minimisation in two stages to find the most stable configuration for a given composition. At first, the configuration shown in fig. 5.1.(b) undergoes an affine rescaling which gives a local minima for the configuration as a function of the overall size of the pattern without adjusting internal configurations, which is given in fig. 5.1.(c). It is to be noted that free energy value in terms of $k_B T$ for the configuration in fig. 5.1.(c) is lower than fig. 5.1.(b). This configuration is then taken as the initial configuration for a minimisation in which all free node positions and periodic repeat vectors are adjusted to obtain the lowest possible value for free energy per chain. This is

achieved by varying the entries of the constraint list to obtain the minimised configuration.

The pattern obtained after minimisation is given in fig. 5.1.(d) in which the periodic patch is tiled together to show a larger portion of the morphology here. As expected for a symmetric configuration of *ABC* star terpolymers all domains are of the same size. The procedure can be repeated for different values of monomer compositions to observe its effect on phase separated structures. An example of a different monomer combination is shown in fig. 5.1.(e). The monomer composition of this phase separated structure is $(\phi_A, \phi_B, \phi_C) = (0.4965, 0.2634, 0.2401)$. Reflecting the composition, domain sizes are also different. As ϕ_A is larger, red domains are bigger than the other two. The blue and yellow domains have almost comparable compositions so they look similar. The free energy per chain for this pattern fig. 5.1.(e) is higher than that of the pattern corresponding to symmetric composition fig. 5.1.(d).

By using the ternary space exploration techniques explained in Chapter 4 free energy per chain for all compositions is determined. The minimised configuration at $\phi_A = \phi_B = \phi_C = \frac{1}{3}$ is taken as the starting point in the ternary space for this exploration. It took 3-4 hrs to explore the entire ternary space which contains 4050 data points on ARC4, part of the High Performance Computing facilities at the University of Leeds, UK. The resulting ternary space with contours of free energy per chain is given in fig. 5.1.(f). The compositions with the lowest free energy per chain are indicated by blue contours. The symmetric configuration is given in fig. 5.1.(d) belongs to the blue contour region in fig. 5.1.(f). As we go away from the blue contour in this composition triangle, free energy per chain increases. The configuration with large red domains in fig. 5.1.(e) belongs to the orange contour where the free energy per chain is larger compared to the blue region. The increase in free energy per chain is symmetric in the ternary space. This free energy map agrees with the free energy map obtained using a single triangle *SSP* in chapter 3 (fig. 3.15) where the interfaces are always perpendicular to the triangle edges. The free energy per chain for [6.6.6] morphology for all valid compositions of *ABC* star terpolymers is determined. As pointed out in chapter 3 and in literature [27, 50, 91, 159], the hexagonal morphology has lower energy penalty when architecture is compositionally symmetric, $(\phi_A, \phi_B, \phi_C) = (\frac{1}{3}, \frac{1}{3}, \frac{1}{3})$. This is once again agreed here from results given in fig. 5.1.(d) and (f).

5. *ABC* star terpolymers morphologies: Periodic

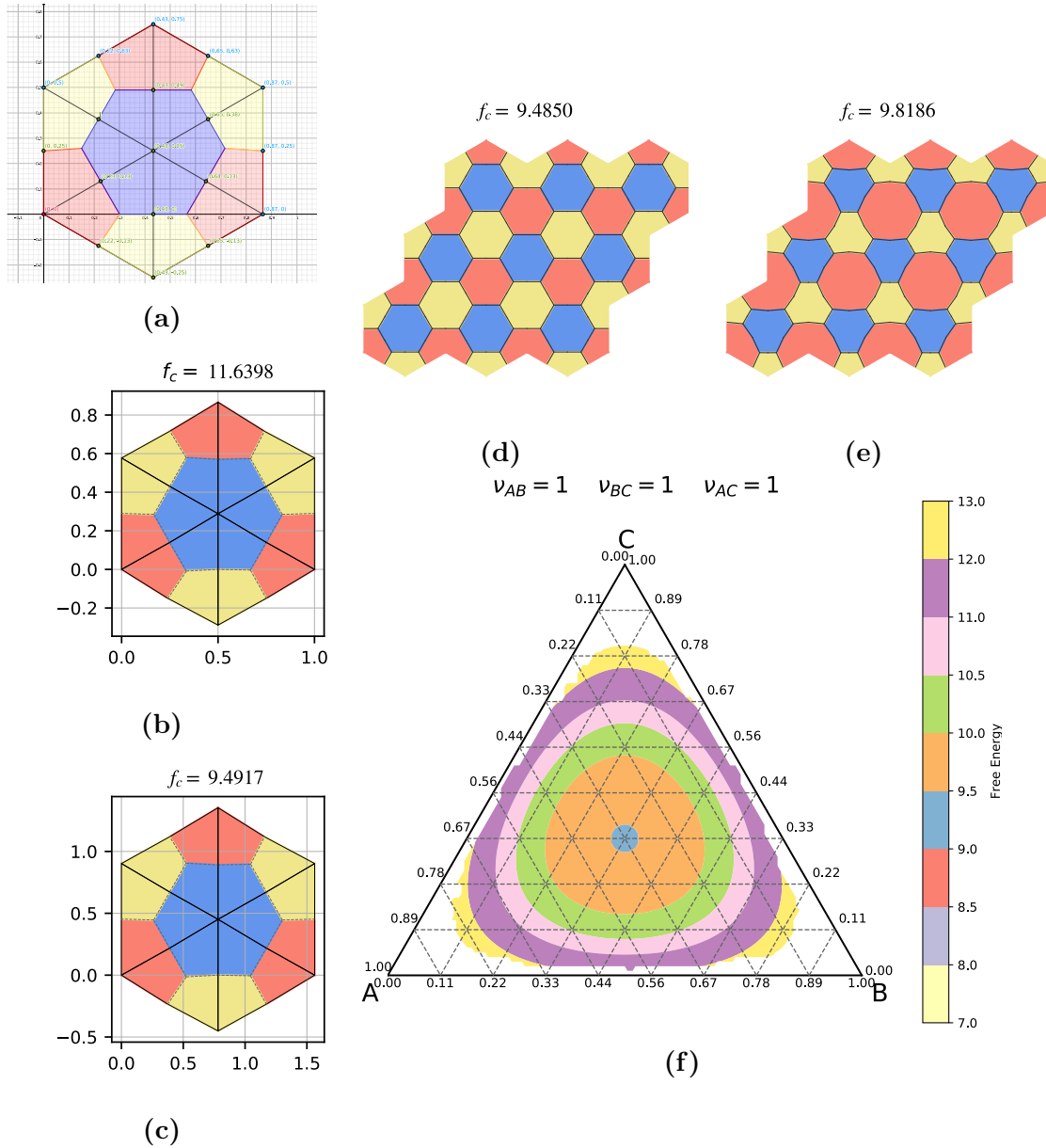


Figure 5.1: Analysis of hexagonal morphology with $[6A.6B.6C]$ is given. The initial design of the configuration is given in (a) with the position coordinates of the nodes. The coordinates from (a) are used to create the initial configuration of the *SSP* periodic patch given in (b). First-stage minimisation results in a scaled version (c) of the initial configuration. Minimised tilings for two different compositions are given in (d) $(\phi_A, \phi_B, \phi_C) = (\frac{1}{3}, \frac{1}{3}, \frac{1}{3})$ and (e) $(\phi_A, \phi_B, \phi_C) = (0.4965, 0.2634, 0.2401)$. Variation of free energy per chain for all possible compositions is given in the ternary contour plot in (f). The free energy per chain contour values are indicated in the colour bar.

5.1.2 [8.8.4]-Square

The square morphology, a common name for the morphology indicated by [8.8.4] is another common 2D morphology obtained in *ABC* star phase separation. This structure is made of one type of *SSP*, which has a single type of core shared between three domains. Two of these domains have 8 neighbouring domains each and the third has 4 neighbouring domains. The periodic patch is demonstrated in fig. 5.2. Here red domain and blue domain are the ones with 8 neighbours and the yellow domain has 4 neighbours.

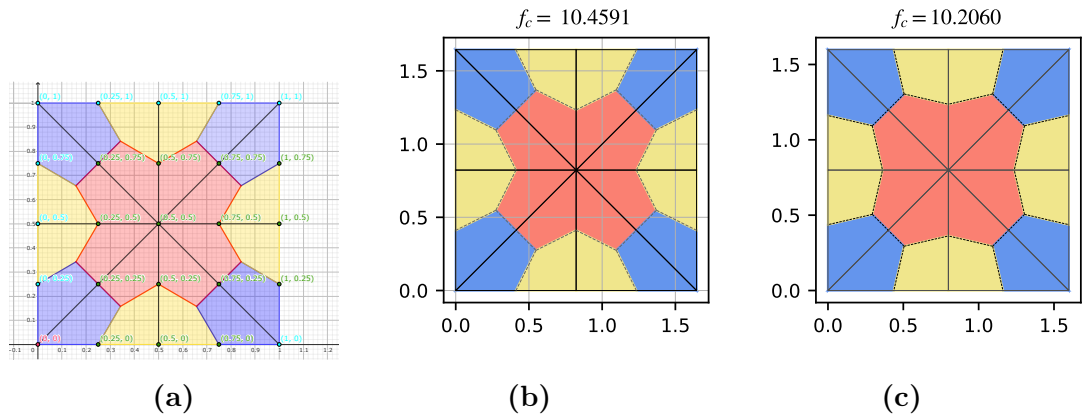


Figure 5.2: Design of [8.8.4] morphology is demonstrated here. A skeleton of the periodic patch for [8.8.4] morphology designed in Geogebra is given in (a) for monomer compositions $\phi_A = \phi_B = \phi_C = \frac{1}{3}$. In (b) *SSPs* are embedded into the skeleton and a valid patch is obtained which has undergone an overall rescaling. the minimised structure for the same composition is given in (c).

The initial configuration designed in Geogebra is shown in fig. 5.2.(a). The configuration has a ‘square’ periodicity with the $v_{xx} = 1$ and $((v_{xy}, v_{yy})) = (0, 1)$ from one blue domain to another. Similar to [6.6.6] the symmetric composition $(\phi_A, \phi_B, \phi_C) = (\frac{1}{3})$ is taken for the initial composition. By choosing the symmetric composition is it easy to decide the initial position coordinates of nodes. When all three monomer types are of same composition the domain areas of each monomer type inside a single *SSP* are equal. The initial configuration gives 25 nodes in which the origin (0,0) is the fixed node (red). Among these nodes, the 15 nodes indicated in green are free nodes and the remaining 9 in blue are periodic nodes. There are different ways of choosing periodic and free nodes. In this work, we conventionally take nodes on two outer sides as free nodes and nodes on the other two sides as periodic. Here the free nodes are selected from the bottom and right edges and periodic nodes are on the top and left edges. With

all nodes classified into free and periodic nodes, *SSPs* are created within them. The periodic patch is made of 8 identical *SSPs*. The constraint list created here has 33 elements. The initial configuration with *SSPs* is given in fig. 5.2.(b). This configuration undergoes overall scaling to obtain the first stage of minimisation and a better starting point for free energy minimisation using the constraint list. The scaled pattern shown in fig. 5.2.(b). This configuration is minimised to obtain the pattern in fig. 5.2.(c). There is only one shape of *SSP*-[8.8.4] in the scaled structure and the minimised structure, i.e. all eight *SSPs* are related by rotations and reflections.

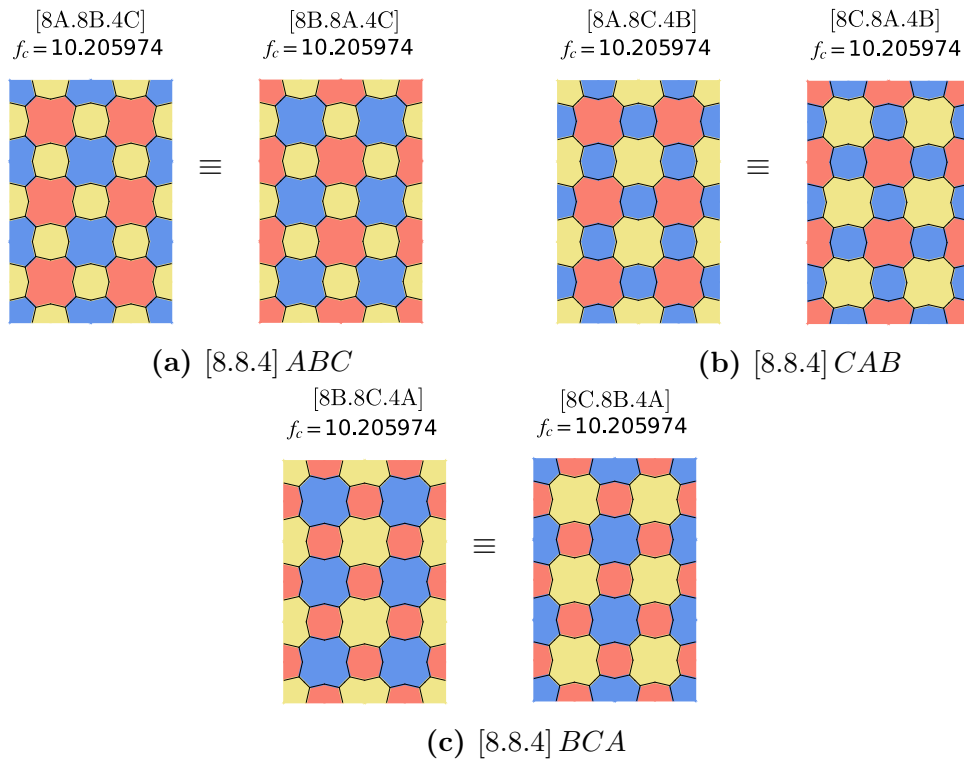


Figure 5.3: Six topological varieties of [8.8.4] morphology and the equivalencies between them are demonstrated. Morphologies shown here are minimised structures with monomer composition $\phi_A = \phi_B = \phi_C = \frac{1}{3}$ for all six sub-classes.

For [6.6.6] morphology, one topological sub-class was enough to describe the behaviour of all possible combinations of domains and monomer types. For [8.8.4], the case is different. Since three domains have different neighbour numbers, all monomer-domain arrangements are not equivalent. Six different motifs of periodic patches are possible by interchanging domains and monomer types contained in them. As two domains have the same neighbours there exists an equivalency in

three pairs of motifs. For instance, morphology indicated as [8A.8B.4C] has red and blue domains with eight neighbours and yellow domains with 4 neighbours. It is equivalent to the morphology indicated by [8B.8A.4C]. The periodic patch of these two will have *SSPs* with domain colours interchanged. On tiling it to a larger patch the equivalency is evident as demonstrated in fig. 5.3.(a). Similarly, pairs [8A.8C.4B] and [8C.8A.4B], and [8B.8C.4A] and [8C.8B.4A] are equivalent. This reduces the relevant topological sub-classes in this morphology to three.

$$[8.8.4]ABC : [8A.8B.4C] \equiv [8B.8A.4C],$$

$$[8.8.4]BCA : [8B.8C.4A] \equiv [8C.8B.4A],$$

$$[8.8.4]CAB : [8C.8A.4B] \equiv [8A.8C.4B].$$

Three sub-classes of [8.8.4] morphology are listed in fig. 5.3 along with their real space equivalencies. The free energy analysis is conducted on these three sub-classes.

Starting with the minimised configuration for $\phi_A = \phi_B = \phi_C = \frac{1}{3}$ for each sub-classes, the ternary space is explored. The free energy per chain is determined for each point in the ternary space, which is divided into 4050 points. The exploration technique takes 4-5 hours to complete all valid configurations. The three different sub-classes are explored separately, and three corresponding free energy maps are obtained and presented in fig. 5.4. The free energy contours are plotted for the same intervals as for the [6.6.6] morphology in fig. 5.1. The contours are along the sides of the composition triangle. The 8.8.4 configuration favours compositions where the volume fraction of the domain with 4 neighbours is small, so the minimum free energy per chain is located halfway along the edge of the composition triangle between the two "8-neighbour" monomer species. The sub-classes with red (*A*) and blue (*B*) 8 neighboured domains lie along the *AB* line. The compositions that give large red and blue domains have lower free energy. An example of such morphology is given in fig. 5.4.(a). The monomer compositions for this pattern are $\phi_A = 0.4397$, $\phi_B = 0.4601$ and $\phi_C = 0.1002$, which lies close to the red/blue border. The red contours in these free energy maps are those compositions that exhibit the lowest free energy per chain. The pattern corresponding to $\phi_A = \phi_B = \phi_C = \frac{1}{3}$ has higher free energy per chain as they belong to the green contour in all free energy maps obtained. The free energy maps for [8.8.4] *CAB* and [8.8.4] *BCA* also exhibit similar characteristics. The [8.8.4] *CAB* morphologies are found along the side *AC* and [8.8.4] *BCA* morphologies are found along the side *BC*. Examples of configurations with lower free energy per chain in both these sub-classes are shown in fig. 5.4.(b) and (c).

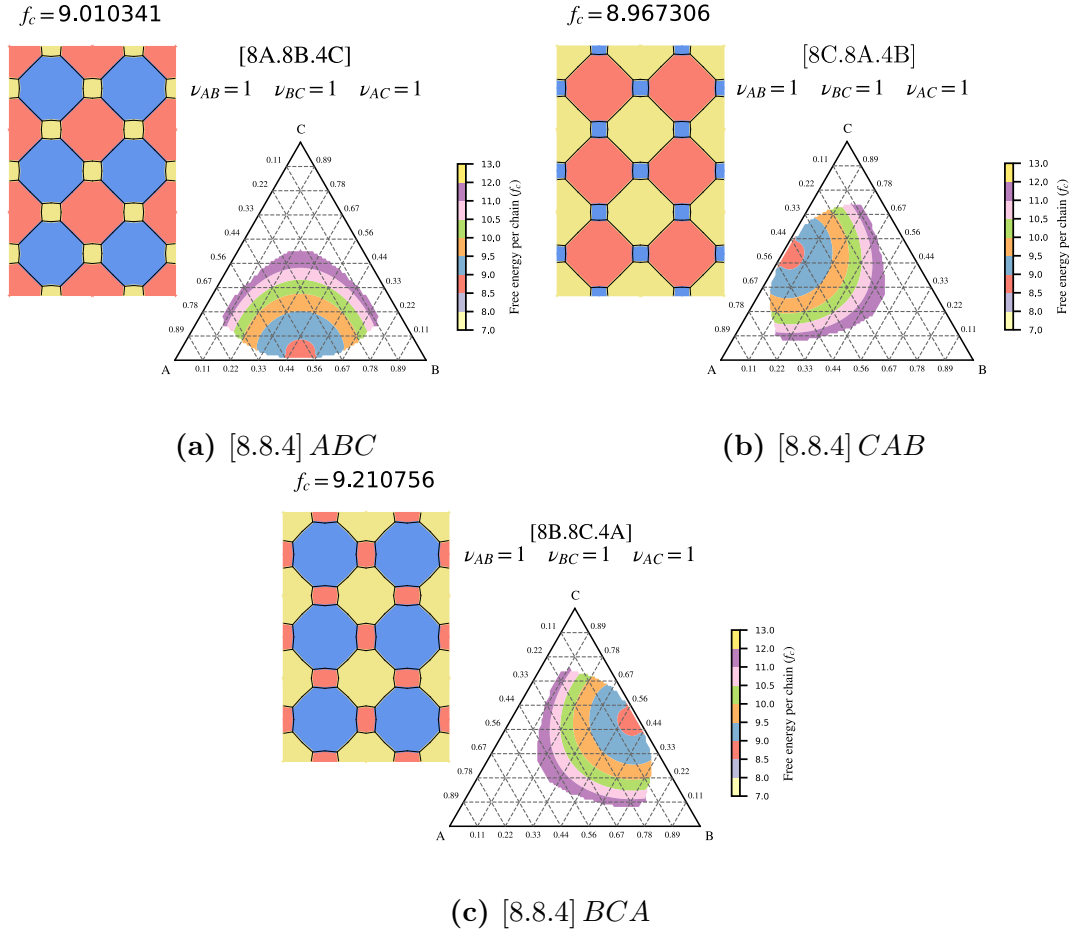


Figure 5.4: The free energy maps for [8.8.4] morphology is given for three sub-classes: *ABC*, *CAB*, *BCA*. An example of the morphology configuration that belongs in the contour with lower free energy values is given for each topological sub-class. Monomer compositions of these configurations are: (a) $\phi_A = 0.4397$, $\phi_B = 0.4601$, $\phi_C = 0.1002$), (b) $\phi_A = 0.4764$, $\phi_B = 0.0753$, $\phi_C = 0.4483$, and (c) $\phi_A = 0.1433$, $\phi_B = 0.4962$, $\phi_C = 0.3605$). Patterns in (a), (b) and (c) are found in blue, red and blue contours in the free energy maps respectively.

5.1.3 [12.6.4]-Triangle

The morphology in which we can trace a triangle between larger domains of the same type is identified as [12.6.4] or triangular morphology. This is another common morphology observed in *ABC* star phase separation. According to the nomenclature convention used, this morphology consists of only one type of *SSP*

5. *ABC* star terpolymers morphologies: Periodic

with a core shared by one domain with 12 neighbours, another domain with 6 neighbours and another domain with 4 neighbours.

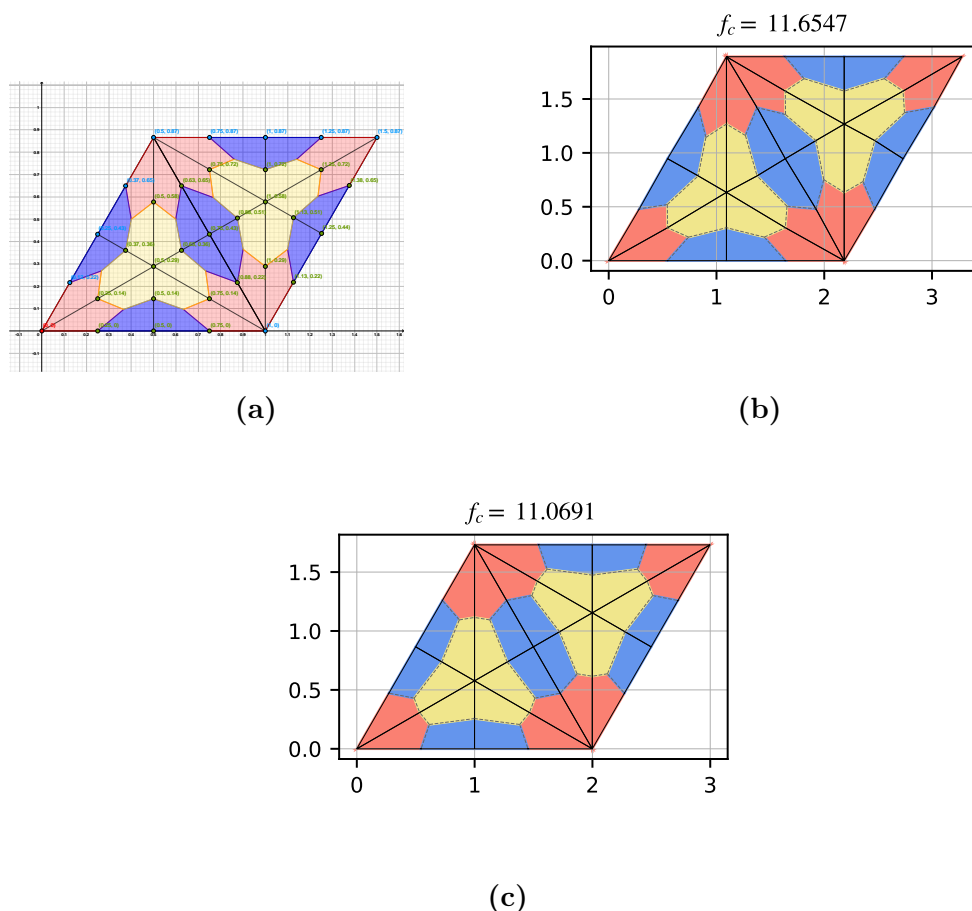


Figure 5.5: The initial configurations of [12.6.4] morphology is given here. The initial design of its periodic patch is shown in (a). Different nodes are indicated in them: fixed nodes (red), free nodes (green) and periodic nodes (blue). On the right (b) is the scaled initial morphology configuration with *SSPs*. The minimised structure is given in (c).

The periodic patch for this morphology contains two triangles whose vertices are at the centre of the largest domains sharing a side to form a rhombus. The initial design of this periodic patch is given in fig. 5.5.(a). Fixed node (red), free nodes (green) and periodic nodes (blue) are identified manually from this initial skeleton. There are 33 nodes in total, of which 23 are free and 9 are periodic. The

initial *SSP* configuration is created by embedding this skeleton with 12 *SSPs* for monomer composition $\phi_A = \phi_B = \phi_C = \frac{1}{3}$. The resulting constraint list will have 49 elements. The structure obtained after minimisation via affine rescaling of the structure is shown in fig. 5.5.(b). This is used as the starting configuration for full minimisation to obtain fig. 5.5.(c). This configuration is a valid local minimum and is used as a starting point for complete minimisation to obtain patterns in fig. 5.6. The minimised pattern also contains a single shape of *SSP* with all *SSPs* being rotations or reflections of each other.

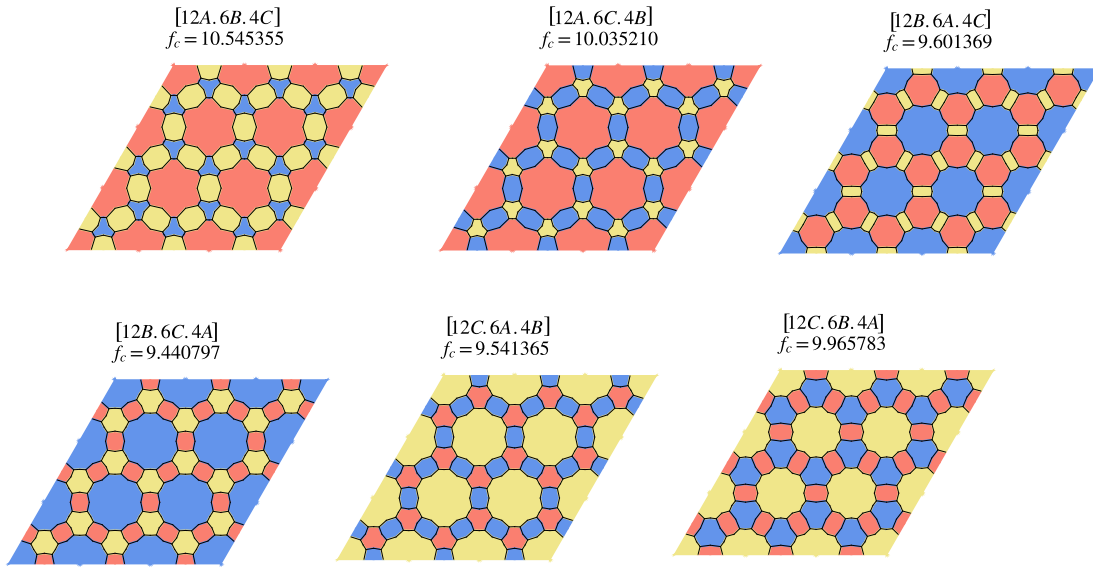


Figure 5.6: Different topological sub-classes in [12.6.4] morphology are illustrated here. The monomer compositions of these structures are: (12A.6B.4C): $\phi_A = 0.4701, \phi_B = 0.1837, \phi_C = 0.3462$; (12A.6C.4B): $\phi_A = 0.5159, \phi_B = 0.3693, \phi_C = 0.1148$; (12B.6A.4C): $\phi_A = 0.3805, \phi_B = 0.4197, \phi_C = 0.1998$; (12B.6C.4A): $\phi_A = 0.2469, \phi_B = 0.5145, \phi_C = 0.2386$; (12C.6A.4B): $\phi_A = 0.2233, \phi_B = 0.2633, \phi_C = 0.5134$; (12C.6B.4A): $\phi_A = 0.2733, \phi_B = 0.2913, \phi_C = 0.4354$.

Unlike [8.8.4] and [6.6.6] morphologies there are no topologically equivalent sub-classes for [12.6.4]. As the domain neighbours are different for three domains we get six distinct tilings with topological sub-classes within the [12.6.4] morphology: 12A.6B.4C, 12A.6C.4B, 12B.6A.4C, 12B.6C.4A, 12C.6A.4B and 12C.6B.4A. For unequal monomer compositions, these topological sub-classes are demonstrated in fig. 5.6.

5. *ABC* star terpolymers morphologies: Periodic

Since there are no topological equivalences, six ternary composition spaces are explored for each of the topological sub-classes. The exploration starts from the minimised configuration for $\phi_A = \phi_B = \phi_C = \frac{1}{3}$ and explores the rest of the ternary space among 4050 points in them. The resulting six free energy spaces are given in fig. 5.7. These free energy contours are accumulated near three corners of the composition triangle. The topological sub-classes with *A* in the 12 neighbored domain have free energy contours near corner *A* where *A* is the majority species. So, for example, from fig. 5.7. (a) where the *B* type monomers occupy the 6 neighbored domain at the region with lower free energy per chain, the compositions are $\phi_A > \phi_B > \phi_C$ so lies along the AB edge of the phase space. Similar characteristics are observed for the other four sub-classes too. The topological sub-classes with 12 sided blue and yellow domains are found near *B* and *C* corners, respectively. The pattern with $\phi_A = \phi_B = \phi_C = \frac{1}{3}$ has a higher free energy per chain in all free energy maps obtained. The morphology patterns given in fig. 5.6 belong either in orange or blue contours in the energy map.

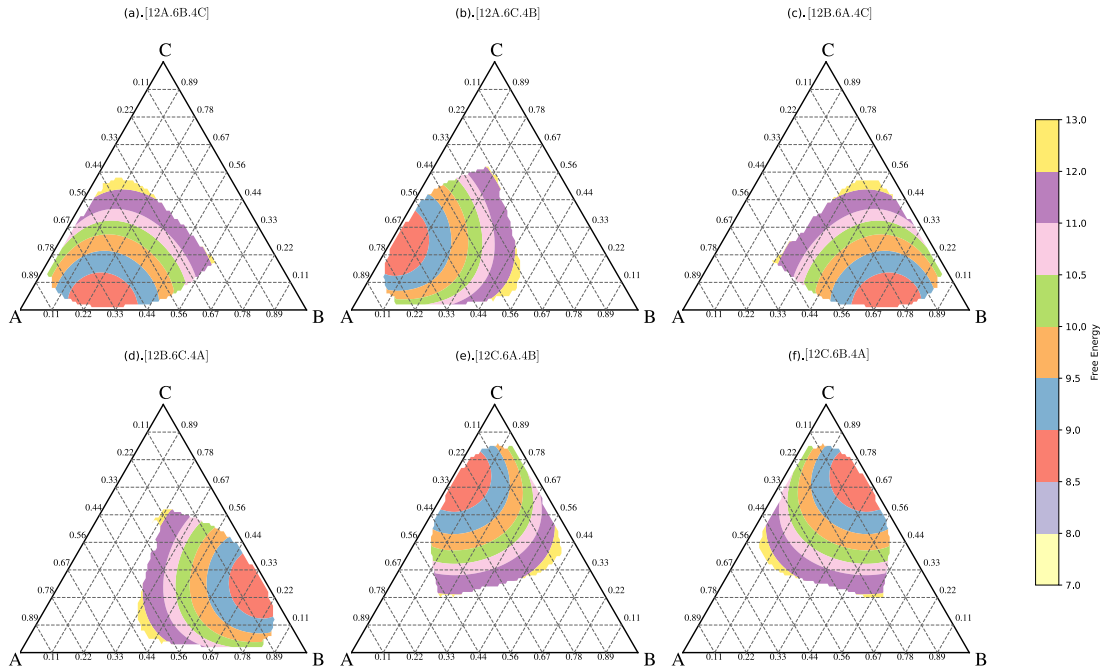


Figure 5.7: Free energy maps for six topological sub-classes of [12.6.4] morphology are given. The colour map for contours is also shown.

5.1.4 [8.6.4; 8.6.4; 8.6.6]

Until now, we looked at simple morphologies whose periodic patches can be described by a single geometrical shape. There exist complex morphologies with more than one core like [8.6.4; 8.6.4; 8.6.6] [27, 50, 91]. This morphology has three types of cores: one shared by 8, 6 and 6 neighboured domains and two others shared by 8, 6 and 4 neighboured domains as given in fig. 5.8.(b). So the nomenclature indicates these three cores, which indicates the three configurations in the morphology separated by a semicolon.

As in previous cases, the initial design is created with the help of Geogebra for $\phi_A = \phi_B = \phi_C = \frac{1}{3}$ as given in fig. 5.8.(a). The nodes obtained are identified as fixed (red), free (green) and periodic (blue) nodes, similar to previous cases. There are 45 vertices in the design, of which 31 are free, and 13 are periodic nodes. The initial configuration of the corresponding periodic patch is created by embedding the *SSPs* into these nodes. The patch contains 16 *SSPs* of two different types. The constraint list for this periodic patch has 65 entries in it. The three different cores lead to the creation of three different *SSPs* which are marked in fig. 5.8.(b). One triangle has a red domain at the right angle indicated by [8.6.6] which has blue and yellow domains that neighbours 6 other domains. Other two triangles are the one with blue ([8.6.4]) and red ([8.6.4]) at the right angles. These blue and red domains each have 4 domains as neighbours. The configuration created from the design is scaled to the local minima in fig. 5.8.(b). On minimising this configuration, we get the structure in fig. 5.8.(c). Unlike previous morphologies upon minimisation, the *SSPs* did not sustain its non-minimised triangular shape (with three straight edges around the outside of the *SSPs*). There are 4 different *SSP* geometry present in the minimised periodic patch while the topology of domains remains the same. In fig. 5.8.(c), from bottom left one *SSP* has a red domain with the right angle, to its left is an *SSP* with yellow/blue edge bending into the polygon, third with yellow/red line inverted into the polygon and fourth is the *SSP* with blue domain in its right angle. Each *SSP* geometry occupies a different area in the minimised structure, and so contains a different number of polymer chains per unit depth (in the out-of-plane direction). Hence, the minimisation procedure represents the transfer of polymer chains between neighbouring *SSPs* in order to find the most optimal structure. This is a feature common to all geometries with non-equivalent *SSPs*, i.e. for all the structures that follow in chapters 5 and 6.

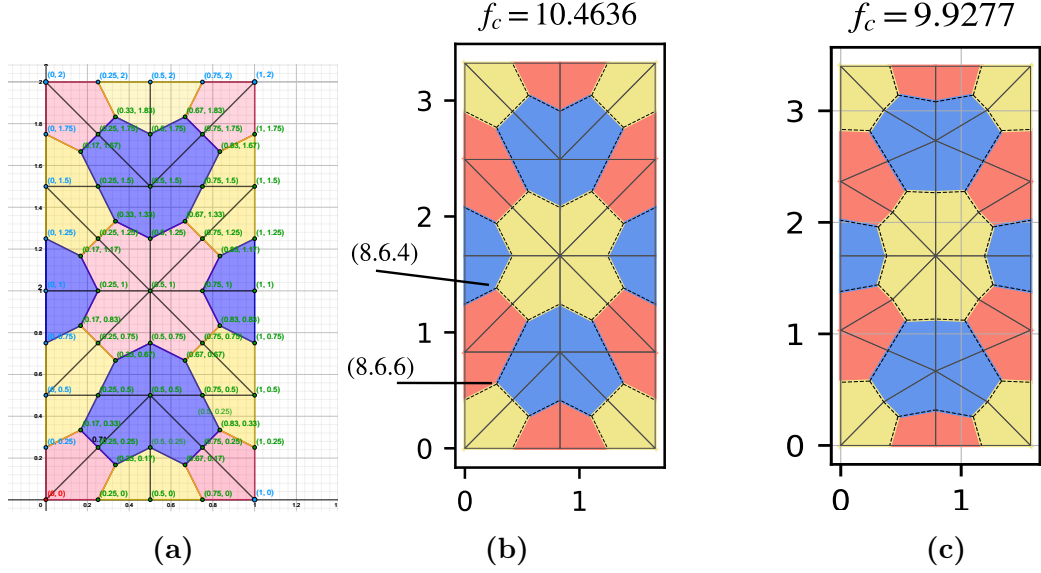


Figure 5.8: Initial configurations of $[8.6.4; 8.6.4; 8.6.6]$ is given here . The first design of the morphology is given in (a) and the configuration with *SSPs* in them is given in (b). In (b) two types of *SSPs* are marked. The minimised configuration for the same monomer composition as (b) is given in (c).

Similar to $[8.8.4]$ morphology there are three topological equivalences between different sub-classes of $[8.6.4; 8.6.4; 8.6.6]$. Example morphologies with *ABC* star terpolymers with equal monomer composition ($\phi_A = \phi_B = \phi_C = \frac{1}{3}$) are given in fig. 5.9 (a)-(c). Looking at a bigger patch of the morphology given in fig. 5.9.(a) yellow *C* domains and blue *B* domains are the same and the pattern remains exactly the same if we interchange them. So there is an equivalency between

$$[8A.6B.4C; 8A.6B.4C; 8A.6B.6C] \equiv [8A.6C.4B; 8A.6C.4B; 8A.6C.6B].$$

In the figure, this topological sub-class is identified as $[8.6.4; 8.6.4; 8.6.6] ABC$ where *ABC* indicates the order in which the domain numbers are assigned. Other equivalent topological sub-classes in this morphology are:

$$[8.6.4; 8.6.4; 8.6.6] BAC :$$

$$[8B.6A.4C; 8B.6A.4C; 8B.6A.6C] \equiv [8B.6C.4A; 8B.6C.4A; 8B.6C.6A],$$

$$[8.6.4; 8.6.4; 8.6.6] CAB :$$

$$[8C.6A.4B; 8C.6A.4B; 8C.6A.6B] \equiv [8C.6B.4A; 8C.6B.4A; 8C.6B.6A].$$

5. ABC star terpolymers morphologies: Periodic

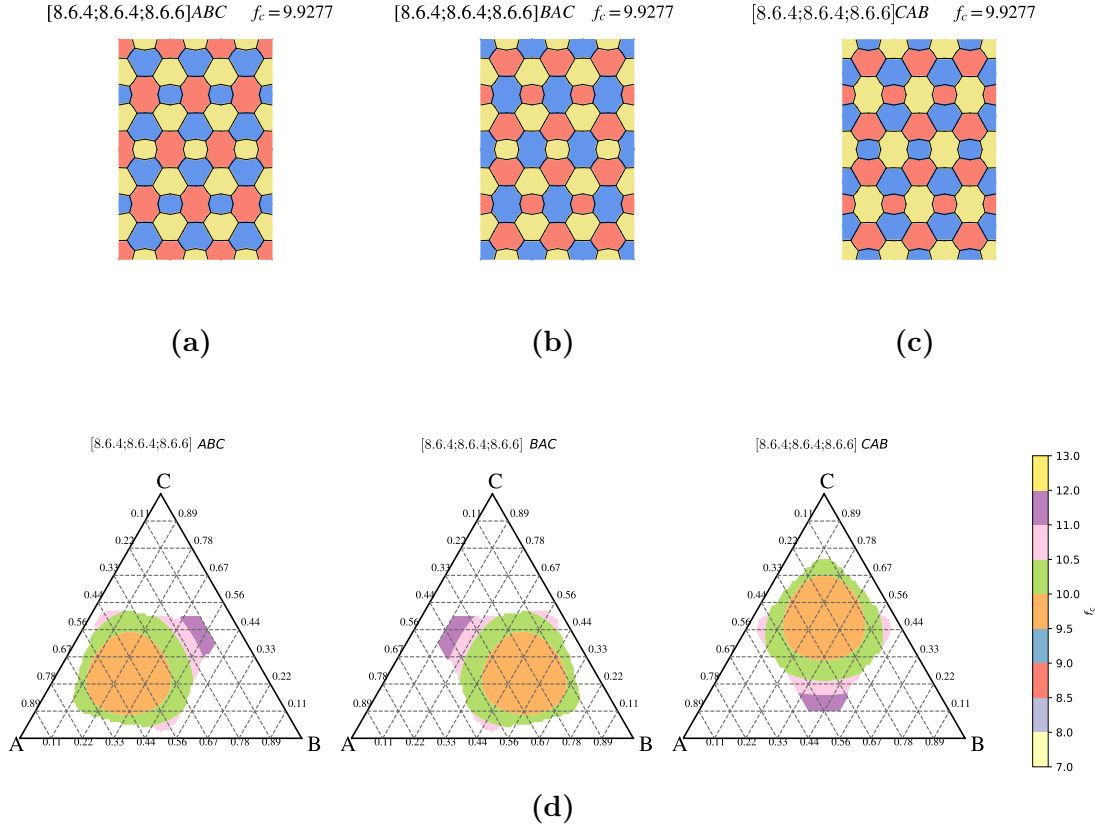


Figure 5.9: Here the morphologies for (a) $[8.6.4;8.6.4;8.6.6]ABC$, (b) $[8.6.4;8.6.4;8.6.6]BAC$ and (c) $[8.6.4;8.6.4;8.6.6]CAB$ are given. These structures are for compositions ($\phi_A = \phi_B = \phi_C = \frac{1}{3}$). Corresponding free energy maps for these topological sub-classes are given in (d). Morphology configurations shown here belong to the orange region which is the lowest energy contour.

Free energy maps for these three topological sub-classes are created using the exploration method as in previous cases and are shown in fig. 5.9. The composition space is explored starting with the symmetric configuration as in previous cases. The contours are plotted for different values of free energy per chain. These contours are found between the corners and centre of the triangle. The region with lower free energy value is large compared to others. The structures with symmetric compositions given in fig. 5.9 belong to the lower free energy contour in orange.

5.1.5 [10.6.4; 10.6.4; 10.6.6]

Another structure with more than one core that has been observed in *ABC* star phase separation is [10.6.4; 10.6.4; 10.6.6] [27, 50, 91]. Similar to [8.6.4; 8.6.4; 8.6.6], this morphology also has more than one core. Here also, there are three cores: two [10.6.4] cores shared by 10, 6 and 4 neighbored domains and one [10.6.6] core shared by 10, 6 and 6 neighbored domains.

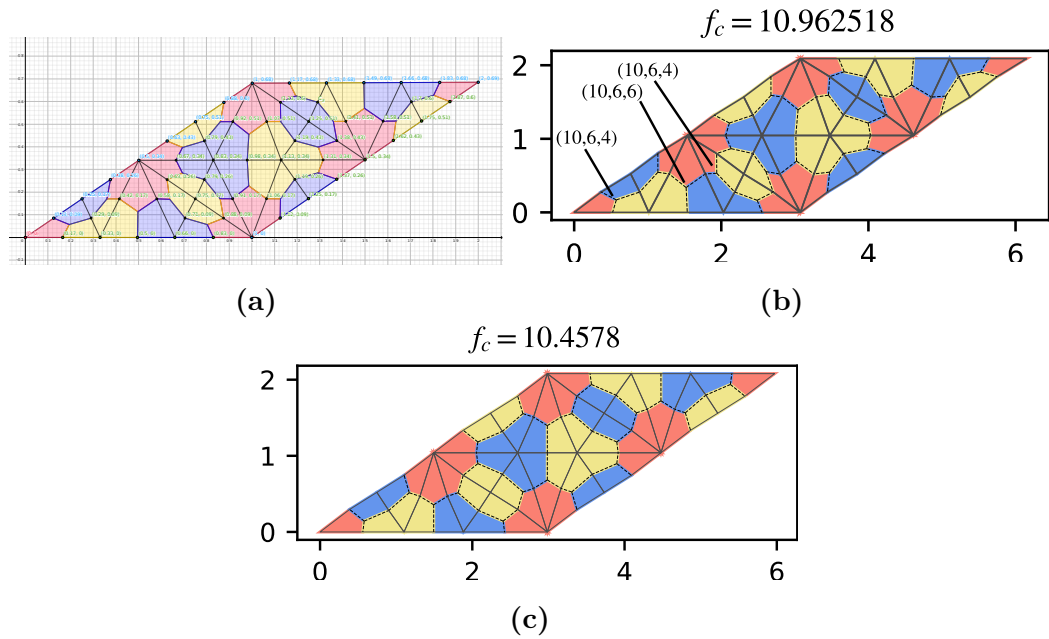


Figure 5.10: Initial configurations of [10.6.4; 10.6.4; 10.6.6] morphology are given here. The first design of the morphology (a), scaled version of the configuration (b) and minimised configuration for $\phi_A = \phi_B = \phi_C = \frac{1}{3}$ are shown. In (b), different *SSPs* that make the periodic patch are indicated.

In this case, the periodic patch is a rhombus. The initial design of the periodic patch is made which will provide with necessary position coordinates of the nodes. The nodes are classified into fixed, free and periodic as in previous cases. There are 55 nodes in the periodic patch out of which 39 are free and 15 are periodic nodes. Three different *SSPs* (indicated in fig. 5.10.(b)) are combined together to form this periodic patch. One *SSP*, (10.6.4) has a blue domain at its right-angled corner, another one, (10.6.6) with no right angles in it and a third (10.6.4) with a yellow domain at the right-angled corner. Upon embedding the nodal skeleton with *SSP* the constraint list is created which in this case has 81 elements. The initial configuration for the periodic patch is scaled to find a better

5. *ABC* star terpolymers morphologies: Periodic

configuration for overall minimisation which is given in fig. 5.10.(b). The constraint list of this scaled configuration undergoes minimisation to get the pattern given in fig. 5.10.(c). In the stable structure, *SSP* borders are slightly curved, but three different types of *SSP*s remain the same topologically, and there is no symmetry breaking into subsets of the three *SSP* types.

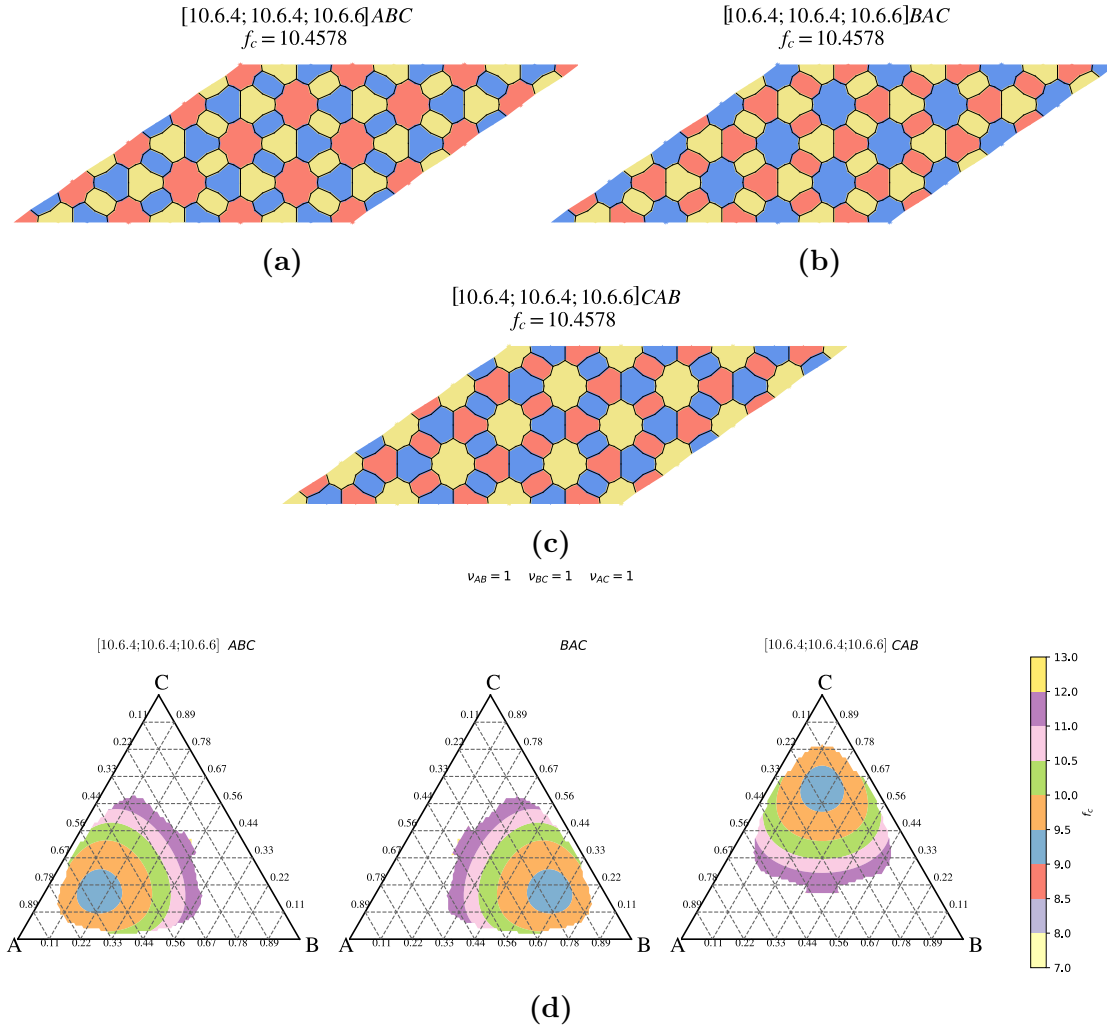


Figure 5.11: Here are the morphologies for (a) $[10.6.4; 10.6.4; 10.6.6]ABC$, (b) $[10.6.4; 10.6.4; 10.6.6]BAC$ and (c) $[10.6.4; 10.6.4; 10.6.6]CAB$ are given. These structures are of the compositions ($\phi_A = \phi_B = \phi_C = \frac{1}{3}$). The free energy maps for these morphologies are given in (d). These configurations of symmetric *ABC* star melt belong to the light pink contour in the free energy maps. The free energy contour values are indicated in the colour bar.

Similar to [8.6.4; 8.6.4; 8.6.6] morphology, topological equivalences exist in this morphology. In fig. 5.10.(c) yellow domains and blue domains are the same. On interchanging the contents in these two domains, the morphological sub-classes remain equal which gives

$$(10A.6B.4C; 10A.6B.4C; 10A.6B.6C) \equiv (10A.6C.4B; 10A.6C.4B; 10A.6C.6B).$$

For the ease of labelling this topological sub-classes is identified [10.6.4; 10.6.4; 10.6.6] *ABC*.

The other two topological sub-classes are,

$$[10.6.4; 10.6.4; 10.6.6]BAC :$$

$$(10B.6A.4C; 10B.6A.4C; 10B.6A.6C) \equiv (10B.6C.4A; 10B.6C.4A; 10B.6C.6A),$$

$$[10.6.4; 10.6.4; 10.6.6]CAB :$$

$$(10C.6A.4B; 10C.6A.4B; 10C.6A.6B) \equiv (10C.6B.4A; 10C.6B.4A; 10C.6B.6A).$$

Examples of these sub-classes are given in fig. 5.11.(a), (b) and (c). Free energy analysis is done for these three sub-classes as before. The resulting free energy maps are given in fig. 5.11.(d). In the resulting maps, the free energy contours are located between the centre and corners of the triangle. The contours are closer to the corner, which indicates the monomer type that fills the domain with 10 neighbours. Compositions in the blue regions have structures with the lowest free energy per chain. The morphologies with symmetric compositions belong to contour bands with larger free energy per chain.

There are many other morphologies reported in the phase separation simulations based on *DPD* and *SCFT* [27, 91] as listed in table 1.1 which could be analysed in the same manner. We are now going to compare these major morphologies to create a phase space.

5.1.6 Phase space and Discussion

A phase space is constructed with above mentioned morphologies to check which morphology is stable for each given composition. All the above free energy maps are combined to form the phase space. The phase space is divided into 4050 points, where each point indicating the composition (ϕ_A, ϕ_B, ϕ_C) is varied with an increment of 0.01. The value of free energy per chain for each morphology

5. *ABC* star terpolymers morphologies: Periodic

is compared for each point in this space. The morphology sub-classes with the lowest free energy per chain are marked at that point according to identifiers indicated for each topological sub-classes in table 5.1. The list of morphologies and their topological species along with the colours which indicate them in the phase space is given in table 5.1.

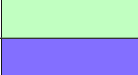
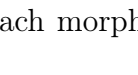
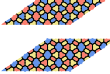
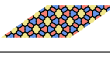
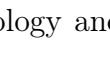
Morphology	Topological sub-classes	Identifier	Pattern
[6.6.6]	<i>ABC</i>		
[8.8.4]	<i>ABC</i> <i>ACB</i> <i>CBA</i>	  	  
[12.6.4]	<i>ABC</i> <i>ACB</i> <i>BAC</i> <i>BCA</i> <i>CAB</i> <i>CBA</i>	     	     
[8.6.4; 8.6.4; 8.6.6]	<i>ABC</i> <i>BCA</i> <i>CBA</i>	  	  
[10.6.4; 10.6.4; 10.6.6]	<i>ABC</i> <i>BCA</i> <i>CBA</i>	  	  

Table 5.1: Table of topological sub-classes in each morphology and identifiers used in the phase space.

As we have seen the morphologies are formed as a result of a perfect packing of

the monomer domains that is felicitated chain stretch and surface interactions. It is known that perfect packing occurs in hexagonal structures, which should be the case when all monomer domains are of similar size. When the size of one domain reduces, morphologies that have higher neighbouring domains (like [12.6.4]) will be favoured. When there are similarly sized two domains, for the same reason to achieve efficient packing, morphologies like [8.8.4] will be favoured. In between these, there can be other packing arrangements that will be chosen by the melt due to the composition and free energy.

The resulting phase space for *ABC* star with symmetric interactions is given fig. 5.12. We obtain a phase space that is mirror symmetric to $\phi_A = \phi_B$, $\phi_B = \phi_C$ and $\phi_A = \phi_C$ lines in the ternary space. This is true when we ignore the topological sub-classes and consider each morphology is indicated by one colour. This occurs because the interactions between the three species are symmetric.

In the resulting phase space in fig. 5.12, we observe a light green region in the middle indicating [6.6.6] morphology. The individual free energy map shows that [6.6.6] morphology is stable when all three branches have comparable lengths, $\phi_A \approx \phi_B \approx \phi_C$. The [8.8.4] morphology is found at the border of this region to three sides of the hexagon towards the centre of the ternary triangle sides. These are indicated by the purple shades on the three sides of the ternary space. They are more stable when two branches are in comparable lengths and the third is smaller than the other two. Taking any point from the purple region along the side *AC*, the compositions will be $\phi_A \approx \phi_C > \phi_B$, the same for the other two topological sub-classes. The teal/light blue regions are [12.6.4] morphologies. They occupy the corner regions of the ternary space where all three chains are extremely different lengths. In this region, one chain is always significantly longer than the other two. For instance, the region with [12.6.4] morphology near the corner *A* given in teal-blue has compositions in order $\phi_A > \phi_B > \phi_C$. The above are the regions where morphologies with a single type core are found. At the intersection of regions with [6.6.6], [8.8.4] and [12.6.4] we find that the morphologies with multiple cores are more stable. Surrounding the light green region with [6.6.6] on three sides are regions of blue shades indicating [8.6.4; 8.6.4; 8.6.6]. This region also indicates comparable branch lengths with one of them longer than the other two. This region shares borders with [8.8.4] and [10.6.4; 10.6.4; 10.6.6] morphologies. The regions of orange shades indicates [10.6.4; 10.6.4; 10.6.6], which has three different *SSP* cores. The region has a triangular shape extending into the region of [12.6.4]. Again as these regions are also closer to the centre, the compositions are comparable, but one is longer than the other two. In these two multi-core cases, none of the three branches is extremely small, like in [8.8.4] and [12.6.4]. In the obtained phase space it is interesting to observe that [8.8.4] and [12.6.4] morphologies occupy the majority of the space.

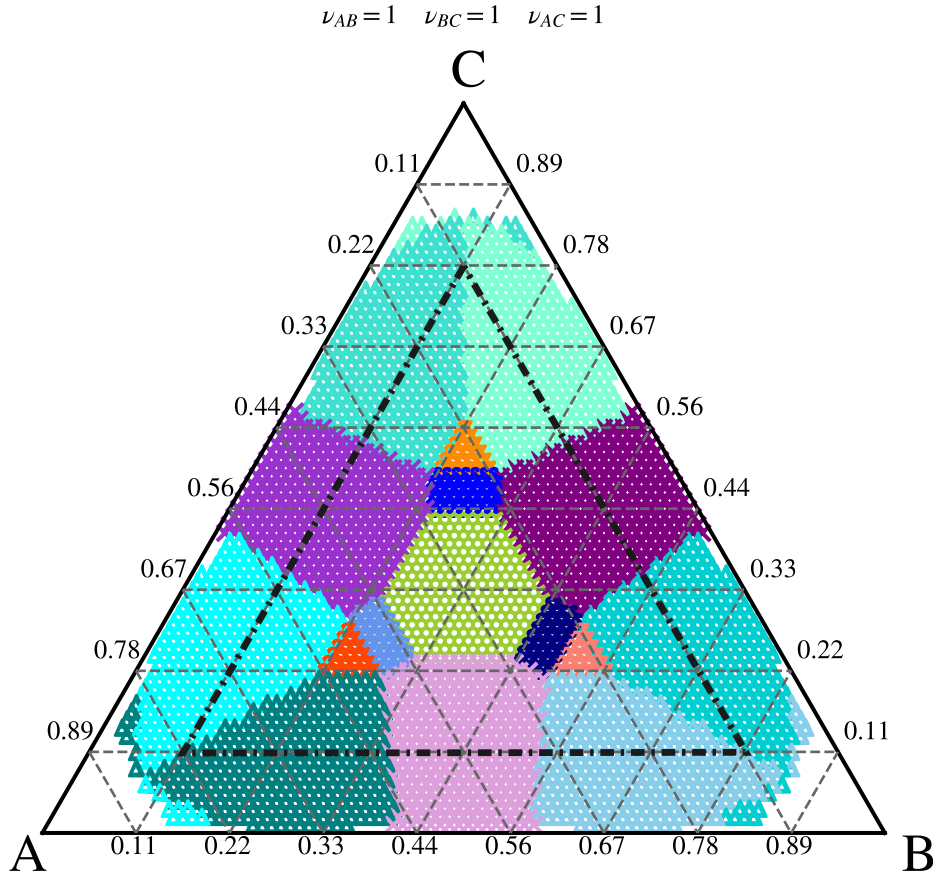


Figure 5.12: Phase space for *ABC* star morphology with [6.6.6], [8.8.4], [12.6.4], [8.6.4; 8.6.4; 8.6.6] and [10.6.4; 10.6.4; 10.6.6]. The triangle inside which 2D phase space is valid is indicated by dashed bold lines. A list of morphologies and corresponding identifiers used is given in table 5.1.

In the above given phase space in fig. 5.12 in a region near the centre, the compositions are almost the same. This results in domains of the same area trying to pack in together. The balance between the interfacial energy and stretching energy forces them to pack in the most efficient way: hexagonal packing as we predicted. As the area of one domain reduces, they form other morphologies to attain the packing equilibrium. When one branch is small and the other two are approximately equal, say $\phi_A = 0.43$, $\phi_B = 0.43$ and $\phi_C = 0.14$, domains formed by *A* and *B* are quite large. The same amount of *A* and *B* chain length will choose to stretch out in the opposite direction to balance the stretching energy making

octagons side by side (refer to fig. 5.4.(a)). When all compositions are different, the interplay between stretching and interfacial energy results in different domain shapes. In the regions favouring [12.6.4], the composition of one branch is always large > 0.5 , which makes structures with large domains surrounded by smaller domains more stable (refer to fig. 5.6).

Our phase space obtained agrees with the one obtained by the Monte Carlo method by Gemma et al [50]. In this work, they vary the composition of one branch keeping the other two the same so that the ratio of $\phi_A : \phi_B : \phi_C$ is $1 : 1 : x$. So in our phase space, this represents the line joining the corner C and AB . At $x = 1$, they report [6.6.6], and we also find the same at $\phi_C = 0.33$. On decreasing the value of x , for a range of values near $x \approx 0.5$, they report [8.8.4]. At $\phi_C = 0.16$ and nearby region we have [8.8.4]. At $x \approx 1.5$, they report [8.6.4; 8.6.4; 8.6.6], which corresponds to $\phi_C = 0.5$ where we also have the same morphology. For $x \approx 2$ they have [12.6.4] which agrees with our predictions at for $\phi_C = 0.66$ and between $x \approx 1.5$ and $x \approx 2$ they find [10.6.4; 10.6.4; 10.6.6] similar to our phase space. Beyond $x = 1.87$ and below $x = 0.37$ they observe various 3D morphologies. These calculations were done with $N\chi \approx 54$ while in ours we choose $N\chi = 60$. Hence, the composition values are almost similar.

A similar comparison can be made for the phase spaces calculated using *SCFT* [91, 173]. These two work reports a similar phase space with a similar order of morphology placement in their phase space. They report a greater range of 2D tilings in their work. They also report lamellar structures near regions where $\phi_A < 0.11$ and $\phi_B < 0.11$ and $\phi_C < 0.11$.

When the composition of one branch is relatively small < 0.11 , our minimisation routine often struggles to find a minimised structure. When one composition value is very small *SSPs* more easily become invalid polygons as the node positions are varied, as compared to compositions nearer the centre. This is understandable as most previous work has reported 3D and 2D structures with lamellar in this region. When one branch is really small, the polymer chain acts similar to a diblock which results in above mentioned complex structures. These structures are out of scope for the present version of our *SSP* methodology. Hence the phase space we present is valid inside the triangle inside the lines corresponding to $\phi_A = 0.11$, $\phi_B = 0.11$ and $\phi_C = 0.11$. This triangle is indicated by bold black dashed lines in fig. 5.12 inside which the phase space we are presenting is valid.

Even though the phase space we have is incomplete, it can be included in more 2D tiling-like morphologies that are reported in the literature. Using Python, the runtime needed to make a symmetric phase space is below 48 hours (this could certainly be made faster by using a pre-compiled language such as C++ or Fortran).

5.2 *ABC* star architectures and phase space for asymmetric interactions

ABC star terpolymers with unequal interaction between the branches are considered asymmetric. While *ABC* stars with symmetric interaction strength between their branches produce interesting morphologies, in order to have phase spaces that are comparable to the experiments, we need to address asymmetric interactions. The phase separation in *ABC* block copolymers has been extensively studied by the Matsushita group [99, 102, 104, 157] using polyisoprene(I), polystyrene(S) and polyvinylpyridine(P) (ISP) star and homopolymer blends. They report a wide variety of morphologies which includes the ones we are addressing in this work. While the exact values of $N\chi$'s of the polymer blends are not mentioned in their work, it is definitely not equal. Nunns et al. used polyisoprene (I), polystyrene (S), and poly(ferrocenylethylmethylsilane) (F) to synthesize ISF star terpolymers that resulted in [8.8.4], [12.6.4] and lamellar morphologies. This molecule also has unequal interactions between its branches [114]. From these two experimental works, it is clear that the interactions do play an important role in morphologies that are been made. It has more prominence when you are hunting for complicated morphologies. Attempts have been made to map a complete phase space for *ABC* star terpolymers with asymmetric morphologies [75, 173] most using the SCFT method. These works find a variety of interesting morphologies within the phase space.

Using the *SSP* technique study of morphologies with asymmetric interaction is much easier. As interactions are controlled by the parameters ($\nu_{AB}, \nu_{BC}, \nu_{AC}$) in our method, they can be varied by changing the values in the geometry script for each morphology sub-classes. Corresponding phase spaces are made by repeating the calculations done for the symmetric case above with these updated geometry scripts. Hence phase spaces and detailed information on the morphological structures are obtained for any set of asymmetric interactions we need. Here we are reporting three different cases of different asymmetric interactions by varying ν and its effect on the structure.

1. $\nu_{AB} = \nu_{BC} = 1, \nu_{AC} < 1$, where there is less repulsion between *A* and *C* monomers with respect to *A* to *B* and *B* to *C* monomer repulsion.
2. $\nu_{AB} = \nu_{BC} = 1, \nu_{AC} > 1$, where there is higher repulsion between *A* and *C* monomers with respect to *A* to *B* and *B* to *C* monomer repulsion.
3. $\nu_{BC} < \nu_{AB} < \nu_{AC}$, where *B* and *C* repels less strongly and *A* and *C* repels more strongly weakly with respect to the interactions between *A* and *B*.

5.2.1 Discussion on effects of asymmetric interactions in *ABC* star terpolymers.

When there are variations in the repulsive strength between the branches, the final morphology is affected. As we have established the domains containing different monomer types assemble in an efficient packing in space depending on the monomer compositions and interactions. When the interaction strengths are equal, the effects of stretching of all branches are the same and interfaces are almost in a straight line.

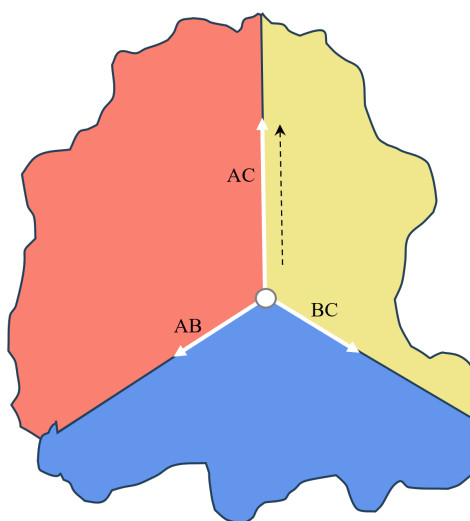


Figure 5.13: Illustration of the effect of asymmetric surface tension on different domains for $\nu_{AB} \approx \nu_{BC} < \nu_{AC}$. The arrows indicate the relative strengths at the interface. The dashed arrow indicated the effective displacement of the core due to asymmetric surface tension.

When there is an asymmetry in the interactions, the stretching of chains results in interesting effects on the interfaces. We will discuss the possible effects of asymmetric interactions considering a melt with $\nu_{AB} = \nu_{BC} < \nu_{AC}$. When ν_{AC} is larger than other interactions the *A* and *C* domains have higher surface tension. We note that the optimal 2D shape with minimal circumference at a fixed area is the circle: hence we expect those domains with the largest surface tension to be perturbed towards the circular shape. In this case, the *A* and *C* domains have the largest surface tension and the remaining interfaces (*AB* and *BC*) become more circular. As the surface tension along *AC* is larger the effective displacement of the core will be in the direction of *AC* as shown in fig. 5.13. This core displacement is satisfied by increasing the length of *AB* and *BC* which will effectively curve

out *A* and *C* domains. Thus when $\nu_{AB} = \nu_{BC} < \nu_{AC}$, the morphologies which can make either *A* or *C* or both domains more circular are favoured. This can happen when there are more domains surrounding a domain like in [12.6.4] or [8.8.4] from our candidate morphologies. The domain will be more circular when the 6 neighboured domain and 4 neighboured domain are comparatively smaller which is when ϕ_B is small. So morphologies [12.6.4] and [8.8.4] should cover more regions in the phase space with this interaction asymmetry. Similar qualitative discussion can be considered for the other two cases of asymmetric interactions.

At the same time, if ν_{AC} is large, the overall value of free energy per chain will be lower typically when all domains have straighter interfacial lengths. With additional penalty in the free energy per chain due to the curving of *AB* and *BC* interfaces is balanced out when the composition of *B* is larger. So when ν_{AC} is larger the value of free energy per chain is lower for melt with higher compositions of ϕ_B . The interaction energy affects single-core morphologies and multi-core morphologies in different ways.

We will now discuss the effect of asymmetric interactions for the three cases enumerated above. We will present detailed discussions on the above mentioned consequences on the structure and morphology in each case.

5.2.2 $\nu_{AB} = \nu_{BC} = 1, \nu_{AC} < 1$

The first case is where the interactions between *B* and the other two branches (*A* and *C*) are equal, while incompatibility between *A* and *C* is less. The interaction scaling for this case is chosen to be $\nu_{AB} = \nu_{BC} = 1$ and $\nu_{AC} = 0.8$. In terms of our chosen reference of Flory interaction parameter $N\chi = 60$, we are considering the case where $N\chi_{AB} = N\chi_{BC} = 60$ and $N\chi_{AC} = 38.4$.

When we take $\nu_{AC} < 1$, we consider a melt of *ABC* star with weaker incompatibility between *A* and *C* monomers. This will affect domain interfaces and structures formed. When *A* – *C* incompatibility is weak it makes the surface tension at that interface weaker compared to the other two interfaces. So within strongly segregated domains in a given morphology, the surface tension at *AB* and *BC* interfaces is large while the *AC* interface has lower surface tension. For any morphological tiling with a specific monomer composition the area fraction of each domain is fixed within the 2D representation, but the interfaces adjust to reflect the balance of surface tensions. In this case, the *B* domain has the largest surface tension (since *A* – *B* and *A* – *C* interactions are the largest) so the *AB* and *BC* should curve outwards from the *B* domain. In a strongly segregated tiling structure interfaces with large surface tension attempt to occupy less area leading to the curving of *AB* and *BC* interfaces. The interface with weak surface tension (*AC*) should remain closer to a straight line because the *A* and *C* interactions are identical.

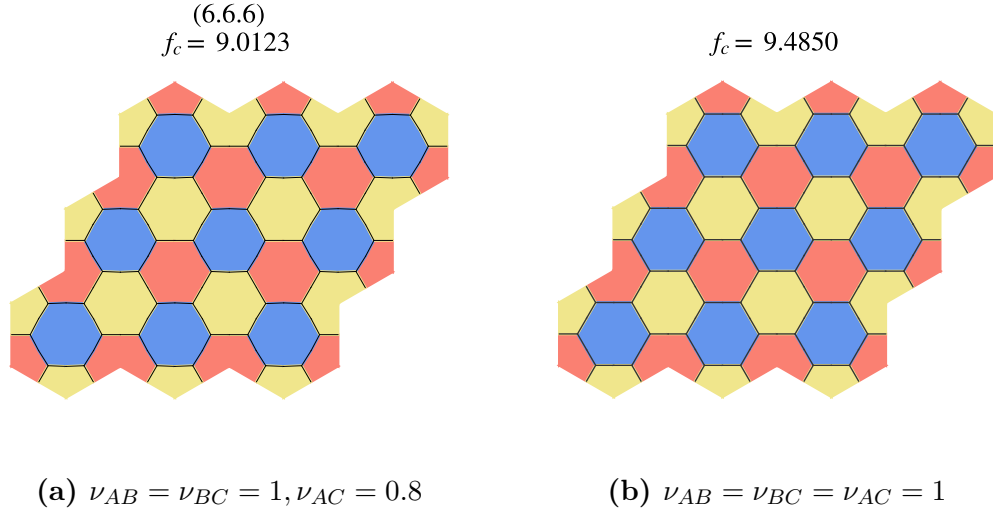


Figure 5.14: Here is the comparison of [6.6.6] morphology with monomer compositions $\phi_A = \phi_B = \phi_C = \frac{1}{3}$ with asymmetric and symmetric interactions. In the left is the minimised structure with monomer interactions (a). $\nu_{AB} = \nu_{BC} = 1, \nu_{AC} = 0.8$. The blue domains are slightly curved out in (a) compared to the structure with symmetric interactions in (b).

Figure 5.14 demonstrates the qualitative effect of asymmetric interaction of $\nu_{AC} < 1$ on phase separated structures taking [6.6.6] morphology as an example. The minimised structures of monomer compositions $\phi_A = \phi_B = \phi_C = \frac{1}{3}$ with asymmetric fig. 5.14.(a) and symmetric fig. 5.14.(b) interactions are shown for comparison. As explained above, asymmetric interactions result in the *AB* and *BC* surface tensions being larger than the *AC* surface tension. This forces *B* domain to apparently curve out as seen in fig. 5.14.(a). Even though this bend is subtle, it is distinguishable when we compare it with a structure with symmetric interaction in fig. 5.14.(b). The outward curve of the *B* interfaces means that the star polymer cores move a little towards the centre of the *B* domain, thus increasing the length of the *AC* interfaces, which is permitted because the *AC* surface tension is smaller. When we compare the equations for free energy per chain (eq. (3.124)) of [6.6.6] for the composition $\phi_A = \phi_B = \phi_C = \frac{1}{3}$ with symmetric and asymmetric interactions, the contribution to the free energy per chain from stretching of the chains remains the same for both cases, but the interfacial energy is different. The interfacial energy varies linearly with ν as in eq. (3.108). So we observe a lower free energy per chain value for the asymmetric structure. If ν_{AC} is decreased further with values reasonable in strong segregation limit, blue domains will get even rounder to preserve the surface energy. This observation is

5. *ABC* star terpolymers morphologies: Periodic

valid for other interaction parameters and domains. If $\nu_{AB} < 1$, yellow domains with *C* will bulge and when $\nu_{BC} < 1$, red domains with *A* will bulge.

A phase space is now constructed with the same morphologies we discussed above with symmetric interactions. In order to construct the phase space all calculations from the symmetric case were repeated with updating the scaled interactions in geometry scripts for each morphology sub-classes. The resulting phase space is given in fig. 5.15. The identifiers used in this phase space are the same as in the symmetric phase space.

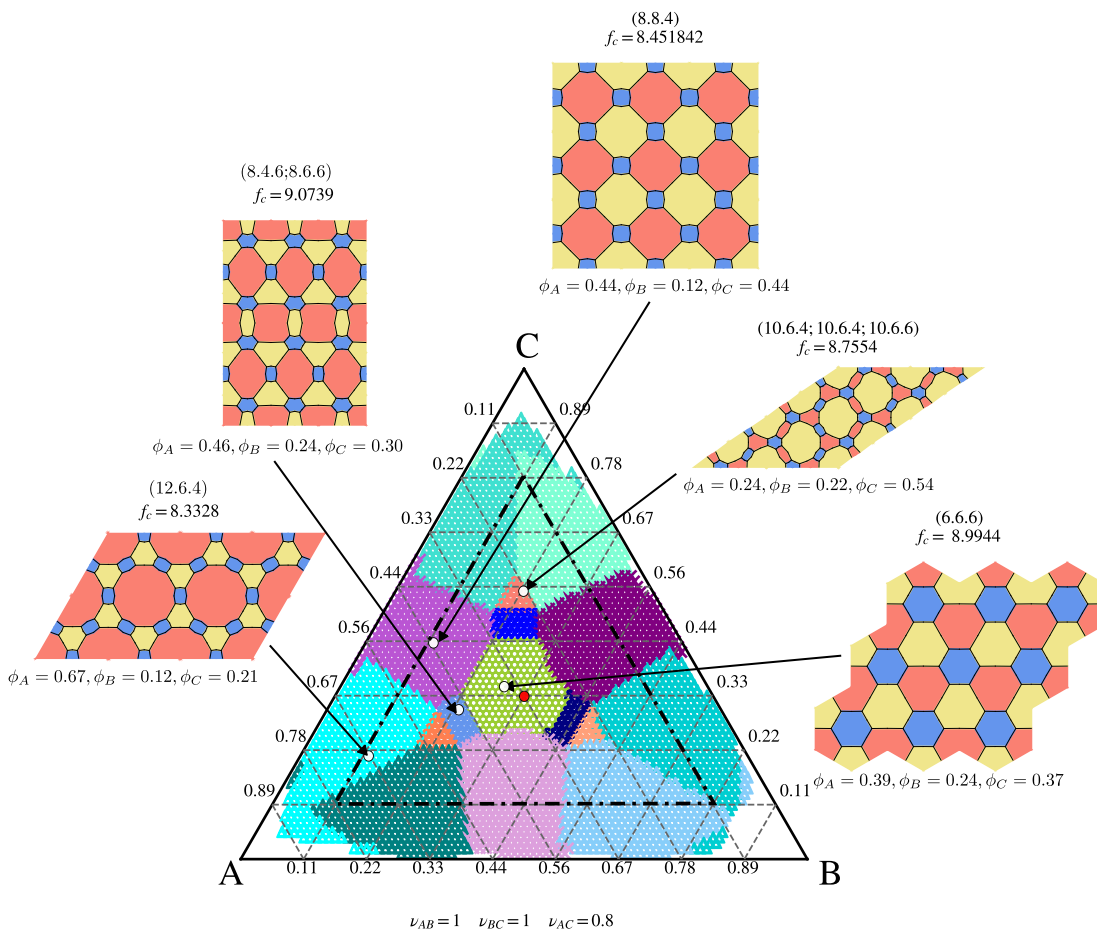


Figure 5.15: The phase space for *ABC* star with interactions: $\nu_{AB} = \nu_{BC} = 1$, $\nu_{AC} = 0.8$ is given. The colour mapping is the same as that of the symmetric phase space. The red dot indicates the centre of the triangle where $\phi_A = \phi_B = \phi_C$. The minimised morphologies from regions where *A* and *C* are dominant, where the free energy values are lower are illustrated.

5. *ABC* star terpolymers morphologies: Periodic

The most interesting observation from this phase space is the shift in the overall phase space away from the corner *B*. The centre of the composition triangle is indicated by a red dot in fig. 5.15. With respect to this dot, the shift in phase space is obvious. The phase space is no longer fully symmetric because the interactions are not symmetric. The relative positions of morphologies in the phase space remain the same. Around the centre of phase space, there is [6.6.6]. Bordering the light green region with [6.6.6] are [8.8.4] (purple shades) and [8.6.4; 8.6.4; 8.6.6] (blue shades). Within the morphologies considered [12.6.4] occupies most of the phase space (cyan/teal shades). At the region two topological sub-classes of [12.6.4] meets, [10.6.4; 10.6.4; 10.6.6] is found (orange shades). Regions occupied by different topological sub-classes within the same morphology are not identical here. The composition spaces for [8.8.4] *ABC* and [8.8.4] *BCA* are larger than [8.8.4] *CAB*. This difference is prominent in morphologies with multiple cores. Regions containing [8.6.4; 8.6.4; 8.6.6] *BAC* and [10.6.4; 10.6.4; 10.6.6] *BAC* are smaller compared to the regions occupied by the other two topological sub-classes in these morphologies.

A mirror symmetry exists in phase space with respect to the line where $\phi_A = \phi_C$. Considering phases along this line, the [12.6.4] morphology is observed for values greater than $\phi_B \approx 0.52$. There is narrower region of [10.6.4; 10.6.4; 10.6.6] *BAC* between $\phi_B \approx 0.46$ to $\phi_B \approx 0.52$. In between $\phi_B \approx 0.41$ and $\phi_B \approx 0.46$, [8.6.4; 8.6.4; 8.6.6] *BAC* is found. The [6.6.6] morphology is observed for values $0.22 \lesssim \phi_B \lesssim 0.41$. For values of $\phi_B < 0.22$ the phase space shows [8.8.4]. The shift in phase space is clear from the analysis of this line. The [6.6.6] region is not evenly distributed in both directions from $\phi_B = 0.33$. Instead, it is shifted to the region where ϕ_B is small.

The morphologies [12*B*.6*A*.4*C*] and [12*B*.6*C*.4*A*] are favoured in this phase space. From the discussion from the earlier section, this morphology will have more circular *B* domains which are interfacially favourable when *AC* interaction is smaller than the other two interactions. In the case of morphologies with multiple cores, the topological species with smaller *B* domains occupy more regions in phase space.

In structures with small compositions of ϕ_B the value of free energy per chain is lower. The energy penalty that arises due to the asymmetry is balanced here due to the presence of more *A* and *C* compositions. When the area containing *B* is small, the interfaces are also small, which reduces the surface tension at the interface. Thus *B* domains are not curved as in fig. 5.14.(a). This reduced the free energy per chain. So, phase space will favour the region with lower compositions of *B* monomers. Examples of structures with *A* and *C* dominance are given along with the phase space in fig. 5.15. In the given structures, *B* domains are not curved as the stretching from *A* and *C* compensates for the curving. All structures are from the compositions present in the phase space indicated by the arrows. In the region dominating *B*, the increase in *B* chains results in a higher contribution

to the free energy due to the stretching of B , thus straightening interfacial curves. At the same time, the structures with larger B domains are more stable. This is because as explained the interfacial energy results in curving out of the B domains and it is feasible when the domain is surrounded by more cores/interfaces. In the case of mult-core morphologies, there is an extra freedom of configurations that makes the structures with smaller $A - B$ and $B - C$ interfaces stable.

5.2.3 $\nu_{AB} = \nu_{BC} = 1, \nu_{AC} > 1$

We now look at the polymer melt of *ABC* star terpolymers with equal interaction strength between B and A and C and a strong incompatibility between A and C . Here interaction scaling in terms of ν are $\nu_{AB} = \nu_{BC} = 1, \nu_{AC} = 1.4$ which in terms of our reference Flory interaction parameters are $N\chi_{AB} = N\chi_{BC} = 60$ and $N\chi_{AC} = 117.6$. The strength of incompatibility between A and C is almost double the incompatibility between the other two pairs.

In experiments that were conducted to explore the phase separation morphologies [100, 102, 114], exact values of Flory interaction parameters $N\chi$ are not given. But the order of interaction strength is $\chi_{IS} \approx \chi_{SP} < \chi_{IP}$ for star terpolymers with polyisoprene(I), polystyrene(S) and polyvinylpyridine(P) (ISP) and $\chi_{SF} \approx \chi_{IS} < \chi_{IF}$ for terpolymers with polyisoprene (I), polystyrene (S), and poly(ferrocenylethylmethylsilane) (F) [75]. Earlier attempts to map the effect of asymmetric interactions report the absence of [6.6.6] in their 1D phase space, varying only one composition [173]. In their work, Jiang et al. attempted to study this case of asymmetric interaction using *SCFT* by choosing $N\chi_{AB} = N\chi_{BC} = 30.0$ and $N\chi_{AC} = 50.0$ [75]. They produced a complete phase space with a lot of morphologies. They compute multiple 1D phase spaces inside the triangular phase space to build half of the phase space, which is then mirrored to create the complete phase space. In *SCFT* calculations, it is reported[173] that for certain $N\chi$ values, the computation of stable phase is difficult.

When $\nu_{AC} > 1$, the incompatibility between A and C monomers is large compared to the other two pairs. This results in higher surface tension in the AC interface compared to AB and BC interfaces. Thus to preserve the total surface area, the interfaces with lower surface tension (AB and BC) curve out into the blue domain. Due to the almost same strong incompatibility between the monomers AC interface remains the same.

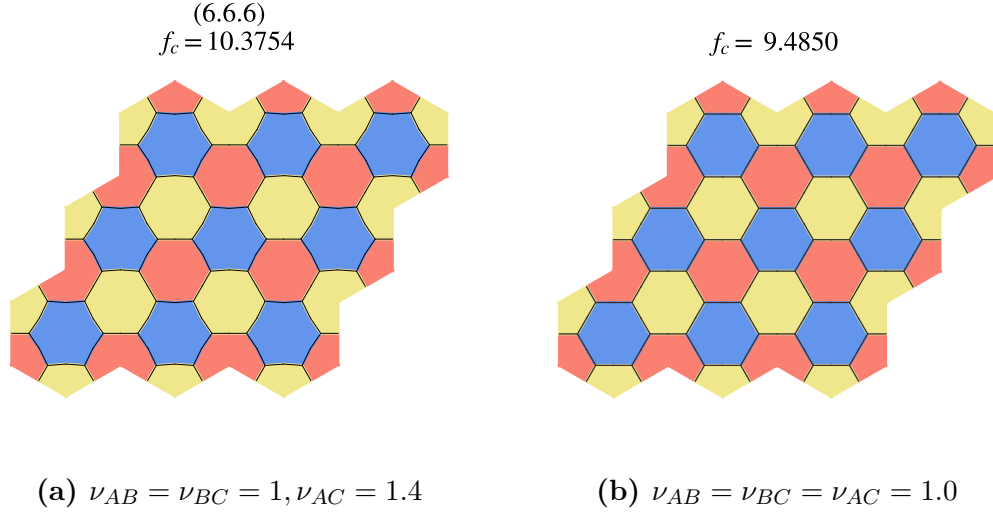


Figure 5.16: Here the comparison of morphological structures with asymmetric interactions (a) $\nu_{AB} = \nu_{BC} = 1, \nu_{AC} = 1.4$ and symmetric interactions (b) $\nu_{AB} = \nu_{BC} = \nu_{AC} = 1$ are given. Both structures are for the same monomer compositions $\phi_A = \phi_B = \phi_C = \frac{1}{3}$. The *B* domains in (a) curved in due to the effect of asymmetric interactions.

The effect of asymmetric interactions on the interfaces is demonstrated in detail by comparing stable structure for [6.6.6] morphology in fig. 5.16. Tiling structures with the same ϕ values are considered for asymmetric and symmetric interactions. As explained above, *AC* interfaces are straight due to the strong surface tension and an equal amount of stretching in the opposite direction is contributed by *A* and *C* branches. In the other two interfaces, the stretching energy is the same, but the surface tension is weak. This leads to the curving of *AB* and *BC* interfaces, visualised as curving in of *B* domains. Following the pattern from case 1, the morphologies with smaller *B* domains are favoured. So we expect a shift in the phase space towards the higher composition of *B*.

After updating the geometry scripts, the phase space is created for this case by repeating all the calculations done for the symmetric interaction case. Free energy maps are determined for each morphological sub-class separately. They are all put together to create the phase space given in fig. 5.17.

5. *ABC* star terpolymers morphologies: Periodic

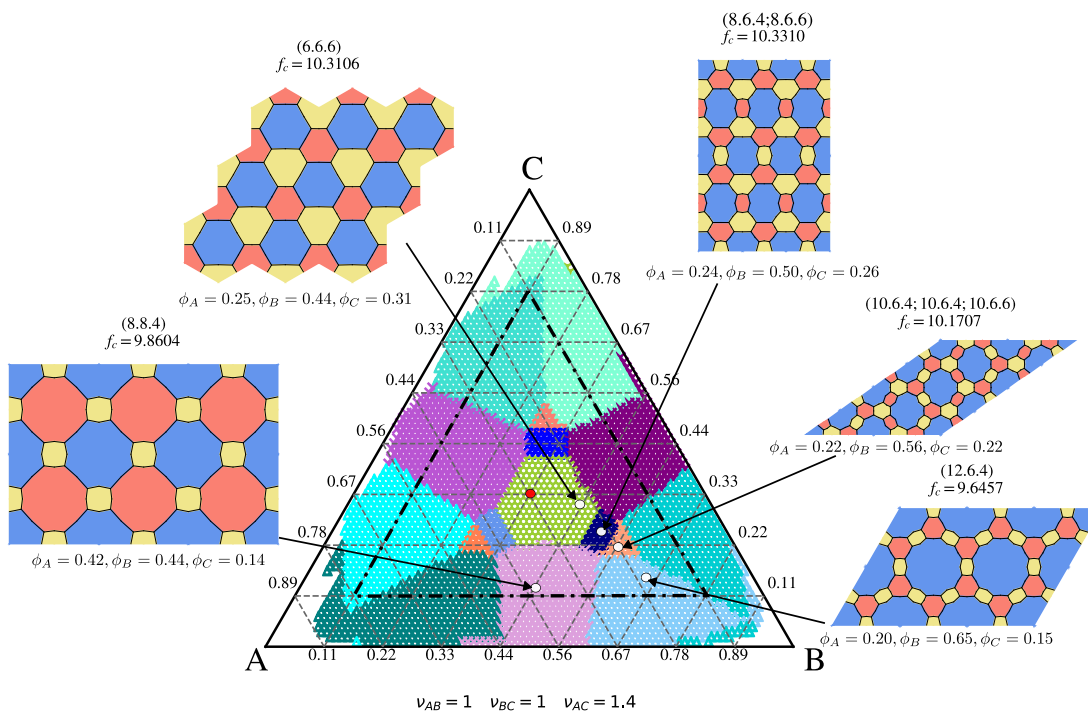


Figure 5.17: Phase space for *ABC* star terpolymers with asymmetric interactions $\nu_{AB} = \nu_{BC} = 1, \nu_{AC} = 1.4$ is given. Morphologies presented in this phase space are: [6.6.6] (light green), [8.8.4] (purple shades), [12.6.4] (teal/cyan shades), [8.6.4; 8.6.4; 8.6.6] (blue shades) and [10.6.4; 10.6.4; 10.6.6] (orange shades). The red dot indicates the centre of the triangle where $\phi_A = \phi_B = \phi_C = \frac{1}{3}$. The morphologies from the region with lower free energy per chain values are given.

Free energy maps determined for all sub-classes of morphologies described above are combined together to form the phase space given in fig. 5.17. The relative position of the morphologies in the phase space remains consistent with the symmetric case, whilst there is an obvious shift in the phase space towards the corner *B*. This shows that morphologies [12A.6C.4B], [8A.8C.4B] and [12C.6A.4B] are more favoured in this case of asymmetric interactions. The red dot in fig. 5.17 indicates the centre of the triangle. The area of phase space covered by each morphological sub-class is not the same in this case. It is to be noted that the region showing [8.6.4; 8.6.4; 8.6.6]*BAC* is slightly smaller than [8.6.4; 8.6.4; 8.6.6]*ABC* and [8.6.4; 8.6.4; 8.6.6]*CAB* regions. Similarly, for [10.6.4; 10.6.4; 10.6.6] morphology, *BAC* sub-classes occupy more composition space than *ABC* and *CAB*. Still, there exists a mirror symmetry along the line $\phi_A = \phi_C$. Jiang et al. produced a phase space with more morphologies using SCFT for a similar type of asymmetry in the interaction. They also observe a slight shift in the phase

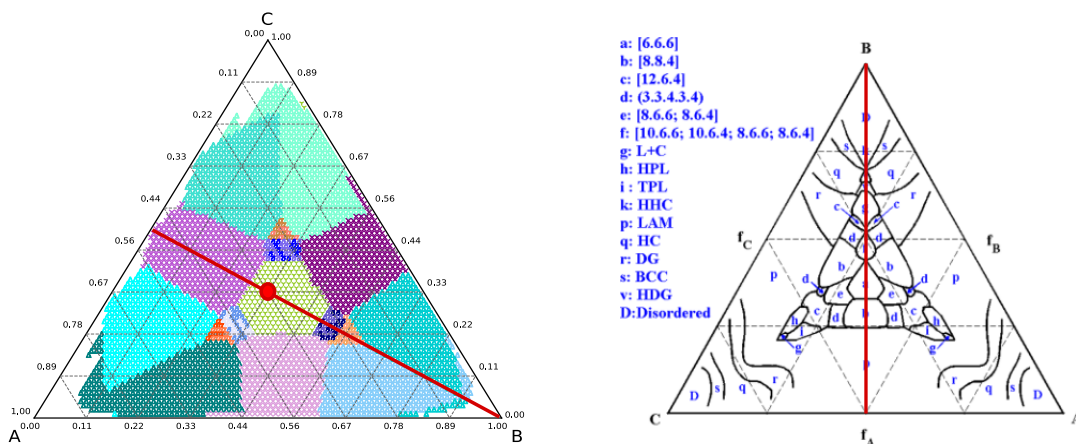


Figure 5.18: Here is the comparison between our phase space and phase space for similar interactions reported by Jiang et al. using *SCFT* [75]. The line that gives $\phi_A = \phi_C$ is given in red. The red dot in our phase space is the centre of the triangle.

spaces towards the region with *B* abundance. They are looking at 16 different morphologies, including 3D and lamellar morphologies as shown in fig. 5.18. There are prominent differences in the placement of morphologies in both phase spaces. Taking the line $\phi_A = \phi_C$ in our phase space, when $\phi_B \approx 0.26$ we have [8.8.4]. When ϕ_B is increased, we find [6.6.6] closer to the centre but the region is shifted compared to the symmetric phase space. The morphology [6.6.6] occupy the area up to $\phi_B \approx 0.5$. For larger values of ϕ_B we find [8.6.4; 8.6.4; 8.6.6], [10.6.4; 10.6.4; 10.6.6] and [12.6.4] in this respective order. In Jiang et al's work [8.6.4; 8.6.4; 8.6.6], [10.6.4; 10.6.4; 10.6.6] disappears, instead they report another combined morphology: [10.6.6; 10.6.4; 8.6.6; 8.6.4]. The interaction parameters and approach taken are entirely different. The interaction parameters they chose were $N_{\chi_{AB}} = N_{\chi_{BC}} = 30$; $N_{\chi_{AC}} = 50$. These values are weaker compared to the ones we are considering. The morphological study is done using SCFT equations. Also, the phase space exploration was conducted by varying $x = \frac{\phi_A}{\phi_C}$ and then comparing the morphologies keeping two compositions constant for one half of the phase space [75]. In our method the exploration is automated as long as it is in the suitable format and phase space comparison is done in extreme segregation limit which can screen out some of the morphologies that were previously reported using SCFT. Still, it is possible to check the presence of the above-mentioned missing morphology in our phase space using the *SSP* method.

We morphologies with smaller *B* domains are favoured with this asymmetric interaction for single core morphologies. The multi-core morphologies are

favoured at the region where *B* domains are larger. This is proved to be true by the phase space shift towards *B*. This shift is supported by existing work. This shift is expected to change with respect to the values of ν_{AC} . Some examples of the morphologies present in the resulting phase space are given in fig. 5.17.

If the asymmetry in the interaction is introduced by ν_{AB} or ν_{BC} , similar effects are observed with corresponding domains for cases 1 and 2.

5.2.4 $\nu_{BC} < \nu_{AB} < \nu_{AC}$

In this case, all the interactions are different, which should be the case for any real *ABC* star molecule. Here we consider the case where the incompatibility between *A* and *C* monomers is the strongest, and the incompatibility between *B* and *C* monomers is the weakest. We choose $\nu_{AB} = 1.0$, $\nu_{BC} = 0.6$ and $\nu_{AC} = 1.6$ as interaction scaling, which in terms of Flory interaction parameters are $N\chi_{AB} = 60$, $N\chi_{BC} = 21.6$ and $N\chi_{AC} = 153.6$ comparing with our reference interaction value $N\chi = 60$. Owing to the extreme values we are using, the effects of asymmetry are expected to be pronounced in this case.

When one interaction is stronger or weaker than the other two in the same way, it is easier to understand what is happening at the interface, as we saw in the previous two cases. In this case, we have two monomers *A* and *C* with extremely strong incompatibility and the other two *B* and *C* with weak incompatibility. So the strength of surface tension between the interfaces will be in the order: $\gamma_{AC} > \gamma_{AB} > \gamma_{BC}$. The effects at the interface are similar to case 2, but the degree of curving for *AB* and *BC* will be different due to the difference in surface tension. As *AC* has strong surface tension compared to *AB* and *BC* it will force these two interfaces to curve out, giving an impression of curving in of the blue domains.

A qualitative demonstration of the effect of asymmetric interactions on the interface is given in fig. 5.19. Similar to the previous cases, we compare the structure of [6.6.6] with the same compositions but different interactions. As explained above, *A*(red) and *C*(yellow) domains get rounded because the *AC* surface tension is high, so that cores are pulled inwards along the *AC* line. This gives the *B* domains concave interfaces. In this case, the difference in the tiling is evident from fig. 5.19.(a) and (b). The difference in the degree of curviness is also observed for *A* and *C* domains. The *A* domain is closer to a circle, while *C* domain is mid-way between a circle and a hexagon. This is the effect of the difference in interfacial surface tension between *AB* and *BC*. The same effect is observed in other morphologies. While the stretching energy remains the same for both structures in fig. 5.19.(a) and (b) according to the eq. (3.124), the interfacial energy is linearly related to the values of ν , which results in a difference in values of free energy per chain.

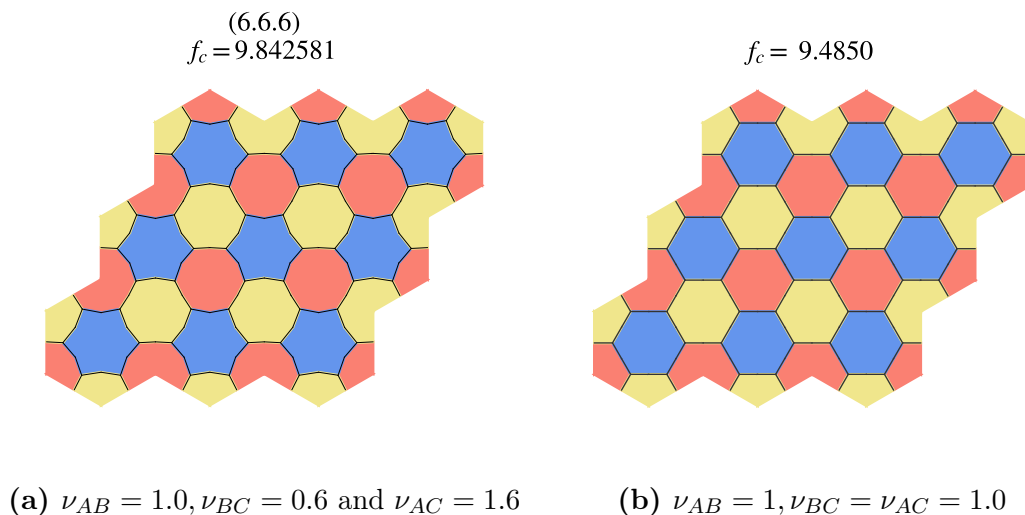


Figure 5.19: Comparison of tiling structure for [6.6.6] morphology with (a) asymmetric interactions and (b) symmetric interactions. Monomer compositions of both tilings are $\phi_A = \phi_B = \phi_C = \frac{1}{3}$.

The phase space is created by repeating previous calculations on morphological sub-classes with updated geometry scripts. All free energy maps obtained are combined together to create the phase space given in fig. 5.20.

In the phase space obtained, we can observe a prominent shift in the morphology placements. The relative positions of the morphologies still remain the same. The [6.6.6] morphology is the light green region which has shared borders with different sub-classes of [8.8.4] and [8.6.4; 8.6.4; 8.6.6]. The cyan/teal shaded region are [12.6.4]. Between [12.6.4] and [8.6.4; 8.6.4; 8.6.6] there is a small region with [10.6.4; 10.6.4; 10.6.6]. The regions occupied by different sub-classes of the same morphology are drastically different in this phase space. The sub-classes [8.8.4] *ACB* occupies larger composition compared to [8.8.4] *CBA*, which is smaller. The shift in phase space is emphasised by locating the red dot, placed at the centre of the phase space, which is now inside the region indicating [8.8.4]. The phase space is shifted to the region with a larger composition of *B*. At the same time it also has an upper shift in the direction to reduce the composition of *A* and *C*. There is no mirror symmetry along easily accessible lines $\phi_A = \phi_B$ or $\phi_B = \phi_C$ or $\phi_A = \phi_C$. A few examples of morphologies from the phase spaces are demonstrated alongside in fig. 5.20. All of them have curved interfaces and *B*, blue dominance.

In this case most favourable morphologies are [12*A*.6*C*.4*B*], [8*A*.8*C*.4*B*] and [12*C*.6*A*.4*B*] that now occupy most of the phase space. The structures with smaller *B* domains let the *A* and *C* domains be more circular as they prefer with

5. *ABC* star terpolymers morphologies: Periodic

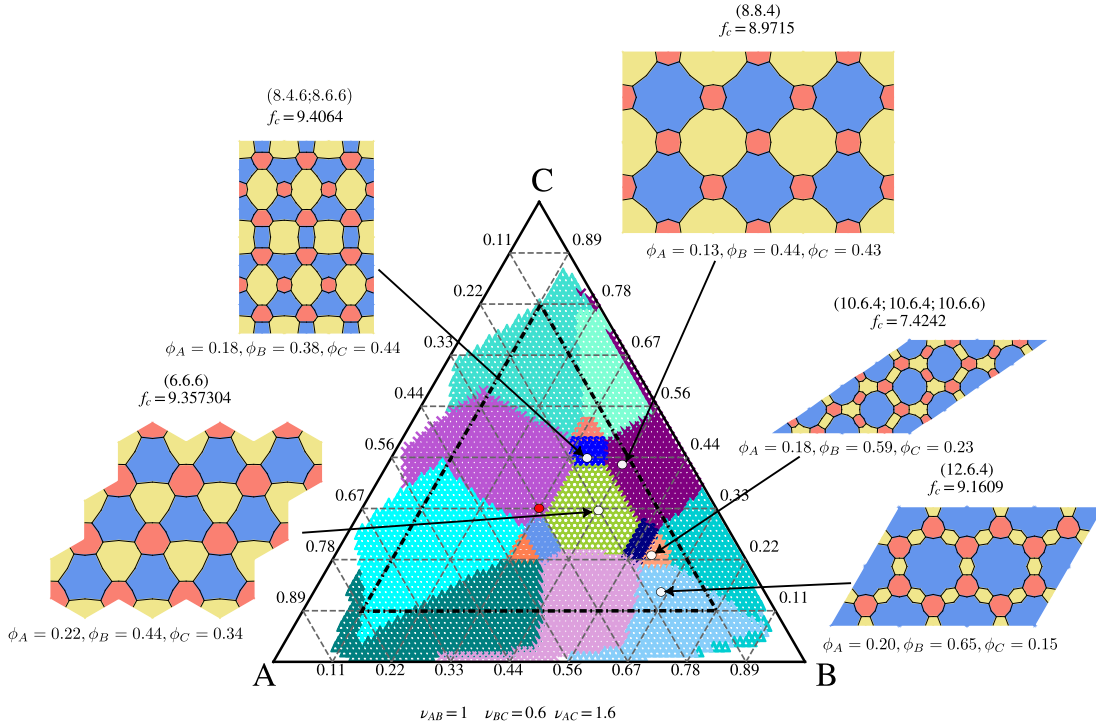


Figure 5.20: Phase space for the asymmetric case where all three interactions are different. The colour map and corresponding morphologies are the same as in the previous cases. The red dot indicates the centre of the triangle. Examples of the morphologies present in the phase space are given.

these asymmetric interactions. At the same time, the free energy values are lower when *B* domains are larger as given in fig. 5.19. Thus there is a shift in the phase space toward the region with larger *B* with an upward lift towards the direction of *C*. In the morphologies present in fig. 5.20, interfaces are less curved, and they have smaller domains of *A* and *C*.

Morphological analysis with this level of asymmetric interactions has not been attempted using any other methods in the literature. As in the previous cases, we have limited the number of morphologies we are looking at. But the nature of the shift agrees with the physics behind phase separation which makes this a promising start to explore more in these phase spaces. The difference in interactions should also promote the possibility of more lamellar related or 3D morphologies which need to be investigated.

In all these cases, at extreme compositions $\phi_A, \phi_B, \phi_C < 0.11$, we expect

the appearance of lamellar phases and other 3D spaces. So phase space inside $\phi_A = \phi_B = \phi_C = 0.11$ is taken to be true. There are obvious chances of more interesting tiling appearing in these phase spaces which does require an extensive database on different structures possible with *ABC* star terpolymer.

5.3 Discussion

This chapter demonstrates that the *SSP* framework we have developed is a powerful and effective tool for studying phase separation in block copolymers in the strong segregation limit. The *SSPs* as presently constructed are useful to study 2D tiling-like morphologies in *ABC* star terpolymers melts and their characteristics. The analytical framework for this method is fairly straightforward compared to SCFT, which is the workhorse of theoretical and computational polymer phase separation studies.

Interfacial and geometrical features for each morphology are accessible by using our methodology. Even though it is straightforward to assume that domain size will increase with the increase in compositions, it is visually proved using our method. The effects of polymer stretching and interfacial surface tension are also demonstrated in our work. Detailed analysis of the effects of composition, stretching and interfaces on phase-separated domains has not been reported in the literature until now. Morphologies with single core ([6.6.6], [8.8.4], etc ..) and multiple cores ([8.6.4; 8.6.4; 8.6.6], and [10.6.4; 10.6.4; 10.6.6]) can be accommodated under the same *SSP* formulation. It is interesting to note that *SSPs* in [8.6.4; 8.6.4; 8.6.6], and [10.6.4; 10.6.4; 10.6.6] change drastically upon minimisation. This feature cannot be identified if the domains are treated in a uniform manner as done in the literature till now.

Phase spaces with all morphologies mentioned in this chapter have been created. The phase space for symmetric interactions agrees with all existing phase spaces in literature developed using Monte Carlo[50], SCFT[75, 91, 173], DPD[27, 81] even with the limited number of morphologies. Most of the existing literature explores the phase space for limited values of monomer compositions. In this work, we span the entire phase space with an increment of 0.01 in ϕ values. While there is a plethora of morphologies reported in computational work, morphologies reported in experimental phase separation of *ABC* star terpolymers are usually [6.6.6], [8.8.4] and [12.6.4][27, 99, 114]. These morphologies are present in our phase spaces.

In this chapter, we also demonstrated the ease of producing phase space for *ABC* star terpolymers with unequal interactions between their branches. We explored three different cases of interaction strengths where their effect on the morphology and phase space were studied. This demonstrates a promising start to build in a complete phase space with 2D morphologies.

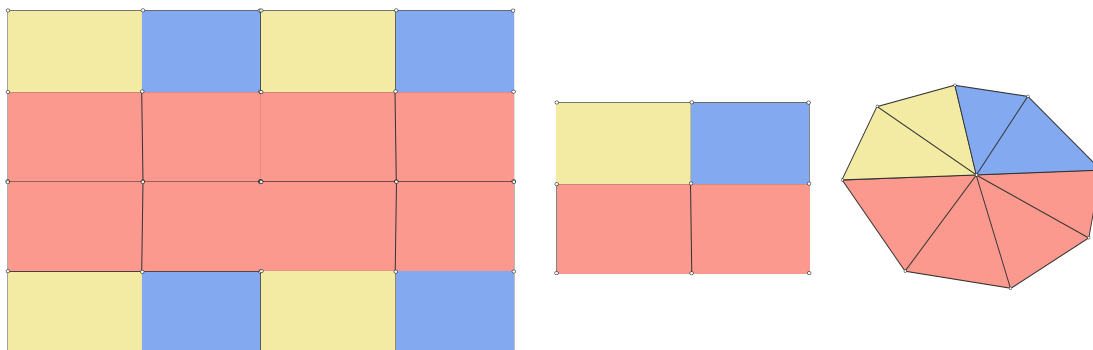


Figure 5.21: Proposed *SSP* for lamellar morphologies.

Our framework demonstrates the flexibility to include any complex 2D morphologies *ABC* star terpolymers is capable of producing, given there is a core between the domains. As mentioned in Chapter 1, *ABC* star terpolymers can form a variety of morphologies with different lengthscales. It is difficult to track all the structures possible in *ABC* star phase separation. In their work on tilings in *ABC* star terpolymer, Kirkensgaard et al. [81], demonstrate possible combinations to assemble *ABC* domains with a core in them using the Spoke method. Our framework provides a platform to take such morphologies to check their presence in phase space. We will demonstrate the analysis of more complex and larger morphologies in the next chapter.

Morphologies with lamellar domains are currently not included in our phase space. These morphologies like lamellar+cylinder ($L + C$) [50, 114] have been reported in experimental phase separation studies. These are found in the region where any one of the monomer compositions is particularly large. Polymer melt behaviour is similar to diblock at these compositions. Thus they can form interesting structures with lamellar domains and 3D morphologies. The current formulation of *SSP* is not equipped to consider lamellar structures, which is why we have narrowed down our valid phase space to the triangle inside $\phi_A = 0.11$, $\phi_B = 0.11$ and $\phi_C = 0.11$. On modifying the edges and increasing the number of nodes in *SSP* as shown in fig. 5.21 it is possible to analyse lamellar morphologies. This modified *SSP* is an octagon that under minimisation can restrict the nodes according to the periodicity to $L + C$ morphology.

As mentioned, the methodology is limited only to 2D morphologies that can tile. This cut off the entire set of 3D morphologies from our phase space. The 2D morphologies find it difficult to minimise at extreme compositions where one composition is too small. This is because the flexibility of interfaces is limited to a straight line. All phase spaces reported in this chapter were created within 2-3 days of computation using Python. We span the composition space for each subclasses in parallel cores utilising ARC4, part of the High-Performance Computing

5. *ABC* star terpolymers morphologies: Periodic

facilities at the University of Leeds. So a better optimisation is necessary for the script to speed up the creation of phase space and to include more complex morphologies. This concept can be interpolated for a 3D equivalent of *SSP* using a Kelvin cell or octahedron [28].

5. *ABC* star terpolymers morphologies: Periodic

Chapter 6

Periodic approximants of Square-Triangle tilings in *ABC* star terpolymers

In this chapter, we are using the *SSP* method to analyse more complex tilings. *ABC* star terpolymer architecture has enough complexity to allow the polymers to phase separate into complex morphologies like quasicrystals. In Chapter 2, the linear analysis of *ABC* star melt shows that certain compositions and monomer interactions can lead to phase separation with lengthscale ratios which favour quasicrystals. Also, the first block copolymer quasicrystal was discovered in *ABC* star terpolymer blend [57]. One way to determine if the phase separated morphology is a quasicrystal is by comparing it to aperiodic tilings. As we have seen in Chapter 5, phase separated morphologies of *ABC* star terpolymers behave like tilings.

Quasicrystals observed in soft matter systems typically exhibit dodecagonal rotational symmetry. Most of these dodecagonal quasicrystals can be described using aperiodic tiling of squares and triangles [57, 172]. In phase spaces from Chapter 5, we observed that the majority of phase spaces are occupied by [8.8.4] (square) and [12.6.4] (triangle) morphologies. This clearly demonstrates that the *ABC* star terpolymer architecture does favour these two morphologies. The Archimedean tiling with squares and triangles called the Σ -phase, also known as (3.3.4.3.4) is also observed in the phase space for *ABC* star morphologies [38, 57, 72, 91]. The Σ -phase belongs to the family of the Frank-Kasper phases, which also includes quasicrystals. All these factors motivate the search for aperiodic tilings with squares and triangles in them using our *SSP* method in *ABC* terpolymer phase separation.

There are different ways to build an aperiodic tiling with squares and triangles. One method is the generalised grid method proposed by Stampfli, in which two hexagonal grid lattices are arranged such that they superimpose so that their symmetry axis crosses by $\frac{\pi}{6}$ [111]. Another method involves inflation based on triangular and square tiles which was also introduced by Stampfli [119]. There are many other complex ways to develop dodecagonal aperiodic tiling with squares and triangles [111, 171]. Recently Imperor-Clerc et al.[71] came up with the method of combining four types of Archimedean tilings that contain squares and triangles: (4.4.4.4) (squares), (3.3.3.3.3.3) (triangles), (3.3.4.3.4) (Σ -phase) and (3.3.3.4.4) (H- phase). The numbering indicates numbers of edges on the polygons shared by a vertex in these tilings. All these methods can produce aperiodic tilings with different arrangements of squares and triangles that can give quasicrystal peaks in their corresponding Fourier spectrum.

All these methods provide aperiodic tiling patches without a periodic boundary. For the *SSP* method to work, we need a periodic patch, so we look for periodic approximants of aperiodic square and triangle tilings. In this chapter we do this by identifying periodic patches in a long-range aperiodic tiling like the one given in the Tiling encyclopedia [136].

6.1 What happens when squares and triangles are put together?

We start the square-triangle analysis by putting squares and triangles together starting with simplest combination of squares and triangles, the Archimedean tiling (3.3.3.4.4) [53], also called the *H*-phase [71]. The periodic patch for this tiling consists of one square and two triangles on top of them. The arrangement is traced by bold black lines in fig. 6.1.(a). The spatial configuration in fig. 6.1.(a) is the initial structure created using the packing routine discussed in chapter 4. The resulting minimised configuration with fig. 6.1.(a) as the initial structure is given in fig. 6.1.(b). Unlike the minimised figures obtained in chapter 5, minimised configuration here has obvious visual differences. While the outline of the periodic patch is sustained for all the morphologies considered previously with straight line edges on the tiles, the outline is curved for H-phase. As discussed in section 4.4 the final minimised configuration was the same for any choice of minimisation method. All attempts provided with the same result of distorted triangles and squares upon minimisation.

It is to be noted that in the periodic arrangement of the patch, when squares are side by side, there are no distortions in shared edges. When squares are next to triangles the shared edge bows in to the square and shared edge between triangles appear curved.

6. Periodic approximants of Square-Triangle tilings in ABC star terpolymers

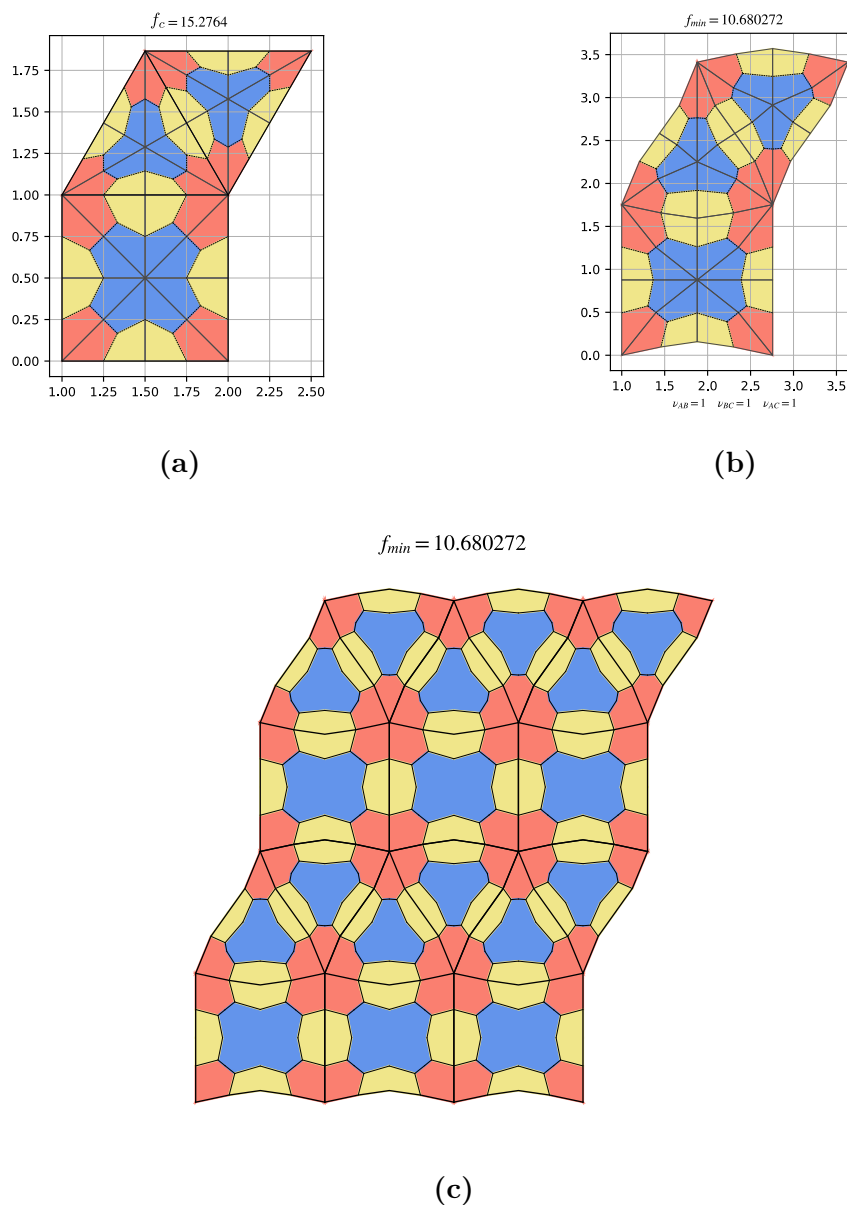


Figure 6.1: Morphological analysis of H -phase at different stages. In (a) the initial configuration of the tiling is given. In (b) configuration is minimised and the obtained morphological structure is given. The periodic arrangement of H phase for a bigger range is given in (c). The interaction strengths between the branches are equal in this case with $\nu_{AB} = \nu_{BC} = \nu_{AC}=1$.

6.2 Σ -phase

The Σ -phase was introduced in chapter 4 to demonstrate the application of the SSP method to larger tilings. The Σ -phase also known as (3.3.4.3.4), is often observed in ABC star phase separation [57, 81, 91, 159].

The initial configuration is created with symmetric interactions between the monomers, as explained in Chapter 4, arranging the squares and triangles as required and then filling them with ABC star $SSPs$. In the initial configuration given in fig. 6.2.(a), there are two different types of cores or $SSPs$ present. One type of core is inside the bold square outline which is [10.8.4], and another is in the bold triangle outline, [10.6.4], following the nomenclature convention we are using in this thesis. Hence this is a multi-core structure. Two cores lead to two different $SSPs$. Here, both of them are right-angled triangles, one inside the square and another inside the triangle. The given periodic patch of Σ -phase has 79 free nodes and 17 periodic nodes. It contains 40 SSP polygons. So the constraint list has 161 elements in it. The periodicity of this patch is a big square that connects the outer vertices of a square to a triangle. Unlike the morphologies in Chapter 5, the initial configuration chosen is not a symmetric architecture with an equal amount of three different monomer compositions. This structure undergoes minimisation in the same way as all other morphologies we have discussed so far. The minimisation of one set of parameters takes approximately 5 minutes using Python.

For the Σ -phase we obtained fig. 6.2.(b) as the final result of minimisation. The resulting configuration also shows curving along the square and triangle borders like the H -phase. The most obvious observation is the curving of the edge shared by a square and triangle indicated by the bold line in fig. 6.2. (a) and (b). Unlike in the H -phase the edge shared by the two triangles remains straight after minimisation. The minimised structure also has new different types of $SSPs$. In the previous chapter, a similar result was obtained with [8.6.6; 8.6.4], where there were new types of $SSPs$ in the minimised structure. In fig. 6.2.(b), the ‘square’ contains same type of $SSPs$, which are all [10.8.4], while there are three different $SSPs$ in the minimised ‘triangle’. All of them are topologically [10.6.4], sharing the border with the same number of domains but geometrically different. There is one SSP ‘triangle’ with a straight ‘hypotenuse’ and two with curved hypotenuses: one curved in and another curved out.

6. Periodic approximants of Square-Triangle tilings in ABC star terpolymers

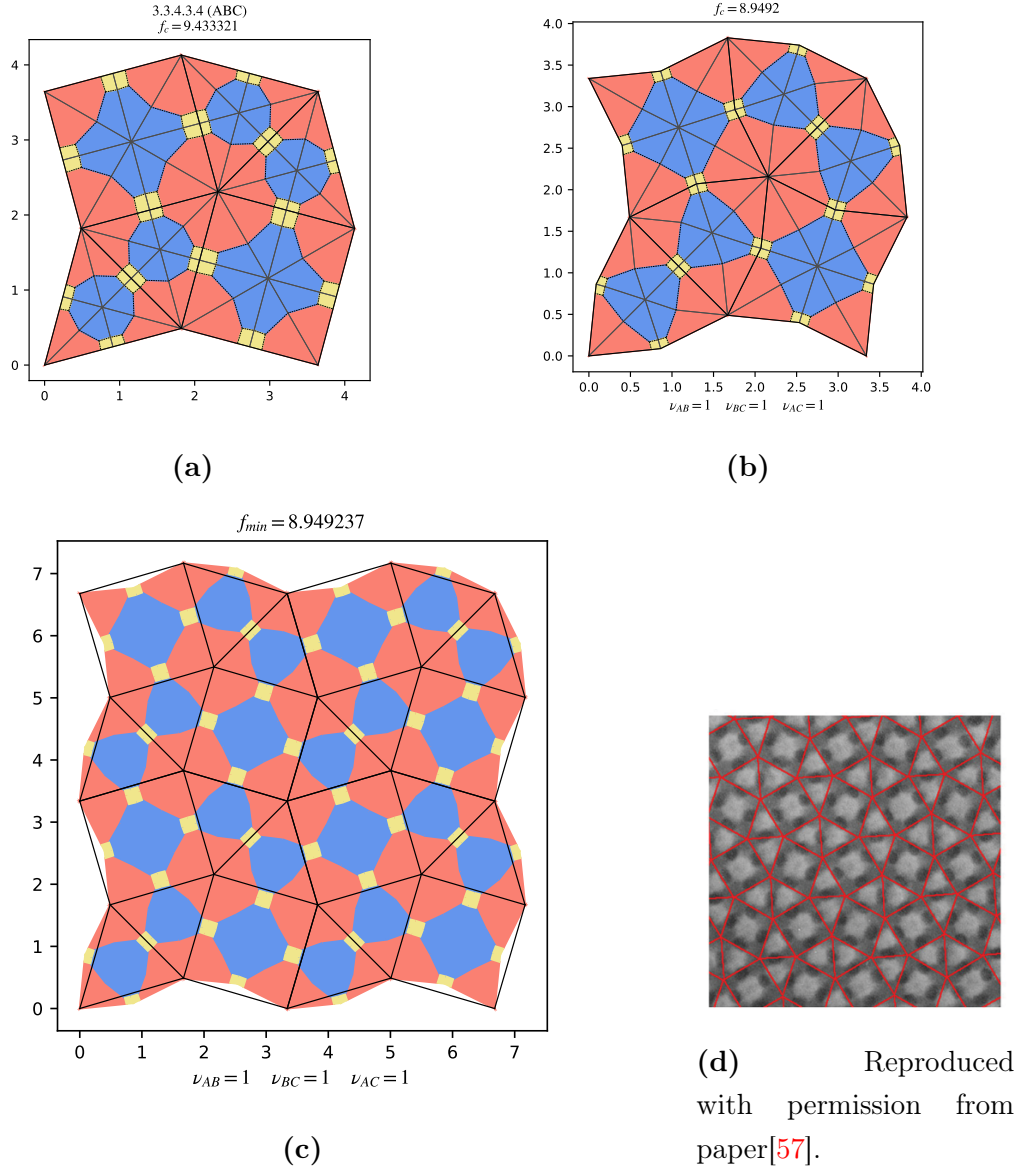


Figure 6.2: Morphology of the Σ -phase in ABC star terpolymer with equal interaction strengths between the branches. In (a) the initial configuration was created by tiling and SSP embedding for monomer composition $\phi_A = 0.5758$, $\phi_B = 0.3813$ and $\phi_C = 0.0429$. This configuration undergoes minimisation to reach the final stable configuration given in (b). In (c) four copies of the minimised structure are shown with the original square triangle tiling overlaid. In (d) the TEM image obtained for a blend of terpolymer of polyisoprene, polystyrene and poly(2-vinylpyridine) (ISP) and homopolymer polystyrene by Hayashida et al. [57] is given.

This morphology is a clear compilation of two prominent morphologies present in ABC star phase separation, [8.8.4] (square) and [12.6.4] (triangle). From the free energy analysis in Chapter 5, we can say that when the monomer compositions are $(\frac{1}{3}, \frac{1}{3}, \frac{1}{3})$, the triangle has a higher free energy value compared to the square morphology. So when we put squares and triangles together, the geometrical restrictions coming from the interfacial and stretching effects of the polymer chains in a triangle morphology is relaxed when it has a square connected to it. The free energy imbalance between these two morphologies is compensated by the curving of their sides. When a triangle shares its side with another triangle, their common side is straight, as there is no additional transfer of interfacial energy. If we compare the minimised free energies of H -phase and Σ -phase, the latter has the lowest free energy for the same set of monomer compositions. The periodic patch of Σ -phase can be taken as a combination of two H -phases. One with square in the bottom and another with the square on top, which can be taken as two interlocked H -phases. This conserves the geometrical symmetry of the patch. By adding $SSPs$ into them, stretching of chains compensated the additional interfacial energy caused by putting squares and triangles together.

On repeating the minimised periodic patch in 2D space, we obtain the pattern given in fig. 6.2.(c). This pattern is overlaid by straight-edged squares and triangles whose vertices are positioned at the centres of the red domains. The edges shared by a square and triangle in this pattern cross the yellow domains along their edges. While the edges shared by two triangles cross the yellow domains across their centres. Figure 6.2.(d) shows the TEM image produced by Hayashida et al [57] for polymer melt that is a blend of terpolymer of polyisoprene, polystyrene and poly(2-vinylpyridine) (ISP) and homopolymer polystyrene also with the phase separated structure overlaid with squares and triangles. In the image, one can also see shared edges between squares and triangles passing over the edges of the black domains and shared edges between two triangles passing through the centres of the black domains. This geometrical resemblance between a simulated pattern and experimental result supports our observation of the edge bending that happens in a square-triangle morphology for ABC star terpolymer. So we can conclude that when we put squares and triangles together with ABC star polymer melt in them, the conformation entropy will drive them to form curved squares and triangles.

Taking the minimised structure for symmetric compositions as the starting point in ternary composition space, the free energy per chain is determined for all possible compositions that will give a valid SSP configuration for Σ -phase. We are also keeping the monomer interaction strengths equal $\nu_{AB} = \nu_{BC} = \nu_{AC} = 1$. As there are no topological equivalencies between the topological sub-class in them, six free energy maps are determined. Combining them with the phase space from Chapter 5 gives a new phase space given in fig. 6.3.

6. Periodic approximants of Square-Triangle tilings in ABC star terpolymers

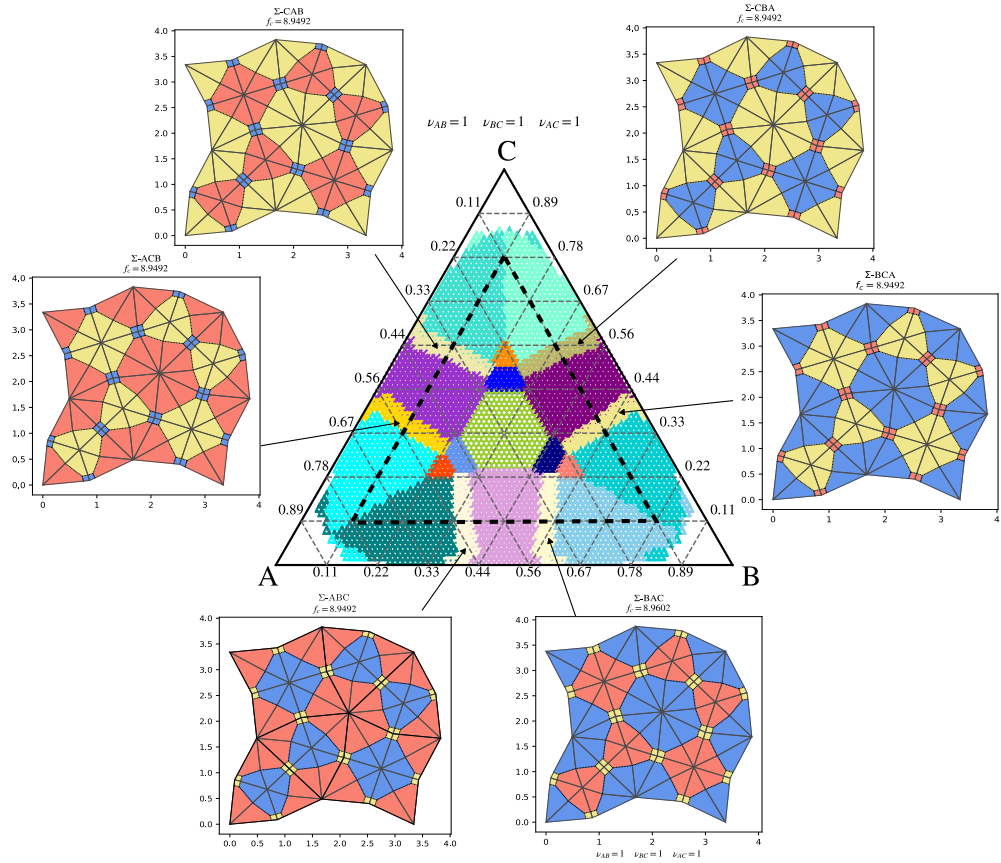


Figure 6.3: Phase space for ABC star terpolymer with equal interaction strength $\nu_{AB} = \nu_{BC} = \nu_{AC} = 1$ between the branches. Regions with yellow shades indicate different topological sub-classes of Σ -phase morphology.

Comparing with the phase space obtained before in fig. 5.12 there are new prominent additions due to Σ -phase in fig. 6.3. We found stripes between the region favouring square and triangular phase where Σ has lower free energy per chain. There are 6 stripes corresponding to different topological sub-classes of this morphology. Since the Σ -phase is a combination of [8.8.4] (square) and [12.6.4] (triangle), it is natural to find them in the phase space in between the regions of [8.8.4] (purple shades) and [12.6.4] (teal shades). In the phase space given in fig. 6.3, all the stripes corresponding to different topological sub-classes of Σ -phase occupy almost equal area.

The presence of the Σ -phase in the phase space of ABC star terpolymer with symmetric interactions is reported in previous work on ABC star terpolymer phase separation done with Monte Carlo [162] and $SCFT$ [91] techniques. We found the Σ -phase at roughly the same position as these works using our SSP method. Previous works report extremely small regions of the Σ -phase.

Our phase space lacks some interesting morphologies (examples: lamellar and bicontinuous phases), but even with this limitation, we do find larger regions in the phase space with Σ -phase. For the same reasons explained in Chapter 5, we are only considering the triangle with $\phi_A \geq 0.11$; $\phi_B \geq 0.11$; $\phi_C \geq 0.11$. This triangle is indicated with a bold dashed line in fig. 6.3.

As discussed above the combination of square and triangular morphology mutually compensates the free energy penalty caused by these morphologies individually. This assumption is supported by the presence of Σ -phase stripes in the phase space between triangles [12.6.4] and square [8.8.4] region. At the same time, H -phase which is also a combination of squares and triangles is not present in the phase space. As explained earlier there is a geometrical asymmetry associated with H -phase. The triangles in the periodic patch of H -phase in fig. 6.1.(a) is inclined to the right. Alternatively, they can also choose to be inclined to the left without making any difference in the final tiling. But when we add the ABC terpolymer domains, its free energy also has a role in the symmetry of the periodic patch. The asymmetrical imbalance H phase elevates its free energy per chain. This imbalance is compensated in Σ -phase as it is two periodic patches of H -phase inversely connected.

It takes almost 5 days to span an entire phase space of 4050 composition points for a single topological sub-class. Free energy map calculation of each topological sub-class is conducted simultaneously by assigning one script to an ARC node. As it is only possible to run the code for 48 hours in ARC4, phase space exploration is conducted in multiple slices of the composition map.

6.2.1 Phase spaces with asymmetric interaction strengths

Motivated by the presence of the Σ -phase in the phase space of ABC star terpolymers with symmetric interactions, we explored the consequence of asymmetric interactions. Calculations for each topological sub-class are repeated for the three different cases of asymmetric interactions we considered in Chapter 5. Spanning of composition space with asymmetric interactions took much more run time (2 weeks for case 3) in ARC4 than it took for the case of symmetric interactions. We compared the free energy per chain for all three cases with different topological sub-classes of Σ -phase. The resulting phase spaces for three cases are given in fig. 6.4.

Three different cases of unequal interaction strengths are (i) $\nu_{AB} = \nu_{BC} = 1$, $\nu_{AC} = 0.8$; (ii) $\nu_{AB} = \nu_{BC} = 1$, $\nu_{AC} = 1.4$; and (iii) $\nu_{AB} = 1$, $\nu_{BC} = 0.6$, $\nu_{AC} = 1.6$. The major effects of these interactions on phase space are discussed in detail in Chapter 5. Along with the shifts in the phase space due to the asymmetric interactions, strips of Σ -phase are present in all three phase spaces as shown in fig. 6.4. The Σ -phase stripes are given in shades of yellow. They are found at the intersection of [8.8.4] and [12.6.4] morphologies as expected. For

the cases where only $\nu_{AB} = \nu_{BC}$ there is a mirror symmetry of the phase space along the line $\phi_A = \phi_C$.

As seen in other multicore morphologies in Chapter 5, the stripes are wider in the phase space where ϕ_B is small when $\nu_{AB} = \nu_{BC} = 1, \nu_{AC} = 0.8$. Here also, as we saw in Chapter 5 the most favourable morphology is the one with more neighbouring domains [12.6.4]. These two stripes correspond to the topological sub-classes ACB and CAB , where monomer type indicates the order of domains in [10.8.4; 10.6.4] (see fig. 6.3). These two types have a lower composition of B hence lowering the surface energy at the interfaces AB and BC . The multicore morphologies bring in the variety in polymer chain configurations that makes results in more compositions favouring them for lower values of ϕ_B . The Σ -phase being a compilation of two prominent morphologies, they are found more in the phase space when ϕ_B is small.

Similar but inverse is true for the case with $\nu_{AB} = \nu_{BC} = 1, \nu_{AC} = 1.4$. Here these unequal interactions result in multicore morphologies with large B domains as we saw in chapter 5. The shift of the phase space towards larger values of ϕ_B is observed as in Chapter 5. At the same time, the Σ - stripes are observed in lesser areas covered by the topological sub-classes ACB and CAB . Mirror symmetry of the phase space along the line $\phi_A = \phi_C$ still prevails even with Σ -phase in it.

The most interesting phase space is when the interactions are $\nu_{AB} = 1, \nu_{BC} = 0.6$ and $\nu_{AC} = 1.6$, which is given in fig. 6.4.(c). In this example, there is a substantial shift in the phase diagram and the widths of the Σ stripes vary dramatically. The cases where B is the 4 neighboured domain almost disappear except for a narrow line. The stripes corresponding to BCA and CBA are wider and shorter. The other two topological sub-classes ABC and BAC have a prominent stripe but they are of different widths. As seen in Chapter 5, extreme differences between interaction strengths favour the curving of different domains. It is clear that this morphology has drastic changes in the $SSPs$ after minimisation. With unequal interaction strengths, the domain interfaces have a choice between the configurational variety or to increase the domain area. In multicore structures like [10.6.4, 10.6.4; 10.6.6], [8.6.4; 8.6.4; 8.6.6] and Σ -phase, the domains with lower interfacial tension here (B) favours for the configurational variety so there are wider strips of sigma at the region with larger ϕ_B . Here too the most favourable morphology is [12.6.4] in which B domains share interfaces with 12 other domains and are almost circular.

There are certain irregularities outside the triangle corresponding to $(\phi_A, \phi_b, \phi_C) = (0.11, 0.11, 0.11)$ as explained in chapter 5. These compositions need detailed study including different lamellar structures. All these phase spaces could have many more feasible morphologies included in order to develop a complete phase space for 2D tilings in ABC star terpolymer phase separation.

6. Periodic approximants of Square-Triangle tilings in ABC star terpolymers

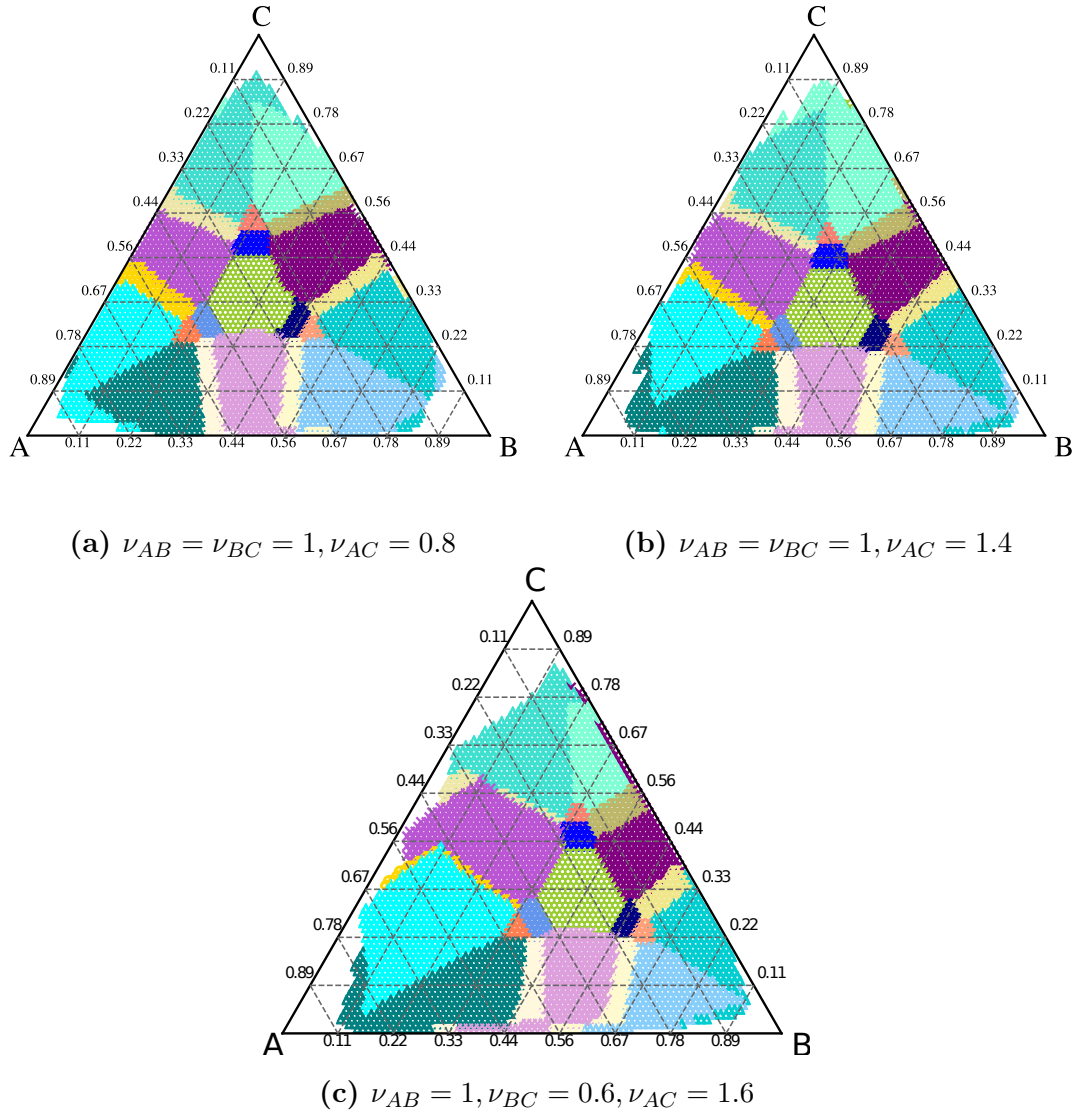


Figure 6.4: Phase spaces for different asymmetric interactions. The strips in different shades of yellow are the Σ -phase.

Our detailed analysis of the Σ -phase results in interesting observations regarding the interfaces and overall structure of the domains. Other phase separation calculations based on self assembly have missed the curving of squares and triangles [75, 80, 91, 162]. The bending of the boundaries between squares and triangles in a soft matter systems was recently reported by Zeng et al. for columnar liquid crystals [170]. Uncanny resemblance to the experimental image from Hayashida et al's work as given in fig. 6.2 supports our observation. The

methodology successfully finds Σ -phase in all four phase spaces. We report more composition points with Σ -phase than any other in literature, owing to the fact that we need to check other $2D$ morphologies with a core in them to finish the phase space. The presence of a relatively wide strip with Σ -phase encourages us to search for more complex square triangle tilings around it. The run time to span Σ -phase in a single core ACR4, part of the High Performance Computing facilities at the University of Leeds is up to a week on an average using Python. This makes it difficult to span bigger periodic patches with more SSP polygons in them in this phase space. So to check the presence of a periodic approximant of quasicrystal with squares and triangles in the phase space one should look around the vicinity of Σ -phase.

6.3 Dodecagonal arrangements of squares and triangles

Periodic approximants of aperiodic tilings with squares and triangles are required to continue our analysis of ABC star terpolymer morphologies in favour of quasicrystals. As mentioned there are different methods to create aperiodic tilings. One main technique is the inflation method developed by Stampfli [119]. In this method, a dodecagon is chosen which is filled with squares and triangles as in fig. 6.5. Dodecagons are placed at each vertex of these squares (Stampfli squares) and triangles (Stampfli triangles) and this process is repeated till you get an aperiodic tiling patch. When four dodecagons are placed side by side we get a Stampfli square. Likewise, when we place three dodecagons in a hexagonal arrangement again side by side we get a Stampfli triangle. At each inflation, there is a reduction of side length by a factor of $\sqrt{2 + \sqrt{3}}$ [119]. For a quasiperiodic tiling in a certain window of the patch, the ratio of the number of triangles to the number of squares is $\frac{4}{\sqrt{3}}$ [119]. There are different orientations in which the dodecagons can be placed at the square or triangle vertices using Stampfli's method which results in different symmetric structures [61]. Another way to create an aperiodic tiling with squares and triangles is using random tiling where the entropy associated with the system will drive the alignment of squares and triangles. In this method, the ratio of squares and triangles in a periodic patch is made equal to $\frac{4}{\sqrt{3}}$ to get a quasicrystalline tile [71, 118].

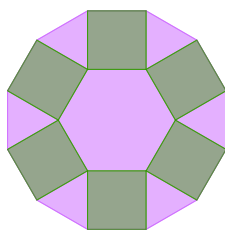


Figure 6.5: A dodecagon with square and triangle arrangement in them.

The *SSP* method demands a periodic patch of tiling. It has the capability to increase the size of periodicity to create a tiling large enough so that it approximates a quasiperiodic tiling. From these available methods of generating aperiodic tilings, we can choose a suitable periodic patch in our search for a stable quasicrystal. In our case, we need a tiling that is favourable for ABC star terpolymer phase separation. In the experimentally observed quasicrystals, the square triangle layout is random with defects in certain places [57]. So we choose some motifs of periodic patches from different arrangements of dodecagons in different orientations to find which has the lowest free energy per chain.

We present a few options of square and rectangular periodic arrangements. This has a mix of Stampfli squares and one where there is an overlap in dodecagons. The square motifs are made by aligning dodecagons side by side while the rectangular one in fig. 6.6.(a) has overlapping dodecagons. The tilings given in fig. 6.6.(b), (c), (d) and (e) use square arrangements with different orientations of dodecagons. The differences between these tilings arise at the edges where the dodecagons touch: whether there is a square next to a square, a triangle next to a triangle or a square next to a triangle. The empty spaces in these tilings are filled by a pattern of a square connected to four triangles. In the rectangular case, where two dodecagons overlap like in fig. 6.6.(a) vacant gaps are filled with two triangles. We will be referring to these arrangements as square (a), square (b), square (c), square (d) and square (e) in this chapter. The arrangements square(a) and square(d) are Stampfli squares used in making the aperiodic tiling given in [136]. The square itself (indicated by a red dashed line) doesn't necessarily make a periodic patch that has translational symmetry. For square (a), and square (c) rectangle and the square itself gives the periodic patch. For square (b) and square (e), the Stampfli square was mirrored in two directions to make the periodic patch indicated by the black dashed line. For square (d), the Stampfli square is mirrored once to get the periodic patch. Considering other orientations and overlappings might lead to other tilings. This method of generating tiling can be combined with the Stampfli inflation rule of placing squares and triangles at the vertices to generate larger approximants.

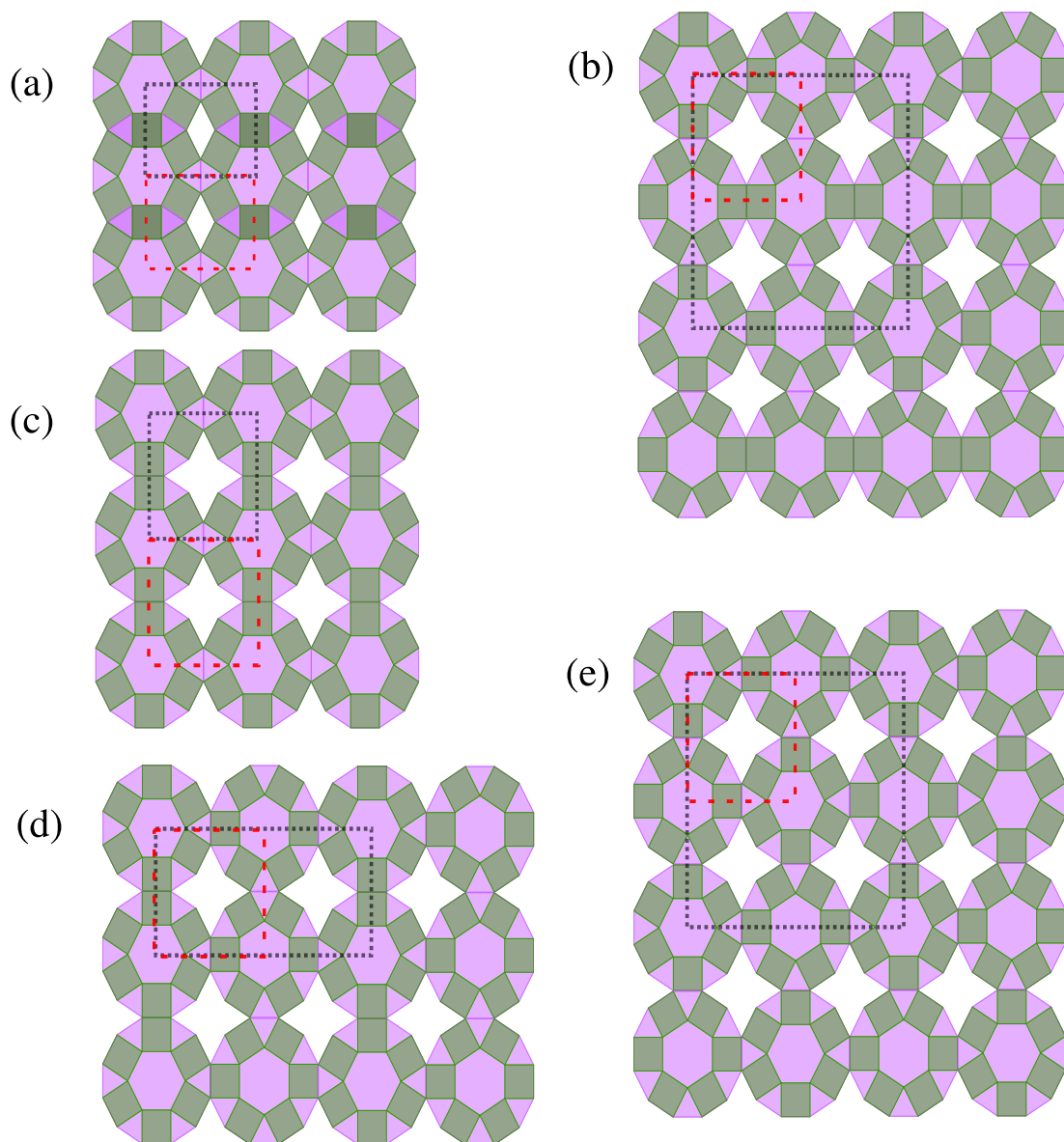


Figure 6.6: Square and rectangular arrangement of dodecagons. Red dashed lines indicate the Stampfli squares. The black dashed line indicates the periodic patch. The white space in the arrangement is filled with two triangles in (a) and with a square and four triangles in (b)-(e).

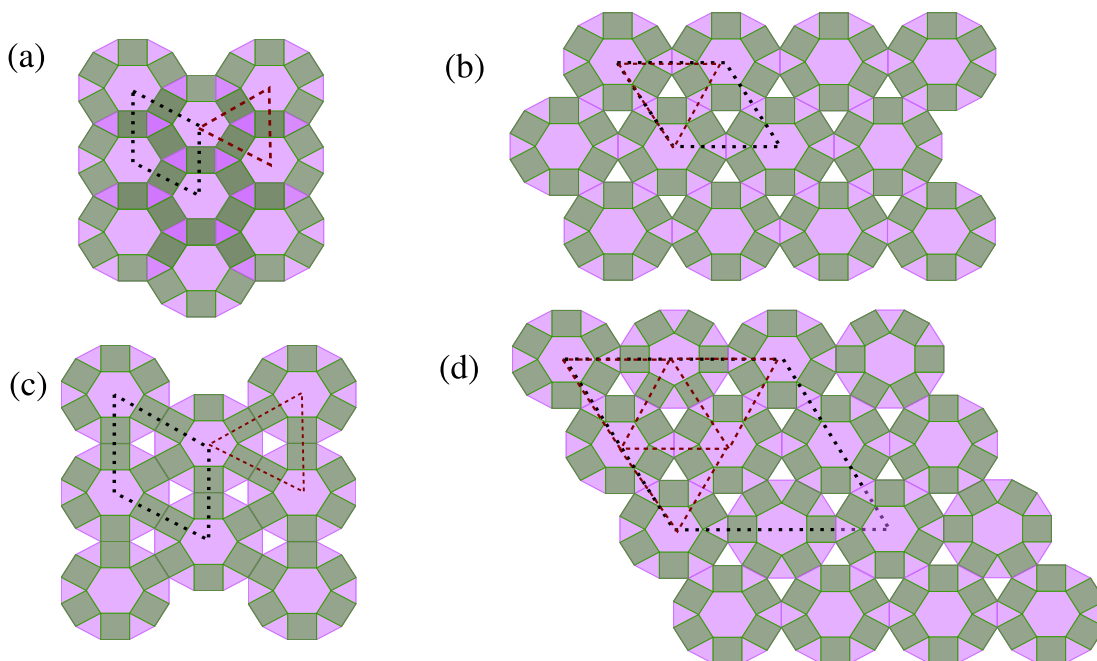


Figure 6.7: Triangular arrangement of squares and triangles in dodecagons. Red dashed lines indicate the Stampfli triangles. Black dashed line indicates the periodic patch. The white region are filled with one triangle in (b), (c) and (d).

Likewise, a variety of square-triangle tilings can be made from triangular arrangements by arranging the dodecagons in a triangular fashion with or without overlapping. We present four such tilings in fig. 6.7. Again, while placing these dodecagons the choice is made whether to place two squares or two triangles or a triangle and square adjacent to each other. The tilings given in fig. 6.7 will be referred as triangle (a), triangle (b), triangle (c) and triangle (d). Triangle (b), triangle (c) and triangle (d) are identified to form 12 fold symmetric structure by Hermisson et al [61]. Triangle (b) and triangle (c) are created by mirroring the Stampfli triangles indicated in red to obtain the periodic patch. Triangle (d) is a combination of two Stampfli triangles indicated in red which are collectively mirrored to create the periodic patch. In all these patterns the periodic patch is indicated by black dashed lines.

We will be looking at each tiling separately by adding ABC star $SSPs$ into them. Periodic patches used in SSP methodology will have uneven edges to comply with the boundary conditions. We use the SSP packing technique introduced in Chapter 4 to embed these tilings with ABC star terpolymer domains.

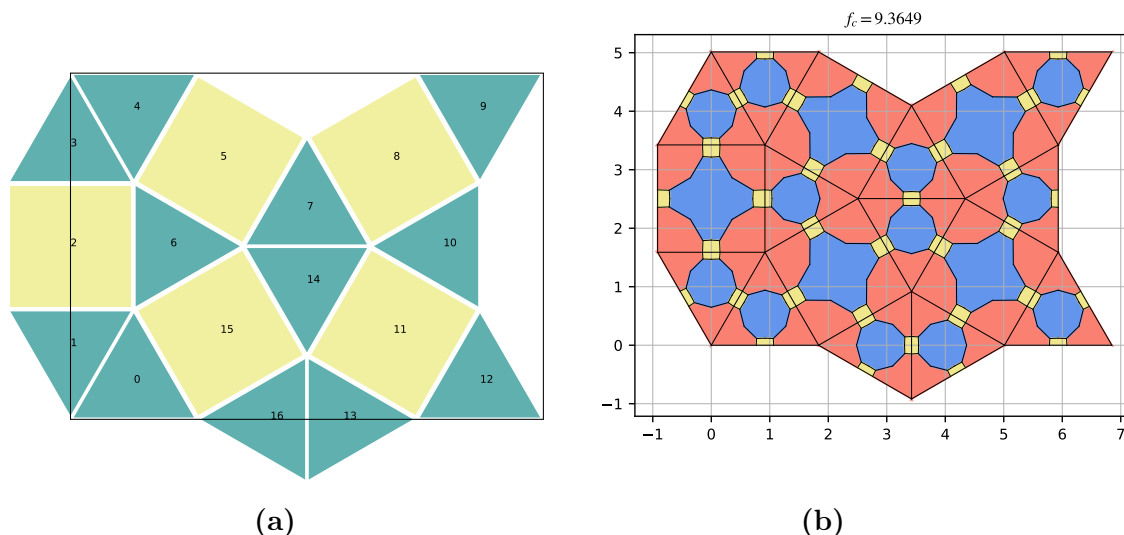


Figure 6.8: Periodic patch with square and triangle tiles is given in (a). Initial configuration with ABC star terpolymer SSP is also given.

6.3.1 Square (a)

In the square-triangle arrangement of square (a) four dodecagons are placed such that two of them overlap in pairs and the pairs are placed such that two triangles are adjacent to each other. The periodic patch will be from one purple hexagon to another in the x and y directions. When we tile this patch to do morphology analysis, we get the pattern in fig. 6.8.(a). As we can see from fig. 6.8 the right and the top edges have vacant spots. At the same time, the bottom and left edges have overflowing tiles which will fill in the vacancy on the right and top sides. The periodic patch contains 12 triangles and 5 squares. The ratio of the number of triangles to squares, τ is 2.4.

The tiling is filled with SSP s using the technique explained in section 4.2. Then we embed the tiling with ABC stars taking all monomers to be of equal compositions. As we have seen in the Σ -phase the square-triangle combination have lower free energy when the 4 sided domain is smaller with lower composition. So the ABC star embedded configuration undergoes a first-stage minimisation with respect to the monomer composition to find a suitable initial configuration to start with. Thus we obtain the initial configuration given in fig. 6.8.(b). There are 112 SSP s in this patch with 29 periodic nodes and 223 free nodes. The constraint list corresponding to this tiling has 449 elements in it, including the periodicity variables. The black rectangle in fig. 6.8.(a) indicates the periodicity. If we try to classify the cores in the initial configuration, there are two types of SSP triangles.

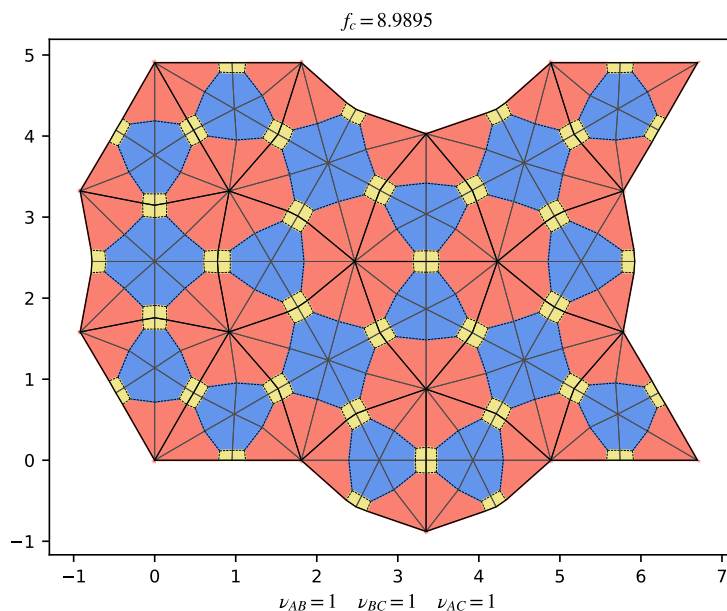


Figure 6.9: Minimised configuration for square (a) in fig. 6.8. The thick black lines in the structure indicate edges of ‘square’ and ‘triangles’.

One within the triangle, [10.6.4] and another within the square [10.8.4]. In this pattern, the arrangement of triangles in a hexagon will introduce a new triangle core: [12.6.4]. So using our conventional nomenclature, this morphology can be called [12.6.4; 10.6.4; 10.8.4].

The resultant configuration after minimisation is given in fig. 6.9. The minimisation of one set of monomer compositions took almost 43 minutes to complete using a single core on ARC4. In this configuration, the squares have their edges curved in and triangles have their edges curved out where they are adjacent. A similar effect on the square triangle arrangement was observed in the Σ -phase arrangement. In the Σ -phase there are two varieties of tiles after minimisation: a curved in ‘square’ and a ‘triangle’ with two sides curved out. In this tiling, there are three varieties of ‘triangles’ in the minimised structure and one type of ‘square’ tile. The triangle varieties are one with one edge curved out, another with two edges curved out and a third with three curved out edges according to the number of adjacent squares. Curving of original tile edges to minimise the overall free energy penalty of the structure here agrees with the results from Σ -phase morphology. The minimised structure has more varieties of SSP s in them. The topology of cores remains the same but SSP shapes are completely different. Classifying them has become a bit cumbersome now.

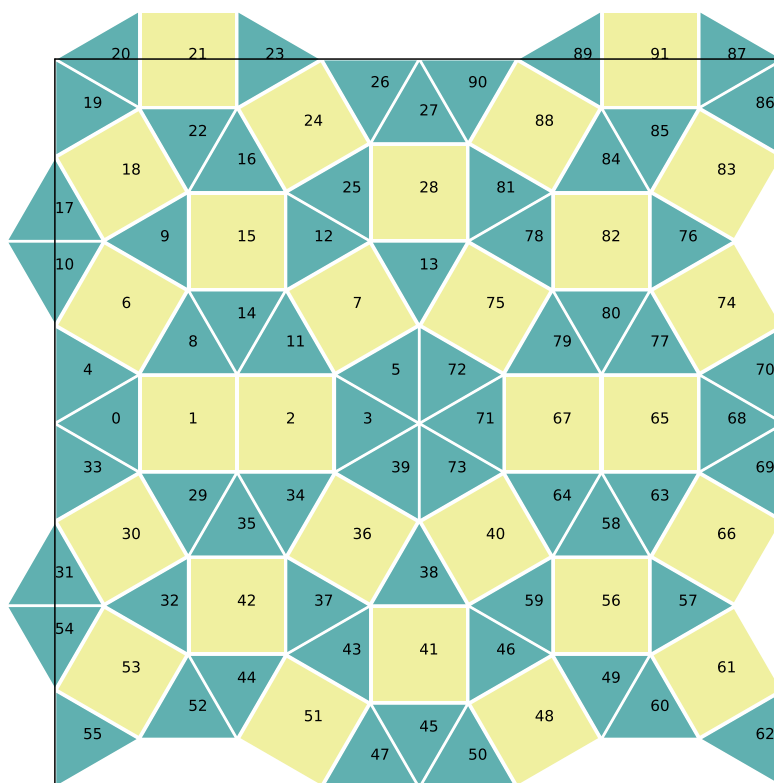


Figure 6.10: Periodic patch of squares and triangles one type of Stampfli square[13].

6.3.2 Square (b)

This arrangement of squares and triangles is from Stampfli's parent square. Square and triangle quasicrystal tiling have this arrangement in them [13]. Also, the soft matter quasicrystals with 12-fold symmetry often refer to this arrangement [58, 72, 171]. The square in dashed red lines indicated in fig. 6.6.(b) is mirrored twice to make this periodic patch enclosed by a large square with black edges. The periodic patch we need for our analysis is created with uneven tile placement at the edges. Here in fig. 6.10 the right and the bottom edges have vacant spots while the top and left edges have overflowing tiles which will fill in the vacancy on the right and bottom sides. This periodic patch is made of 28 squares and 63 triangles. Thus the ratio of the number of triangles to squares τ is 2.25. This is a bigger periodic patch compared to square (a). This arrangement has more variety of alignments of squares and triangles in them. A hexagonal

arrangement of triangles is present at the centre and the corners of this tiling. These square-triangle placements can be broadly classified using their vertices. Here one vertex is shared by six triangles. The remaining vertices in the periodic patch are shared between five tiles: two squares and three triangles. The alignment of these five tiles can be different. There are four vertices in the given patch where two squares are placed adjacent to each other. Squares and triangles are arranged in the Σ way around the remaining vertices shared by five tiles.

This periodic patch of squares and triangles is embedded with our ABC terpolymer $SSPs$. An initial configuration of the tiling with ABC star domains in it is obtained. There are 608 $SSPs$ in this periodic patch which is made from 1281 nodes. Among these nodes, 1215 nodes are free and 65 nodes are periodic. This makes a constraint list that has 2433 entries. This is quite a large size for the constraint list and the minimisation procedure must vary all these elements to obtain a stable configuration. This version of the code written in Python takes a long time to achieve a complete minimisation. So the minimisation of this structure is executed in multiple steps. Once the tiling is embedded with $SSPs$, the configuration undergoes a first-stage minimisation to obtain a good monomer composition that is not $\phi_A = \phi_B = \phi_C = \frac{1}{3}$ to start with. In this minimisation there are only 6 variables associated; three monomer compositions and three positions where new nodes are placed on the original square triangle tile as in section 4.2.(a). The resultant initial configuration after this minimisation is given in fig. 6.11.(a). This initial configuration undergoes detailed minimisation to find a stable configuration for given monomer compositions shown in fig. 6.11.(b). The constraint list is large here so this minimisation is also conducted in different stages with difference tolerance as demonstrated in table 4.1. The $BFGS$ method with tolerance 0.01 provided final function value which is four significant digits same as the true value in less amount of time. So for this big structure, minimisation was conducted in two stages with different tolerances, each starting from an initial configuration closer to the true value of free energy per chain. The minimisation of one set of monomer compositions took almost 18 hours to complete using a single core in ARC4.

If we attempt to classify the cores with our conventional nomenclature, we can find three different cores in this initial patch. There are [12.6.4] inside every hexagon made by 6 triangles, [10.6.4] inside each triangle and [10.8.4] inside each square. This is the same as the cores identified in the initial configuration of square (a). In this patch even if we define the cores, we cannot define the patches as the arrangement and proportion of these cores are different. For instance, when two squares are adjacent, cores associated with that patch are still the same but now with a different arrangement. Hence the topological nomenclature of the initial configuration does not make any sense any more as this structure is big enough to introduce the aperiodic complexities of quasicrystal.

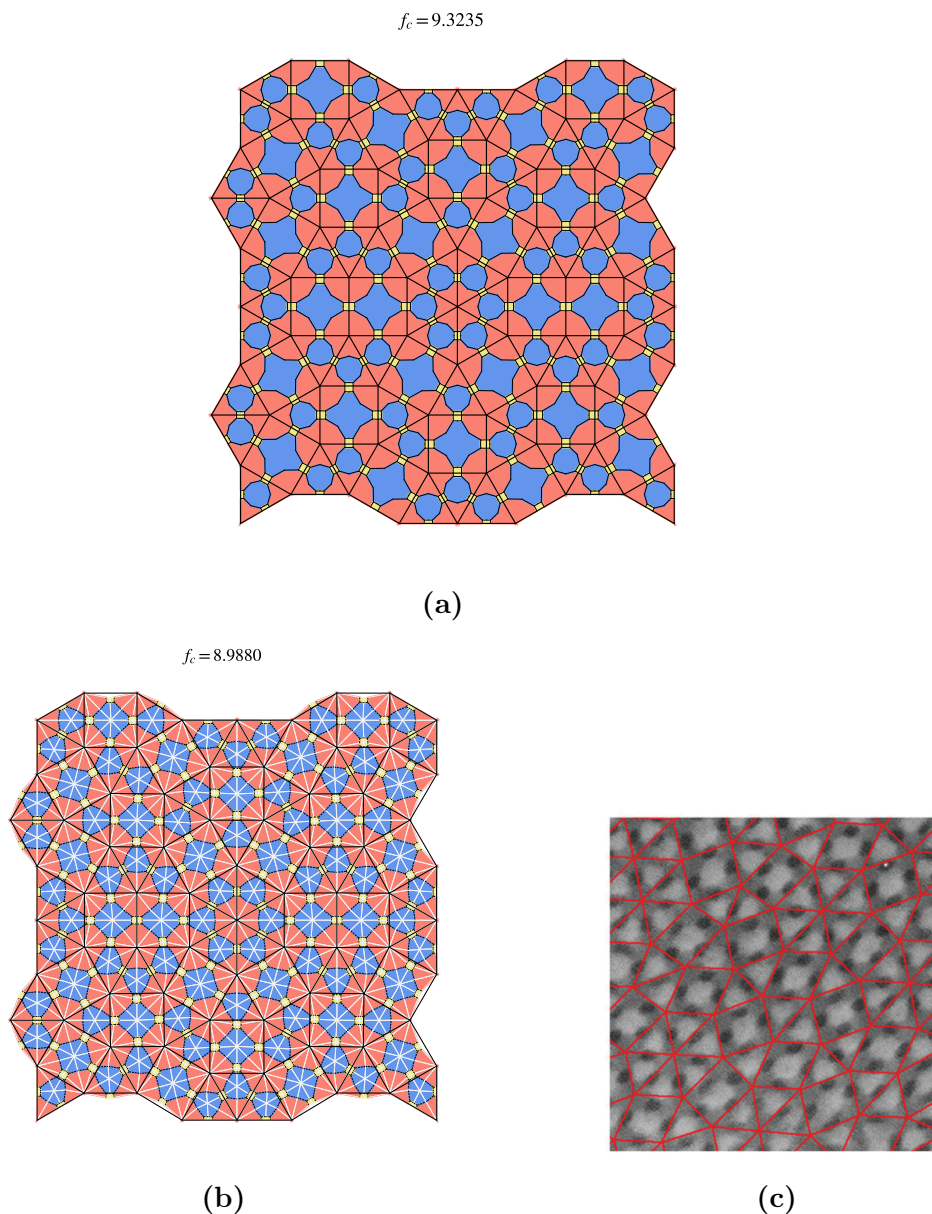


Figure 6.11: Periodic patch of square (b) arrangement with SSP for embedded in them. The tiling in (a) is the initial configuration obtained from the first stage of minimisation for monomer compositions $\phi_A = 0.5671$, $\phi_B = 0.3671$ and $\phi_C = 0.0658$. Original triangle and square outlines are given in black lines. The tiling in (b) is the minimised configuration for the same set of compositions. White lines are SSP edges and black lines are the square and triangle edges. The TEM image of ISP reported by Hayashida et al. [57] is adapted in (c) with the author's permission.

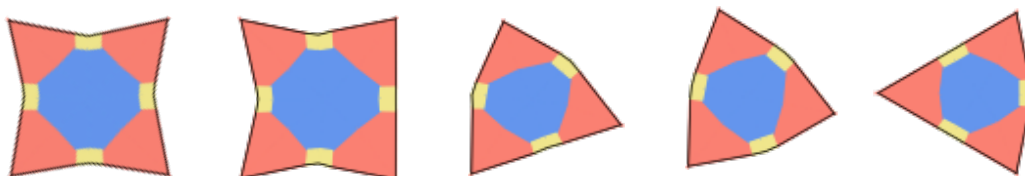


Figure 6.12: Different varieties of squares and triangles obtained after minimisation.

The stable configuration after multiple stages of minimisation is given in fig. 6.11.(b). This configuration also exhibits the curving of tile edges that was observed in Σ and square (a). Here we obtain 5 tiles given in fig. 6.12 after minimisation. This patch contains all possible local arrangements of squares and triangles in a dodecagonal tiling. Hence for any square triangle tiling we are considering, the minimised structure will contain different combinations of these 5 tiles. When a square is shared by triangles from four sides, the minimised square is shrunk at four edges. A triangle that is shared by three squares is bulged at its edges. If the edges are shared by the same shape then that edge is straight. Any other combination of square triangle arrangement is impossible with the dodecagonal arrangement we follow. If we look closely at each minimised tile, we can see that two tiles of are same topological sub-classes are not entirely identical.

In fig. 6.11.(b), white lines are SSP edges. Upon minimisation, there are many varieties of $SSPs$. This agrees with our observations from square (a) and Σ -phase. As this structure is quite big, it is not practical to manually count the different $SSPs$ and their features. We will need a detailed evaluation of the structure using Fourier analysis.

Black lines in fig. 6.11.(b) are the skeleton of square-triangle tiling being overlaid on the minimised structure. In this structure, black edges shared between a square and a triangle cross yellow domains along the domain edge. A similar characteristic was seen in Σ -phase in fig. 6.2.(c). As discussed in section 6.2 this characteristic is observed in experimental results of ABC star terpolymer phase separation. Image of the quasicrystalline phase obtained by Hayashida et al. is given in fig. 6.11.(c). In this, they attempt to overlay the structure with squares and triangles and it is obvious that the edge shared by a square and a triangle crosses the black domain along its edge like in our simulation. In this image, all the squares are not identical and they are skewed as they didn't take the bending into account. There are adjacent squares and hexagonal arrangements of triangles in this pattern which are present in the minimised configuration of the square-(b) in fig. 6.11.(b).

6.3.3 Square (c)

In this arrangement, the periodic patch is smaller compared to square (b). Here, two dodecagons are placed such that two squares and two triangles are adjacent to each other. The periodic patch is the same as a parent square tile with vertices at hexagon centres. A periodic patch suitable for tiling is given in fig. 6.13.(a) whose periodicity is indicated by a black square. The triangle-to-square ratio τ for this periodic patch is 2.28. All vertices inside the periodic patch are shared by two squares and three triangles arranged in a different order. When tiled, the border will give the hexagonal arrangement of triangles.

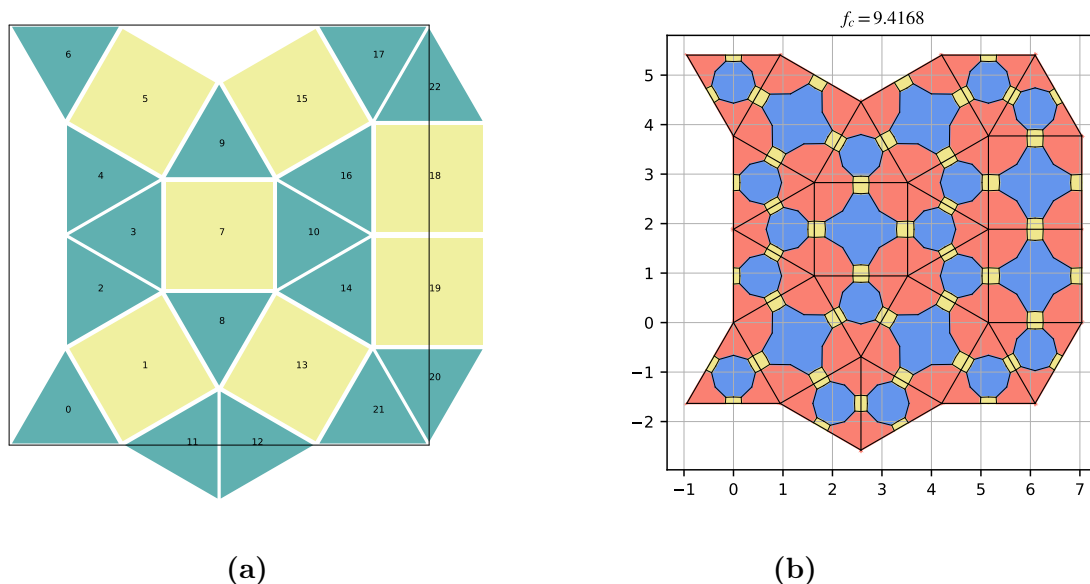


Figure 6.13: Periodic patch for square (c) arrangement is given in (a). Its periodicity is indicated by black solid lines, which is the parent square. Initial configuration with $SSPs$ embedded in the tiling for monomer composition $\phi_A = 0.5573$, $\phi_B = 0.3641$ and $\phi_C = 0.0786$.

Upon adding ABC star domains, there are 152 $SSPs$ in total and the constraint list has 609 entries. Even though this configuration is not as big as square (b), the initial first stage minimisation to find the right monomer composition for the arrangement was done and the result of this first stage minimisation is given in fig. 6.13.(b). We can find three different standard cores [12.6.4; 10.8.4; 10.6.4] in this initial configuration, as in the previous two cases. Their arrangement is different, which makes this nomenclature not unique for this configuration.

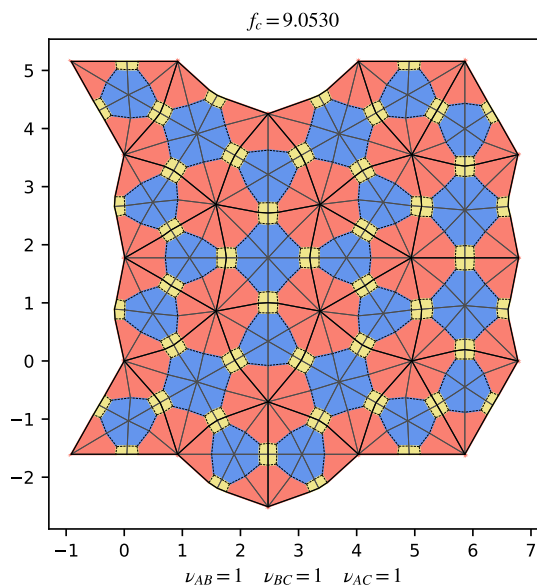


Figure 6.14: The minimised configuration for square (c) arrangement from the initial configuration given in fig. 6.13.(b).

The minimised tiling corresponding to the initial configuration given in fig. 6.13 is given in fig. 6.14. Minimisation for one set of monomer compositions took almost 1.5 hours to complete using a single core in ARC4. Curving of square and triangle edges is observed in this case too. This minimised configuration contains all five curved tiles identified from the previous case. This also has a square-square arrangement which introduced yet another type of SSP geometry/core upon minimisation. The characteristics of the minimised structure are the same as square (a) and square (b) except for the difference in arrangement. It is to be noted that there are adjacent squares in square (b) and square (c). The free energy per chain for minimised square (c) is larger than square (b) for almost the same monomer composition.

6.3.4 Triangle (a)

This is a triangular arrangement of dodecagons given in fig. 6.7.(a). In this, the parent triangle is smaller than the regular Stampfli triangle. Three dodecagons are overlapped such that they have four common triangles and three common squares. Unlike other arrangements we have, there are no gaps in this one. This tiling has two vertices, one shared by three triangles and another shared by three triangles and two squares $[3^6, 3^2.4.3.4]$ [72]. This square-triangle arrangement

is found in the quasicrystal patch reported by Hayashida et al [57]. The periodic patch here is chosen to be a rectangle indicated by the solid black lines in fig. 6.15.(a). The triangle-to-square number ratio τ is 2.67.

The initial configuration is created from square-triangle tiling in exactly the same way as in previous cases. The initial configuration is deduced from a first-stage minimisation to determine the asymmetric monomer compositions similar to the previous cases. With the chosen periodic patch ABC , star tilings will have 144 $SSPs$. The periodic patch has 287 free nodes and 33 periodic nodes and the constraint list corresponding to this periodic patch has 577 elements. It is possible to choose another periodic patch which is smaller in size for this case.

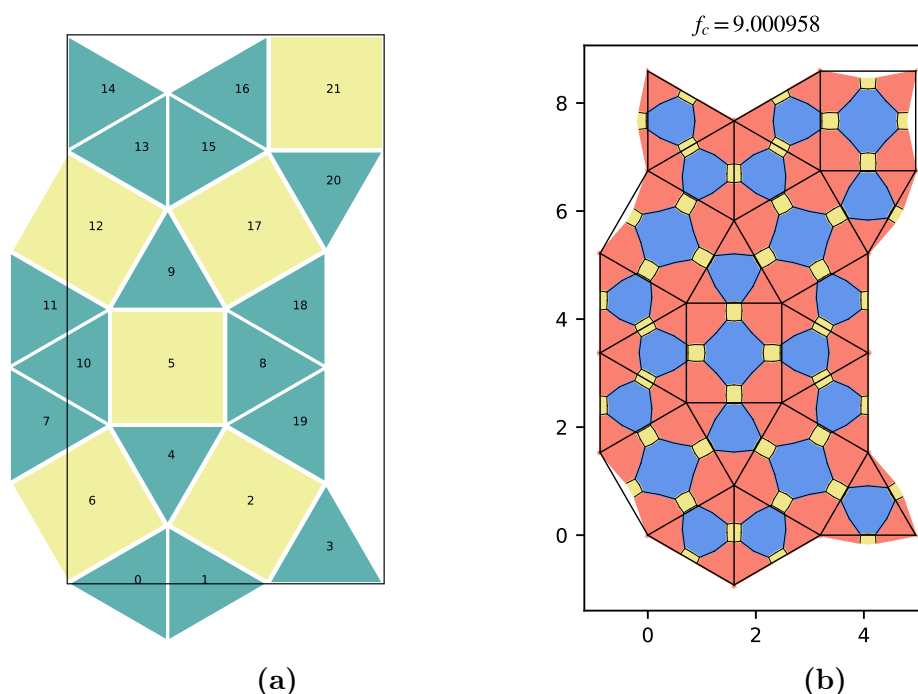


Figure 6.15: Periodic patch corresponding to triangle (a) square-triangle arrangement is given in (a). The minimised structure for monomer composition $\phi_A = 0.5658$, $\phi_B = 0.3568$ and $\phi_C = 0.0774$ is given in (b). Regular square-triangle tiling is overlaid on top of the minimised tiling to detect the curving.

The minimisation of one set of monomer compositions took almost 2 hours to complete using a single core in ARC4. Upon minimisation, this configuration also exhibits tile curving for squares and triangles as shown in fig. 6.15.(b). It also has different $SSPs$ in it after minimisation. The square triangle tiling is overlaid on top of the minimised structure and curving of the tiling is visible in fig. 6.15.(b). In this minimised tiling there are three types of minimised tiles

6. Periodic approximants of Square-Triangle tilings in ABC star terpolymers

here, a square curved in all sides, a triangle with one curved side and another triangle with three curved sides.

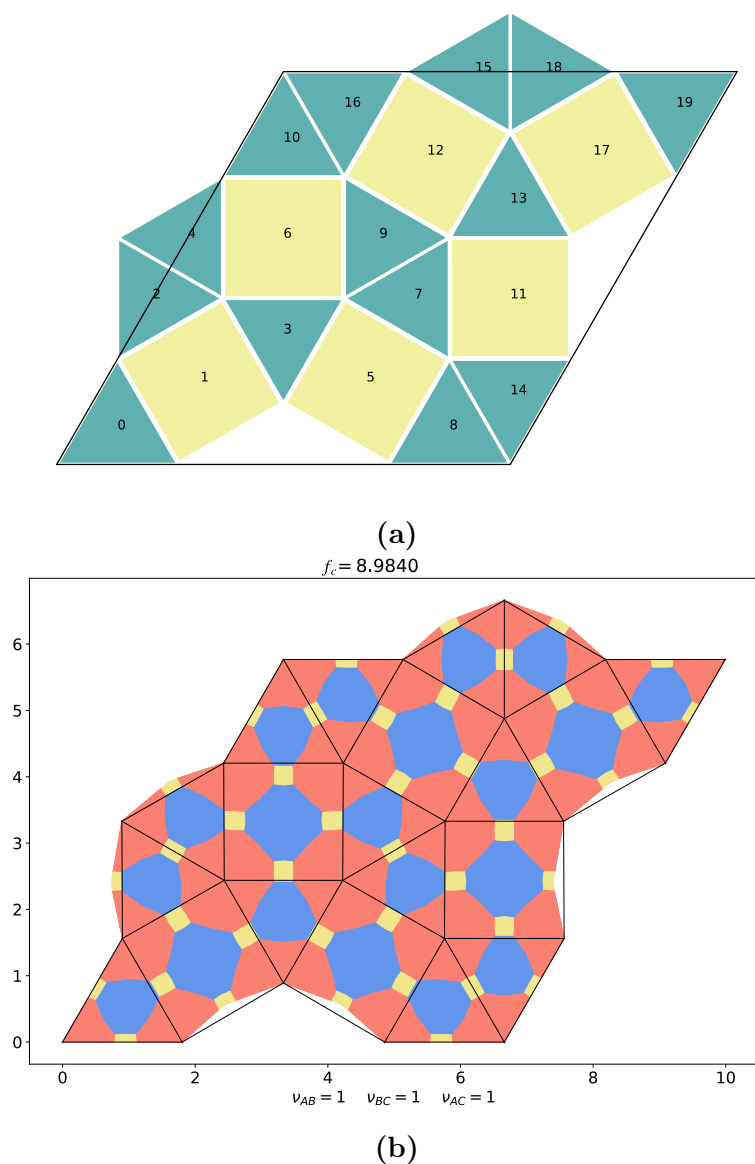


Figure 6.16: Periodic patch of the triangle (b) arrangement of the square-triangle tiling is given in (a). Minimised structure for monomer compositions $\phi_A = 0.5671$, $\phi_B = 0.3671$ and $\phi_C = 0.0658$ for this arrangement is given in (b).

6.3.5 Triangle (b)

Triangle (b) is another Stampfli parent triangle where dodecagons are placed at the corners. These dodecagons are placed such that two triangles face each other where two dodecagons meet. This arrangement is found in soft matter quasicrystal tilings [57, 72]. The triangle-to-square number ratio τ is 2.33 for this arrangement, which is closer to quasicrystal tiling favourable ratio $\frac{4}{\sqrt{3}}$. The periodic patch here is a rhombus indicated by solid black lines in fig. 6.16.

The minimisation procedure is the same as in the previous square triangle cases. After a minimisation based on the tiling and monomer composition, an initial configuration is obtained. There are 132 SSP polygons in this periodic patch. The corresponding constraint list consists of 529 entries.

The final configuration after minimising with the constraint list is given in fig. 6.16. (b). The minimisation of one set of monomer compositions took almost 1.6 hours to complete using a single core in ARC4. This configuration also exhibits square and triangle curving. There are four types of minimised tiles in this configuration. As two squares are never adjacent to each other in this arrangement, there is only one type of minimised square here. On overlaying regular tiling on the minimised pattern, square triangle edges cross yellow domains along their edge. This also has all the characteristics we have seen in minimised structures of previous cases.

We can continue this kind of analysis by checking different square-triangle arrangements in a similar manner, expecting to find similar pattern characteristics in different combinations. From the above analysis we can conclude that when we place the ABC star in a square triangle tiling, the tiling will be curved from the effects of monomer interactions and stretching. When you have squares or triangles adjacent to each other, the edge shared between them remains straight. When a square shares edges with a triangle, those edges curve into the square. The methodology is equipped to analyse square triangle tiling of any periodicity length. It is clear from the above cases arrangement of a square-triangle affects the final free energy of the morphology. Figuring out if any of these arrangements are present in the phase space is the next task. We are using a different approach to check their presence in phase space, which will be demonstrated in the upcoming section.

6.4 Linear phase spaces

We have five varieties of square triangle arrangements to compare in order to find which one has the lowest free energy per chain. We are also interested in knowing if any of these are present in ABC star phase space. In section 6.3, we saw that minimisation time for these configurations varies from 1 hour to 18 hours for one

6. Periodic approximants of Square-Triangle tilings in ABC star terpolymers

single data point in the phase space. In our ternary phase space, we calculate up to 4050 data points. This scale of phase space exploration is very time-consuming as well as not computationally feasible with the present version of the script using Python. So we undertook a linear phase space exploration where a line is taken across the phase space taking one monomer composition to be constant.

In ABC star terpolymer with symmetric interactions, we found Σ -phase at the intersection of squares [8.8.4] and triangles [12.6.4]. This encourages us to anticipate the presence of other square-triangle phases around the same region. These Σ -phase strips in fig. 6.3 and fig. 6.4 are uniform along their lengths, even when the widths change due to differences in interactions. So if we take a straight line across the Σ strip from the square to the triangle region, we can see if there are any square triangle arrangements in the phase space. We will compare square [8.8.4], triangle [12.6.4], Σ -phase, square (a), square (b), square (c), triangle (a) and triangle (b) along this line.

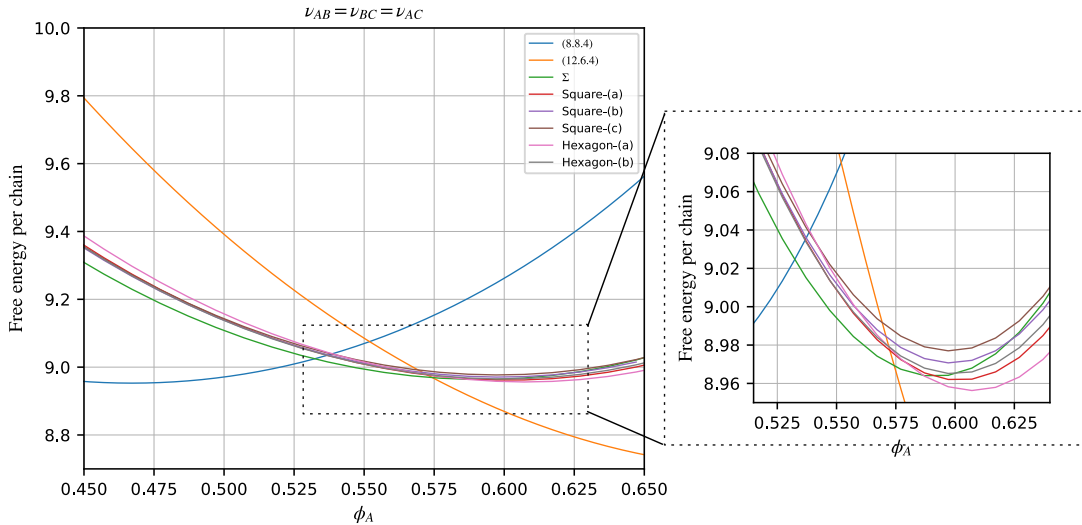


Figure 6.17: Linear phase space varying only ϕ_A for different varieties of square-triangle tilings for ABC star terpolymer with equal interaction between branches. Here $\nu_{AB} = \nu_{BC} = \nu_{AC} = 1$ and the monomer compositions of C and B are $\phi_C = 0.065$ and $\phi_B = 0.935 - \phi_A$. The magnified region where all square-triangle lines are crowded together is also given in the box on the side.

In the phase space of ABC star with same interaction strength between its branches, the Σ region is identical for all topological sub-classes. The phase space is symmetric in all directions. If we take a line across one topological

6. Periodic approximants of Square-Triangle tilings in ABC star terpolymers

sub-class of Σ -phase, it will be same for the other five regions. We take a straight line across topological sub-classes ABC which has A monomer in large domains and C monomer in small domains. We take the line corresponding to $\phi_C = 0.065$, varying ϕ_A with $\phi_B = 0.935 - \phi_A$, and evaluate the free energy for all the morphologies mentioned. The resulting slice of the phase space is given in fig. 6.17.

Tiling arrangement	$\tau = \frac{N_{triangle}}{N_{square}},$ $\tau_Q = 2.309$	Value free energy per chain ($k_B T$) at $\phi_A = 0.568$	Time of one minimisation
[12.6.4]	Not applicable	8.9974	30 seconds
Square (a)	2.40	8.9818	43.12 minutes
Square (b)	2.25	8.9871	18 hours
Square (c)	2.28	8.9927	1.5 hours
Triangle (a)	2.67	8.9842	2 hours
Triangle (b)	2.33	8.9832	1.6 hours
Σ -phase	2.00	8.9735	4 minutes

Table 6.1: Free energy values of different morphologies given in linear phase space when $\phi_A = 0.568$. The time taken for a complete minimisation is also given.

In the resulting linear phase space, the blue line is square morphology and the orange indicates the triangular morphology. As we go along the x axis in fig. 6.17, for values of ϕ_A from 0.450 to 0.54, the square morphology has the lowest free energy. For values larger than 0.575 the triangle morphology has the lowest free energy. Near to the value of ϕ_A where these two lines intersect, morphologies with square-triangle arrangements have lower free energy values. Free energy lines corresponding to different square triangle arrangements are close and crowded together in this region. On a closer look at the magnified figure on the right, it is clear that Σ -phase has the lowest free energy among the square-triangle tilings we have. This means the phase space will be the same as fig. 6.3 with no other morphologies popping in at least for this value of ϕ_C . The free energy values of these morphologies at $\phi_A = 0.568$ are listed in table 6.1. From the table and graphs it is obvious that square (b) and square (a) have higher free energy values. Among these morphologies triangle (a), square (a) and triangle (b) have lower free energy per chain values than Σ -phase when $\phi_A \gtrsim 0.6$. Free energy minima for square-triangle morphologies lie in the region where [12.6.4] has the lowest

6. Periodic approximants of Square-Triangle tilings in ABC star terpolymers

free energy. There are two adjacent squares in square (b) and square (c). This alignment of squares tend to increase the free energy of a given morphology. This value of ϕ_A is close to where lines corresponding to square-triangle morphologies intersect with [12.6.4]. From this table, it is clear that the free energy value is closer to each other to the extent that they are the same for two significant digits. Thus any perturbation to the monomer density can introduce a phase transition in this system that will favour complex square-triangle tiling-like morphology.

In order to see the effects of unequal interactions between ABC branches similar linear phases are plotted for three cases introduced in Chapter 5. In the modified phase spaces introduced earlier, strips with Σ -phase have uneven width. We chose the straight line across the wider strips in each phase space. Square (b) in the symmetric case has higher free energy compared to other square-triangle morphologies and it takes 18 hours for the minimisation of one set of composition. Hence, we omit square (b) in the phase space study with unequal interactions. For the case where $\nu_{AB} = \nu_{BC} = 1, \nu_{AC} = 0.8$ we chose the line $\phi_B = 0.099$ where ACB sub-class are favoured. With $\nu_{AB} = \nu_{BC} = 1, \nu_{AC} = 1.4$, we take the line $\phi_C = 0.068$ where the class BAC is favoured. Finally for the case where $\nu_{AB} = 1, \nu_{BC} = 0.6, \nu_{AC} = 1.6$ we take the line $\phi_A = 0.114$ where the sub-class CBA is favoured. In this case ϕ_B is varied. For all these cases, calculations for melt with symmetric interactions are repeated with updated interactions in its scripts and free energy lines are plotted in figs. 6.18 to 6.20.

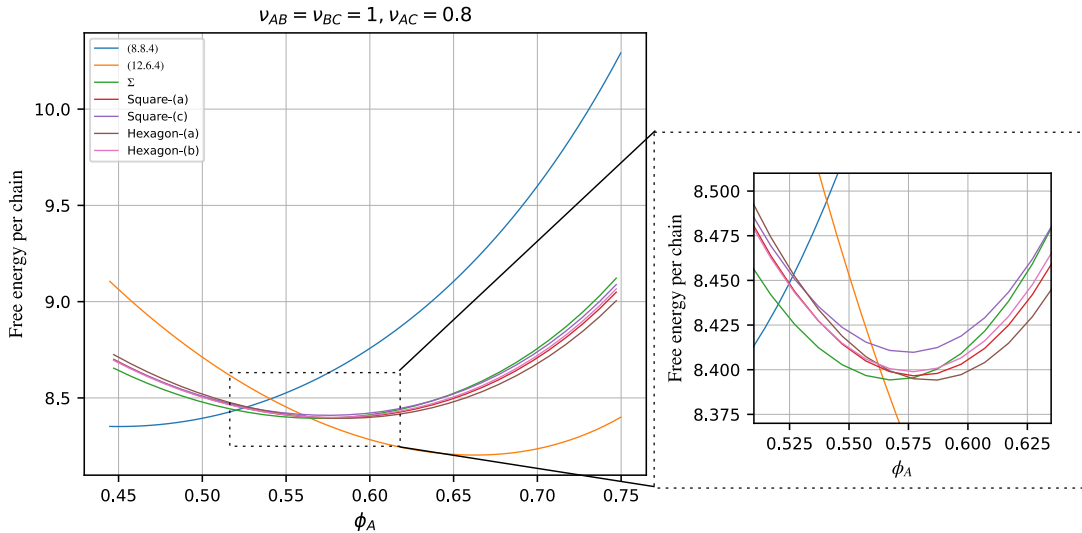


Figure 6.18: Linear phase space for $\nu_{AB} = \nu_{BC} = 1, \nu_{AC} = 0.8$ across the Σ stripe for ACB topological sub-class. Here value of $(\phi_A, \phi_B, \phi_C) = (\phi_A, 0.099, 0.901 - \phi_A)$.

6. Periodic approximants of Square-Triangle tilings in ABC star terpolymers

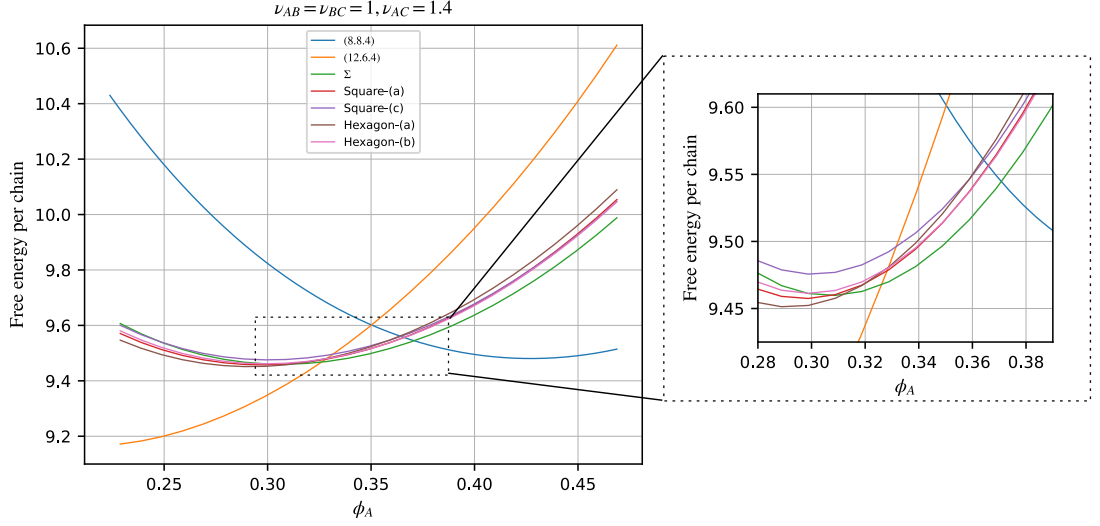


Figure 6.19: Linear phase space for $\nu_{AB} = \nu_{BC} = 1, \nu_{AC} = 1.4$ across the Σ stripe for BAC topological sub-class. Here the value of $\phi_C = 0.068$ is kept constant and ϕ_A is varied with $\phi_B = 0.932 - \phi_A$.

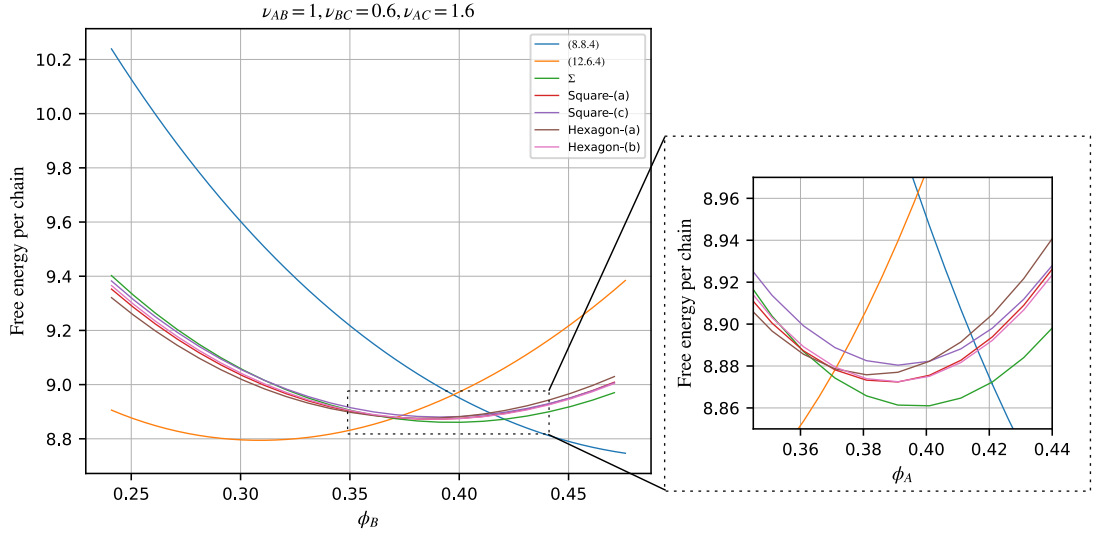


Figure 6.20: Linear phase space for $\nu_{AB} = 1, \nu_{BC} = 0.6, \nu_{AC} = 1.6$ across the Σ stripe for CBA topological sub-class. Here the value of $\phi_A = 0.114$ is kept constant and ϕ_B is varied with $\phi_C = 0.886 - \phi_B$.

In all three plots, at the point where the lines corresponding to [8.8.4] and [12.6.4] intersect the square-triangle tiling morphologies all have lower free energy. All lines corresponding to these morphologies are close to each other, the Σ -phase always has the lowest free energy per chain in these linear explorations and so is present in the phase space. In all three linear phase spaces, the red line corresponding to square (c) has the highest free energy amongst square-triangle morphologies. The triangle (a) and square (a) are both smaller periodic patches and have lower free energies after the Σ -phase. The height difference between the intersection point between Σ -phase line and [12.6.4] and square (a) and [12.6.4] (green line - teal line) are 0.0065, 0.0096 and 0.0025 in fig. 6.18, fig. 6.19 and fig. 6.20 respectively. For any of the square-triangle arrangements to appear in the phase space, these values have to be less than zero. We can see that the interactions are inducing shifts in intersection points, but we are yet to find the right perturbation that will make square-triangle tilings stable.

From this analysis, it is suggested that an arrangement with two squares adjacent to each other is not favourable for ABC star phase separations. The abundance of triangles in the tiling reduces the free energy value. Hence we are not considering the square (d) and triangle (c) in our analysis. Square (e) and triangle (d) are large patches which will take almost the same amount of time or more time as square (b). So we are not attempting those morphologies in the focus of this chapter.

6.5 Fourier analysis of square-triangle tilings

The lengthscales that emerge in these tilings with ABC star domains can be studied in a qualitative way from their Fourier spectrum. In our tiling patterns, monomer domains are of different shapes and colours, in square, rectangular and rhombic periodic boxes. Hence we need to use wavevectors \mathbf{Q} specific for each tiling. The reciprocal lattice space for each tiling is created using the indices (m_1, m_2) such that the wavevector $\mathbf{Q} = m_1\mathbf{Q}_1 + m_2\mathbf{Q}_2$ using the expression in eq. (4.11). Depending on the periodic box, this reciprocal lattice can be a square, rectangle or rhombus. The value of the indices m_1 and m_2 are chosen separately for each tiling and it will set the range for a given periodic patch. For simpler tiling patterns like square and triangle, $(m_1, m_2) = (10, 10)$ will provide all necessary sharp peaks and their higher order peaks. Large and more complex patterns like square (b) require higher indices $(m_1, m_2) = (25, 25)$ so that the reciprocal lattice is closely packed and we do not miss sharp peaks.

The tiling is converted into a black and white pattern by taking $\rho_A = 0$, $\rho_B = 1$ and $\rho_C = 1$ in eq. (4.15). The tiling now has red domains empty or in white, and yellow and blue domains in black. Thus the scattering density $\rho_{\Delta_{0ij}}(\mathbf{Q})$ in eq. (4.15) is determined for an SSP for each spot in the tile that corresponds

to some wavevector $\mathbf{Q} = q_x \mathbf{i} + q_y \mathbf{j}$ in the reciprocal lattice. For each point in the reciprocal lattice, the total scattering density is determined by summing up the scattering density for all *SSPs* involved in that periodic patch multiplied by an appropriate phase factor. This total value is then squared to get the scattering intensity at each wavevector due to the patterns in the tiling.

While plotting the intensity in the reciprocal lattice, omitting the peak at $\mathbf{Q} = 0$, we highlight the point corresponding to the wavevector that undergoes the strongest scattering. For each tiling, the intensities obtained for each point in this reciprocal lattice is divided by the largest intensity value. Then we take the logarithm of the obtained scaled intensity. This scaling will let us identify the prominent peaks available in each tiling. The dot size and colour of each point in the reciprocal lattice are scaled according to these normalised values. All Fourier spectrum are plotted between $q_x = [-10, 10]$ and $q_y = [-10, 10]$.

We have compared the Fourier spectra for each tiling pattern discussed in this chapter and are reporting some of them in fig. 6.21. All these spectra are determined for minimised tiling patterns with monomer compositions $(\phi_A, \phi_B, \phi_C) = (0.5671, 0.3670, 0.0659)$. We present the morphologies: [8.8.4], [12.6.4], square (a), square (b), triangle (a) and triangle (c). The blue circles in these spectra correspond to the length between the centres of two red domains. There are no distinctive peaks inside the blue circle in all examples, so the patterns are uniform at lengthscale larger than the ones indicated by a blue circle.

The spectrum for the [8.8.4] morphology in fig. 6.21 (top left) has four prominent dots separated by an angle of $\frac{\pi}{2}$ just outside the blue circle. This indicates the lengthscale associated with the [8.8.4] morphology. On the blue circle there are four smaller dots indicating the red domains. The pattern demonstrates 4-fold symmetry. There are more Fourier dots present with the same symmetry as we go away from the centre.

In the Fourier spectrum associated with [12.6.4] morphology in fig. 6.21, there are 6 sharp and distinct spots separated by an angle of $\frac{\pi}{3}$. They indicate the presence of red domains distributed in a hexagonal pattern in the tilings. This shows the tiling has six-fold rotational symmetry. There is only one prominent lengthscale here. Scattering at higher order is indicated by dots in a hexagonal lattice as we go away from the centre.

The Σ -phase exhibits more prominent peaks in the chosen range of \mathbf{Q} . Just outside the blue circle, it has a set of three dots on four sides indicating the existence of a prominent four-fold symmetry in the tiling. But this pattern is more complicated than [8.8.4] and [12.6.4]. Along with the 4 dots on the blue circle due to some red domains, four-fold symmetry is demonstrated by other domains which are more prominent.

6. Periodic approximants of Square-Triangle tilings in ABC star terpolymers

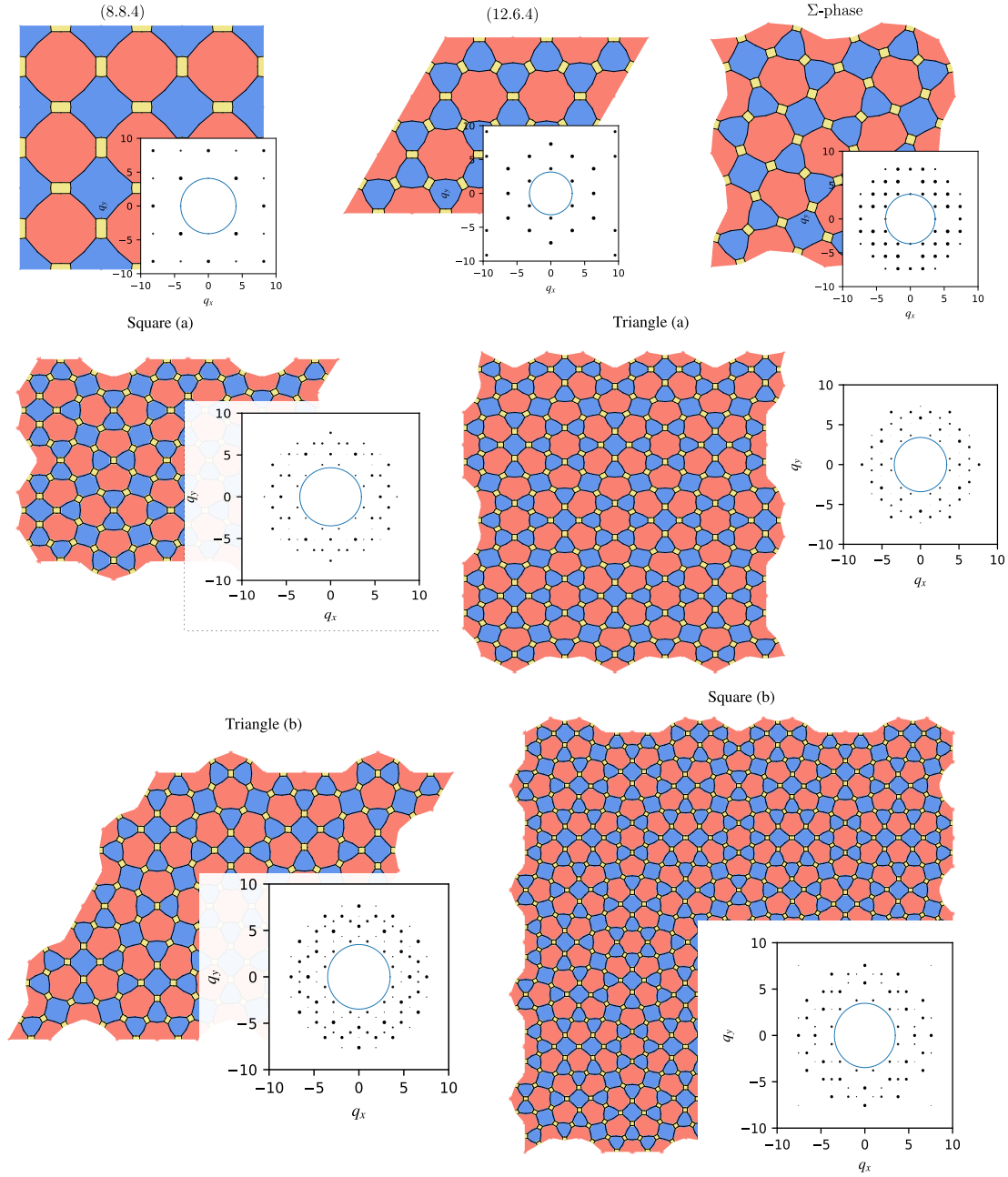


Figure 6.21: Morphologies and their corresponding Fourier spectra are listed. Morphologies [8.8.4], [12, 6, 4] and Σ -phase are in the first row from the top, square (a) and triangle (a) are in the second row and triangle (b) and square (b) are in the third row. The blue circle indicates 2π over the length between the centres of two red domains in the given structures.

When we consider more complex square-triangle patterns, there are more Fourier dots in the spectrum. In square (a) and triangle (a), we see an emergence of 12 dots in the inner circle. They are not equidistant so lengthscale corresponding to 6-fold symmetry is prominent in square (a) pattern. The twelve dots are more equi-spaced for larger examples like triangle (b) and square (b).

The tiling triangle (a) displays Fourier peak characteristics similar to square (a). Here there are 12 dots just outside the blue circle indicating red to red distance. In this pairs of dots are more closer to each other compared to the spectrum of square (a). The hexagonal symmetry associated is more pronounced in this spectrum, as are sharper peaks among the higher order scattering peaks.

In the spectrum corresponding to triangle (b), there are 12 dots aligned in a circle closest to the centre. These dots are almost equidistant hence they exhibit 12-fold rotational symmetry. The most prominent peaks are the ones from higher-order scattering. So the prominent lengthscales here are smaller than red to red length.

Looking into the largest square-triangle tiling we have in this chapter, the spectrum for square (b) also has 12 distinct peaks aligned in a circle close to the centre. These peaks are almost equidistant to each other separated by an angle of $\frac{\pi}{12}$. In this spectrum, there are three prominent rings with darkest spots. The most prominent spots are observed at lengthscales smaller than red-to-red distance.

From Chapter 2 we know that in *ABC* star there exist composition parameters that can potentially lead to phase separation into morphologies with two lengthscales in a weakly segregated regime. In these strongly segregated morphologies, we are looking for prominent lengthscales to identify the emergence of two lengthscales. In both triangle (b) and square (b) we can see 12-fold symmetry emerging and there are several prominent rings of peaks in the spectrum which indicates the presence of more than one lengthscale. These are square-triangle periodic patches made from Stampfli parent triangle and square [119]. Now compared to a quasicrystal, the two tilings we have are short-ranged, hence the presence of two prominent lengthscales is not explicit from the obtained spectrum. The spectrum also detects intermediate lengthscales that can be caused by the twining or overlapping of two lengthscales. When these two tiles are combined together to create a larger periodic approximants of square-triangle aperiodic tiling, a more interesting Fourier spectrum with quasicrystalline features can be obtained.

In these Fourier spectra, the prominent lengths are not entirely evident, since this is a quick conversion of domains to the reciprocal lattice with a discontinuous density. Non-smooth interfaces make it difficult to calculate the true scattering spectrum of the structure. The reciprocal lattice is limited to packed square dots which limit the placement of the dots. The analysis has its limitations, but the emergence of 12 approximately equidistant peaks and concentric circles suggests the connection to the idea that having two lengthscales plays a role in quasicrystal

morphology in *ABC* star phase separation. Using the methodology we can have tiling with larger periodicities can be analysed, and we hope to be able to find a second prominent set of peaks as predicted in Chapter 2.

6.6 Discussion

In this chapter, we saw that our *SSP* methodology works well with large complex morphologies. We have produced phase spaces which are presented in chapters 5 and 6 and that agree with existing phase spaces in the literature. Despite only considering the free energy balance between the stretching of polymer chains and interfacial energy of the domains, we successfully reproduced the same phase space with limited morphologies as the one produced using SCFT [91]. In addition to that, our work shines a light on new interesting observations regarding the square-triangle morphologies found in *ABC* star terpolymers. In our work, we present the analysis of various square-triangle tilings within the *ABC* star terpolymer system focusing on aperiodic tiling for the first time. Until now, researchers did find square-triangle tilings in the *ABC* star melt [57], but the cause of its formation remains unsolved.

We arranged the classical square-triangle dodecagons given in fig. 6.5 in different ways to create periodic patches of tiling that vary in length and arrangement. The *ABC* star terpolymers are added to these tiling patterns to evaluate the free energy per chain for the arrangement in each tiling and hence determine its stable configuration. The most noticeable observation from these morphologies is the curving of squares and triangles at their stable configuration. This feature is supported by the qualitative comparison with experimental results [57]. The curving of squares and triangles is observed in all tiling patterns we have considered in this chapter, and we expect it should persist for all square-triangle arrangements. This curving is dependent on the placement of squares and triangles in the tiling. When a triangle shares a side with a square, the shared side curves into the square. When a triangle or square shares a side with another triangle or square respectively, the edges are straight. We assume the curving helps the efficient packing of the chains and curved edges contribute to lowering the total free energy per chain.

Among the tilings we have analysed, the Σ -phase is the most stable square-triangle arrangement. The Σ -phase remains the stable square-triangle configuration even with asymmetric monomer interactions in the melt. It also appears in all phase spaces. With asymmetric interactions, the area of regions of Σ -phase varies within each phase space. This observation is new to the *ABC* phase separation study. The Σ -phase is reported as stable structure in other phase spaces in the literature [27, 34, 91]. All other square-triangle arrangements are observed

to have very close free energy values to the Σ -phase. As these are large complex structures we conducted a line-based exploration in our phase spaces. From these linear phase spaces in figs. 6.17 to 6.20 for square-triangle arrangements, it is clear that placement of squares and triangles contributes towards stability of the patch. The periodic patches that contain two adjacent squares as in square (b) and square (c) have higher free energy per chain. The square (c) is a comparably simple configuration which surprisingly has the highest free energy per chain amongst all square-triangle arrangements we are considering. The important feature of this arrangement is two adjacent squares. With this information, we propose that for a square-triangle tiling in ABC star morphology to be stable it should have as few adjacent pairs of squares as possible. The minima for most of the square-triangle combinations are found in the phase spaces in regions where the triangle morphologies are most stable. The triangle morphology is favoured more by ABC star terpolymers in all our phase spaces owing to its overlaying hexagonal packing. Thus we need more triangles in the pattern to achieve the desired triangle-square ratio. It is also seen that the tilings with more triangles in them are more stable.

This chapter started with the search for stable quasicrystal structures in ABC star terpolymer melt but in fact, we find that the square-triangle morphology with the lowest free energy is the periodic Σ -phase. The experimentally reported morphology that gives twelve-fold rotational symmetry is an arrangement of squares and triangles in random order with structural defects in it [57]. The Matsushita lab used polymer melt which is a blend of ISP star terpolymer composed of polyisoprene, polystyrene, and poly(2-vinylpyridine) and homopolymer polystyrene (S) for their extensive work on ABC star terpolymer morphologies. The change of compositions to compare different morphologies is achieved by the addition of homopolymer instead of changing the branch length as we are proposing in our work. In our work, the melt considered consists only of the terpolymer and it is expected to reach a stable state without any external stimulus. In addition to the composition disparity, in the experiment, the quasicrystalline film is obtained after casting, drying and annealing at $170^\circ C$ for three days [57]. All these factors might have introduced the necessary energy perturbation we suggested for a square-triangle arrangement to achieve lower free energy than the Σ -phase.

In this chapter, we have a computational setup in which any periodic patch dodecagonal 2D tiling can be explored irrespective of the arrangement of prototiles in them and their overall size. We observe the emergence of 12 fold symmetry in the Fourier spectrum for square (b) arrangement. For an actual quasicrystal, we need a much bigger structure. So in order to continue the search in the right direction, we need a larger patch that is favoured by ABC star terpolymer. Until now, in most of the literature, the quest has been for a dodecagonal arrangement. We are posing the question of which tiling is more probable to

appear. From this chapter, we are equipped with the tools to answer that question. Our observations propose a tiling with the following conditions satisfied to be a favourable quasicrystalline candidate for ABC star terpolymers. We need a periodic patch where, (i) the triangles to square ratio $\tau = \frac{4}{\sqrt{3}}$ as reported in the literature [57, 119, 172]; (ii) there should be no adjacent squares in them; and (iii) upon minimisation it should have 12 sharp equidistant peaks. Until now, all work on dodecagonal quasicrystal tilings didn't require conditions on the alignment of prototiles in them. These restrictions are introduced by the soft matter system we are considering: ABC star terpolymers. So depending on the soft matter system and its architecture the quasicrystal tilings differ. Recently Zeng et al [170] also reported different features in their quasicrystalline tiling, which features squares, triangles and other quadrilaterals, dependent on the molecule structure [70].

While our method is capable of accommodating tilings of any size and arrangement, computation time is a major limitation. For the biggest structure, square (b), it took 18 hours to minimise the configuration for one set of monomer compositions. Increasing the tiling size or complete spanning of the phase space is not practical with the current version of the scripts written in Python. We need a custom-made minimisation routine for this problem which can take the constraint list of any size and compute the stable configuration. Rewriting the script in a faster programming language and/or implementing a more powerful minimisation scheme is proposed.

Chapter 7

Conclusion

In this thesis, we have investigated how to design block copolymer architectures so that they can phase separate into stable quasicrystal structures. In that process, we developed two methods to analyse phase separation in block copolymers at two stages of monomer segregation. In the first method, we aim to predict the lengthscales that emerge in phase-separation of a homogeneous melt of block copolymer, based on their monomer composition. We explicitly look for simultaneous occurrence of two lengthscales such that their ratios will be favourable for quasicrystals. In the second method, we analyse morphologies of ABC star terpolymers in the strongly segregated melt, in which domains of different polymer types form patterns similar to tilings. We compare the free energy of different morphologies using this technique to find the stable structure for a given monomer composition. Results obtained from both these projects provide significant insights into understanding the phase separation and stability of quasicrystals in block copolymers.

In Chapter 2 we use the *RPA* to investigate the structure factor of polymer melts. We consider two classes of block copolymer models. The first has alternating lengths of polymers of two different types, and the second has three different monomer types in a terpolymer star configuration. In both cases, while there is phase separation in a single lengthscale, we also see significant regions in the composition space where two lengthscales emerge at phase separation. The transition from one to two length scales occurs at a point (a cusp) in the parameter space when the length scale ratio is one. Beyond this cusp, the length scale ratio can be made much larger than one. In principle, the ideas and techniques developed here apply to arbitrary configurations of different types of monomers: we have explored only the simplest examples. Prior work in this area [110] took $\phi_A = \phi_B$; our work covers parameter values that would allow considerably easier synthesis of the polymers in regimes that ought to favour the formation of quasicrystals. In two component systems with alternating blocks, experimental observations

have found only relatively simple structures, such as hexagons and lamellae with several layer thicknesses [44]. To our knowledge, ours is the first presentation of phase separation with two length scales in the ABC star terpolymer system. This system is where quasicrystals and close approximants have been found experimentally [57]. As in the $A_L(BA_S)_n$ case, values of the three $N\chi$ parameters are quite large, suggesting that self-consistent field theory or strong segregation theory would be an appropriate next step.

We chose to proceed with the analysis of morphologies in the ABC star terpolymer system using strong segregation theory (SST) in which there are two contributions to the free energy, from the stretching of monomers and from the interfaces between regions of different monomers. The remarkable similarity between the phase-separated structures observed in this terpolymer melt and square-triangle tilings inspired us to use SST . In our approach, we have developed a novel methodology where we have entities called Strongly Segregated Polygons ($SSPs$), which can be tiled together to create phase separated patterns in two dimensions. An SSP is a six-sided polygon with adjustable edges, which contains one terpolymer core where three phase-separated domains meet. In our method, we pack these $SSPs$ in a periodic box such that when tiled it will form the required phase separated structure. We successfully developed the theoretical framework and computational platform using Python. Our method has the capability to accept any 2D morphology as input and provide the corresponding structure with the lowest free energy.

The software *Surface Evolver* is extensively used to minimise the surface area in tessellations and Euclidean and Non-Euclidean surfaces based on a given geometry [2, 24]. In the SSP framework we are developing a platform designed specifically for ABC terpolymers which minimises a given pattern based on its geometry as well as the chemical behaviour of the polymers in it. In chapters 3 and 4 we explained the theory and numerical tools developed to create the SSP framework.

In Chapter 5, we used the SSP method to investigate all experimentally known morphologies except lamellae observed in phase separation of ABC star terpolymers. For the purpose of this thesis, we have focused on the following morphologies: [6.6.6], [8.8.4], [12.6.4], [8.6.4; 8.6.4; 8.8.6], and [10.6.4; 10.6.4.; 10.6.6]. Our analysis involves a qualitative assessment of each morphology formed by polymer melt at the mesoscopic lengthscale scale. Notably, we have successfully generated phase spaces with these morphologies, that align with existing phase spaces in the literature. Additionally, we have extended our investigation to include phase spaces for ABC terpolymers with different interaction strengths between branches. This is a novel contribution since modifying the interaction potential is typically challenging, but it is necessary to produce results that can be experimentally reproduced. This demonstrates the potential for creating phase spaces for any desired monomer interactions. Phase spaces of ABC terpolymer

with asymmetric branch interactions show shifts in the composition regions in accordance with the interaction strengths. This is an effective methodology that has the potential to become the initial step in phase separation studies to have an idea of morphologies in the phase space. Once the phase space is made it can be checked for accuracy using *SCFT*. Even with a limited number of morphologies, we have demonstrated the potential of our framework to accommodate any complex morphology. More morphologies can be added into the phase space just by identifying their periodic patches.

We demonstrate the capability of our *SSP* framework to accommodate more complex morphologies in chapter 6. Here we seek stable square-triangle periodic approximants exploring various arrangements of square and triangle motifs to identify the most stable configuration for *ABC* star terpolymers. We examine square-triangle periodic patches of different sizes constructed using the systematic techniques explained in Chapter 4. Through this study, we gain a deeper understanding of square-triangle patterns and their influence on the structures produced by the self-assembly of *ABC* star terpolymers. Notably, we discover the tendency of squares and triangles to exhibit curved edges to attain stability. This observation is visible in experimentally reported square-triangle patches observed in *ABC* star terpolymers [57]. Additionally, our analysis reveals a prominent presence of the Σ -phase in our phase spaces. We examined six different periodic approximants of square-triangle tilings constructed by rearranging dodecagons made of squares and triangles. Interestingly, the free energy values associated with these arrangements were found to be extremely close to each other. This indicates that a slight perturbation in the appropriate direction would be sufficient to position a periodic approximant or an aperiodic arrangement of square triangle tiling in the *ABC* terpolymer phase space.

When investigating the phase separation of *ABC* star terpolymers, a crucial question arises: What is the optimal square-triangle arrangement for achieving a quasicrystalline structure? Our research has provided evidence that simply relying on an aperiodic arrangement is insufficient to ensure the stability of the structure containing *ABC* terpolymers. Therefore, finding the right square-triangle arrangement becomes a critical consideration in the quest for a stable quasicrystalline phase.

Our *SSP* platform offers a reliable, efficient and fast tool for studying and analysing the stability of morphologies compared to existing morphological analysis. In comparison to the computational and mathematical intake that is required to build phase spaces using other methodologies (*SCFT*, *DPD* and Monte Carlo), ours uses straight forward mathematics and significantly less computational time even using Python. This framework demonstrates remarkable computational potential, enabling us to perform these intensive calculations on large

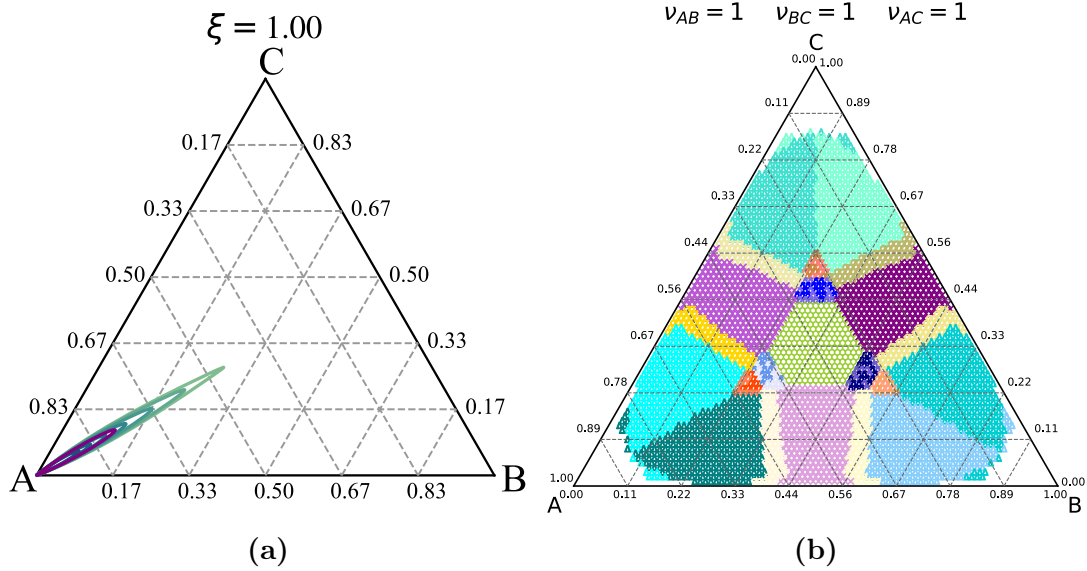


Figure 7.1: The phase spaces obtained for ABC star terpolymer with symmetric interactions between its branches at (a) weakly segregated limit and (b) strongly segregated limit.

periodic patches like a square (b) with manageable effort. Given enough computational resources, our methodology is capable of analysing square-triangle periodic approximant of any large size and arrangement and with any combination of interaction strengths between the ABC terpolymer branches.

In Chapter 2 we predict block copolymer architectures that can induce self-assembly of domains in multiple lengthscales simultaneously at the point of phase separation. The rest of the thesis treats the stability of strongly segregated structures. In both cases, we have composition spaces for ABC star terpolymers that indicate the regions where complex morphologies could be found. The composition spaces for terpolymer with symmetric interactions between the branches for weakly and strongly segregated melt are figs. 2.24 and 6.3 respectively which are presented again in fig. 7.1. In our SST phase space, complex morphologies are expected to be observed around the vicinity of Σ -phase in fig. 7.1.(b) closer to the centre of the composition triangle. In contrast in the composition space of the weakly segregated melt the two lengthscales that would favour a dodecagonal phase are found closer to the corners in fig. 7.1.(a). There are regions closer to the centre of the tip of the curves in fig. 7.1.(a) coincide with the Σ -phase region in fig. 7.1.(b). As we are analysing phase separation at two stages of segregation, there is an evident disparity in these phase spaces. We have not covered what happens between these two stages in this thesis. This could be done using *SCFT* [91] or *DPD*[27].

7. Conclusion

A preliminary investigation of polymer self assembly was done using Kirkensgaard et al's [81] script to simulate phase separation in an ABC star terpolymer melt. This approach uses molecular dynamics based on Dissipative Particle Dynamics (DPD) [52]. In this framework, a coarse-grained polymer chain is considered as a chain of beads, as shown in fig. 7.2.(a). Here each bead represents the aggregated section of the polymer chain on a lengthscale similar to the Kuhn length in our methodology. The simulation is conducted using the extensive molecular dynamics library HOOMD [6, 123], which facilitates large scale geometrical and MD simulations. Here, the ABC star terpolymer is designed as three chains of beads attached to a common bead (white), which is equivalent to the core illustrated in fig. 7.2.(a). The total number of beads including the core is fixed. Here it is 21. We can choose the number of beads to agree with the necessary monomer composition. Here we choose $(n_A, n_B, n_C) = (9, 6, 5)$ which roughly corresponds to $(\phi_A, \phi_B, \phi_C) = (0.4285, 0.2857, 0.2380)$. In our phase space, this point is close to the Σ -phase region. The presence of core particles makes the composition conversion not accurate. The box size (height, length, width) = $(20, 20, 3)$ is chosen in accordance with the scaling in [81]. A thin periodic box is chosen to enable 2D phase separation to give tilings. The initial state before the simulation is given in fig. 7.2.(b), which is a random arrangement of the ABC terpolymer molecules. There are 14385 beads in 685 molecules in this box. The simulation resulted in the arrangement in fig. 7.2.(c), where domains are well defined.

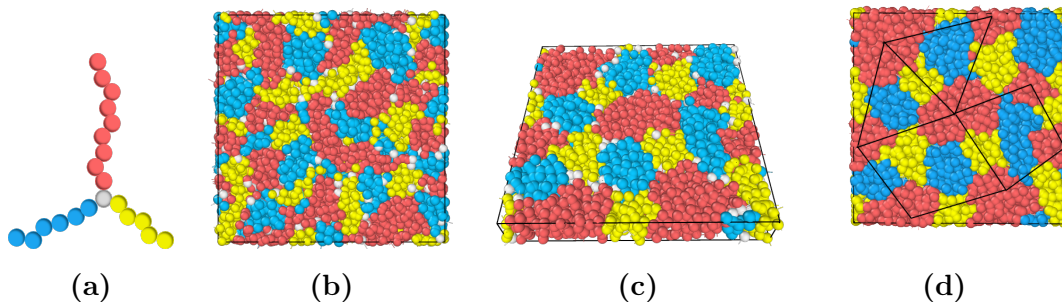


Figure 7.2: Results of DPD simulation are summarised. We consider a polymer molecule assuming it is beads in a chain as given in (a). In (b) the initial state of the simulation is given where the chains are randomly assembled. The final stage is given in (c) and (d) which has well-defined domains of red, blue and yellow beads with core beads popping up in the interfacial junctions. We attempt to detect the underlying morphology by joining red domains with straight lines in (d).

In the final state of the simulation, there are core beads lining along the

junction where three domains align as expected for ABC terpolymer phase separation. The morphology is not evident in fig. 7.2.(c) from the chosen box size. So we tried to overlay the obtained pattern with straight lines to recognise the morphology. The domain size for each monomer type varies within the box. We choose straight lines such that they join two red domains and pass through or close to a yellow domain. This results in the image given in fig. 7.2.(d), where there are two quadrilaterals (similar to squares) and two triangles. It is clear that the simulation requires a larger box size to identify the morphology which is time-consuming: one set of monomer composition took approximately 45 minutes to simulate even without any attempt to optimise the domain size. This indicates that it will require a lot of time to create phase diagrams similar to the ones we have created in this thesis.

Through this thesis, we address the question of which parameters will encourage self-assembly of block copolymers in complex and interesting morphologies. From our work, we provide experimentally feasible sets of parameters that can produce complex and quasicrystalline structures along with a simple framework to analyse these morphology. The two projects together provide a jump start for structural analysis when looking for complex morphologies like quasicrystals and bicontinuous structures.

7.1 Future research proposed

This thesis is a part of a long-term investigation into designing stable quasicrystals in soft matter. We have applied known stability criteria to a practical system like block copolymers, where phase separation is an important self-driven phenomenon. We have presented experimentally feasible results thorough our work, which can be proceeded in different directions, of which a few are mentioned here.

Our results in Chapter 2 provide the initial screening of monomer compositions. One could study further the stability of different morphologies in a weakly segregated melt by considering the third and fourth terms of the free energy [87]. Stability analysis of different morphologies can be done using weak segregation theory in the same way we have done with Strong Segregation Theory in chapters 3-6. Work has been conducted to study the stability of morphologies in this segregation limit for alternating AB blocks [108, 110]. We have found a window of parameters in which complex morphologies will be encouraged. This provides a good starting point for a full stability analysis in this limit. Morphological analysis for block copolymers with three components has been conducted in the weak segregation limit, but only for fairly simple morphologies [43] and with symmetric compositions. A similar analysis is possible for our terpolymer. Hence the phase space for ABC star terpolymers in the weak segregation limit can be created.

Quasicrystals are reported in block copolymers with two components [86, 90, 93]. The majority of investigations into phase separation in two component systems in search of quasicrystals have been conducted on blends containing diblock melts or branched block copolymers. In these cases diblock will assemble as micelles which then assemble into interesting crystallographic motifs. There is very limited analysis on the alternating AB block copolymer model we consider. Thus we cannot predict real space structures for these models yet. They may form micelles for certain monomer compositions or they can form some other microphase separated structure due to the incompatibility introduced by alternating blocks of different lengths. Self assembly of these alternating block copolymer models can be studied by using the $SCFT$ formulation or molecular dynamics. This is a straightforward direction to proceed with the monodisperse models $A_L(BA_S)_n$ and ABC star terpolymer in chapter 2. Our polydisperse model offers practical parameters that should be comparatively easy to manufacture in the laboratory.

We have presented the beginning of a phase space for ABC terpolymer in a strong segregation limit. Although we have presented all the experimentally observed morphologies for ABC star terpolymers there are many other combinations of domain tilings we have yet to explore. Between different phase spaces present in literature, there is a disparity between the presence of multi-core morphologies [75, 81, 91, 102]. Most of the structures reported here and in the literature can be formed in a melt containing a blend of A , B and C polymer chains in different proportions. It can be a pure ABC star terpolymer blend as we have considered in our work, a blend of the terpolymer and homopolymer of one component or blend of terpolymer and triblock. In their work, Kirkensgaard et al. [81] proposes the Spoke method to identify all topological arrangements of A , B and C domains where they are connected by a core. It is advisable to check all existing 2D morphologies reported in ABC star phase separation to build the complete phase space. This phase space will only show those structures that will be formed in a homogeneous blend of ABC star terpolymers.

In order to include all possible 2D tiling morphologies, structural limitations present in Strongly Segregated Polygons (SSP) need to be addressed. The current version of the SSP method uses hexagons which is unable to accommodate any morphology with lamellae in it. This can be solved by increasing the number of nodes in the polygon. To attain flexibility at the interfaces, the number of nodes can be increased to the extent of finite element methods, such that the edges of SSP polygons can form curves. We have reported curving of interfaces in our square-triangle arrangements even without limited edge flexibility. Further other 3D morphologies like lamellar+sphere, gyroids, etc can be considered if we consider packing of modified Kelvin cell or truncated octahedron [28] filled with monomer volumes. In the 3D equivalent of SSP , the cores can be considered as a curve.

One urgent development required for this work is improving the efficiency of the script. This efficiency is necessary for both scripting and implementing a better minimisation scheme. Stimulated annealing is a candidate method for minimisation. It will be beneficial to convert the script into a high-level programming language for improved performance.

The quest for stable quasicrystals in *ABC* star terpolymer is continuing. From our work, it is conclusive that stability of the morphology is dependent on the arrangement of squares and triangles in the tilings. We have a candidate periodic approximant, which satisfies the absence of two adjacent square conditions, triangle (d). This has two different Stampfli triangles in it. Once the script is efficient this is an interesting arrangement to study. Alternatively, periodic patches can be made by the random arrangement of square-triangle tiling using the random tiling method proposed by Imperor et al. [71] The quasicrystal patch discovered by Hayashida et al [57], consists of random arrangement of squares and triangles with structural defects. Hence random tiling of squares and triangles can be another potential candidate motif to look at.

Recently it has been discovered that soft matter quasicrystals can also form tilings from three tiles: squares, equilateral triangles and thin rhombuses [70, 170]. These aperiodic tiling arrangements prove to have fewer defects in a columnar liquid crystal system compared to the square-triangle tilings. It would be intriguing to investigate other dodecagonal aperiodic tilings with more than two prototiles, the third tile being a rhombus or a shield purely for the sake of exploration and expanding our understanding of these systems [170].

There is an evident connection between phase separation at weak and strong segregation regimes, but there are gaps in our understanding that need to be addressed. A detailed study of the lengthscales emerging in the strongly segregated regime is required. We started the Fourier analysis to identify the overall lengthscales and rotational symmetry of the structure. This needs more exploration to fill in the gaps between phase separation at weakly segregated and strongly segregated stages.

Appendix A

A.1 Calculation of internal energy in polymer melt of one component

Here is the detailed derivation for internal energy for one component polymer melt in Fourier space given in eq. (2.22). Consider the internal energy between two monomer units at positions in chain α and α' be \mathbf{r}_l^α and $\mathbf{r}_{l'}^{\alpha'}$,

$$\frac{U}{k_B T} = \frac{1}{2} \sum_{\substack{\alpha, l \\ \alpha', l'}} V(\mathbf{r}_l^\alpha - \mathbf{r}_{l'}^{\alpha'}) \quad (\text{A.1})$$

Now multiplying the above term with delta functions at \mathbf{r}_l^α and $\mathbf{r}_{l'}^{\alpha'}$, we get:

$$\frac{U\{\rho\}}{k_B T} = \frac{1}{2} \sum_{\substack{\alpha, l \\ \alpha', l'}} \int d^3 \mathbf{r}_l^\alpha \delta(\mathbf{r} - \mathbf{r}_l^\alpha) \int d^3 \mathbf{r}_{l'}^{\alpha'} \delta(\mathbf{r} - \mathbf{r}_{l'}^{\alpha'}) V(\mathbf{r}_l^\alpha - \mathbf{r}_{l'}^{\alpha'}) \quad (\text{A.2})$$

In terms of monomer density at these positions,

$$\frac{U\{\rho\}}{k_B T} = \frac{1}{2} \int d^3 \mathbf{r}_l^\alpha \rho(\mathbf{r}_l^\alpha) \int d^3 \mathbf{r}_{l'}^{\alpha'} \rho(\mathbf{r}_{l'}^{\alpha'}) V(\mathbf{r}_l^\alpha - \mathbf{r}_{l'}^{\alpha'}) \quad (\text{A.3})$$

Now taking the Fourier transform of the above expression for wave vector \mathbf{q} ,

$$\begin{aligned} \frac{U_{\mathbf{q}}}{k_B T} &= \frac{1}{2} \int d^3 \mathbf{r}_l^\alpha \rho(\mathbf{r}_l^\alpha) \int d^3 \mathbf{r}_{l'}^{\alpha'} \frac{1}{\Omega} \rho_{\mathbf{q}} e^{-i\mathbf{q} \cdot \mathbf{r}_{l'}^{\alpha'}} \frac{1}{\Omega} V_{\mathbf{q}} e^{-i\mathbf{q} \cdot (\mathbf{r}_l^\alpha - \mathbf{r}_{l'}^{\alpha'})} \\ &= \frac{1}{2\Omega^2} \int d^3 \mathbf{r}_l^\alpha \rho(\mathbf{r}_l^\alpha) \int d^3 \mathbf{r}_{l'}^{\alpha'} \rho_{\mathbf{q}} e^{-i\mathbf{q} \cdot \mathbf{r}_{l'}^{\alpha'}} V_{\mathbf{q}} e^{-i\mathbf{q} \cdot (\mathbf{r}_l^\alpha - \mathbf{r}_{l'}^{\alpha'})} \end{aligned} \quad (\text{A.4})$$

Rewriting the integral as summation over \mathbf{q}' ,

$$\frac{U_{\mathbf{q}}}{k_B T} = \frac{1}{2\Omega^2} \int d^3 \mathbf{r}_l^\alpha \rho(\mathbf{r}_l^\alpha) \sum_{\mathbf{q}'} \Omega \delta(\mathbf{q} - \mathbf{q}') \rho_{\mathbf{q}'} e^{-i\mathbf{q} \cdot \mathbf{r}_l^\alpha} V_{\mathbf{q}'} \quad (\text{A.5})$$

A.

When $\mathbf{q} = \mathbf{q}'$, the delta function will be 1. Along with it $\int d^3\mathbf{r}_i^\alpha \rho(\mathbf{r}_i^\alpha) e^{-i\mathbf{q}\cdot\mathbf{r}_i^\alpha} = \rho_{-\mathbf{q}}$. So in Fourier space, the internal free energy becomes:

$$\frac{U_{\mathbf{q}}}{k_B T} = \frac{1}{2\Omega} \sum_{\mathbf{q}} \rho_{\mathbf{q}} \rho_{-\mathbf{q}} V_{\mathbf{q}} \quad (\text{A.6})$$

A.2 Calculation of $\widetilde{W}_{\mathbf{q}}$

Here we describe the calculation of $\widetilde{W}_{\mathbf{q}}$ in (2.69).

Partition function Z for a three component system in (2.66) is in a three-by-three matrix. After imposing incompressibility this three-by-three matrix is reduced to a two by two matrix. The monomer density distribution for the three component system is

$$\psi_0(\{\rho_q^A, \rho_q^B, \rho_q^C\}) = \exp \left(-\frac{1}{2} \sum_{\mathbf{q}} \begin{bmatrix} \rho_q^A & \rho_q^B & \rho_q^C \end{bmatrix} S_{\mathbf{q}}^{-1} \begin{bmatrix} \rho_{-\mathbf{q}}^A \\ \rho_{-\mathbf{q}}^B \\ \rho_{-\mathbf{q}}^C \end{bmatrix} \right), \quad (\text{A.7})$$

where $S_{\mathbf{q}}^{-1}$ is the inverse of the structure factor matrix,

$$S_{\mathbf{q}}^{-1} = \frac{1}{\Omega \rho N} \begin{bmatrix} \Gamma^{AA} & \Gamma^{AB} & \Gamma^{AC} \\ \Gamma^{AB} & \Gamma^{BB} & \Gamma^{BC} \\ \Gamma^{AC} & \Gamma^{BC} & \Gamma^{CC} \end{bmatrix}. \quad (\text{A.8})$$

On applying incompressibility condition,

$$\rho_q^C = -(\rho_q^A + \rho_q^B), \quad (\text{A.9})$$

to the expression for the distribution function, the matrices inside the exponential are rewritten as

$$\begin{bmatrix} \rho_q^A & \rho_q^B & -(\rho_q^A + \rho_q^B) \end{bmatrix} \begin{bmatrix} \Gamma^{AA} & \Gamma^{AB} & \Gamma^{AC} \\ \Gamma^{AB} & \Gamma^{BB} & \Gamma^{BC} \\ \Gamma^{AC} & \Gamma^{BC} & \Gamma^{CC} \end{bmatrix} \begin{bmatrix} \rho_{-\mathbf{q}}^A \\ \rho_{-\mathbf{q}}^B \\ -(\rho_{-\mathbf{q}}^A + \rho_{-\mathbf{q}}^B) \end{bmatrix}. \quad (\text{A.10})$$

A.

Using matrix multiplication the expression is expanded and later re-written in terms of ρ_q^A and ρ_q^B . The worked-out expansion is given below:

$$\begin{aligned}
& \begin{bmatrix} \rho_q^A & \rho_q^B & -(\rho_q^A + \rho_q^B) \end{bmatrix} \begin{bmatrix} \Gamma^{AA} & \Gamma^{AB} & \Gamma^{AC} \\ \Gamma^{AB} & \Gamma^{BB} & \Gamma^{BC} \\ \Gamma^{AC} & \Gamma^{BC} & \Gamma^{CC} \end{bmatrix} \begin{bmatrix} \rho_{-q}^A \\ \rho_{-q}^B \\ -(\rho_q^A + \rho_q^B) \end{bmatrix} = \\
& \rho_q^A \Gamma^{AA} \rho_{-q}^A + \rho_q^B \Gamma^{AB} \rho_{-q}^A - \rho_q^A \Gamma^{AC} \rho_{-q}^A - \rho_q^B \Gamma^{AC} \rho_{-q}^A + \\
& \rho_q^A \Gamma^{AB} \rho_{-q}^B + \rho_q^B \Gamma^{BB} \rho_{-q}^B - \rho_q^A \Gamma^{BC} \rho_{-q}^B - \rho_q^B \Gamma^{BC} \rho_{-q}^B - \\
& \rho_q^A \Gamma^{AC} \rho_{-q}^A - \rho_q^A \Gamma^{AC} \rho_{-q}^B - \rho_q^B \Gamma^{BC} \rho_{-q}^A - \rho_q^B \Gamma^{BC} \rho_{-q}^B + \\
& \rho_q^A \Gamma^{CC} \rho_{-q}^A + \rho_q^A \Gamma^{CC} \rho_{-q}^B + \rho_q^B \Gamma^{CC} \rho_{-q}^A + \rho_q^B \Gamma^{CC} \rho_{-q}^B \\
& = \rho_q^A (\Gamma^{AA} - 2\Gamma^{AC} + \Gamma^{CC}) \rho_{-q}^A + \rho_q^B (\Gamma^{AB} - \Gamma^{AC} - \Gamma^{BC} + \Gamma^{CC}) \rho_{-q}^A + \\
& \rho_q^A (\Gamma^{AB} - \Gamma^{BC} - \Gamma^{AC} + \Gamma^{CC}) \rho_{-q}^B + \rho_q^B (\Gamma^{BB} - 2\Gamma^{BC} + \Gamma^{CC}) \rho_{-q}^B \\
& = \begin{bmatrix} \rho_q^A & \rho_q^B \end{bmatrix} \begin{bmatrix} \Gamma^{AA} - 2\Gamma^{AC} + \Gamma^{CC} & \Gamma^{AB} - \Gamma^{AC} - \Gamma^{BC} + \Gamma^{CC} \\ \Gamma^{AB} - \Gamma^{AC} - \Gamma^{BC} + \Gamma^{CC} & \Gamma^{BB} - 2\Gamma^{BC} + \Gamma^{CC} \end{bmatrix} \begin{bmatrix} \rho_{-q}^A \\ \rho_{-q}^B \end{bmatrix}. \tag{A.11}
\end{aligned}$$

Thus ψ_0 in terms of ρ_q^A and ρ_q^B is,

$$\begin{aligned}
\psi_0 = \exp \left(-\frac{1}{2\Omega\rho N} \sum_q \begin{bmatrix} \rho_q^A & \rho_q^B \end{bmatrix} \times \right. \\
\left. \begin{bmatrix} \Gamma^{AA} - 2\Gamma^{AC} + \Gamma^{CC} & \Gamma^{AB} - \Gamma^{AC} - \Gamma^{BC} + \Gamma^{CC} \\ \Gamma^{AB} - \Gamma^{AC} - \Gamma^{BC} + \Gamma^{CC} & \Gamma^{BB} - 2\Gamma^{BC} + \Gamma^{CC} \end{bmatrix} \times \right. \\
\left. \begin{bmatrix} \rho_{-q}^A \\ \rho_{-q}^B \end{bmatrix} \right). \tag{A.12}
\end{aligned}$$

A.

Similarly, the internal energy matrix can also be reduced to a 2×2 matrix. The internal energy for a three component system is written as,

$$\frac{U(\{\rho_q^A, \rho_q^B, \rho_q^C\})}{k_B T} = \frac{1}{2\Omega} \sum_q \begin{bmatrix} \rho_q^A & \rho_q^B & \rho_q^C \end{bmatrix} \begin{bmatrix} V_{AA} & V_{AB} & V_{AC} \\ V_{AB} & V_{BB} & V_{BC} \\ V_{AC} & V_{BC} & V_{CC} \end{bmatrix} \begin{bmatrix} \rho_{-q}^A \\ \rho_{-q}^B \\ \rho_{-q}^C \end{bmatrix}. \quad (\text{A.13})$$

On applying the same simplification as above we get

$$\begin{bmatrix} \rho_q^A & \rho_q^B & -(\rho_q^A + \rho_q^B) \end{bmatrix} \begin{bmatrix} V_{AA} & V_{AB} & V_{AC} \\ V_{AB} & V_{BB} & V_{BC} \\ V_{AC} & V_{BC} & V_{CC} \end{bmatrix} \begin{bmatrix} \rho_{-q}^A \\ \rho_{-q}^B \\ -(\rho_q^A + \rho_q^B) \end{bmatrix} = \quad (\text{A.14})$$

$$\begin{bmatrix} \rho_q^A & \rho_q^B \end{bmatrix} \begin{bmatrix} V_{AA} - 2V_{AC} + V_{CC} & V_{AB} - V_{AC} - V_{BC} + V_{CC} \\ V_{AB} - V_{AC} - V_{BC} + V_{CC} & V_{BB} - 2V_{BC} + V_{CC} \end{bmatrix} \begin{bmatrix} \rho_{-q}^A \\ \rho_{-q}^B \end{bmatrix}$$

But Flory's interaction parameters, χ_{AB} , χ_{BC} , χ_{AC} is introduced to the matrix from its definition (2.65) as

$$\begin{aligned} V_{AA} - 2V_{AC} + V_{CC} &= -\frac{2\chi_{AC}}{\rho}, \\ V_{BB} - 2V_{BC} + V_{CC} &= -\frac{2\chi_{BC}}{\rho}, \\ \frac{2\chi_{AB}}{\rho} - \frac{2\chi_{AC}}{\rho} - \frac{2\chi_{BC}}{\rho} &= -V_{AA} - V_{BB} + 2V_{AB} + V_{AA} + \\ &V_{CC} - 2V_{AC} + V_{BB} + V_{CC} - 2V_{BC}, \\ \implies \frac{\chi_{AB} - \chi_{AC} - \chi_{BC}}{\rho} &= V_{AB} - V_{AC} - V_{BC} + V_{CC}. \end{aligned} \quad (\text{A.15})$$

So the internal energy will become,

$$\frac{U(\{\rho_q^A, \rho_q^B, \rho_q^C\})}{k_B T} = \frac{1}{2\Omega\rho} \begin{bmatrix} \rho_q^A & \rho_q^B \end{bmatrix} \begin{bmatrix} -2\chi_{AC} & \chi_{AB} - \chi_{BC} - \chi_{AC} \\ \chi_{AB} - \chi_{BC} - \chi_{AC} & -2\chi_{BC} \end{bmatrix} \begin{bmatrix} \rho_{-q}^A \\ \rho_{-q}^B \end{bmatrix}. \quad (\text{A.16})$$

A.

Combining all these the partition function Z is rewritten as

$$\begin{aligned}
Z = & \int D\rho_q^A D\rho_q^B \exp \left(-\frac{1}{2} \sum_q \begin{bmatrix} \rho_q^A & \rho_q^B \end{bmatrix} \right. \\
& \left(\frac{1}{\Omega\rho N} \begin{bmatrix} \Gamma^{AA} - 2\Gamma^{AC} + \Gamma^{CC} & \Gamma^{AB} - \Gamma^{AC} - \Gamma^{BC} + \Gamma^{CC} \\ \Gamma^{AB} - \Gamma^{AC} - \Gamma^{BC} + \Gamma^{CC} & \Gamma^{BB} - 2\Gamma^{BC} + \Gamma^{CC} \end{bmatrix} + \right. \\
& \left. \frac{1}{\Omega\rho} \begin{bmatrix} -2\chi_{AC} & \chi_{AB} - \chi_{BC} - \chi_{AC} \\ \chi_{AB} - \chi_{BC} - \chi_{AC} & -2\chi_{BC} \end{bmatrix} \right) \begin{bmatrix} \rho_{-q}^A \\ \rho_{-q}^B \end{bmatrix} \Bigg). \quad (\text{A.17})
\end{aligned}$$

Here W_q is defined as,

$$\begin{aligned}
W_q = & \frac{1}{\Omega\rho N} \left(\begin{bmatrix} \Gamma^{AA} - 2\Gamma^{AC} + \Gamma^{CC} & \Gamma^{AB} - \Gamma^{AC} - \Gamma^{BC} + \Gamma^{CC} \\ \Gamma^{AB} - \Gamma^{AC} - \Gamma^{BC} + \Gamma^{CC} & \Gamma^{BB} - 2\Gamma^{BC} + \Gamma^{CC} \end{bmatrix} + \right. \\
& \left. N \begin{bmatrix} -2\chi_{AC} & \chi_{AB} - \chi_{BC} - \chi_{AC} \\ \chi_{AB} - \chi_{BC} - \chi_{AC} & -2\chi_{BC} \end{bmatrix} \right). \quad (\text{A.18})
\end{aligned}$$

Now we define $\widetilde{W}_q = N\Omega\rho W_q$ and find the eigenvalues of \widetilde{W}_q as explained in section 2.1.3.

$$Z = \int D\rho_q^A D\rho_q^B \exp \left(-\frac{1}{2} \sum_q \begin{bmatrix} \rho_{-q}^A & \rho_{-q}^B \end{bmatrix} \widetilde{W}_q \begin{bmatrix} \rho_q^A \\ \rho_q^B \end{bmatrix} \right) \quad (\text{A.19})$$

A.

Appendix B

B.1 Stretching free energy for a wedge

Now stretching energy due to this wedge is to be determined. As the number of chains per cross sectional area σ changes according to the height, the stretching energy due to A type monomers in the wedge is

$$f_{stretch_A} = \int_0^{N_A} \frac{3\pi^2 h^2(\sigma_A)}{8N_A b_A^2} dn. \quad (\text{B.1})$$

Here $h(\sigma_A)$ gives the height of cross section where chain per area is $\sigma_A = \frac{N_A}{a(\beta)}$. This concerns the red region in fig 3.5. Similarly for B part the stretching energy is

$$f_{stretch_B} = \int_0^{N_B} \frac{3\pi^2 h^2(\sigma_B)}{8N_B b_B^2} dn. \quad (\text{B.2})$$

Since the height is dependent on the chains per unit area the expression is rewritten in terms of the monomer compositions. Given that there are N_A monomer units in the wedge of type A , the total volume occupied by A type monomers, V_A is defined in terms of the height of the interface as

$$V_A = N_A \Omega_A = v(z_w) - v(z_w - h_A) \quad (\text{B.3})$$

where Ω_A is the volume of a single A type monomer unit and h_A is the height of A section in the wedge. If total volume of contents in the wedge is Ω , then monomer fraction for type A , $\phi_A = \frac{\Omega_A}{\Omega}$ and monomer fraction for type B , $\phi_B = \frac{\Omega_B}{\Omega}$. Rewriting the above expression in terms of σ_A and β as in [117],

$$\frac{\sigma_A a(\beta) \phi_A \Omega}{R_w} = v(\beta) - v\left(\beta - \frac{h_A}{R_w}\right). \quad (\text{B.4})$$

B.

Similarly for B part of the wedge relation between chains per cross section and height is

$$\frac{\sigma_B a(\beta) \phi_B \Omega}{R_w} = v(\beta) - v\left(\beta + \frac{h_B}{R_w}\right). \quad (\text{B.5})$$

Thus the variation in the monomer density with cross section is accounted in terms of the chain height. The change in height is reflected as the change in chains per unit area. In terms of the chains per unit area the number of monomer units for A and B will be $N_A = \sigma_A a(z_w)$ and $N_B = \sigma_B a(z_w)$. Also if the total number of chains in the wedge is n_w , then $n_w = \sigma_w a(z_w)$, where σ is the chains per cross section at the interface. If the change in the monomers with height is dn_A and dn_B for A and B respectively, then

$$dn_A = d\sigma_A a(z_w) \quad (\text{B.6})$$

$$dn_B = d\sigma_B a(z_w).$$

With this the expression for stretching free energy for A type monomers and B type monomers will be

$$\begin{aligned} f_{stretch_A} &= \int_0^{\sigma_w} \frac{3\pi^2 h^2(\sigma_A)}{8R_A^2} a(z_w) d\sigma_A \\ f_{stretch_B} &= \int_0^{\sigma_w} \frac{3\pi^2 h^2(\sigma_B)}{8R_B^2} a(z_w) d\sigma_B. \end{aligned} \quad (\text{B.7})$$

The stretching free energy per chain contribution by A and B type monomers are

$$\begin{aligned} f_{stretch_A} &= \frac{1}{n_w} \int_0^{\sigma_w} \frac{3\pi^2 h^2(\sigma_A)}{8R_A^2} a(z_w) d\sigma_A \\ &= \frac{1}{\sigma_w} \int_0^{\sigma_w} \frac{3\pi^2 h^2(\sigma_A)}{8R_A^2} d\sigma_A \\ f_{stretch_B} &= \frac{1}{\sigma_w} \int_0^{\sigma_w} \frac{3\pi^2 h^2(\sigma_B)}{8R_B^2} d\sigma_B. \end{aligned} \quad (\text{B.8})$$

Following the expressions for chains per cross sectional area in eq. (B.4) and eq. (B.5) the change in cross sectional areas are

$$d\sigma_A = \frac{a(\beta - \frac{h_A}{R_w})}{\Omega \phi_A a(\beta)} dh_A \quad (\text{B.9})$$

$$d\sigma_B = \frac{a(\beta + \frac{h_B}{R_w})}{\Omega \phi_B a(\beta)} dh_B. \quad (\text{B.10})$$

B.

Substituting $d\sigma$ to the expressions for stretching energy we get

$$\begin{aligned} f_{stretch_A} &= \frac{3\pi^2}{8\sigma_w\Omega a(\beta)} \int_0^{z_w} \frac{h_A^2}{R_A^2} \frac{a(\beta - \frac{h_A}{R_w})}{\phi_A} dh_A \\ f_{stretch_B} &= \frac{3\pi^2}{8\sigma_w\Omega a(\beta)} \int_0^{z_w} \frac{h_B^2}{R_B^2} \frac{a(\beta + \frac{h_B}{R_w})}{\phi_B} dh_B. \end{aligned} \quad (\text{B.11})$$

In order to simplify the integrals we substitute $\frac{h_m}{R_w} = y$ for monomer type m in the above equation. Then the expressions will become

$$\begin{aligned} f_{stretch_A} &= \frac{3\pi^2 R_w^3}{8\sigma_w\Omega a(\beta)} \int_0^\beta \frac{y^2}{R_A^2} \frac{a(\beta - y)}{\phi_A} dy \\ f_{stretch_B} &= \frac{3\pi^2 R_w^3}{8\sigma_w\Omega a(\beta)} \int_0^\beta \frac{y^2}{R_B^2} \frac{a(\beta + y)}{\phi_B} dy. \end{aligned} \quad (\text{B.12})$$

In the above expression $a(\beta) = \frac{a(z_w)}{a(R_w)}$. This will allow us to define the volume of the wedge as $v(R_w) = R_w A(R_w)$. Also from [117] $v(\beta) = v(1)\phi_A$. Taking the stretching free energy for A type monomers

$$\begin{aligned} f_{stretch_A} &= \frac{3\pi^2 R_w^3 a(R_w)}{8\sigma_w\Omega a(z_w)} \int_0^\beta \frac{y^2}{R_A^2} \frac{a(\beta - y)}{\phi_A} dy, \\ &= \frac{3\pi^2 R_w^2 v(R_w)}{8n_w\Omega} \int_0^\beta \frac{y^2}{R_A^2} \frac{a(\beta - y)}{\phi_A} dy, \\ &= \frac{3\pi^2 R_w^2}{8v(1)} \int_0^\beta \frac{y^2}{R_A^2} \frac{a(\beta - y)}{\phi_A} dy. \end{aligned} \quad (\text{B.13})$$

For the B type region in the wedge, the contribution to stretching free energy per chain will be

$$f_{stretch_B} = \frac{3\pi^2 R_w^2}{8v(1)} \int_0^{1-\beta} \frac{y^2}{R_B^2} \frac{a(\beta + y)}{\phi_B} dy. \quad (\text{B.14})$$

B.2 Input file structure

Here is the template for the input.txt file for Σ -phase. All details regarding the polymer composition and geometry saved here. This can be uploaded to create the constraint list for monomer composition given in the '.txt' file. The file contains the monomer compositions of ϕ_A and ϕ_B indicated by '#Phi values'. The interaction strengths ($\nu_{AB}, \nu_{BC}, \nu_{AC}$) between A and B , B and C and A and C is given in th line below '#Chi values'. The core to step length ratio R_d is chosen to be 10. The periodicites v_{xx}, v_{xy} and v_{yy} are given the lines after '#Periodicity from constraint list'. The number of vertices and the x and y coordinates of the vertices are also listed. The identifiers for the free nodes are listed after '#Free nodes'. The periodic nodes are listed after '#Periodic nodes'. The four entries in each line are identifiers of the free node, the node at the given periodicity and indices of the patch (l, m). The nodes associated with the SSP s are also listed in the order of nodes. This file will make a valid SSP patch for Σ -phase.

B.

```
#Phi values
0.5757514382719816 0.38133001897103386
#Chi values
1.0 1.0 1.0
Rd 10.0
#Periodicity from constraint list
3.338768699431094
-6.177059853472972e-06
3.3387693982284024
#Number of vertices:
97
#Initial values of vertices with its id:
0 0.0 0.0
1 1.6693820653694853 0.48918419600230045
2 0.48918720037217683 1.669384353090657
.
.
.
95 2.8149180332422956 2.6824140792798885
96 3.633722800009016 2.5034044235461215
#Number of free nodes:
79
#Free nodes:
2
4
15
16
.
.
.
94
95
96
#Number of periodic nodes:
17
#Periodic nodes:
0 5 0.0 1.0
0 6 1.0 0.0
.
.
.
43 34 0.0 -1.0
44 35 0.0 -1.0
#SSP arrangement
#Number of polygons:
40
52 51 57 16 17 0
52 51 55 10 9 0
.
.
.
93 90 95 46 45 8
93 90 96 49 48 8
```

B.

References

- [1] <https://www.rubi.com/us/blog/penrose-tiling/>. 2
- [2] Surface Evolver. <http://facstaff.susqu.edu/brakke/evolver/evolver.html>. 19, 228
- [3] NIST and the Nobel: Dan Shechtman. <https://www.nist.gov/nist-and-nobel/dan-shechtman>, 9 2016. 2
- [4] C. V. Achim, M. Schmiedeberg, and H. Löwen. Growth modes of quasicrystals. *Phys. Rev. Lett.*, 112:255501, Jun 2014. 7
- [5] K. Aissou, H. K. Choi, A. Nunns, I. Manners, and C. A. Ross. Ordered nanoscale archimedean tilings of a templated 3-miktoarm star terpolymer. *Nano Letters*, 13(2):835–839, 2 2013. 17
- [6] J. A. Anderson, J. Glaser, and S. C. Glotzer. HOOMD-blue: A Python package for high-performance molecular dynamics and hard particle Monte Carlo simulations. *Computational Materials Science*, 173, 2020. 231
- [7] A. J. Archer, T. Dotera, and A. M. Rucklidge. Rectangle-triangle soft-matter quasicrystals with hexagonal symmetry. *Physical Review E*, 106(4):044602, 10 2022. 134
- [8] A. J. Archer, A. M. Rucklidge, and E. Knobloch. Quasicrystalline order and a crystal-liquid state in a soft-core fluid. *Physical Review Letters*, 111(16):1–5, 2013. 7
- [9] A. J. Archer, A. M. Rucklidge, and E. Knobloch. Soft-core particles freezing to form a quasicrystal and a crystal-liquid phase. *Physical Review E*, 92(1):012324, 7 2015. 7
- [10] S. Ariaee, B. Jakobsen, P. Norby, D.-M. Smilgies, K. Almdal, and D. Poselt. Thin film and bulk morphology of pi-ps-pmma miktoarm star terpolymers with both weakly and strongly segregated arm pairs. *Polymer*, 283:126202, 2023. 17

REFERENCES

- [11] A. Arora, J. Qin, D. C. Morse, K. T. Delaney, G. H. Fredrickson, F. S. Bates, and K. D. Dorfman. Broadly Accessible Self-Consistent Field Theory for Block Polymer Materials Discovery. *Macromolecules*, 49(13):4675–4690, 6 2016. [13](#)
- [12] A. B. Chang and F. S. Bates. The ABCs of Block Polymers. *Macromolecules*, 53(8):2765–2768, 4 2020. [38](#)
- [13] M. Baake, R. Klitzing, and M. Schlottmann. Fractally shaped acceptance domains of quasiperiodic square-triangle tilings with dedecagonal symmetry. *Physica A: Statistical Mechanics and its Applications*, 191(1-4):554–558, 12 1992. [207](#)
- [14] M. Baake, R. V. Moody, and M. Schlottmann. Limit-(quasi)periodic point sets as quasicrystals with \mathbf{p} -adic internal spaces. *Journal of Physics A: Mathematical and General*, 31(27):5755–5765, 7 1998. [3](#)
- [15] R. C. Ball, J. F. Marko, T. A. Witten, and S. T. Milner. Polymers Grafted to a Convex Surface. *Macromolecules*, 24(3):693–703, 1991. [84](#), [101](#)
- [16] K. Barkan, H. Diamant, and R. Lifshitz. Stability of quasicrystals composed of soft isotropic particles. *Physical Review B - Condensed Matter and Materials Physics*, 83(17):1–4, 2011. [7](#)
- [17] F. S. Bates, R. E. Cohen, and C. V. Berney. Small-Angle Neutron Scattering Determination of Macrolattice Structure in a Polystyrene-Polybutadiene Diblock Copolymer. *Macromolecules*, 1982. [92](#)
- [18] F. S. Bates and G. H. Fredrickson. Block Copolymer Thermodynamics: Theory and Experiment. *Annu. Rev. Phys. Chem.*, 41:525–57, 1990. [13](#)
- [19] F. S. Bates and G. H. Fredrickson. Block Copolymers—Designer Soft Materials. *Physics Today*, 52(2):32–38, 2 1999. [8](#), [9](#)
- [20] D. C. Bentley and A. M. Rucklidge. Localized patterns in a generalized Swift-Hohenberg equation with a quartic marginal stability curve \dagger . *IMA Journal of Applied Mathematics*, 86:944–983, 2021. [53](#)
- [21] L. Bindi, P. J. Steinhardt, N. Yao, and P. J. Lu. Natural quasicrystals. *Science*, 324(5932):1306–1309, 2009. [1](#)
- [22] T. M. Birshtein, A. A. Polotsky, and V. Abetz. Theory of the lamellar superstructure of an ABC 3-miktoarm star-terpolymer. *Macromolecular Theory and Simulations*, 13(6):512–519, 7 2004. [16](#)

REFERENCES

- [23] Y. Bohbot-Raviv and Z.-G. Wang. Discovering new ordered phases of block copolymers. *Physical Review Letters*, 85(16):3428, 2000. [11](#), [15](#), [16](#), [79](#)
- [24] K. A. Brakke. The surface evolver. *Experimental Mathematics*, 1(2):141 – 165, 1992. [228](#)
- [25] J. K. Castelino, D. J. Ratliff, A. M. Rucklidge, P. Subramanian, and C. M. Topaz. Spatiotemporal chaos and quasipatterns in coupled reaction–diffusion systems. *Physica D: Nonlinear Phenomena*, 409:132475, 8 2020. [7](#), [62](#)
- [26] S. Chanpuriya, K. Kim, J. Zhang, S. Lee, A. Arora, K. D. Dorfman, K. T. Delaney, G. H. Fredrickson, and F. S. Bates. Cornucopia of Nanoscale Ordered Phases in Sphere-Forming Tetrablock Terpolymers. *ACS Nano*, 10:11, 2016. [5](#)
- [27] S. Chernyy, J. J. K. Kirkensgaard, J. P. Mahalik, H. Kim, M. M. Arras, R. Kumar, B. G. Sumpster, G. S. Smith, K. Mortensen, T. P. Russell, and K. Almdal. Bulk and Surface Morphologies of ABC Miktoarm Star Terpolymers Composed of PDMS, PI, and PMMA Arms. *Macromolecules*, 51(3):1041–1051, 2018. [9](#), [17](#), [19](#), [100](#), [134](#), [155](#), [164](#), [167](#), [169](#), [187](#), [224](#), [230](#)
- [28] S. J. Cox, F. Graner, R. Mosseri, and J. F. Sadoc. Quasicrystalline three-dimensional foams. *Journal of Physics: Condensed Matter*, 29(11):114001, 2 2017. [128](#), [189](#), [233](#)
- [29] M. De Boissieu. Stability of quasicrystals: Energy, entropy and phason modes. *Philosophical Magazine*, 86(6-8):1115–1122, 2 2006. [1](#)
- [30] L. De Campo, T. Castle, and S. T. Hyde. Optimal packings of Three-Arm star polyphiles: From tricontinuous to quasi-uniformly striped bicontinuous forms. *Interface Focus*, 7(4), 2017. [9](#)
- [31] P. G. De Gennes. Theory of X-ray scattering by liquid macromolecules with heavy atom labels. *Journal de Physique*, 31(2-3):235–238, 1970. [25](#), [29](#)
- [32] M. Doi and S. F. Edwards. *The theory of polymer dynamics*, volume 73. oxford university press, 1988. [25](#), [27](#)
- [33] K. D. Dorfman. Frank-Kasper Phases in Block Polymers. *Macromolecules*, 54(22):10251–10270, 11 2021. [8](#), [9](#), [13](#), [38](#)
- [34] T. Dotera. Mean-field theory of Archimedean and quasicrystalline tilings Mean-field theory of Archimedean and quasicrystalline tilings. *Philosophical Magazine*, 87:3011–3019, 2010. [19](#), [224](#)

REFERENCES

- [35] T. Dotera, S. Bekku, and P. Ziherl. Bronze-mean hexagonal quasicrystal. *Nature Materials* 2017 16:10, 16(10):987–992, 8 2017. [134](#)
- [36] T. Dotera and T. Gemma. Dodecagonal quasicrystal in a polymeric alloy. *Taylor & Francis Group*, 86(6-8):1085–1091, 2 2006. [17](#), [18](#), [19](#)
- [37] T. Dotera and A. Hatano. The diagonal bond method: A new lattice polymer model for simulation study of block copolymers . *J. Chem. Phys.*, 105:8413–8427, 1996. [16](#)
- [38] T. Dotera, T. Oshiro, and P. Ziherl. Mosaic two-lengthscale quasicrystals. *Nature*, 506(7487):208–211, 2014. [5](#), [191](#)
- [39] T. Dotera and P. J. Steinhardt. Ising-like transition and phason unlocking in icosahedral quasicrystals. *Physical Review Letters*, 72(11):1670, 3 1994. [8](#)
- [40] C. Duan, M. Zhao, Y. Qiang, L. Chen, W. Li, F. Qiu, and A.-C. Shi. Stability of Two-Dimensional Dodecagonal Quasicrystalline Phase of Block Copolymers. *Macromolecules*, 51(19):7713–7721, 9 2018. [8](#)
- [41] W. S. Edwards and S. Fauve. Patterns and quasi-patterns in the Faraday experiment. *Journal of Fluid Mechanics*, 278(II):123–148, 11 1994. [3](#)
- [42] M. Engel, P. F. Damasceno, C. L. Phillips, and S. C. Glotzer. Computational self-assembly of a one-component icosahedral quasicrystal. *Nat. Mater.*, 14, 2015. [5](#)
- [43] I. Y. Erukhimovich. Weak segregation theory and non-conventional morphologies in the ternary ABC triblock copolymers. *Eur. Phys. J. E*, 18:383–406, 2005. [11](#), [79](#), [232](#)
- [44] M. Faber, V. S. D. Voet, G. ten Brinke, and K. Loos. Preparation and self-assembly of two-length-scale A-b-(B-b-A)_n-b-B multiblock copolymers. *Soft Matter*, 8(16):4479, 2012. [13](#), [228](#)
- [45] E. Fayen, M. Imp eror-Clerc, L. Filion, G. Foffi, and F. Smallenburg. Self-assembly of dodecagonal and octagonal quasicrystals in hard spheres on a plane . *Soft Matter*, 19:2654, 2023. [3](#), [4](#), [62](#)
- [46] X. S. Feng and C. Y. Pan. Block and star block copolymers by mechanism transformation. 7. Synthesis of polytetrahydrofuran/poly(1,3-dioxepane)/polystyrene ABC miktoarm star copolymers by combination of CROP and ATRP. *Macromolecules*, 35(6), 2002. [4](#)

REFERENCES

- [47] S. Fischer, A. Exner, K. Zielske, J. Perlich, S. Deloudi, W. Steurer, P. Lindner, and S. Förstere. Colloidal quasicrystals with 12-fold and 18-fold diffraction symmetry. *Proceedings of the National Academy of Sciences of the United States of America*, 108(5):1810–1814, 2011. [3](#), [4](#), [62](#)
- [48] G. H. Fredrickson and E. Helfand. Block copolymer microstructures in the intermediate-segregation regime. *Citation: The Journal of Chemical Physics*, 87(November 1996), 1987. [10](#)
- [49] T. Fujimoto, H. Zhang, T. Kazama, Y. Isono, H. Hasegawa, and T. Hashimoto. Preparation and characterization of novel star-shaped copolymers having three different branches. *Polymer*, 33(10):2208–2213, 1992. [15](#)
- [50] T. Gemma, A. Hatano, and T. Dotera. Monte Carlo simulations of the morphology of ABC star polymers using the diagonal bond method. *Macromolecules*, 35(8):3225–3237, 2002. [13](#), [16](#), [18](#), [19](#), [72](#), [79](#), [100](#), [108](#), [115](#), [127](#), [134](#), [155](#), [164](#), [167](#), [173](#), [187](#), [188](#)
- [51] T. M. Gillard, S. Lee, and F. S. Bates. Dodecagonal quasicrystalline order in a diblock copolymer melt. *Proceedings of the National Academy of Sciences*, 113(19):5167–5172, 5 2016. [4](#), [5](#)
- [52] R. D. Groot and P. B. Warren. Dissipative particle dynamics: Bridging the gap between atomistic and mesoscopic simulation. *Journal of Chemical Physics*, 107(11):4423–4435, 9 1997. [231](#)
- [53] B. Grünbaum and G. Shephard. Tilings and patterns. *WH Freeman, New York*, 1987. [viii](#), [3](#), [192](#)
- [54] N. Hadjichristidis, H. Iatrou, S. K. Behal, J. J. Chludzinski, M. M. Disko, R. T. Garner, K. S. Liang, D. J. Lohse, and S. T. Milner. Morphology and Miscibility of Miktoarm Styrene-Diene Copolymers and Terpolymers. *Macromolecules*, 26(21), 1993. [15](#)
- [55] A. Haji-Akbari, M. Engel, and S. C. Glotzer. Phase diagram of hard tetrahedra. *Journal of Chemical Physics*, 135(19), 2011. [5](#)
- [56] I. W. Hamley. *The physics of block copolymers*. Oxford University Press, 1998. [10](#)
- [57] K. Hayashida, T. Dotera, A. Takano, and Y. Matsushita. Polymeric Quasicrystal: Mesoscopic Quasicrystalline Tiling in A B C Star Polymers. *Physical Review Letters*, 98(19):195502, 5 2007. [3](#), [5](#), [6](#), [7](#), [8](#), [17](#), [19](#), [62](#), [72](#), [83](#), [134](#), [191](#), [194](#), [195](#), [196](#), [202](#), [209](#), [213](#), [215](#), [224](#), [225](#), [226](#), [228](#), [229](#), [234](#)

REFERENCES

- [58] K. Hayashida, A. Takano, S. Arai, Y. Shinohara, Y. Amemiya, and Y. Matsushita. Systematic Transitions of Tiling Patterns Formed by ABC Star-Shaped Terpolymers. *Macromolecules*, 39(26):9402–9408, 12 2006. [3](#), [4](#), [17](#), [207](#)
- [59] X. He, L. Huang, and H. Liang. Localizations of junction points of 3-miktoarm star terpolymers. *J. Chem. Phys.*, 118:9861, 2003. [15](#)
- [60] E. Helfand and Y. Tagami. Theory of the Interface between Immiscible Polymers. II. *Journal of Chemical Physics*, 56:1812, 1972. [88](#), [108](#)
- [61] J. Hermisson, C. Richard, and M. Baake. A Guide to the Symmetry Structure of Quasiperiodic Tiling Classes. *Journal de Physique I*, 7(8):1003–1018, 8 1997. [201](#), [204](#)
- [62] C.-I. Huang, H.-K. Fang, and C.-H. Lin. Morphological transition behavior of ABC star copolymers by varying the interaction parameters. *Physical review E*, 77, 2008. [100](#)
- [63] C. I. Huang and H. T. Yu. Microphase separation and molecular conformation of AB₂ miktoarm star copolymers by dissipative particle dynamics. *Polymer*, 48(15):4537–4546, 7 2007. [17](#), [18](#)
- [64] M. Huang, K. Yue, J. Wang, C.-H. Hsu, L. Wang, S. Z. D Cheng, and C. SZD Frank-Kasper and. Frank-Kasper and related quasicrystal spherical phases in macromolecules. *Soft Matter Science and Technology*, 61(1):61, 2018. [5](#)
- [65] M. Huang, K. Yue, J. Wang, C.-H. Hsu, L. Wang, S. Z. D Cheng, and C. SZD Frank-Kasper and. Frank-Kasper and related quasicrystal spherical phases in macromolecules. *Soft Matter Science and Technology*, 61(1):61, 2018. [9](#)
- [66] H. Hückstädt, A. Göpfert, and V. Abetz. Synthesis and morphology of ABC heteroarm star terpolymers of polystyrene, polybutadiene and poly(2-vinylpyridine). *Macromolecular Chemistry and Physics*, 201:296–307, 2000. [15](#), [16](#)
- [67] H. Hückstädt, V. Abetz, and R. Stadler. Synthesis of a polystyrene-arm-polybutadiene-arm-poly(methyl methacrylate) triarm star copolymer. *Macromolecular Rapid Communications*, 17(8):599–606, 1996. [15](#)
- [68] C. R. Iacovella, A. S. Keys, and S. C. Glotzer. Self-assembly of soft-matter quasicrystals and their approximants. *Proceedings of the National Academy of Sciences of the United States of America*, 108(52):20935–20940, 12 2011. [5](#)

REFERENCES

- [69] H. Iatrou and N. Hadjichristidis. Synthesis of a model 3-miktoarm star terpolymer. *Macromolecules*, 25(18):4649–4651, 1992. 15
- [70] M. Impéror-Clerc. A liquid quasicrystal of columns. *Nature Chemistry 2023* 15:5, 15(5):591–592, 4 2023. 4, 226, 234
- [71] M. Impéror-Clerc, A. Jagannathan, P. Kalugin, and J. F. Sadoc. Square-triangle tilings: an infinite playground for soft matter. *Soft Matter*, 17(42):9560–9575, 11 2021. 3, 4, 8, 83, 192, 201, 234
- [72] T. Ishimasa. Dodecagonal Quasicrystals Still in Progress. *Israel Journal of Chemistry*, 51(11-12):1216–1225, 12 2011. 191, 207, 212, 215
- [73] IUCr. Report of the Executive Committee for 1991. *Acta Crystallographica Section A*, 48(6):922–946, 11 1992. 1
- [74] A. Jayaraman, C. M. Baez-Cotto, T. J. Mann, and M. K. Mahanthappa. Dodecagonal quasicrystals of oil-swollen ionic surfactant micelles. *Proceedings of the National Academy of Sciences of the United States of America*, 118(31), 8 2021. 4
- [75] K. Jiang, J. Zhang, and Q. Liang. Self-Assembly of Asymmetrically Interacting ABC Star Triblock Copolymer Melts. *Journal of Physical Chemistry B*, 119(45):14551–14562, 11 2015. 13, 17, 19, 174, 180, 183, 187, 200, 233
- [76] K. Jiang, P. Zhang, and A. C. Shi. Stability of icosahedral quasicrystals in a simple model with two-length scales. *Journal of Physics Condensed Matter*, 29(12), 2017. 7
- [77] Z. Jiang, S. Quan, N. Xu, L. He, and Y. Ni. Growth modes of quasicrystals involving intermediate phases and a multistep behavior studied by phase field crystal model. *Physical Review Materials*, 4(2):023403, 2 2020. 7
- [78] M. Kalman. The Quasicrystal Laureate, Nobel Prize winner Dan Shechtman discusses the potential uses for quasicrystals. <https://www.technologyreview.com/2011/10/12/190784/the-quasicrystal-laureate/>, 10 2011. 2
- [79] J. K. Kim, K. Kimishima, and T. Hashimoto. Random-Phase Approximation Calculation of the Scattering Function for Multicomponent Polymer Systems. *Macromolecules*, 26(1):125–136, 1993. 10
- [80] J. J. K. Kirkensgaard. Kaleidoscopic tilings, networks and hierarchical structures in blends of 3-miktoarm star terpolymers. *Interface Focus*, 2(5):602–607, 10 2012. 100, 200

REFERENCES

- [81] J. J. K. Kirkensgaard, M. C. Pedersen, and S. T. Hyde. Tiling patterns from ABC star molecules: 3-colored foams? *Soft Matter*, 10(37):7182–7194, 2014. [17](#), [18](#), [19](#), [100](#), [187](#), [188](#), [194](#), [231](#), [233](#)
- [82] Y. A. Kriksin, I. Y. Erukhimovich, P. G. Khalatur, Y. G. Smirnova, and G. Ten Brinke. Nonconventional morphologies in two-length scale block copolymer systems beyond the weak segregation theory. *The Journal of Chemical Physics*, 128(24):244903, 6 2008. [11](#)
- [83] S. Kuchanov, V. Pichugin, and G. Ten Brinke. Phase transitions in block copolymers resulting in a discontinuous change of the spatial period of mesophases. *Europhysics Letters*, 76(5):959–964, 2006. [10](#), [53](#), [61](#)
- [84] H. Kyoon Choi, A. Nunns, X. Yin Sun, I. Manners, C. A. Ross, H. K. Choi, X. Y. Sun, C. A. Ross, A. Nunns, and I. Manners. Thin Film Knitting Pattern Morphology from a Miktoarm Star Terpolymer. *Advanced Materials*, 26(16):2474–2479, 4 2014. [17](#)
- [85] O. Lambert, S. Reutenauer, G. Hurtrez, G. Riess, and P. Dumas. Synthesis of amphiphilic triarm star block copolymers. *Polymer Bulletin*, 40(2-3):143–149, 1998. [15](#)
- [86] S. Lee, M. J. Bluemle, and F. S. Bates. Discovery of a Frank-Kasper σ Phase in Sphere-Forming Block Copolymer Melts. *New Series*, 330(6002):349–353, 2010. [9](#), [233](#)
- [87] L. Leibler. Theory of Microphase Separation in Block Copolymers. *Macromolecules*, 13(6):1602–1617, 1980. [8](#), [9](#), [10](#), [12](#), [23](#), [26](#), [84](#), [89](#), [92](#), [232](#)
- [88] D. Levine and P. J. Steinhardt. Quasicrystals: A new class of ordered structures. *Physical Review Letters*, 53(26):2477–2480, 1984. [3](#)
- [89] S. Li, Y. Jiang, and J. Z. Chen. Morphologies and phase diagrams of ABC star triblock copolymers confined in a spherical cavity. *Soft Matter*, 9(19):4843–4854, 4 2013. [17](#)
- [90] W. Li, C. Duan, and A. C. Shi. Nonclassical Spherical Packing Phases Self-Assembled from AB-Type Block Copolymers. *ACS Macro Letters*, 6(11):1257–1262, 11 2017. [233](#)
- [91] W. Li, Y. Xu, G. Zhang, F. Qiu, Y. Yang, and A. C. Shi. Real-space self-consistent mean-field theory study of ABC star triblock copolymers. *Journal of Chemical Physics*, 133(6), 8 2010. [17](#), [18](#), [19](#), [100](#), [134](#), [155](#), [164](#), [167](#), [169](#), [173](#), [187](#), [191](#), [194](#), [197](#), [200](#), [224](#), [230](#), [233](#)

REFERENCES

- [92] R. Lifshitz and D. M. Petrich. Theoretical Model for Faraday Waves with Multiple-Frequency Forcing. *Physical Review Letters*, 79(7):1261–1264, 4 1997. [6](#)
- [93] A. P. Lindsay, R. M. Lewis, B. Lee, A. J. Peterson, T. P. Lodge, and F. S. Bates. A15, σ , and a Quasicrystal: Access to Complex Particle Packings via Bidisperse Diblock Copolymer Blends. *ACS Macro Letters*, 9(2):197–203, 2 2020. [5](#), [9](#), [233](#)
- [94] A. L. Mackay. Crystallography and the penrose pattern. *Physica A: Statistical Mechanics and its Applications*, 114(1-3):609–613, 8 1982. [2](#)
- [95] W. Man, M. Megens, P. J. Steinhardt, and P. M. Chaikin. Experimental measurement of the photonic properties of icosahedral quasicrystals. *Nature*, 436, 2005. [2](#)
- [96] M. W. Matsen. Gyroid versus double-diamond in ABC triblock copolymer melts. *The Journal of Chemical Physics, J.Chem. Phys.*, 108:2436, 1998. [9](#)
- [97] M. W. Matsen and F. S. Bates. Unifying weak- and strong-segregation block copolymer theories. *Macromolecules*, 29(4):1091–1098, 1996. [13](#), [84](#), [89](#)
- [98] M. W. Matsen, F. S. Bates, and B. Copolymers. Block copolymer microstructures in the intermediate-segregation regime. *Designer Soft Materials Physics Today*, 106:7139, 1997. [23](#), [108](#)
- [99] Y. Matsushita. Creation of Hierarchically Ordered Nanophase Structures in Block Polymers Having Various Competing Interactions. *Macromolecules*, 40(4):771–776, 2 2007. [17](#), [174](#), [187](#)
- [100] Y. Matsushita. Creation of Hierarchically Ordered Nanophase Structures in Block Polymers Having Various Competing Interactions. *Macromolecules*, 40, 2007. [180](#)
- [101] Y. Matsushita, K. Hayashida, T. Dotera, and A. Takano. Kaleidoscopic morphologies from ABC star-shaped terpolymers. *Journal of Physics: Condensed Matter*, 23(28):284111, 7 2011. [17](#), [79](#)
- [102] Y. Matsushita, K. Hayashida, and A. Takano. Jewelry Box of Morphologies with Mesoscopic Length Scales – ABC Star-shaped Terpolymers. *Macromolecular Rapid Communications*, 31(18):1579–1587, 9 2010. [17](#), [174](#), [180](#), [233](#)
- [103] J. Mikhael, J. Roth, L. Helden, and C. Bechinger. Archimedean-like tiling on decagonal quasicrystalline surfaces. *Nature*, 454, 2008. [4](#)

REFERENCES

- [104] H. Miyase, Y. Asai, A. Takano, and Y. Matsushita. Kaleidoscopic Tiling Patterns with Large Unit Cells from ABC Star-Shaped Terpolymer/Diblock Copolymer Blends with Hydrogen Bonding Interaction. *Macromolecules*, 50(3):979–986, 2017. [174](#)
- [105] Y. Mogi, H. Kotsuji, Y. Kaneko, K. Mori, Y. Matsushita, and I. Noda. Preparation and morphology of triblock copolymers of the abc type. *Macromolecules*, 25(20):5408–5411, 1992. [15](#)
- [106] D. Moschovas, G.-M. Manesi, A. Karydis-Messinis, G. Zapsas, K. Ntetsikas, N. E. Zafeiropoulos, A. A. Pirayazev, E. L. Thomas, N. Hadjichristidis, D. A. Ivanov, and A. Avgeropoulos. Alternating gyroid network structure in an abc miktoarm terpolymer comprised of polystyrene and two polydienes. *Nanomaterials*, 10:1497, 7 2020. [9](#)
- [107] A. J. Mueller, A. P. Lindsay, A. Jayaraman, T. P. Lodge, M. K. Mahanthappa, and F. S. Bates. Quasicrystals and their approximants in a crystalline–amorphous diblock copolymer. *Macromolecules*, 54:2647–2660, 3 2021. [5](#)
- [108] R. Nap, I. Erukhimovich, and G. T. Brinke. Self-assembling block copolymer systems involving competing length scales: A route toward responsive materials. *Macromolecules*, 37(11):4296–4303, 6 2004. [232](#)
- [109] R. Nap, N. Sushko, I. Erukhimovich, and G. ten Brinke. Double Periodic Lamellar-in-Lamellar Structure in Multiblock Copolymer Melts with Competing Length Scales. *Macromolecules*, 39(19):6765–6770, 9 2006. [11](#), [13](#), [61](#), [62](#)
- [110] R. J. Nap, C. Kok, G. Ten Brinke, and S. I. Kuchanov. Microphase separation at two length scales. *Eur. Phys. J. E*, 4:515–519, 2001. [10](#), [53](#), [61](#), [227](#), [232](#)
- [111] N. Niizeki and H. Mitani. Two-dimensional dodecagonal quasilattices. *Journal of Physics A: Mathematical and General*, 20(6):L405–L410, 4 1987. [192](#)
- [112] J. Nocedal and S. J. Wright. *Numerical Optimization Second Edition*. Springer, 2006. [145](#)
- [113] P. Nozières and D. Pines. Electron interaction in solids. the nature of the elementary excitations. *Physical Review*, 1958. [25](#)
- [114] A. Nunns, C. A. Ross, and I. Manners. Synthesis and bulk self-assembly of ABC star terpolymers with a polyferrocenylsilane metalloblock. *Macromolecules*, 46(7):2628–2635, 4 2013. [17](#), [174](#), [180](#), [187](#), [188](#)

REFERENCES

- [115] T. Ohta and K. Kawasaki. Equilibrium Morphology of Block Copolymer Melts. *Macromolecules*, 19(10):2621–2632, 10 1986. [13](#)
- [116] S. Okamoto, H. Hasegawa, T. Hashimoto, T. Fujimoto, H. Zhang, T. Kazama, A. Takano, and Y. Isono. Morphology of model three-component three-arm star-shaped copolymers. *Polymer*, 38(21):5275–5281, 1997. [16](#)
- [117] P. D. Olmsted and S. T. Milner. Strong segregation theory of bicontinuous phases in block copolymers. *Macromolecules*, 31(12):4011–4022, 1998. [9](#), [12](#), [83](#), [84](#), [89](#), [92](#), [93](#), [99](#), [241](#), [243](#)
- [118] M. Oxborrow and C. L. Henley. Random square-triangle tilings: A model for twelfold-symmetric quasicrystals. *Physical Review B*, 48(10):6966–6998, 9 1993. [8](#), [201](#)
- [119] P. Stampfli. A dodecagonal quasiperiodic lattice in two dimensions. *Helvetica Physica Acta*, 1986. [3](#), [8](#), [192](#), [201](#), [223](#), [226](#)
- [120] H. Pattabhiraman and M. Dijkstra. Phase behaviour of quasicrystal forming systems of core-corona particles. *The Journal of Chemical Physics*, 146:114901, 2017. [5](#)
- [121] R. W. Pennisi and L. J. Fetters. Preparation of asymmetric 3-arm polybutadiene and polystyrene stars. *Macromolecules*, 21(4):1094–1099, 1988. [15](#)
- [122] R. Penrose. The role of aesthetics in pure and applied mathematical research. *Bull. Inst. Math. Appl.*, 10:266–271, 1974. [2](#)
- [123] C. L. Phillips, J. A. Anderson, and S. C. Glotzer. Pseudo-random number generation for Brownian Dynamics and Dissipative Particle Dynamics simulations on GPU devices. *Journal of Computational Physics*, 230(19):7191–7201, 8 2011. [231](#)
- [124] A. Plati, R. Maire, E. Fayen, F. Boulogne, F. Restagno, F. Smallenburg, and G. Foffi. Quasi-crystalline order in vibrated granular matter. 7 2023. [4](#)
- [125] D. J. Ratliff, A. J. Archer, P. Subramanian, and A. M. Rucklidge. Which Wave Numbers Determine the Thermodynamic Stability of Soft Matter Quasicrystals? *Physical Review Letters*, 123(14):148004, 10 2019. [7](#)
- [126] D. J. Read. Mean field theory for phase separation during polycondensation reactions and calculation of structure factors for copolymers of arbitrary architecture. *Macromolecules*, 31(3):899–911, 1998. [41](#), [42](#), [64](#), [65](#), [73](#)

REFERENCES

- [127] D. J. Read, M. G. Brereton, and T. C. McLeish. Theory of the Order-Disorder Phase Transition in Cross-Linked Polymer Blends. *Journal de Physique II*, 1995. [63](#)
- [128] M. Rubinstein and R. H. Colby. Polymer physics, 2003. [24](#), [25](#), [36](#)
- [129] A. M. Rucklidge and M. Silber. Quasipatterns in parametrically forced systems. *Physical Review E*, 75(5):1–4, 2007. [7](#)
- [130] A. M. Rucklidge and M. Silber. Design of Parametrically Forced Patterns and Quasipatterns. *SIAM Journal on Applied Dynamical Systems*, 8(1):43, 2009. [3](#)
- [131] A. M. Rucklidge, M. Silber, and A. C. Skeldon. Three-wave interactions and spatiotemporal chaos. *Physical Review Letters*, 108(7), 2012. [7](#)
- [132] J. Ruokolainen, M. Saariaho, O. Ikkala, G. ten Brinke, E. L. Thomas, M. Torkkeli, and R. Serimaa. Supramolecular Routes to Hierarchical Structures: "Comb-Coil Diblock Copolymers Organized with Two Length Scales. *Macromolecules*, 32(4):1152–1158, 2 1999. [13](#)
- [133] J. F. Sadoc and R. Mosseri. Quasiperiodic Frank–Kasper phases derived from the square–triangle dodecagonal tiling. *Structural Chemistry*, 28(1):63–73, 2 2017. [5](#)
- [134] S. Savitz, M. Babadi, R. Lifshitz, C. Raymond, and B. Sackler. Multiple-scale structures: from Faraday waves to soft-matter quasicrystals. *Topical Reviews IUCrJ*, 5:247–268, 2018. [7](#)
- [135] A. Scacchi, W. R. Somerville, D. M. Buzza, and A. J. Archer. Quasicrystal formation in binary soft matter mixtures. *Physical Review Research*, 2(3), 2020. [5](#), [7](#)
- [136] M. Schlottmann. Tilings Encyclopedia | Square-triangle. <https://tilings.math.uni-bielefeld.de/substitution/square-triangle/>. [192](#), [202](#)
- [137] M. W. Schulze, R. M. Lewis, J. H. Lettow, R. J. Hickey, T. M. Gillard, M. A. Hillmyer, and F. S. Bates. Conformational Asymmetry and Quasicrystal Approximants in Linear Diblock Copolymers. *Physical Review Letters*, 118(20):207801, 5 2017. [5](#), [8](#)
- [138] A. N. Semenov. Contribution to the theory of microphase layering in block-copolymer melts. *Zh. Eksp. Teor. Fiz*, 88(November 1984):1242–1256, 1985. [11](#), [12](#), [23](#), [83](#), [89](#), [92](#)

REFERENCES

- [139] M. Senechal. *Quasicrystals and geometry*. CUP Archive, 1996. [2](#)
- [140] D. Shechtman, I. Blech, D. Gratias, and J. W. Cahn. Metallic phase with long-range orientational order and no translational symmetry. *Physical Review Letters*, 1984. [1](#), [2](#)
- [141] A.-C. Shi. Frustration in block copolymer assemblies. *Journal of Physics: Condensed Matter*, 33(25):253001, 6 2021. [13](#)
- [142] A. D. Sinelnik, I. I. Shishkin, X. Yu, K. B. Samusev, P. A. Belov, M. F. Limonov, P. Ginzburg, and M. V. Rybin. Experimental Observation of Intrinsic Light Localization in Photonic Icosahedral Quasicrystals. *Advanced Optical Materials*, 8(21), 11 2020. [6](#)
- [143] S. Sioula, N. Hadjichristidis, and E. L. Thomas. Direct Evidence for Confinement of Junctions to Lines in an 3 Miktoarm Star Terpolymer Microdomain Structure. *Macromolecules*, 31(23):8429–8432, 10 1998. [15](#), [16](#), [17](#)
- [144] S. Sioula, N. Hadjichristidis, and E. L. Thomas. Novel 2-dimensionally periodic non-constant mean curvature morphologies of 3-miktoarm star terpolymers of styrene, isoprene, and methyl methacrylate. *Macromolecules*, 31(16):5272–5277, 8 1998. [16](#)
- [145] S. Sioula, Y. Tselikas, and N. Hadjichristidis. Synthesis of Model 3-Miktoarm Star Terpolymers of Styrene, Isoprene, and Methyl Methacrylate. *Macromolecules*, 30(5):1518–1520, 3 1997. [15](#)
- [146] D. Smith, J. S. Myers, C. S. Kaplan, and C. Goodman-Strauss. An aperiodic monotile. 2023. [2](#)
- [147] W. R. C. Somerville, A. D. Law, M. Rey, N. Vogel, A. J. Archer, D. Martin, and A. Buzza. Pattern formation in two-dimensional hard-core/ soft-shell systems with variable soft shell profiles . *Soft Matter*, 16:3564, 2020. [5](#)
- [148] W. Steurer. Quasicrystals: What do we know ? What do we want to know? What can we know?. *Acta Crystallographica Section A*, 74(1):1–11, Jan 2018. [1](#), [3](#)
- [149] W. Steurer and D. Sutter-Widmer. Photonic and phononic quasicrystals. *Journal of Physics D: Applied Physics*, 40(13):R229–R247, 7 2007. [2](#)
- [150] Y. Su, X. Rong, H. Li, X. Huang, L. Chen, B. Liu, and Y. S. Hu. High-Entropy Microdomain Interlocking Polymer Electrolytes for Advanced All-Solid-State Battery Chemistries. *Advanced Materials*, 35(1):2209402, 1 2023. [19](#)

REFERENCES

- [151] P. Subramanian, A. J. Archer, E. Knobloch, and A. M. Rucklidge. Three-Dimensional Icosahedral Phase Field Quasicrystal. *Physical Review Letters*, 117(7):0–5, 2016. [7](#)
- [152] Y. Sun, K. Ma, T. Kao, K. A. Spoth, H. Sai, D. Zhang, L. F. Kourkoutis, V. Elser, and U. Wiesner. Formation pathways of mesoporous silica nanoparticles with dodecagonal tiling. *Nature Communications*, 8(1), 2017. [4](#)
- [153] Y. Sun, R. Tan, Z. Ma, Z. Gan, G. Li, D. Zhou, Y. Shao, W.-B. Zhang, R. Zhang, and X.-H. Dong. Discrete Block Copolymers with Diverse Architectures: Resolving Complex Spherical Phases with One Monomer Resolution. *ACS Central Science*, 6(8):1386–1393, 7 2020. [5](#)
- [154] S. T. Milner, T. A. Witten, and M. E. Cates. Theory of the grafted polymer brush. *Macromolecules*, 21(8):2610–2619, 5 2002. [86](#)
- [155] H. Takagi, R. Hashimoto, N. Igarashi, S. Kishimoto, and K. Yamamoto. Frank–Kasper σ phase in polybutadiene-poly(ϵ -caprolactone) diblock copolymer/polybutadiene blends. *Journal of Physics: Condensed Matter*, 29(20):204002, 5 2017. [9](#)
- [156] A. Takano, W. Kawashima, A. Noro, Y. Isono, N. Tanaka, T. Dotera, and Y. Matsushita. A Mesoscopic Archimedean Tiling Having a New Complexity in an ABC Star Polymer. *J Polym Sci Part B: Polym Phys*, 43:2427–2432, 2005. [17](#), [100](#)
- [157] A. Takano, S. Wada, S. Sato, T. Araki, K. Hirahara, T. Kazama, S. Kawahara, Y. Isono, A. Ohno, N. Tanaka, and Y. Matsushita. Observation of Cylinder-Based Microphase-Separated Structures from ABC Star-Shaped Terpolymers Investigated by Electron Computerized Tomography. *Macromolecules*, 37(26):9941–9946, 12 2004. [16](#), [174](#)
- [158] D. V. Talapin, E. V. Shevchenko, M. I. Bodnarchuk, X. Ye, J. Chen, and C. B. Murray. Quasicrystalline order in self-assembled binary nanoparticle superlattices. *Nature*, 2009. [4](#)
- [159] P. Tang, F. Qiu, H. Zhang, and Y. Yang. Morphology and phase diagram of complex block copolymers: ABC star triblock copolymers. *Journal of Physical Chemistry B*, 108(24):8434–8438, 6 2004. [18](#), [79](#), [100](#), [115](#), [155](#), [194](#)
- [160] S. Tang, Z. Wang, J. Wang, K. Jiang, C. Liang, Y. Ma, W. Liu, and Y. Du. An atomic scale study of two-dimensional quasicrystal nucleation controlled by multiple length scale interactions. *5718 / Soft Matter*, 16:5718, 2020. [7](#)

REFERENCES

- [161] A.-P. Tsai, A. Inoue, and T. Masumoto. A Stable Quasicrystal in Al-Cu-Fe System. *Japanese Journal of Applied Physics*, 26(9A):L1505, 9 1987. [1](#), [3](#)
- [162] K. Ueda, T. Dotera, and T. Gemma. Photonic band structure calculations of two-dimensional Archimedean tiling patterns. *Physical Review B*, 75(195122), 2007. [19](#), [197](#), [200](#)
- [163] J. I. Urgel, D. Écija, G. Lyu, R. Zhang, C. A. Palma, W. Auwärter, N. Lin, and J. V. Barth. Quasicrystallinity expressed in two-dimensional coordination networks. *Nature Chemistry 2016 8:7*, 8(7):657–662, 5 2016. [4](#)
- [164] M. S. Vitiello, M. Nobile, A. Ronzani, A. Tredicucci, F. Castellano, V. Talora, L. Li, E. H. Linfield, and A. G. Davies. Photonic quasi-crystal terahertz lasers. *Nature Communications*, 5, 2014. [6](#)
- [165] M. C. Walters, P. Subramanian, A. J. Archer, and R. Evans. Structural crossover in a model fluid exhibiting two length scales: Repercussions for quasicrystal formation. *Physical Review E*, 98(1):012606, 7 2018. [7](#)
- [166] N. Wang, H. Chen, and K. H. Kuo. Two-dimensional quasicrystal with eightfold rotational symmetry. *Physical Review Letters*, 59(9):1010–1013, 8 1987. [3](#)
- [167] C. Xiao, N. Fujita, K. Miyasaka, Y. Sakamoto, and O. Terasaki. Dodecagonal tiling in mesoporous silica. *Nature*, 487(7407):349–353, 7 2012. [4](#)
- [168] W. Xu, K. Jiang, P. Zhang, and A.-C. Shi. A Strategy to Explore Stable and Metastable Ordered Phases of Block Copolymers. *The Journal of Physical Chemistry B*, 117(17):5296–5305, 4 2013. [17](#)
- [169] K. Yue, M. Huang, R. L. Marson, J. Hec, J. Huang, Z. Zhou, J. Wang, C. Liu, X. Yan, K. Wu, Z. Guo, H. Liu, W. Zhang, P. Ni, C. Wesdemiotis, W. B. Zhang, S. C. Glotzer, and S. Z. Cheng. Geometry induced sequence of nanoscale Frank-Kasper and quasicrystal mesophases in giant surfactants. *Proceedings of the National Academy of Sciences of the United States of America*, 113(50):14195–14200, 2016. [4](#), [5](#)
- [170] X. Zeng, B. Glettner, U. Baumeister, B. Chen, G. Ungar, F. Liu, and C. Tschierske. A columnar liquid quasicrystal with a honeycomb structure that consists of triangular, square and trapezoidal cells. *Nature Chemistry 2023 15:5*, 15(5):625–632, 3 2023. [4](#), [200](#), [226](#), [234](#)
- [171] X. Zeng and G. Ungar. Philosophical Magazine Inflation rules of square-triangle tilings: from approximants to dodecagonal liquid quasicrystals. *Philosophical Magazine*, 86(6–8):1093–1103 Inflation, 2006. [192](#), [207](#)

REFERENCES

- [172] X. Zeng, G. Ungar, Y. Liu, V. Percec, A. E. Dulcey, and J. K. Hobbs. Supramolecular dendritic liquid quasicrystals. *Nature*, 428(6979):157–160, 2004. [3](#), [7](#), [62](#), [191](#), [226](#)
- [173] G. Zhang, F. Qiu, H. Zhang, Y. Yang, and A. C. Shi. SCFT study of tiling patterns in ABC star terpolymers. *Macromolecules*, 43(6):2981–2989, 2010. [17](#), [19](#), [173](#), [174](#), [180](#), [187](#)
- [174] J. Zhang and F. S. Bates. Dodecagonal Quasicrystalline Morphology in a Poly(styrene- b -isoprene- b -styrene- b -ethylene oxide) Tetrablock Terpolymer. *Journal of the American Chemical Society*, 134(18):7636–7639, 5 2012. [5](#)
- [175] B. Zhao, W. Jiang, L. Chen, W. Li, F. Qiu, and A. C. Shi. Emergence and Stability of a Hybrid Lamella-Sphere Structure from Linear ABAB Tetrablock Copolymers. *ACS Macro Letters*, 7(1):95–99, 1 2018. [62](#)